



THE HONG KONG
POLYTECHNIC UNIVERSITY

香港理工大學

Pao Yue-kong Library

包玉剛圖書館

Copyright Undertaking

This thesis is protected by copyright, with all rights reserved.

By reading and using the thesis, the reader understands and agrees to the following terms:

1. The reader will abide by the rules and legal ordinances governing copyright regarding the use of the thesis.
2. The reader will use the thesis for the purpose of research or private study only and not for distribution or further reproduction or any other purpose.
3. The reader agrees to indemnify and hold the University harmless from and against any loss, damage, cost, liability or expenses arising from copyright infringement or unauthorized usage.

IMPORTANT

If you have reasons to believe that any materials in this thesis are deemed not suitable to be distributed in this form, or a copyright owner having difficulty with the material being included in our database, please contact lbsys@polyu.edu.hk providing details. The Library will look into your claim and consider taking remedial action upon receipt of the written requests.

FRP-COATED STEEL REBARS FOR DURABLE
CONCRETE STRUCTURES: DEVELOPMENT
AND PERFORMANCE

ZHANG YIWEN

PhD

The Hong Kong Polytechnic University

2024

The Hong Kong Polytechnic University
Department of Civil and Environmental Engineering

FRP-coated Steel Rebars for Durable Concrete Structures:
Development and Performance

Zhang Yiwen

A thesis submitted in partial fulfillment of the requirements for
the degree of Doctor of Philosophy
August 2023

CERTIFICATE OF ORIGINALITY

I hereby declare that this thesis is my own work and that, to the best of my knowledge and belief, it reproduces no material previously published or written, nor material that has been accepted for the award of any other degree or diploma, except where due acknowledgment has been made in the text.

Signature: _____

Name of Student: Zhang Yiwen

DEDICATION

*To my family
For their love and support*

ABSTRACT

Many possibilities have been explored to enhance the durability of RC structures, and a common approach is the use of corrosion-resistant rebars, including stainless steel rebars, fibre-reinforced polymer (FRP) rebars, galvanized steel rebars and epoxy-coated steel rebars. However, these existing solutions suffer from high costs and/or various performance issues (e.g., inadequate durability of epoxy-coated steel rebars and brittleness of FRP rebars). Against this background, this PhD thesis presents the results from a research programme concerned with the development and performance of a new type of rebars that are both highly durable and cost-effective. These novel rebars, referred to as FRP-coated steel rebars (FCSRs), consist of a steel rebar as the core component and a thin FRP layer (i.e., the FRP coating layer) formed using the filament winding technique.

Two methods for manufacturing FCSRs were first explored in this research programme: filament winding with in-line resin impregnation and filament winding with vacuum-assisted resin infusion. The influence of winding configuration, i.e., the number of fibre plies and the fibre winding angle(s), on the microstructure of both the coating-steel interface and coating layer was investigated. The physical properties of the FRP coating layer, including its glass transition temperature coefficient of thermal expansion, roughness, and thickness were examined. The mechanical properties, including the tensile and compressive properties of FCSRs, were also studied. The in-line resin impregnation option was chosen as the preferred method for further investigations based on the test results.

The second part of this PhD research programme was focused on the corrosion and impact resistance of FCSRs. Electrochemical tests were utilised to understand the corrosion state and evolution of FCSRs. The test results were compared with those of uncoated/epoxy-coated steel rebars. The following exposure tests were conducted on FCSRs to evaluate their corrosion resistance: (a) 6-month exposure to the outdoor atmospheric environment of Hong Kong; (b) 12-month immersion in 3.5 wt% NaCl solution; (c) 2-year field exposure at a marine site near the Hong Kong-Zhuhai-Macao bridge. A systematic experimental study on the post-impact corrosion resistance of FCSRs was also carried out to evaluate the impact resistance of the FRP coating layer. The test results indicated excellent corrosion and impact resistance of FCSRs.

The third part of the PhD research programme involved experimental studies of the structurally-related performance of FCSRs. The bond performance of FCSRs in concrete and the flexural performance of concrete beams reinforced with FCSRs were studied. A modified local bond stress-slip model was established, which was found to predict closely the bond strength and stiffness for FCSRs in concrete. The results of the four-point bending beam experiments demonstrated that the structural performance of FCSR-reinforced concrete beams is comparable to uncoated steel rebars- reinforced concrete beams.

Finally, the thesis introduces two field demonstration projects which included FCSRs as one of the reinforcing materials. These projects demonstrated the process of practical implementation of FCSRs.

LIST OF PUBLICATIONS

Conference paper

Teng, J.G., **Zhang, Y.W.**, Xiang, Y., Wong, H.T., Yu, T. and Xu, F. (2022). “FRP-coated steel rebars for the reinforcement of concrete structures: Concept, manufacturing process, corrosion resistance and bond performance”, in: *Joint Conference of the 15th International Symposium on Fiber Reinforced Polymers for Reinforced Concrete Structures (FRPRCS-15) & the 8th Asia-Pacific Conference on Fiber Reinforced Polymers in Structures (APFIS-2022)*, Shenzhen, China., 10-14 December 2022 (To be published in the conference proceedings which is under preparation).

ACKNOWLEDGEMENTS

This thesis is the culmination of my odyssey to challenging myself, which I was only able to make as a result of so much love, support and inspiration lavished on me from so many people along the way. I would like to acknowledge and express my sincerest gratitude to all of them.

The deepest thanks go out to my chief supervisor, Prof. Jin-Guang TENG, for his continuous and invaluable motivation, guidance and support throughout this six-year journey. I felt blessed for having had the best supervisor far beyond my imagination before I entered the PhD programme. Prof. TENG's open-minded attitude and passion towards academic research, a wealth of experience in tackling engineering problems in practice, and unique insight into research topics have benefited me, and I aspire to become a lifelong learner just like him. I truly understand how lucky I am to have had such a supervisor who is professional and caring at the same time, taking care of both my academic progress and well-being.

I would also like to convey my heartfelt gratitude to my co-supervisors, Dr Yu XIANG, Prof. Tao YU, and Prof. Jun-Jie ZENG, for providing me with invaluable suggestions and technical help during my PhD research programme. I also owe a debt of gratitude to Dr XIANG for his guidance in every experiment detail, his encouragement during my PhD study and his guidance during the preparation of the thesis. Thanks to Dr XIANG for being incredibly supportive and patient throughout my research work.

Although it is too difficult to list all the people who have supported me in completing my work in many different ways, I would always acknowledge their help in my heart.

Special thanks go to Prof. Fei XU, Prof. Pei LI, Dr Guan LIN, Dr Pan ZHANG and Dr Siqi DING for their help and constructive comments from the very beginning of my study. I also appreciate the technical help from Mr Zhen-Xiong WANG, Mr Kwok-Lung CHEUNG, Mr Hoi-Cheung LEUNG, Mr Kim-Fung YIP, Dr Mai-po HO, Ms Dorothy CHAN, Ms Fion CHENG and Mr Raymond LEUNG for the experimental work I have done.

I am grateful for the opportunity of meeting so many lovely colleagues and friends over the past six years. I would like to extend my thanks to Dr Qiu-Lin WANG, Dr Dong-Mei LIN, Dr Ying-Ying XU, Dr Cheng JIANG, Dr Bo-Tong ZHENG, Dr Kai-Cheng LIU, Ms Xin-Yun LI, Ms Chu-Ying CUI, Mr Rui-Long LI, Dr Meng-Han ZHAO, Mr Dong HAN and Dr Yun-Ke LUO for the joyful moments we have had, which motivated me when I was down and struggling.

The financial support from the Hong Kong Research Grants Council (Project No.: T22-502/18-R, Project Title: Sustainable Marine Infrastructure Enabled by the Innovative Use of Seawater Sea-Sand Concrete and Fibre-Reinforced Polymer Composites) and The Hong Kong Polytechnic University are gratefully acknowledged. With the excellent research environment and research facilities offered at The Hong Kong Polytechnic University, I was able to complete the experimental work included in this thesis.

Last but not the least, my deepest gratitude goes to my beloved parents, to whom this thesis is dedicated. I would never have become who I am today without their unconditional love and relentless support. I would also thank my partner, Effie, for her company, encouragement, and devoted love.

TABLE OF CONTENTS

ABSTRACT	I
LIST OF PUBLICATIONS.....	III
ACKNOWLEDGEMENTS.....	IV
CONTENT	VI
LIST OF ACRONYMS.....	XIII
NOTATION.....	XV
LIST OF FIGURES	XIX
LIST OF TABLES.....	XXV
CHAPTER 1 INTRODUCTION.....	1
1.1 BACKGROUND.....	1
1.1.1 Corrosion of Steel in the Construction Industry	1
1.1.2 Corrosion Mechanism of Steel in RC Structures.....	2
1.1.3 Corrosion Prevention for Steel in RC Structures.....	3
1.2 FRP-COATED STEEL REBARS	6
1.3 RESEARCH OBJECTIVES.....	9
1.4 LAYOUT OF THE THESIS.....	10
1.5 REFERENCES.....	12
CHAPTER 2 LITERATURE REVIEW.....	21
2.1 INTRODUCTION.....	21
2.2 EPOXY-COATED STEEL REBARS (ECSRs).....	22

2.2.1 Background	22
2.2.2 Corrosion Resistance of ECSRs	22
2.2.3 Structurally-Related Performance of ECSRs	26
2.3 FIBRE-REINFORCED POLYMER (FRP) REBARS	27
2.3.1 Background	27
2.3.2 Corrosion Resistance of FRP Rebars	28
2.3.3 Structurally-Related Performance of FRP Rebars	30
2.4 STEEL-FRP COMPOSITE BARS (SFCBs)	33
2.4.1 Background	33
2.4.2 Corrosion Resistance of SFCBs	34
2.4.3 Structurally-Related Performance of SFCBs	35
2.5 STAINLESS STEEL REBARS	37
2.5.1 Background	37
2.5.2 Corrosion Resistance of Stainless Steel Rebars	39
2.5.3 Structurally-Related Performance of Stainless Steel Rebars	40
2.6 OTHER CORROSION-RESISTANT REBARS	41
2.7 CONCLUSIONS	42
2.8 REFERENCES	43

CHAPTER 3 MANUFACTURING PROCESS AND PROPERTIES OF FRP-COATED STEEL REBARS.....57

3.1 INTRODUCTION	57
3.2 MANUFACTURING PROCESSES	59
3.2.1 Filament Winding with In-line Impregnation (FWII)	59
3.2.2 Filament Winding with Vacuum-Assisted Resin Infusion (FWVARI)	60
3.2.3 Raw Materials	62

3.2.4 Specimen Preparation	62
3.2.5 Scanning Electron Spectroscopy (SEM)	63
3.3 MECHANICAL PROPERTIES	65
3.3.1 Test Matrix.....	65
3.3.2 Experimental Programme	66
3.3.3 Tensile Test Results and Discussions	66
3.3.4 Compressive Test Results and Discussions	67
3.4 THERMAL PROPERTIES	67
3.4.1 Coefficient of Thermal Expansion.....	67
3.4.2 Glass Transition Temperature.....	68
3.5 PHYSICAL PROPERTIES	69
3.5.1 Coating Thickness	69
3.5.2 Surface Roughness.....	70
3.6 CONCLUSIONS	71
3.7 REFERENCES.....	72
CHAPTER 4 CORROSION RESISTANCE	89
4.1 INTRODUCTION.....	89
4.2 EXPERIMENTAL PROGRAMME.....	90
4.2.1 Test Matrix.....	91
4.2.2 Raw Materials	91
4.2.3 Specimen Preparation	91
4.2.4 56-Day Electrochemical Corrosion Monitoring	92
4.2.4.1 <i>Open circuit potential (OCP)</i>	93
4.2.4.2 <i>Electrochemical impedance spectroscopy (EIS)</i>	93
4.2.4.3 <i>Potentiodynamic polarisation (PP)</i>	94

4.2.4.4 <i>Linear polarisation resistance (LRP)</i>	94
4.2.5 Six-Month Outdoor and One-Year Laboratory Exposure.....	95
4.2.6 Two-Year Marine Exposure.....	95
4.3 RESULTS AND DISCUSSIONS	96
4.3.1 Open Circuit Potential (OCP)	96
4.3.2 Electrochemical Impedance Spectroscopy (EIS)	98
4.3.3 Potentiodynamic Polarisation (PP).....	102
4.3.4 Linear Polarisation Resistance (LRP)	103
4.3.5 Six Months of Outdoor and One Year of Laboratory Exposure	104
4.3.6 Two Years of Marine Exposure	105
4.4 CONCLUSIONS	105
4.5 REFERENCES	107
CHAPTER 5 IMPACT RESISTANCE.....	127
5.1 INTRODUCTION	127
5.2 EXPERIMENTAL PROGRAMME	129
5.2.1 Test Matrix	129
5.2.2 Specimens Preparation	130
5.2.3 Impact Tests	131
5.2.4 Coating Damage Observations.....	132
5.2.5 Post-Impact Electrochemical Tests	132
5.3 RESULTS AND DISCUSSIONS	133
5.3.1 Coating Damage	134
5.3.2 Open Circuit Potential	134
5.3.3 Potentiodynamic Polarisation.....	137
5.3.4 Electrochemical Impedance Spectroscopy	139
5.4 CONCLUSIONS	142

5.5 REFERENCES.....	143
CHAPTER 6 BOND PERFORMANCE OF FRP-COATED STEEL REBARS IN CONCRETE.....	169
6.1 INTRODUCTION.....	169
6.2 EXPERIMENTAL PROGRAMME.....	170
6.2.1 Test Matrix.....	170
6.2.2 Materials	171
6.2.3 Specimen Preparation	172
6.2.4 Methodology	173
6.3 EXPERIMENTAL RESULTS	174
6.3.1 Failure Modes	175
6.3.2 Bond Stress-Slip Curves	175
6.4 ANALYSIS AND DISCUSSIONS	175
6.4.1 Failure Modes	175
6.4.2 Effect of Coating Materials	177
6.4.3 Effect of FRP Coating Thickness	178
6.4.4 Effect of Winding Configuration.....	179
6.5 LOCAL BOND STRESS-SLIP MODEL FOR FRP-COATED STEEL REBARS.....	181
6.6 CONCLUSIONS.....	184
6.7 REFERENCES.....	185
CHAPTER 7 FLEXURAL PERFORMANCE OF CONCRETE BEAMS REINFORCED WITH FRP-COATED STEEL REBARS	213
7.1 INTRODUCTION.....	213
7.2 EXPERIMENTAL PROGRAMME.....	214

7.2.1 Materials	214
7.2.2 Specimen Design and Fabrication	215
7.2.3 Methodology	216
7.2.4 Instrumentation.....	216
7.3 TEST RESULTS	218
7.3.1 Crack Patterns and Load-deflection Responses	218
7.3.2 Failure Process	219
7.3.3 Strain of FCSRs.....	219
7.3.4 Strain Profile and Maximum Crack Width of Concrete.....	220
7.4 ANALYSIS AND DISCUSSIONS.....	222
7.4.1 Flexural Tests	222
7.4.2 Performance Evaluation Indexes.....	223
7.4.3 Theoretical Analysis.....	225
7.5 CONCLUSIONS	227
7.6 REFERENCES	229

CHAPTER 8 PRACTICAL IMPLEMENTATION OF FRP-COATED STEEL REBARS IN CONCRETE STRUCTURES251

8.1 INTRODUCTION	251
8.2 USE OF FCSRS AS DOWEL BARS IN SSC PAVEMENT	252
8.2.1 Pavement Design.....	252
8.2.2 Demonstration Plan	253
8.2.3 On-Site Installation and Monitoring	254
8.3 USE OF FCSRS AS REINFORCEMENT OF SSC BEAMS.....	255
8.4 CONCLUSIONS	256
8.5 REFERENCES	257

CHAPTER 9 CONCLUSIONS.....	264
9.1 INTRODUCTION.....	264
9.2 MANUFACTURING PROCESS AND PROPERTIES.....	265
9.3 CORROSION AND IMPACT RESISTANCE	266
9.4 STRUCTURALLY-RELATED PERFORMANCE	268
9.5 PRACTICAL IMPLEMENTATION	270
9.6 FUTURE RESEARCH.....	271
9.7 REFERENCES.....	272

LIST OF ACRONYMS

AFRP	Aramid fibre-reinforced polymer
BFRP	Basalt fibre-reinforced polymer
CFRP	Carbon fibre-reinforced polymer
CR	Corrosion rate
CPE	Constant phase element
CRS	Crescent-ribbed steel
CTE	Coefficient of thermal expansion
DIC	Digital image correlation
DSC	Differential scanning calorimeter
ECSR _s	Epoxy-coated steel rebars
EEC	Electrical equivalent circuit
EIS	Electrical impedance spectroscopy
FBE	Fusion-bonded epoxy
FBER _s	Fusion-bonded epoxy-coated steel rebars
FCFBER _s	FRP-coated fusion-bonded epoxy-coated steel rebars
FCSR _s	FRP-coated steel rebars
FRP	Fibre-reinforced polymer
FWII	Filament winding with in-line impregnation
FWVARI	Filament winding with vacuum-assisted resin infusion

GFRP	Glass fibre-reinforced polymer
GSRs	Galvanized steel rebars
LPR	Linear polarisation resistance
LVDTs	Linear variable differential transformers
MCW	Maximum crack width
NaCl	Sodium chloride
OCP	Open circuit potential
PP	Potentiodynamic polarisation
RC	Reinforced concrete
SCE	Saturated calomel electrode
SFCBs	Steel-FRP composite bars
SEM	Scanning electron spectroscopy
SSC	Seawater sea-sand concrete
STS	Screw-thread steel
UCSRs	Uncoated steel rebars
UTM	Universal testing machine
VARI	Vacuum-assisted resin infusion
wt%	Weight percentage

NOTATION

A_{te}	Effective section area of concrete in tension
A_s	Cross-sectional area of the tensile rebars
A'_s	Cross-sectional area of the compressive rebars
α_E	Ratio of the elastic modulus of steel to concrete
a'_s	Distance between the centre of the compressive rebars and the edge of the compressive zone
b	Section width of the beam
β	Coefficient related to bond stiffness of rebars
β_s	Short-term stiffness of a beam
B	Stiffness of the beam with rectangular cross-section
C	Capacitance
C_{dl}	Double-layer capacitance
C_E	Specific ratio of impact energy to specimen thickness
d	Nominal diameter of steel rebars
Δ_{cr}	Cracking deflection
Δ_y	Yielding deflection
Δ_{ul}	Ultimate deflection
E_s	Elastic modulus of steel
E_{OCP}	Open circuit potential

E_{corr}	Corrosion potential
E_{ul}	Ultimate energy
E_y	Yielding energy
f_c	Design value of axial compressive strength of concrete
f_{tk}	Standard tensile strength of concrete
f_y	Yielding stress of the tensile steel rebars
f'_y	Yielding stress of the compressive steel rebars
f	Beam deflection
φ	Strain non-uniformity coefficient of the tensile rebars between cracks
Φ	Diameter of steel rebars
g	Acceleration due to gravity
γ	Plastic influence coefficient of the sectional resistance moment
H	Drop height of the impactor
h_0	Effective height of the beam section
K_1, K_2, K_3	Initial, post-cracking and post-yielding stiffness
i_{corr}	Corrosion rate
l_0	Span length of the beam
m_d	Mass of the impactor

M_{cr}^t	Theoretical cracking moment
M_y^t	Theoretical yielding moment
M_{cr}^e	Experimentally measured cracking moment
M_y^e	Experimentally measured yielding moment
ρ	Reinforcement ratio of longitudinal tensile rebars
R_a	Arithmetic average height parameter
R_z	Maximum height parameter
R_c	Resistance of coating layer
R_{ct}	Charge transfer resistance
R_p	Polarisation resistance
R_s	Resistance of electrolytes
l	Embedment length of the rebars in concrete
S	Deflection coefficient
s	Relative displacement parallel to the bar axis
s_1, s_2, s_3	Characteristic slippage values of rebars in pull-out test
σ_d	Designed concrete strength
σ_t	Tested concrete strength
τ	Average bond strength
τ_t	Tested bond strength
τ_n	Normalized bond strength

τ_{max}	Maximum bond strength
τ_f	Residual bond stress
T_g	Glass transition temperature
P	Load of the specimen
P_{cr}	Cracking load of the beam
P_y	Yielding load of the beam
P_{ul}	Ultimate load of the beam
μ_{Δ}	Ductility of the beam calculated by deflection
μ_E	Ductility of the beam calculated by Energy
W_0	Section modulus of the beam
ω	Angular frequency
Z	Impedance

LIST OF FIGURES

Figure 1.1 Corrosion mechanism of steel	17
Figure 1.2 Corrosion protection methods for reinforced concrete structures.....	19
Figure 1.3 Schematic diagram of the FRP-coated steel rebar	20
Figure 3.1 Filament winding machine: (1) delivery part; (2) mandrel part; (3) supporting frame; (4) controller.	75
Figure 3.2 Filament winding with in-line impregnation (FWII) for manufacturing FCSRs.....	76
Figure 3.3 Filament winding with vacuum-assisted resin infusion (FWVARI) for manufacturing FCSRs.....	77
Figure 3.4 Placement of vacuum bag from different views	78
Figure 3.5 FRP coating layers of FCSRs manufactured by two different methods .	79
Figure 3.6 Coating-to-steel interfaces of different types of rebars.....	80
Figure 3.7 Schematic diagrams of specimens for material property tests	81
Figure 3.8 Setups for material property tests.....	82
Figure 3.9 Tensile stress-strain curves of uncoated steel rebars (UC), FCSRs (FWII), and FCSRs (FWVARI).....	82
Figure 3.10 Development of coating peeling during a tensile test	83
Figure 3.11 Failed specimens	83
Figure 3.12 Dimensional change of the FRP coating layer and the steel rebar as a function of temperature	84
Figure 3.13 The results of differential scanning calorimeter (DSC) tests on the FRP coating layer of five parallel specimens	84

Figure 3.14 Measurement of coating thickness	85
Figure 3.15 Definition of the roughness-related parameters [Extracted from Gadelmawla et al. (2002)].....	85
Figure 3.16 Surface roughness values of ECSRs and FCSRs	86
Figure 4.1 Examples of FRP-coated steel rebars for electrochemical tests.....	111
Figure 4.2 Test setups for electrochemical tests	111
Figure 4.3 Electrical equivalent circuit (EEC) model for data fitting.....	111
Figure 4.4 OCP evolution diagrams for different types of steel rebars	113
Figure 4.5 Variation of average OCP values of all groups	114
Figure 4.6 Bode plots of different types of steel rebars.....	117
Figure 4.7 Impedance spectra for specimens after being immersed in 3.5 wt% NaCl solution for up to 56 days.....	119
Figure 4.8 Corrosion potential extracted from potentiodynamic polarisation tests	120
Figure 4.9 Polarisation resistance evolutions of specimens immersed in 3.5 wt% NaCl solution for up to 56 days.....	120
Figure 4.10 Corrosion rate evolutions of specimens immersed in 3.5 wt% NaCl solution for up to 56 days.....	121
Figure 4.11 Corrosion state of rebars after exposure to the outdoor atmospheric environment for six months[(a)-(c)] and after immersion in 3.5 wt% NaCl solution for 12 months [(d)-(f)].....	121
Figure 4.12 Corrosion state of specimens after exposure to the splash zone near the Hong Kong-Zhuhai-Macao Bridge for different periods	122
Figure 4.13 SEM images of the cross-sections of different types of steel rebars..	123
Figure 5.1 Facility used to induce impact damage	147

Figure 5.2 Comparison of coated steel rebars before and after impact	148
Figure 5.3 Cutting a rebar for SEM observation	148
Figure 5.4 Cold mounting of specimens in a plastic mould	149
Figure 5.5 Polishing the observation surface of cold-mounted specimens	149
Figure 5.6 Typical Tafel curve for potentiodynamic analysis.....	150
Figure 5.7 Microstructures of FCSRs impacted with different levels of energy....	152
Figure 5.8 OCP values of specimens with different numbers of fibre plies after impact with different levels of energy	154
Figure 5.9 OCP values of two-ply FCSRs with different winding angle(s) after impact with different levels of energy	156
Figure 5.10 OCP values of three-ply FCSRs with different winding angle(s) after impact with different levels of energy	157
Figure 5.11 Evolutions of the corrosion current density and polarisation resistance of different types of steel rebars after impact with energy of 10.7 J	158
Figure 5.12 Corrosion current density (i_{corr}) evolutions of FCSRs with two fibre plies of different winding angle combinations after impact with different levels of energy	160
Figure 5.13 Corrosion current density (i_{corr}) evolutions of three-ply FCSRs with different winding angle combinations after impact with different levels of energy	161
Figure 5.14 Bode plots of different groups of impacted specimens after being immersed in NaCl solution for different periods.....	165
Figure 5.15 Equivalent electrical circuit (EEC) models for different types of steel rebars	165

Figure 5.16 Resistance of coating layer after impact with different levels of energy (L1=2.8 J; L2=6.7 J; L3=10.7 J)	166
Figure 5.17 Coating resistance of two-ply FCSRs with different winding angle(s) after impact with energy of 17.1 J.....	166
Figure 6.1 Steel rebars with different rib patterns	188
Figure 6.2 Compression test equipment.....	188
Figure 6.3 Dimensions and details of the pull-out specimen.....	189
Figure 6.4 Setup for pull-out tests.....	189
Figure 6.5 Typical failure mode of specimens.....	190
Figure 6.6 Local bond stress-slip curves of screw-thread steel (STS) rebars in concrete	193
Figure 6.7 Local bond stress-slip curves of crescent-ribbed steel (CRS) rebars in concrete	196
Figure 6.8 Rebar/concrete interface of failed pull-out specimens embedded with screw-thread steel rebars	197
Figure 6.9 Rebar/concrete interface of failed pull-out specimens embedded crescent- ribbed steel rebars	198
Figure 6.10 Sketch maps of failure surfaces of pull-out specimens with different steel rebars.....	199
Figure 6.11 Bond strength of screw-thread steel rebars with different types of coating materials	200
Figure 6.12 Bond strength of crescent-ribbed steel rebars with different types of coating materials	200
Figure 6.13 Bond strength of FRP-coated STS rebars with different coating thicknesses	201

Figure 6.14 Bond strength of FRP-coated CRS rebars with different coating thicknesses	201
Figure 6.15 Bond strength of two-ply FRP-coated STS rebars with different winding angles	202
Figure 6.16 Bond strength of two-ply FRP-coated CRS rebars with different winding angles	202
Figure 6.17 Comparison of the bond strengths of different types of coated steel rebars	203
Figure 6.18 Comparison between experimental and theoretical local bond stress-slip curves	205
Figure 6.19 Fitting results of α for FRP-coated steel rebars	206
Figure 6.20 Modified local bond stress-slip model for FCSRs with different rib patterns.....	207
Figure 7.1 Steel rebars for manufacturing FCSRs.....	231
Figure 7.2 Framework of FCSR beam	231
Figure 7.3 Dimensions and reinforcement details of the beam specimen	232
Figure 7.4 Arrangement of strain gauges	232
Figure 7.5 Processes to attach strain gauges (SGs)	233
Figure 7.6 Surface preparation for DIC measurements	233
Figure 7.7 Setup for four-point bending beam tests	234
Figure 7.8 Crack patterns of beam specimens at failure.....	237
Figure 7.9 Load-displacement curves of concrete beams reinforced with different types of steel rebars	240

Figure 7.10 Cracking stress, yielding stress and ultimate stress of concrete beams reinforced with different types of steel rebars	241
Figure 7.11 Load-strain curves of compressive rebars	241
Figure 7.12 Comparisons of the load-strain curves of different types of tensile steel rebars.....	243
Figure 7.13 The strain profiles of concrete beams reinforced with different types of steel rebars.....	245
Figure 7.14 Comparisons of the maximum crack width developments of concrete beams reinforced with different types of steel rebars	246
Figure 7.15 Parameters relevant to the ductility index calculation.....	247
Figure 7.16 Comparisons between theoretical and experimental moments	247
Figure 8.1 Layout of the pavement (unit: mm).....	258
Figure 8.2 Different groups of dowel bars.....	258
Figure 8.3 Arrangement of dowel bars on pavements	259
Figure 8.4 Installation of dowel bars	259
Figure 8.5 View of the three-story concrete frame	260
Figure 8.6 Layout of the FCSR beams.....	260
Figure 8.7 Welded anchorage to the FCSR	261
Figure 8.8 Details of the steel ring anchor of an FCSR.....	261
Figure 8.9 Field installation of the frame.....	262

LIST OF TABLES

Table 3.1 Mechanical properties of core steel rebars	87
Table 3.2 Mechanical properties of Sika EPOLAM 2031/2031 epoxy resin.....	87
Table 3.3 Mechanical properties of glass fibre filaments.....	87
Table 3.4 Key results of tensile tests	88
Table 3.5 Key results of compressive tests	88
Table 3.6 Thicknesses of all groups	88
Table 4.1 Mechanical properties of crescent-ribbed steel rebars	124
Table 4.2 Mechanical properties of epoxy resin	124
Table 4.3 Mechanical properties of glass fibres filaments	124
Table 4.4 Test matrix for experiments	124
Table 4.5 Parameters of the EEC model obtained by experimental data fitting	125
Table 5.1 Mechanical properties of core steel rebars	167
Table 5.2 Mechanical properties of epoxy resin	167
Table 5.3 Mechanical properties of glass fibre filaments.....	167
Table 5.4 Impact energy levels for different types of steel rebars	167
Table 5.5 Test matrix for impact tests	168
Table 6.1 Test matrix for pull-out tests	208
Table 6.2 Parameters of steel rebars	210
Table 6.3 Mechanical properties of glass fibres filaments	210

Table 6.4 Concrete mix for pull-out specimens (unit: kg per m ³)	210
Table 6.5 Key results of pull-out tests	211
Table 6.6 Parameters define the modified local bond stress-slip model.....	212
Table 7.1 Mechanical properties of steel rebars	248
Table 7.2 Test matrix for flexural behavior of reinforced concrete beams	248
Table 7.3 Key results of four-point bending beam tests	249
Table 7.4 Stiffness and ductility coefficients of all groups	250
Table 7.5 Comparisons of the theoretical and experimental results on the cracking and yielding moments	250
Table 8.1 Details of the dowel bars in pavements	263

CHAPTER 1

INTRODUCTION

1.1 BACKGROUND

1.1.1 Corrosion of Steel in the Construction Industry

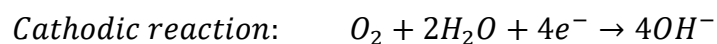
It has been estimated that a tonne of rust is formed every 90 seconds around the world. After a comprehensive investigation of the corrosion state in more than 30 industries, Hou (2019) estimated that the cost of preventing carbon steel corrosion reached 2,100 billion Yuan in China in 2014, equalling 3.34% of the GDP of the whole nation in 2014. The corrosion cost worldwide was estimated at 2,500 billion US dollars, which equals 3.40% of the global GDP in 2013 (Koch *et al.* 2016). Therefore, steel corrosion continues to pose significant obstacles to the sustainable development of the world.

Steel-reinforced concrete (RC) plays a pivotal role in the construction industry, serving as a vital component in the development of infrastructure like bridges, buildings, platforms, tunnels, and pipelines (Böhni 2005). Corrosion of steel in RC structures has caused massive economic losses as well as a significant threat to structural and life safety. In particular, repair or even replacement of corroded components is essential for structures that have experienced corrosion of steel reinforcement and significant concrete cracking. The maintenance work requires

extra labour, materials, and time, which increases the cost of the structures from a life-cycle perspective. Consequently, how to eliminate the corrosion issue is essential and imperative to enhance the sustainability of infrastructure.

1.1.2 Corrosion Mechanism of Steel in RC Structures

Chloride attacks and carbonation are the two major causes of steel corrosion in RC structures. The influence of the two causes depends on the location of the structure, as its environmental conditions vary over time and by location. Chloride attacks dominates the corrosion process in the temperate zones, while carbonation is more prominent in the tropical zone. The carbonation of concrete that is caused by the diffusion of carbon oxide (CO_2), which not only lowers the pH value of concrete, thereby destroying the passive iron oxide film (Fe_2O_3) formed on the steel surface but also lowers the chloride threshold for corrosion initiation thus resulting in an accelerated corrosion process (Ekolu 2016). Steel corrosion will reduce the cross-sectional area of steel reinforcements and produce corrosive products in RC structures, which will lead to early cracking and spalling of concrete cover and thus result in a more severe situation. Corrosion of the steel embedded in concrete is driven by electrochemical reactions, as depicted with the following reaction equations:



Where the anodic reaction illustrates the dissolution process of steel, the flux of electrons and ions is usually taken as an index to measure the corrosion rate of steel (Böhni 2005).

The initiation of corrosion must satisfy several conditions. As shown in Figure 1.1 and illustrated in the cathodic reaction formula above, oxygen is as necessary as water for the corrosion occurrence of steel. The carbonation of concrete consumes the alkaline components inside the concrete, which results in the pH value of the pore solution in the concrete decreasing from over 12.5 to 6 ~ 9. The evolved acidic environment would be detrimental to steel rebars since the depassivation threshold is around 9.5 for steel rebars (Šavija and Luković 2016; Qiu 2020).

1.1.3 Corrosion Prevention for Steel in RC Structures

Many efforts have been made for decades to address the corrosion issue. Based on the corrosion mechanism of steel in RC structures, the essential elements involved in the corrosion process are water, oxygen, and steel reinforcement. The corrosion-prevention methods utilised in the construction industry in the design stage can accordingly be divided into four categories: (1) to replace the conventional steel rebars with corrosion-resistant rebars [e.g., stainless steel rebars, fibre-reinforced polymer (FRP) rebars, steel-FRP composite bars (SFCBs), epoxy-coated steel rebars (ECSRs), galvanized steel rebars (GSRs), etc.] (Brown and Bartholomew 1993; Wu *et al.* 2010; Elsener *et al.* 2011); (2) to apply surface treatment materials on concrete to prevent the ingress of water, oxygen, carbon oxide, sulphate and other corrosive substances (Brown and Bartholomew 1993; Almusallam *et al.* 2003; Aguiar *et al.* 2008); (3) to add corrosion inhibitors or other additives into concrete (Ormellese *et*

al. 2006; Söylev and Richardson 2008); (4) to utilise electrochemical techniques to prevent steel corrosion (Böhni 2005; Koleva *et al.* 2007; Page and Page 2007). Examples of each category are shown in Figure 1.2.

Fibre-reinforced polymer (FRP) rebars have been utilised as a viable alternative to traditional steel rebars in civil construction projects since the 1970s to overcome the corrosion problem of RC structures, especially for those located in harsh environments, such as wastewater treatment plants, underwater structures, floating docks, near sea constructions (Brown and Bartholomew 1993). FRP rebar-reinforced concrete structures have been found to have comparable performance with steel-reinforced concrete structures. The performance of FRP rebars has also been enhanced with the improvement of manufacturing technology and raw materials. Brown and Bartholomew (1993) concluded that the bond performance of FRP rebars in concrete was around two-thirds of that of steel rebars, while Rolland *et al.* (2018) found that glass FRP (GFRP) rebars with a diameter of 12.7 mm used in their experiments exhibited a slightly higher bond strength than the reference deformed steel rebars. The deterioration mechanism of the FRP products is still not sufficiently well understood for the reliable prediction of the design life of FRP rebar-reinforced concrete structures (Benmokrane and Ali 2018; Benmokrane *et al.* 2018). The service life of FRP rebar-reinforced concrete structures predicted using current models is expected to underestimate their durability performance.

Coated steel rebars have been developed, with different types of coating materials employed to protect the core steel rebar against the diffusion of aggressive substances (Monetta 1993). ECSRs are the most widely used coated steel rebars in the world, with a relatively mature manufacturing method. Uncoated steel rebars of any shape

or diameter are first blasted and then put into a chamber to be heated to a high temperature of around 230°C. After that, powder epoxy is electrostatically sprayed around the steel rebars, and the floating epoxy powder is then led by a designated magnetic field to be fused onto the steel surface. The products are next quenched in water for cooling (Nguyen and Martin 2004). However, the fusion-bonded epoxy coating can be easily damaged by bending or dragging of the rebars at construction sites. ECSRs are not recommended or even forbidden in many areas (e.g., the US, Canada, etc.) because of their unsatisfactory performance (Kamde and Pillai 2021). The effect of adding additives (e.g., sand and polymer) in the epoxy to enhance the performance of the epoxy coating layer has been investigated by some researchers. Chen *et al.* (2018) added fly ash cenospheres and short glass fibres into epoxy resin to improve the erosion behaviour of the epoxy coating layer. Li *et al.* (2020) used a novel type of hybrid filler consisting of graphene oxide-fly ash cenospheres to improve the wearing resistance as well as the corrosion resistance of the coating layer. Weishaar *et al.* (2018) mixed self-healing microcapsules into epoxy resin to remedy the damage that might be caused at the worksites. However, the enhanced properties provided by those additives are limited as the coating thickness of those coated rebars was still relatively small. Therefore, the impact damage on the coating layers cannot be avoided during the transportation and installation process of ECSRs.

Concrete surface treatment is a method used to retard the ingress of aggressive substances and thereby delaying the carbonation of concrete (Page and Page 2007). Surface treatment materials are usually categorised as follows: (i) pore blockage; (ii) hydrophobic impregnation (pore liners); and (iii) coating based on the functional mechanism. It has been proved that additional materials, such as polymers, can be added into the coating to improve the roughness, strength, adhesions, and

impermeability and mitigate the shrinkage of cementitious coating (Di Mundo *et al.* 2020). Cement-based materials, geopolymers, and polymeric materials are popular choices for the protection or renewal of infrastructure with either hand application or spraying methods. Proper surface preparation of concrete is crucial before applying the coating as the surface condition influences the adhesion of the coating to the concrete, and thus the quality and durability of the coatings (Zhu *et al.* 2021). Moreover, the reported premature failure cases of the coating indicate that further efforts are still needed to improve their infield performance (Wang *et al.* 2020).

1.2 FRP-COATED STEEL REBARS

FRP-coated steel rebars (FCSRs) are a novel type of corrosion-resistant steel rebars for the reinforcement of RC structures, which was proposed by Teng *et al.* (2022). A schematic diagram is shown of FCSRs is shown in Figure 1.3.

Two related FRP-steel rebars have previously been explored: steel-FRP composite bars (SFCBs) and hybrid steel-FRP rebars (HSFRs). SFCBs were produced by the pultrusion technology by adding a layer of FRP composite onto the steel rebar surface, thereby enclosing the steel material with FRPs to prevent the corrosion of the core steel (Wu *et al.* 2010). HSFRs were made of a braided FRP skin with a steel core (Nanni *et al.* 1994). However, both SFCBs and HSFRs are inconvenient in practical implementations as their bi-linear property may result in a brittle failure mode of concrete structures. More factors, such as the safety reduction factor, should be introduced when designing concrete structures reinforced with these types of steel rebars. FCSRs are designed to provide corrosion protection for steel rebars without

changing their ductile property. FCSRs are manufactured by the filament-winding technology. More specifically, impregnated long continuous fibres are wound on the steel rebar surface with the pre-specified angles (e.g., in the hoop direction, at 60° to the longitudinal axis, etc.) and the required number of fibre plies to form the coating layers. A small tensile force is applied to fibre filaments during the winding process to ensure tight contact between the FRP coating and steel rebar substrate. A vital and distinct aspect of the filament-winding process for FCSRs is to reflect the rib geometric features of the rebar through the coating layer to the most significant extent so that the surface of the resulting FCSR retains the original bond performance of the original steel rebar. An FRP coating layer can be seen as an enhanced version of an epoxy coating layer by incorporating continuous fibre plies. These fibre plies enhance the mechanical properties of the epoxy coating, which has been reported to be easily damaged during the transportation and construction process. Such damage is detrimental to the corrosion resistance of an epoxy coating layer. The FRP coating layer on FCSRs can be expected to be much more resistant to unavoidable impact loading than the epoxy coating layer on ECSRs.

Different from the additives mentioned in the previous section, the filament-wound fibre plies in the FRP coating layer of FCSRs not only greatly enhances the mechanical properties of the coating layer itself but also substantially improves the adhesion ability of the coating layer to the steel rebar surface. The ameliorated adhesion performance can be attributed to the tensioning of the fibres during the filament-winding process, as this tensioning helps prevent the coating layer peeling away from the steel substrate due to any unexpected external forces. FCSRs are believed to have great potential for use in civil construction as an approach to address corrosion issues.

The initial material cost of FCSRs is roughly estimated to be within 4500 HK\$/tonne based on the technology introduced in the present thesis. By contrast, stainless steel rebars (SSRs) with comparable corrosion resistance have an initial cost of about HK\$ 20,000 (i.e., 4.8 times the initial cost of conventional steel rebars as mentioned in the abstract). The initial material costs of epoxy-coated steel rebars (ECSRs) and galvanized steel rebars (GSRs) are about HK\$ 5800 and HK\$ 4800, respectively, which are also higher than that of FCSRs, even though the former is much inferior to FCSRs in corrosion-resistance. Therefore, FCSRs have the highest cost-effectiveness among all the existing types of corrosion-resistant steel rebars and are believed to be much more cost-effective than conventional steel rebars in consideration of the life-cycle costs of reinforced concrete structures. Compared with other types of corrosion-resistant rebars, FCSRs are expected to have the following advantages (Teng *et al.* 2022):

- (1) FCSRs are superior in corrosion resistance to ECSRs. Through the use of multiple plies of fibres at different angles as distributed reinforcement for the coating layer, the thickness and lamination structure of the FRP coating layer can be controlled to minimise permeability and enhance durability. In addition, the ingress of external corrosive agents towards the core steel rebar surface is likely to be intercepted by interlaminar paths in the laminar structure of the FRP coating layer.
- (2) An FRP coating layer has much better impact and peel resistance than an epoxy coating layer. This superior performance of an FRP coating layer is due to the use of continuous fibres as reinforcement to minimise/constrain cracks and avoid through-cracks in the coating layer and the use of the filament

winding technique to ensure tight contact between the FRP coating layer and the core steel rebar.

- (3) FCSRs are much cheaper than stainless steel and FRP rebars. As only a thin FRP coating layer is needed in FCSRs, they are only slightly more expensive than conventional steel rebars and are thus much cheaper than stainless steel rebars and FRP rebars for the achievement of the same level of short-term structurally-related performance.
- (4) FCSRs are much more ductile than FRP rebars. The mechanical behaviour of an FCSR is very similar to that of the core steel rebar, so an FCSR retains almost all the ductility of the core steel rebar.

1.3 RESEARCH OBJECTIVES

In summary, this thesis presents the results of a research programme on FCSRs, from their manufacturing methods, mechanical properties, physical properties, and electrochemical properties to their structurally-related performance in concrete structures. The implementation of FCSRs in two practical engineering structures is also introduced. The main objectives of the research programme presented in the present thesis are:

- (1) To find cost-effective manufacturing methods for FCSRs with satisfactory physical and mechanical properties (Chapter 3);
- (2) To investigate the corrosion resistance, especially the electrochemical behaviour of FCSRs in aggressive environments (Chapter 4);

- (3) To investigate the impact resistance, especially the post-impact electrochemical behaviour of FCSRs in aggressive environments (Chapter 5);
- (4) To investigate the bond performance of FCSRs embedded in concrete with pull-out tests (Chapter 6);
- (5) To investigate the flexural performance of FCSR-reinforced concrete beams with four-point bending tests (Chapter 7);
- (6) To explore the feasibility of implementing the newly developed FCSRs in practical engineering structures (Chapter 8).

1.4 LAYOUT OF THE THESIS

This thesis consists of nine chapters in total, and the contents of each chapter are summarised as follows.

Chapter 1 gives an introduction to the background of this PhD research programme and describes the necessity and significance of this research programme.

Chapter 2 presents a literature review of previous research work on corrosion-resistant rebars, which are relevant to the research on FCSRs, covering their manufacturing methods, physical and mechanical properties, bond performance, durability performance, and cost-effectiveness. The types of such rebars covered include fusion-bonded ECSRs, FRP rebars, SFCBs, and stainless steel rebars. The existing local bond stress-slip models for different types of rebars embedded in

concrete are summarised and compared. The limitations of the existing types of rebars to mitigate the corrosion issues of RC structures are also discussed.

Chapter 3 introduces two manufacturing methods suitable for producing FCSRs. The influences of winding configurations, i.e., the number and the winding angle(s) of the fibre plies in the FRP coating layer, on the microstructure of both the coating layer and the steel-coating interface were investigated. The physical properties, including the glass transition temperature, roughness, thickness, and the coefficient of thermal expansion of the FRP coating layer, were measured. The mechanical properties, including the tensile and compressive properties of FCSRs, were studied. Filament winding with in-line impregnation of resin was identified as the preferred method for manufacturing FCSRs in subsequent experimental investigations.

The corrosion resistance of the steel rebars embedded in concrete structures is a major parameter that governs the durability of the structures. Chapter 4 therefore investigates the corrosion resistance of the FCSRs with different numbers of fibre plies through a series of electrochemical tests. In addition, different types of exposure tests were also conducted on FCSRs, including 6-month exposure to the outdoor atmospheric environment of Hong Kong, 12-month immersion in 3.5 wt% NaCl solution and 2-year field exposure near the Hong Kong-Zhuhai-Macao bridge.

One of the main limitations of the existing coated steel rebars (e.g., ECSRs, GSRs, etc.) is their susceptibility to impact loading, which often causes the break and peel of the coating layer, and thus influences the durability of the rebars. Chapter 5 therefore investigates the impact resistance of FCSRs by taking a series of impact tests together with post-impact electrochemical tests. Different levels of impact

energy were employed to induce different levels of impact damage on the FRP coating layer.

Chapter 6 experimentally studies the bond performance of the FCSRs embedded in concrete blocks by carrying out pull-out tests on 48 specimens. The rib patterns of the core steel rebar and the number and winding angle(s) of fibre plies in the FRP coating layer, which might influence the bond performance of FCSRs to concrete, were thoroughly investigated. Furthermore, a modified local bond stress-slip model for FCSRs in concrete was proposed based on a model for UCSRs in Model Code 2010 (Taerwe and Matthys 2013).

Chapter 7 presents an experimental investigation on the flexural performance of concrete beams reinforced with FCSRs. A total of sixteen 1.6-metre-long beams with cross-sectional dimensions of $140\text{ mm} \times 190\text{ mm}$ were prepared and tested to demonstrate the excellent structurally-related performance of FCSRs. The test results were compared with the theoretical predictions based on different design codes. The flexural performance of concrete beams reinforced with FCSRs is comparable to that of concrete beams reinforced with UCSRs and is superior to that of concrete beams reinforced with ECSRs.

Apart from a series of laboratory experiments that were designed and carried out to verify the excellent corrosion resistance, impact resistance, and structurally-related performance of FCSRs, Chapter 8 demonstrates two practical implementations of FCSRs. The success of the two demonstration projects has provided a reference for the promotion and application of FCSRs.

The main conclusions obtained from the previous 8 chapters are summarised in Chapter 9 with a highlighting of the limitations of the present research and the work worth further investigation.

1.5 REFERENCES

- Aguiar, J.B., Camões, A. and Moreira, P.M. (2008). “Coatings for concrete protection against aggressive environments”, *Journal of Advanced Concrete Technology*, Vol. 6, No. 1, pp. 243-250.
- Almusallam, A.A., Khan, F.M., Dulaijan, S.U. and Al-Amoudi, O.S.B. (2003). “Effectiveness of surface coatings in improving concrete durability”, *Cement and Concrete Composites*, Vol. 25, No. 4-5, pp. 473-481.
- Benmokrane, B. and Ali, A.H. (2018). “Durability and long-term performance of fiber-reinforced polymer as a new civil engineering material”, in: *Proceedings of International Congress on Polymers in Concrete (ICPIC 2018)*, pp. 49-59.
- Benmokrane, B., Mohamed, H.M. and Ali, A.H. (2018). “Service-life-prediction and field application of glass fiber-reinforced polymer tubular and solid bolts based on laboratory physical and mechanical assessment”, *Journal of Composite Materials*, Vol. 52, No. 24, pp. 3309-3323.
- Böhni, H. (2005). *Corrosion in Reinforced Concrete Structures*, CRC Press, Boston, New York, Washington, DC.

- Brown, V.L. and Bartholomew, C.L. (1993). "FRP reinforcing bars in reinforced concrete members", *ACI Materials Journal*, Vol. 90, No. 1, pp. 34-39.
- CEB-FIP. (2010). *Model Code for Concrete Structures*. Thomas Telford Services Ltd., London.
- Chen, P., Wang, Y., Li, J., Wang, H. and Zhang, L. (2018). "Adhesion and erosion properties of epoxy resin composite coatings reinforced with fly ash cenospheres and short glass fibers", *Progress in Organic Coatings*, Vol. 125, pp. 489-499.
- Di Mundo, R., Labianca, C., Carbone, G. and Notarnicola, M. (2020). "Recent advances in hydrophobic and icephobic surface treatments of concrete", *Coatings*, Vol. 10, No. 5, pp. 1-35.
- Ekolu, S.O. (2016). "A review on effects of curing, sheltering, and CO₂ concentration upon natural carbonation of concrete", *Construction and Building Materials*, Vol. 127, pp. 306-320.
- Elsener, B., Addari, D., Coray, S. and Rossi, A. (2011). "Stainless steel reinforcing bars-reason for their high pitting corrosion resistance", *Materials and Corrosion*, Vol. 62, No. 2, pp. 111-119.
- Hou, B. (2019). "Introduction to a study on corrosion status and control strategy in China." *The Cost of Corrosion in China*, Science Press, Beijing, China, 1-33.
- Kamde, D.K. and Pillai, R.G. (2021). "Corrosion initiation mechanisms and service life estimation of concrete systems with fusion-bonded-epoxy (FBE) coated steel exposed to chlorides", *Construction and Building Materials*, Vol. 277, No. 122314.

- Koch, G., Varney, J., Thompson, N., Moghissi, O., Gould, M. and Payer, J. (2016). *The international measures of prevention, application, and economics of corrosion technologies*, NACE International, Houston, Texas, USA.
- Koleva, D.A., De Wit, J.H.W., Van Breugel, K., Lodhi, Z.F. and Van Westing, E. (2007). “Investigation of corrosion and cathodic protection in reinforced concrete: I. Application of electrochemical techniques”, *Journal of The Electrochemical Society*, Vol. 154, No. 4, pp. 52-61.
- Li, J., Chen, P. and Wang, Y. (2020). “Tribological and corrosion performance of epoxy resin composite coatings reinforced with graphene oxide and fly ash cenospheres”, *Journal of Applied Polymer Science*, Vol. 138, No. 11, pp. 50042.
- Monetta, T., Bellucci, F., Nicodemo, L., & Nicolais, L. (1993). “Protective properties of epoxy-based organic coatings on mild steel”, *Progress in Organic Coatings*, Vol. 21, No. 4, pp. 353-369.
- Nanni, A., Henneke, M.J. and Okamoto, T. (1994). “Tensile properties of hybrid rods for concrete reinforcement”, *Construction and Building Materials*, Vol. 8, No. 1, pp. 27-34.
- Nguyen, T. and Martin, J.W. (2004). “Modes and mechanisms for the degradation of fusion-bonded epoxy-coated steel in a marine concrete”, *Journal of Coatings Technology and Research*, Vol. 1, No. 2, pp. 81-92.
- Ormellese, M., Berra, M., Bolzoni, F. and Pastore, T. (2006). “Corrosion inhibitors for chlorides induced corrosion in reinforced concrete structures”, *Cement and Concrete Research*, Vol. 36, No. 3, pp. 536-547.

Page, C.L. and Page, M.M. (2007). *Durability of Concrete and Cement Composites*, CRC Press, Boston, New York, Washington, DC.

Qiu, Q. (2020). “A state-of-the-art review on the carbonation process in cementitious materials: Fundamentals and characterization techniques”, *Construction and Building Materials*, Vol. 247, No. 118503.

Rolland, A., Quiertant, M., Khadour, A., Chataigner, S., Benzarti, K. and Argoul, P. (2018). “Experimental investigations on the bond behavior between concrete and FRP reinforcing bars”, *Construction and Building Materials*, Vol. 173, pp. 136-148.

Šavija, B. and Luković, M. (2016). “Carbonation of cement paste: Understanding, challenges, and opportunities”, *Construction and Building Materials*, Vol. 117, pp. 285-301.

Söylev, T.A. and Richardson, M.G. (2008). “Corrosion inhibitors for steel in concrete: State-of-the-art report”, *Construction and Building Materials*, Vol. 22, No. 4, pp. 609-622.

Teng, J.G., Zhang, Y.W., Xiang, Y., Wong, H.T., Yu, T. and Xu, F. (2022). “FRP-coated steel rebars for the reinforcement of concrete structures: Concept, manufacturing process, corrosion resistance and bond performance”, in: *Proceedings of Joint Conference of the 15th International Symposium on Fiber Reinforced Polymers for Reinforced Concrete Structures (FRPRCS-15) & the 8th Asia-Pacific Conference on Fiber Reinforced Polymers in Structures (APFIS-2022)*,

Wang, T., Wu, K., Kan, L. and Wu, M. (2020). “Current understanding on microbiologically induced corrosion of concrete in sewer structures: a review

of the evaluation methods and mitigation measures”, *Construction and Building Materials*, Vol. 247, No. 118539 .

Weishaar, A., Carpenter, M., Loucks, R., Sakulich, A. and Peterson, A.M. (2018). “Evaluation of self-healing epoxy coatings for steel reinforcement”, *Construction and Building Materials*, Vol. 191, pp. 125-135.

Wu, G., Wu, Z.S., Luo, Y.B., Sun, Z.Y. and Hu, X.Q. (2010). “Mechanical properties of steel-FRP composite bar under uniaxial and cyclic tensile loads”, *Journal of Materials in Civil Engineering*, Vol. 22, No. 10, pp. 1056-1066.

Zhu, H., Wang, T., Wang, Y. and Li, V.C. (2021). “Trenchless rehabilitation for concrete pipelines of water infrastructure: A review from the structural perspective”, *Cement and Concrete Composites*, Vol. 123, No. 104193.

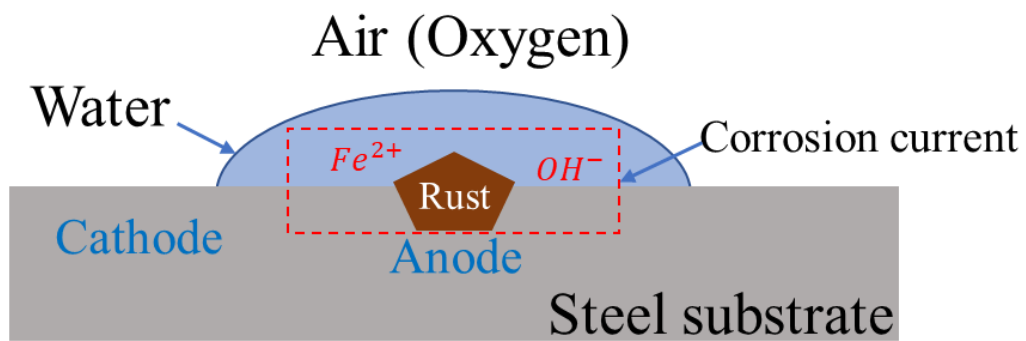
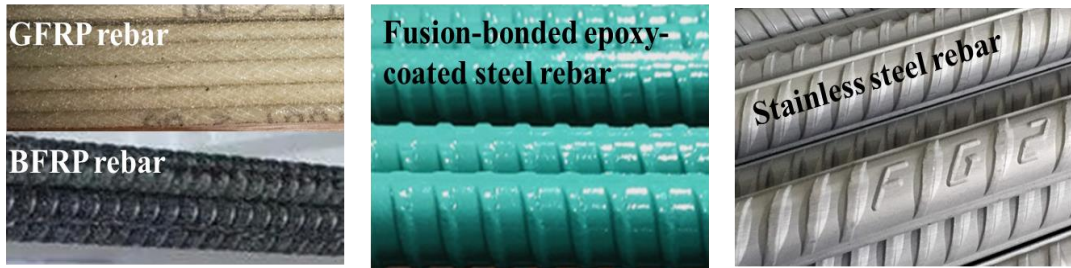
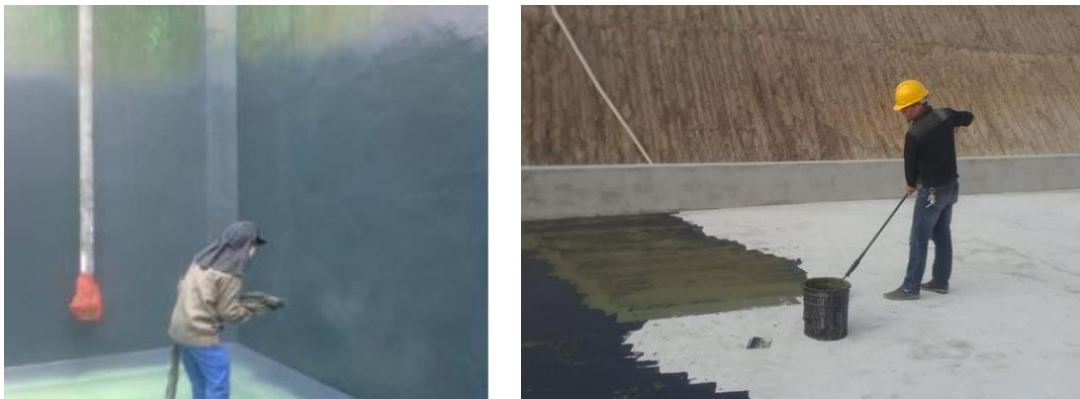


Figure 1.1 Corrosion mechanism of steel



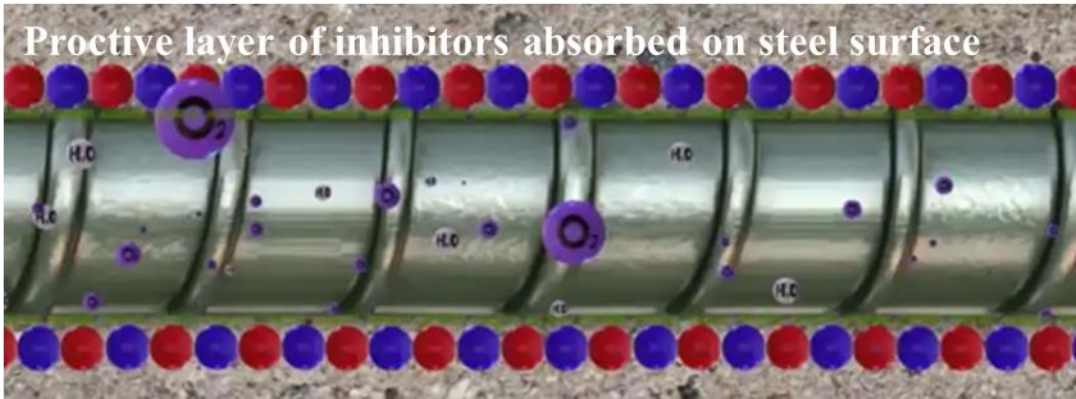
(a) Corrosion resistant rebars

(Extracted from <http://fusteelrebar.com/prestressing-screw-thread-steel-bar/> and <http://fusteelrebar.com/stainless-steel-rebar/> Accessed on 17-01-2023)



(b) Waterproof coatings on structural surfaces

(Extracted from https://www.qdpua.cn/pro/dongfang_pro1/254.html, and <https://www.meipian.cn/hwx3i2p?from=groupmessage> accessed on 17-01-2023)



(c) Corrosion inhibitors in concrete
(Extracted from <https://theconstructor.org/concrete/corrosion-inhibiting-admixtures/6765/>, assessed on 17-01-2023)



(d) Sacrificial metal connected to an RC bridge pier
[Extracted from Larrsen (2018)]

Figure 1.2 Corrosion protection methods for reinforced concrete structures

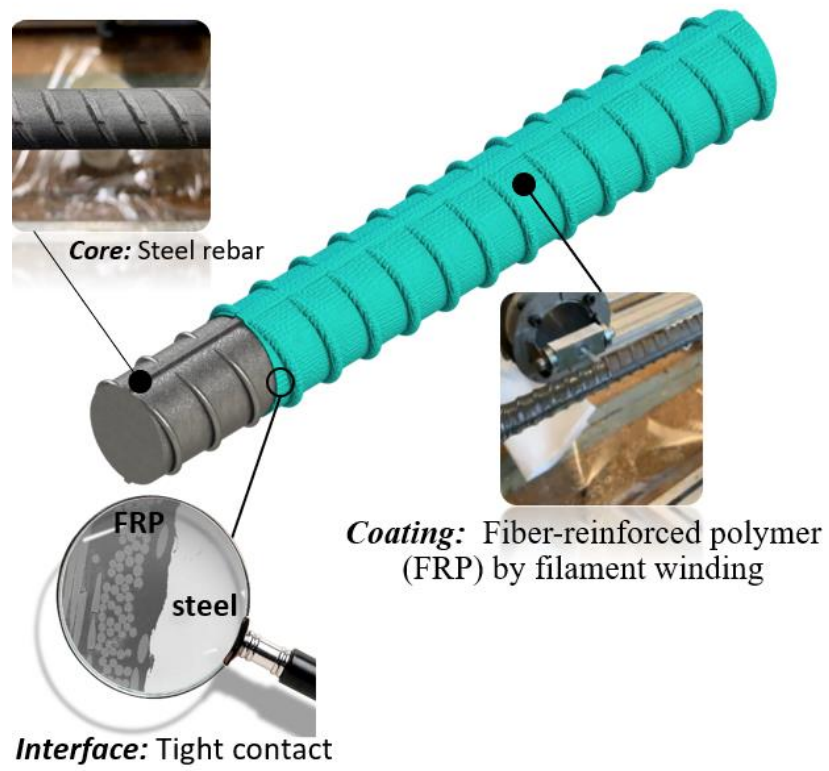


Figure 1.3 Schematic diagram of an FRP-coated steel rebar

CHAPTER 2

LITERATURE REVIEW

2.1 INTRODUCTION

Corrosion of steel in concrete structures leads to distress in concrete and causes concrete spalling, which further decreases the service life of the structures and requires more maintenance during their service, especially for those exposed to a chloride-existed environment such as the marine environment, bridge decks where de-icing salts are used. As mentioned in the previous chapter, many approaches have been developed and applied to alleviate corrosion-related problems. This chapter reviews several corrosion-resistant or non-corrosive reinforcement bars that are either readily available on the market or have great potential to be applied to reinforced concrete structures in the near future. In detail, the manufacture methods, mechanical properties, durability, structurally-related performance, and relevant analysis models of the epoxy-coated steel rebars (ECSRs), fibre-reinforced polymer (FRP) rebars, FRP-steel composite rebars, stainless steel rebars, and galvanized steel rebars (GSRs) are reviewed in this chapter.

2.2 EPOXY-COATED STEEL REBARS (ECSRs)

2.2.1 Background

The epoxy used to manufacture the epoxy-steel rebars can be classified into liquid and powder epoxy. The liquid epoxy is used by brushing, spraying, and dipping process, while the powder epoxy is usually applied by methods of electrostatic spraying and fluidized bed dipping for thermoset powder and thermoplastic powder, respectively (Cao and Liu 2005; Du *et al.* 2016). After evaluating 47 different coating materials, Clifton *et al.* (1974) found both epoxy and polyvinyl chloride coating should adequately protect the steel reinforcement from corrosion. Still, the acceptable bond and creep properties were only found for epoxy-coated rebars when reinforcing the concrete, and powder epoxy coating overall performed better than the liquid epoxy resins.

2.2.2 Corrosion Resistance of ECSRs

ECSRs were first used in 1973 on a bridge in Pennsylvania to improve the service life of the bridge and now have been widely used in high bridge construction for corrosion protection. It has been used in bridges, airports, highway roads, submarine pipelines, and underground passages. The manufacturing methods, as well as the field practice specification, were immature at the beginning stage, the low quality of the produced ECSRs compounding the rough storage of the ECSRs, and careless operation of the vibrator for consolidation of the concrete caused more holidays and defects on the epoxy-coated rebars, leading to poor corrosion resistance as anticipated. Four substructure components of five major structures that were reinforced with epoxy-

coated rebars and situated within the splash zone on the Florida Keys first showed extensive corrosion problems as concrete spalling caused by corroded steel was observed after 5-7 years of construction (Smith *et al.* 1993). The hoop bars in a single pile in Oregon were also found to be corroded after nine years of exposure to the marine environment (Manning 1996). Spalling and delamination were found in a parking structure reinforced with epoxy-coated rebars after being constructed for ten years as it was exposed to a large amount of de-icing salt with a small concrete cover (Clear 1992). However, ECSRs utilised in many other field structures showed good performance. For example, the epoxy coating in bridges built in 1985 in Carolina was found to be in good condition after eight years of exposure and coated reinforcement in 12 bridge decks in Virginia was in good condition after 17-19 years' service compared with uncoated steel, which had delamination in the range of 5% to 20% of the deck area (Manning 1996). A tunnel structure reinforced with ECSRs was exposed to a harsh environment that combined with the action of chloride and extreme change in temperature. However, only a few rust stains and cracks were observed in the structure 18 years after construction. ECSRs exhibited a better performance when compared with uncoated rebars as a steel-reinforced roof experienced failure after 17 years of construction (Montes *et al.* 2004). Montes *et al.* (2004) concluded that fusion-bonded epoxy coating can significantly extend the service life of uncoated steel rebars (UCSRs).

Although the controversial field performance was reported, the poor performance of the ECSRs mentioned above was attributed to the poor quality of both concrete and epoxy-coated rebars used in the construction due to the mild requirements in the manufacturing and construction specifications at that time, as many holidays and thin coating thickness were found in those rebars. The corrosion seldom happened after

the improvement of the manufacturing methods and higher requirements on the quality of the epoxy-coated rebars. The acceptable number of holidays in ASTM A775/A775M specification was reduced from six to three per metre in 1989, and the required coating thickness changed from $175 \pm 50 \mu\text{m}$ to $175 - 300 \mu\text{m}$ in 1993, the severity-of-bending tests were increased to 180° in 1994.

Except for plenty of research to investigate the field performance of the epoxy-coated reinforcement available in the market, many efforts have been made to enhance the performance of the coating layer, improve the adhesion ability of the coating layer to the steel rebars, and strengthen the bond properties between the epoxy-coated reinforcement and concrete. Inadequate adhesion and cohesion make the coating susceptible to peeling off from the underlying steel surface. Various techniques have been developed to enhance adhesion, such as mechanical polishing and laser irradiation to modify the metal surface properties; acid or alkaline etching to create a roughened texture on the metal surface; anodic oxidation to create an oxide layer on the metal surface and thus enhancing its bond property; silane coupling agent and filler modification to increase the adhesion ability of the coating layer to steel substrates (Wei *et al.* 2020). In short, adhesion strength is derived from a combination of factors, including mechanical interlocking and chemical forces (primary and secondary bond force). The concept of mechanical interlocking was first introduced by MacBain and Hopkins (1925) as the oldest proposed adhesion mechanism; however, it has not been widely accepted, as in most cases, the enhanced adhesion was attributed to the increased interfacial area, which helps develop a stronger adhesion between smooth surfaces. Wang *et al.* (2018) studied how the roughness of the steel rebar surface influenced the adhesion strength between the coating and the steel rebar. They found the sandblast had a positive effect on the adhesion

improvement as it cleaned all the dust on the steel surface. However, with the increase of the surface roughness, the adhesion strength increased when roughness increased from 1.0 μm to 3.3 μm but decreased when roughness exceeded 3.3. μm .

Phosphate conversion coatings have gained extensive applications in the industry to pre-treat the steel bodies before applying organic coating as it increases the adhesion between the substrate and the coating and has lower toxicity than chromate-based conversion (Wei *et al.* 2020). Chen *et al.* (2018) increased the surface roughness and pre-treated the steel substrate with resin acetone solution to improve the adhesion strength of the coating to steel substrates. Riazaty *et al.* (2019) found Samarium (III)-based conversion could improve the adhesion between epoxy/steel by up to 78% by increasing the roughness of the surface and improving the surface free energy.

Due to the intrinsic property of the epoxy, ECSRs are easy to be damaged during transportation and installation. The local damages would form before concrete hardening and thus diminish the corrosion resistance as local corrosion would occur in those positions. Ping *et al.* (2018) combined fly ash cenospheres and short glass fibres into epoxy to improve the erosion properties of the coating. Li *et al.* (2020) introduced a novel filler comprised of graphene oxide and fly ash cenospheres to enhance both the wearing resistance and corrosion resistance of the epoxy coating layer. Weishaar *et al.* (2018) mixed self-healing microcapsules into the epoxy coating to remedy the damage on the epoxy coating that was caused on the worksites. The results showed that self-healing coating could heal coating damage and prevent corrosion from the damage induced during installation and could still delay the corrosion process when damaged beyond its ability to heal compared with the non-healing coating. However, though many efforts have been made to solve this problem, the most widely available ECSRs still only have a layer of epoxy coating.

2.2.3 Structurally-Related Performance of ECSRs

The epoxy coating reduced the bond strength between the steel rebars and concrete due to the slipperiness of the epoxy material. The development length of ribbed ECSRs was suggested to increase by 20-50% in the ACI code (ACI committee, 2019) to account for the reduced mechanical interlock effect and friction between ECSRs and concrete.

Treece and Jirsa (1987) evaluated the bond properties of ECSRs by carrying out beam-end tests and concluded that uncoated rebars developed a higher bond strength of 17% than ECSRs, and similar results were obtained in fatigue tests and static tests. The reduction of the bond strength was found to be independent of the concrete strength, bar size, and coating thickness. Therefore, they recommended a 15% increased development length for epoxy-coated reinforcing rebars in the application of concrete structures. Experiments taken by Huang *et al.* (2021) also showed an approximately 15% lower bond strength for epoxy-coated rebars compared with conventional uncoated rebars, whether in normal concrete, seawater sea-sand concrete (SSC), or recycled aggregate concrete. Experiments taken by Murphy (2021) indicated a poor bond performance of ECSRs in concrete and, consequently, a worse crack control ability when compared with UCSRs, GSRs, and textured ECSRs. Choi *et al.* (1991) concluded that the bond strength reduction caused by the epoxy coating would be increased with the diameter of steel rebars, and the reduction magnitude was affected by the deformation patterns of steel rebars. The extent of the reduction caused by the coating layer was smaller than the modification factors of reinforcement development length as required in the ACI building code. Chase (1993) evaluated the flexural performance of the concrete slabs reinforced with the ECSRs that had a disbondment degree of 20-30% between the coating layer and the steel

substrate. The results showed that this disbondment range would not influence the structural capacity of one-way slabs.

Assaad and Issa (2012) found the bond strength of epoxy-coated reinforcement was smaller than uncoated reinforcement due to the reduced friction coefficient for the epoxy surface, and the bond strength was further reduced for specimens conditioned underwater. However, contradictory results were reported by some researchers. For example, El-Hawary (1999) assessed the bond performance of ECSRs in concrete that was exposed to marine environments and found the bond strength reduction of the coated steel rebars was not significant, which was only 6.47% compared to the UCSRs. The bond strength even became larger than that of UCSRs after 18 months' exposure in the tidal zone.

2.3 FIBRE-REINFORCED POLYMER (FRP) REBARS

2.3.1 Background

In the last several decades, FRP products have been popular studies in various fields. They have shown excellent performance in the structure construction, car, aeroplane, and ship industries. FRP rebars have been developed for civil construction due to their high strength-to-weight ratio and corrosion-resistant properties. The FRP products have been classified into different types based on the types of long continuous fibre that are used to produce the FRP composites. Among the various FRP rebars, glass fibre-reinforced polymer (GFRP) rebars and basalt fibre-reinforced polymer (BFRP) rebars are the two most popular products that now can be easily obtained from the market since the cost of these two materials is much less than other

fibres, such as the aramid fibre-reinforced polymer (AFRP), carbon fibre-reinforced polymer (CFRP) and polyethylene terephthalate fibre-reinforced polymer (PET-FRP). The use of FRP rebars in civil construction has become more and more universal, especially in harsh environments, such as bridge decks in cold regions that experience the freeze-thaw cycle and salt is usually used for de-icing purposes (Gooranorimi and Nanni 2017).

2.3.2 Corrosion Resistance of FRP Rebars

The general definition of corrosion is a process to oxidise the atoms on the metal surface, so the corrosion does not occur in FRP composites as they are non-metallic materials. This is the reason why they have been chosen as corrosion-resistant materials to replace conventional steel reinforcement, especially in harsh environments. Corrosion is the deterioration mechanism for steel rebars and steel-reinforced concrete structures. Although FRP rebars do not suffer from corrosion, they also deteriorate in hostile environments. This type of deterioration has now been regarded as the “corrosion” problem of FRP composites (Manoj Prabhakar *et al.* 2019). So, the corrosion resistance of FRP rebars emphasised in this thesis refers to their durability in various environments.

Many laboratory experiments have been carried out to study the corrosion resistance of FRP rebars. Hojo *et al.* (1991) reported three forms of corrosion that might occur in different types of FRP composites: the surface reaction type corrosion refers to the reaction in the resin where ester bonds are attacked and dissolved in alkaline solutions; the corrosion layer forming type is similar to the surface reaction type where ester bonds are corroded, but the crosslinked polymer chain remains to form a corrosion

residual layer; and the penetration corrosion type represents the situation that the strength of FRP composites will decrease after the saturated absorption of the liquid from the environment. Won *et al.* (2008) examined the deterioration of GFRP rebars exposed to alkaline solutions and tap water environments. They found the residual strength of the GFRP rebars after immersion in tap water for 50 days and 100 days was 99% and 97%, respectively, and the residual strength for specimens exposed to 20°C and 80°C alkaline solutions after 300 days' immersion was around 83% and 60%, respectively, which indicated the alkaline solution and elevated temperature would severely “corrode” the FRP composites. The hydrolysis of the resin was regarded as the primary cause of the degradation of FRP composites in tap water as well as in seawater (Feng *et al.* 2022a). Similar results were obtained in the studies by Almusallam *et al.* (2012).

The “corrosion” of the FRP rebars is significant when the bare rebars are directly exposed to a solution environment. It will be more difficult to corrode when they are wrapped in concrete. Almusallam *et al.* (2012) found the GFRP rebars covered by concrete degraded by around 6.0%, 23.5%, and 22.0% after 18 months of immersion in room temperature water, 50 °C hot water, and 50 °C alkaline solution, respectively. The degree of the degradation of the GFRP rebars embedded in concrete was only half of that of bare GFRP rebars (Won *et al.* 2008; Almusallam *et al.* 2012).

Moreover, the monitoring results from a field application of FRP-reinforced concrete bridge decks showed that the FRP rebars possessed good corrosion resistance after experiencing the use of de-icing salts, freeze-thaw cycles, elevated temperature, and heavy traffic loads (Benmokrane *et al.* 2004). GFRP rebars applied in the Gulf area and Riyadh area, which had a hot-humid condition and a hot-dry condition,

respectively, showed no degradation occurred after 18 months of exposure (Almusallam *et al.* 2012).

There is no doubt that an alkaline aqueous condition is the most “corrosive” environment for FRP products. The contradictory results between the laboratory experiments and field exposure tests are mainly attributed to the different exposure conditions as the current reported field application results were obtained from the bridge structures that were not kept in aqueous environments. Although many laboratory experiments have been carried out, the deterioration mechanisms of FRP composites are still unclear, and that is why the service life of FRP composites cannot be accurately predicted at the present stage (Ceroni *et al.* 2006). Therefore, the great conservative utilisation of FRP rebars is universally existed in civil construction.

2.3.3 Structurally-Related Performance of FRP Rebars

FRPs are linear, elastic brittle materials that have high tensile strength along the longitudinal directions of the inner fibres but low tensile strength in the direction away from the fibres’ alignment, as fibres can only sustain the loads along their alignment direction. For circumstances where loads deviate from the fibres’ longitudinal direction, the resin bears the forces loaded on the composites due to their orthotropic material nature (Sen 2003). The experiments conducted by Farid *et al.* (2020) illustrated that the compressive strength ranged from 300 MPa to 600 MPa for GFRP rebars with a diameter of 17.5 mm to 27.2 mm and 368 MPa to 470 MPa for BFRP rebars with a diameter of 17.6 mm to 21.8 mm based on the different loading rates. The compressive tests for #15 GFRP rebars performed by Deitz *et al.* (2003) showed that the non-slender GFRP specimens had a compressive strength of

approximately 50% of their tensile strength. Although results from Koosa and Pedram (2021) exhibited a high compressive to tensile strength ratio, which could reach 99% for some specimens, a small ratio of 55% was also noticed for rebars produced by different manufacturers, thus they recommended taking the compressive tests before the use of each batch of the FRP rebars rather than deduce the compressive strength from the tensile strength.

Tighiouart *et al.* (1998) attributed the lower bond strength between GFRP rebars and concrete to the decreased adhesion and friction between the GFRP rebars and concrete, which dominated the bond strength when comparing the performance of conventional steel rebars. With the progress of the raw materials and manufacturing methods, the bond performance of the FRP rebars was verified to be different in some cases. Okelo and Yuan (2005) found that similar deformation on the FRP rebars to that on the steel rebar surface would enhance the bond performance of the FRP rebars when compared to other deformations or indentations. However, the bond strength of the three types of FRP rebars (GFRP rebars, AFRP rebars, CFRP rebars) exhibited a large discreteness which varied from 40% to 100% of the steel rebars' bond strength. Antonietta *et al.* (2007) obtained more results that deformed FRP rebars displayed a bond strength of 3-4 times that of the sand-coated rebars. After taking pull-out tests of BFRP/GFRP rebars in concrete, El Refai *et al.* (2015) suggested a mean value of 0.048 and 0.023 by curve fitting of experimental data for the parameter α and p in the analytical model that was used to define the local bond stress-slip model between the sand-coated BFRP rebars and concrete, while the average values of these two parameters are 0.05 and 0.167 for sand-coated GFRP rebars.

Alves *et al.* (2011) found that fatigue loading would significantly decrease the bond strength by at least 29% between the GFRP rebars and concrete, while the freeze-

thaw cycles would increase the peak slip and bond strength of GFRP rebars in concrete that sustained the tensile loading at the conditioned time, though the experimental results were inconsistent with the conclusions drawn by Kumar and GangaRao (1998) who concluded that fatigue would not cause bond loss between the FRP rebars and concrete in FRP reinforced concrete deck steel stringers.

The flexural design of FRP-reinforced concrete beams should control the failure mode to be concrete crush rather than reinforcement rupture since FRP rebars do not yield. Nanni (1993) suggested that the working-stress methods were more suitable for FRP rebars than the ultimate-strength methods when designing the FRP-reinforced flexural members in order to avoid the brittle failure of FRP materials. Al-Sunna *et al.* (2012) evaluated the deflection behaviour of GFRP/CFRP rebar-reinforced concrete beams and slabs, and they attributed the more considerable overall deformation of the structural members to shear cracking, shrinkage and bond loss between the FRP rebars and concrete when compared to that reinforced with steel rebars. Moreover, the plane section of the FRP-reinforced concrete members might not remain plane across the entire section when high-level loading was exerted. Similar to the results obtained by Wang and Belarbi (2005), who utilised polypropylene fibre-reinforced concrete to improve the ductility and decrease the crack width of FRP-reinforced concrete beams. Maranan *et al.* (2015) also proved that the flexural performance of the GFRP rebar-reinforced concrete beams could be enhanced by using geopolymer concrete and sand-coated GFRP rebars. Their results showed a higher bending-moment capacity than the previous experimental results, and the values were calculated based on the predictive equation in the codes of ACI 4401.R-06 and CSA 806-12. These enhancements might be attributed to the improved concrete strength caused by the geopolymers or polypropylene fibres.

2.4 STEEL-FRP COMPOSITE BARS (SFCBs)

2.4.1 Background

To cope with the brittle property of FRP rebars and to further avoid the brittle failure of FRP-reinforced concrete structures, a novel reinforcement rebar was invented and produced by Wu *et al.* (2009; 2010), aiming to combine the corrosion resistance of the FRP composites and the ductile property of the steel rebars. SFCBs are manufactured by pultruding the outer FRP layers onto the steel surface. The configuration of the SFCBs is shown in Figure 2.1. After a large number of studies, the ribbed steel rebars were recommended by Wu *et al.* (2010) as the bond strength between the core steel rebars and outer FRP layers could thus be guaranteed, unlike that manufactured by plain round bars. The gaps between the deformations on the steel rebars were first filled by the roving fibres to avoid the pultruded fibres buckling due to the existence of the protuberant deformations on the steel rebars' surface. The raw materials used to produce the pultruded FRP layers of the SFCBs are the same as that of pultruded FRP rebars. Different types of fibres and resins can be selected according to the application scenario and construction requirements. Zhao *et al.* (2020) developed a type of SFCB using round plain steel rebars by first wrapping a fibre cloth on the rebar surface. This new method can simplify the manufacturing process of SFCBs that are produced using conventional ribbed steel rebars, though the bond strength of the SFCBs with round steel rebars exhibited a lower bond strength than SFCBs with ribbed steel rebars in concrete, the authors attributed the lower bond strength to the different surface treatment.

2.4.2 Corrosion Resistance of SFCBs

The corrosion resistance of the SFCBs was commonly assessed by the mechanical deterioration of SFCBs or SFCB-reinforced concrete structures in harsh environments. Gu *et al.* (2021) studied the tensile properties and bond performance of SFCBs under chloride attacks. The SFCBs showed better corrosion resistance than steel rebars and worse performance than FRP rebars in terms of tensile strength, and the basalt-type SFCBs exhibited higher strength retention than glass-type SFCBs after 135 days of immersion in NaCl solution. However, the glass-type SFCBs that were subjected to a sustained load showed the lowest tensile retention after 135 days of immersion. The bond strength of SFCBs in sea sand concrete for those kept in a wet-dry cycling condition for up to 90 days was tested to be improved, while the results of steel rebars in the same conditions exhibited a decreasing trend (Dong *et al.* 2016). Although the bond strength decreased for specimens immersed in the 40 °C seawater, the deterioration rate was diminished when compared to the results of steel rebars due to the barrier effect of the FRP layer. However, the SFCB-reinforced concrete beams under a sustained load that was conditioned with wet-dry cycling for 90 days illustrated a decreased bearing capacity despite the fact that enhancements were made to the flexural stiffness and energy ductility, and the increase in crack widths was not significant when comparing with the steel rebar-reinforced concrete beams (Dong *et al.* 2017). Dong *et al.* (2018) predicted that the bond strength retentions of SFCBs embedded in SSC immersed in the 40 °C and 50 °C seawater after 50 years are 84% and 96%, respectively. SFCBs are believed to perform better than steel rebars. In short, the corrosion resistance of SFCBs depends on the corrosion resistance of the outer FRP layer, and the core steel rebars will not be corroded before the outer FRP layer loses its protective efficiency. However, the bond strength of the

SFCBs in concrete blocks under coupling action of sustained load and 3.5 wt% NaCl corrosive solutions showed a lower retention than that of steel rebars and FRP rebars after being conditioned for 180 days (Ge *et al.* 2021). Both the yielding load and the maximum load of the SFCB-reinforced beams decreased with the ageing time, while the flexural stiffness increased after 180 days of ageing (Ding *et al.* 2021).

Zhou *et al.* (2019) measured the corrosion rate of carbon-type and glass-type SFCBs by taking electrochemical tests to accelerate the corrosion process of rebars and found that the corrosion rate was 1/10 that of steel rebars for the former and 1/100 that of steel rebars for the latter, which proved that SFCBs made by carbon fibre behave worse against corrosion. The corrosion rate of SFCBs was influenced by fibre types, coating quality and manufacturing process. For example, the SFCBs with a thread surface texture exhibited a more significant corrosion rate than those with an indented surface texture. Zhou *et al.* (2020) recommended utilising carbon-type SFCBs as assistant anode in an impressed current cathodic system to protect the RC structures, as SFCBs can provide extra reinforcement for structures. The corrosion resistance of the carbon-type SFCBs was worse than CFRP rebars, as the service life of the former one was estimated to be seven years with an impressed current density of 20 mA/m² while the service duration for the CFRP rebars was evaluated to be near nine times of SFCBs under the same conditions.

2.4.3 Structurally-Related Performance of SFCBs

The high modulus of elasticity and ultimate tensile strength, as well as a stable post-yield property of SFCBs, were displayed through uniaxial and cyclic tensile tests (Wu *et al.* 2012), as shown in Figure 2.2. The mixture rule was verified to successfully

predict the mechanical properties of SFCBs under monotonic load, while the stress-strain restoring force model constructed by Wu *et al.* (2010) was proved to describe the behaviour of SFCBs under cyclic loads more accurately. Sun *et al.* (2017) studied the compressive behaviour of SFCBs and three failure modes: elastic buckling before steel yielding, post-yielding buckling, and no buckling were observed, which was influenced by the length-to-diameter ratio of SFCBs. The same results were also obtained by Tang *et al.* (2019). When the slenderness ratio was smaller than 4, post-yield buckling would happen due to either the splitting or buckling of the outer fibre layers. When the slenderness ratio was larger than 12, the overall buckling of the specimens would be observed.

Different SFCB-reinforced concrete structures have been tested by many researchers to verify their structural performance. Wu *et al.* (2012) studied the bond performance of SFCBs in concrete, which showed a favourable result through an improved manufacturing method suggested by the authors. They used SFCBs to strengthen steel-reinforced concrete beams by using the near-surface-mounted methods, which proved to promote stiffness and the bearing capacity of the beams. Ding *et al.* (2021) studied the flexural performance deterioration of SFCB-reinforced concrete beams. The results proved a better crack control ability of SFCBs while the ductility of SFCB-reinforced concrete beams was inferior compared with steel rebar-reinforced concrete beams. Sun *et al.* (2011b) pointed out that the steel/FRP ratio would influence the failure mode of the near-surface-mounted-SFCBs strengthened concrete beam, where a high ratio would lead to the “concrete-crushing” failure after the yielding of core steel rebar and a low ratio would result in the “concrete-cover-debonding” failure after the core steel rebars yielding. Except for the single use of SFCBs in concrete structures, Yang *et al.* (2019) and Yang *et al.* (2020) hybridised

the SFCBs with steel rebars and BFRP rebars, respectively, to reinforce the concrete beams, which explored the broader application of SFCBs.

Fahmy *et al.* (2010) verified the feasibility of utilising the SFCBs in reinforced concrete bridge columns, which showed an improved recoverability limit for lateral drift. The same results were also obtained by Sun *et al.* (2011a) and Wu *et al.* (2012). The SFCB-reinforced concrete column showed a post-yield stiffness that decreased the residual displacement, which means the structures possess better reparability after the earthquake. The steel-basalt-fibre-composite rebar-reinforced concrete column performed better than that reinforced with steel-carbon-fibre-composite rebars due to the better ductility of the basalt fibres. Fang *et al.* (2023) utilised SFCBs to replace the FRP rebars in FRP-reinforced SSC columns with a square cross-section. The outcomes of the axial compressive tests verified the feasibility of applying SFCBs in this structure. Different from concrete columns reinforced with longitudinal FRP rebars, the SFCB-reinforced SSC columns could give a warning before their failure because of the pseudo-ductile property of SFCBs.

2.5 STAINLESS STEEL REBARS

2.5.1 Background

Stainless-steel rebars, which possess good weldability, ductility, high and low-temperature mechanical properties, excellent corrosion resistance, and little galvanic corrosion problem, have been utilised in some structures located in hostile environments, such as the deck of bridges where de-icing salts were frequently used,

marines structures like wharf and piers, offshore platforms, etc. (McGurn 1998). The Hong Kong-Zhuhai-Macao Bridge, Temburong Bridge, Lam Tin Tunnel, Tseung Kwan O Bridge, Qingshan Yangtze River Bridge, etc., have applied stainless steel rebars to mitigate the risk of premature cracking of the concrete caused by corrosive products.

According to the composition of alloying elements and microstructures, stainless steel is usually divided into five categories: martensite, ferrite, austenitic steel, duplex, and precipitation-hardening stainless steel (Ahmed *et al.* 2021). The properties of stainless steel are also influenced by the content of composited alloying elements. For example, intergranular corrosion can be prevented by controlling the carbon content of stainless steel rebars at a low level, which is graded using “LN”. The localized corrosion resistance can be enhanced by adding more molybdenum elements (Castro *et al.* 2003).

However, the high price of stainless steel rebars is the primary reason that has stopped its popularization in the construction industry. Only those essential structures that face the threat of corrosion and have a design life over 75 years would consider utilising stainless steel rebars, as the high initial material cost of stainless steel rebars can be 10% of the total project cost or even more (Cramer *et al.* 2002), though the cost of the stainless steel rebars would decrease to a smaller value when considering the accumulated cost over the design life of the structures by reducing the maintenance fee (Cadenazzi *et al.* 2019; Hasan *et al.* 2019).

2.5.2 Corrosion Resistance of Stainless Steel Rebars

Although a reinforced concrete pier in the Progreso Port in Mexico, which first adopted the stainless steel rebars for girder reinforcement to reduce the corrosion risk, reported no visible deterioration after 60 years of service, the stress corrosion cracking and a few pitting corrosions were observed (Castro-Borges *et al.* 2002). The corrosion resistance of stainless rebars varies between stainless steel with different grades. The presence of higher levels of Cr(III) oxy-hydroxide and Mo(VI) within the film, along with the underlying nickel layer, contributes to the better corrosion resistance of the duplex steel when compared with nickel-free stainless steel (Elsener *et al.* 2011). The alternating temperature would cause more pitting initiation sites on 304 stainless steel than those kept under consistent temperature (Feng *et al.* 2022b). Duarte *et al.* (Duarte *et al.* 2014) reported austenitic stainless steel (grade 304 and 316), as well as duplex stainless steel (grade 2205), presented higher corrosion resistance compared with carbon steel when embedded in the concrete specimen and exposed to the simulated seawater environment. Calderon-Uriszar-Aldaca *et al.* (2018) also concluded that the 2205 duplex stainless steel rebars and 304 austenitic stainless steel, 316 austenitic stainless steel possess better corrosion resistance than lean duplex stainless steel which possess less nickel content after immersing them in the simulated tidal zone conditions for six months, though all their behaviour were superior than the standard carbon steel. Pérez-Quiroz *et al.* (2008) found that the co-use of carbon steel rebars and stainless steel rebars would not increase the corrosion risk on carbon steel even in the high-corrosion-risk conditions as the galvanic corrosion was negligible between stainless steel and carbon steel. Therefore, the stainless steel rebars could be a good candidate for concrete structure rehabilitation. Martin *et al.* (2020) investigated the stress corrosion cracking susceptibility of 316

austenitic stainless steel rebars in simulated concrete pore solution with chloride ions, and the results showed that the passive films ruptured once the yield stress reached, then metastable pits were therefore developed, and the presence of chloride ions enhanced the pitting process.

2.5.3 Structurally-Related Performance of Stainless Steel Rebars

It has been verified that stainless steel rebars possess both higher yield strength and ultimate strength as well as deformability than those of carbon steel rebars. Although 201-grade stainless steel rebars could improve the performance of reinforced concrete beams at the low steel ratio, the stainless steel rebar-reinforced concrete beams exhibited a lower ultimate moment capacity by 12-36% than the recommended values from the codes (Ahmed *et al.* 2021). Pauletta *et al.* (2020) investigated the bond performance of stainless steel rebars, and their results illustrated that the stainless steel rebars exhibited comparable performance to that of carbon steel rebars. Calderon-Uriszar-Aldaca *et al.* (2018) found that the bond strength of 316 austenitic stainless steel rebars and 2304 lean duplex stainless steel were smaller than the reference carbon steel rebars after three months' curing of the concrete, but their bond strength was increased after nine-month curing, which was opposite for carbon steel rebars as the bond strength of carbon steel rebars decreased nearly 20% after nine-month curing. Duarte *et al.* (2014) observed that the bond strength of four types of stainless steel rebars in concrete was much smaller than carbon steel rebars after exposure to simulated seawater for 12 months and 18 months. They attributed the higher bond strength of the carbon steel to the corrosion products produced at the rebar surface, which improved the adhesion by mechanical effect since the corrosion

increased the roughness of the rebar surface and increased the volume of the rebars. The results reported by Duarte *et al.* (2014) were restricted to a short exposure period, and the bond performance after longer exposure periods would be more convincing from the life-cycle perspective.

2.6 OTHER CORROSION-RESISTANT REBARS

Except for the coated steel rebars mentioned above, there are many other kinds of coated rebars, such as galvanized steel reinforcement, which is produced by applying zinc to the steel surface (Yeomans 1994). The zinc coating is metallurgically bonded to the steel as the molten zinc would react with the steel to form an iron-zinc alloy layer at the steel/zinc interface, which makes the coating layer adhered more firmly to the steel substrate and thus results in a better abrasion resistance (Yeomans 2004).

Ceramic porcelain enamel has also been applied as coating materials for steel reinforcement (Hock *et al.* 2008; Tang *et al.* 2012), and the enamel-coated steel rebars were outperformed by the fusion-bonded ECSRs in the corrosion protection.

Ultra-high-performance concrete has been employed as a coating layer on the surface of reinforcing steel for corrosion protection (Eom *et al.* 2022). Moreover, Binici *et al.* (2012) mixed additives such as ground granulated blast furnace slag, barite colemanite, pumice, and basaltic into the coating material to improve the corrosion resistance of steel rebars.

Many efforts have also been made to modify the existing corrosion-resistant rebars. Since the longer development length might cause inconvenience in structural designing, Chang *et al.* (2002) mixed river sand in epoxy to improve the bond

strength between ECSRs and concrete. They studied the influence of the sand size and sand-to-epoxy ratio on the bond properties of their products. The single rebar pull-out test results revealed that the bond strength of sand-epoxy-coated rebar could be improved by mixing river sand in the epoxy and adjusting by changing the particle size and sand-to-epoxy ratio. Yeih *et al.* (2004) added fly ash to improve the bond strength of ECSRs to concrete and found a 0.5 weight ratio of fly ash/epoxy could develop the same bond strength as the uncoated rebar.

Kim and Andrawes (2019) applied textured epoxy to coat the reinforcing rebars to improve the slip resistance and decrease the crack width, as well as reduce the propagation of cracks in the reinforced concrete beams.

2.7 CONCLUSIONS

This chapter has presented a systematic review of the existing corrosion-resistant rebar technologies. The corrosion resistance and structurally-related performance of various types of corrosion-resistant rebars were compared. The comparisons and discussions allow the following conclusions to be drawn:

- (1) The corrosion resistance of epoxy-coated steel rebars (ECSRs) will be significantly decreased once the coating layer is slightly damaged by the impact and scratch during the transportation, storing and handling processes. The bond performance of ECSRs to concrete is far inferior to that of uncoated steel rebars (UCSRs), although a few attempts have been made to enhance the bond performance.

- (2) FRP rebars possess excellent durability in aggressive environments, e.g., marine and coastal areas. However, the durability of FRP rebars underwater is still unclear; the more significant deflection and wider cracks of a beam reinforced with FRP rebars than those of a beam reinforced with steel rebars limit the broader application of FRP rebars.
- (3) The newly developed steel-FRP composite bars (SFCBs) exhibit inferior durability when compared to FRP rebars but better than steel rebars. However, SFCBs are inconvenient in practical implementations as their bi-linear tensile behaviour is different from the elastic-plastic tensile behaviour of normal steel rebars that have been well-accepted by engineers/designers in the construction industry. Such a difference may result in a significant change in the current standards/codes for reinforced concrete structure design.
- (4) Many efforts have been made to improve either the corrosion resistance or the structural performance of the existing corrosion-resistant rebars. It is necessary to explore and develop a type of reinforcement that possesses both good corrosion resistance and structurally-related performance.

2.8 REFERENCES

- Abed, F., Mehaini, Z., Oucif, C., Abdul-Latif, A. and Baleh, R. (2020). “Quasi-static and dynamic response of GFRP and BFRP bars under compression”, *Composites Part C: Open Access*, Vol. 2, No. 100034.
- ACI Committee. (2019) “Building code requirements for structural concrete (ACI 318-19)”. American Concrete Institute.

- Ahmed, K.S., Habib, M.A. and Asef, M.F. (2021). “Flexural response of stainless steel reinforced concrete beam”, *Structures*, Vol. 34, pp. 589-603.
- Al-Sunna, R., Pilakoutas, K., Hajirasouliha, I. and Guadagnini, M. (2012). “Deflection behaviour of FRP reinforced concrete beams and slabs: An experimental investigation”, *Composites Part B: Engineering*, Vol. 43, No. 5, pp. 2125-2134.
- Almusallam, T.H., Al-Salloum, Y.A., Alsayed, S.H., El-Gamal, S. and Aqel, M. (2012). “Tensile properties degradation of glass fiber-reinforced polymer bars embedded in concrete under severe laboratory and field environmental conditions”, *Journal of Composite Materials*, Vol. 47, No. 4, pp. 393-407.
- Alves, J., El-Ragaby, A. and El-Salakawy, E. (2011). “Durability of GFRP bars’ bond to concrete under different loading and environmental conditions”, *Journal of Composites for Construction*, Vol. 15, No. 3, pp. 249-262.
- Antonietta Aiello, M., Leone, M. and Pecce, M. (2007). “Bond performances of FRP rebars-reinforced concrete”, *Journal of materials in civil engineering*, Vol. 19, No. 3, pp. 205-213.
- Assaad, J.J. and Issa, C.A. (2012). “Bond strength of epoxy-coated bars in underwater concrete”, *Construction and Building Materials*, Vol. 30, pp. 667-674.
- Benmokrane, B., El-Salakawy, E., El-Ragaby, A., Desgagné, G. and Lackey, T. (2004). “Design, construction and monitoring of four innovative concrete bridge decks using non-corrosive FRP composite bars”, *Proc., Annual Conference of the Transportation Association of Canada*,

- Binici, H., Aksogan, O. and Durgun, M.Y. (2012). “Corrosion of basaltic pumice, colemanite, barite and blast furnace slag coated rebars in concretes”, *Construction and Building Materials*, Vol. 37, pp. 629-637.
- Cadenazzi, T., Dotelli, G., Rossini, M., Nolan, S. and Nanni, A. (2019). “Cost and environmental analyses of reinforcement alternatives for a concrete bridge”, *Structure and Infrastructure Engineering*, Vol. 16, No. 4, pp. 787-802.
- Calderon-Uriszar-Aldaca, I., Briz, E., Larrinaga, P. and Garcia, H. (2018). “Bonding strength of stainless steel rebars in concretes exposed to marine environments”, *Construction and Building Materials*, Vol. 172, pp. 125-133.
- Cao, J.Z. and Liu, G.G. (2005). “The application of epoxy-coated reinforcement in steel reinforced concrete structure”, in: *Proceedings of 12th China Coastal Engineering Symposium*, China Ocean Press, pp. 783-785 [in Chinese].
- Castro-Borges, P., Troconis-Rincon, O., Moreno, E.I., Torres-Acosta, A.A., Martinez-Madrid, M. and Knudsen, A. (2002). “Performance of a 60-year-old concrete pier with stainless steel reinforcement”, *Materials Performance*, Vol. 41, No. 10, pp. 50-55.
- Castro, H., Rodriguez, C., Belzunce, F.J. and Canteli, A.F. (2003). “Mechanical properties and corrosion behaviour of stainless steel reinforcing bars”, *Journal of Materials Processing Technology*, Vol. 143, pp. 134-137.
- Ceroni, F., Cosenza, E., Gaetano, M. and Pecce, M. (2006). “Durability issues of FRP rebars in reinforced concrete members”, *Cement and Concrete Composites*, Vol. 28, No. 10, pp. 857-868.

- Chang, J.J., Yeih, W. and Tsai, C.L. (2002). "Enhancement of bond strength for epoxy-coated rebar using river sand", *Construction and Building Materials*, Vol. 16, No. 8, pp. 465-472.
- Chase, S. (1993). *Structural Effects of Epoxy Coating Disbondment*, Federal Highway Administration. Office of Engineering and Highway Operations R&D, McLean, Virginia, United States.
- Chen, P., Wang, Y., Li, J., Wang, H. and Zhang, L. (2018). "Adhesion and erosion properties of epoxy resin composite coatings reinforced with fly ash cenospheres and short glass fibers", *Progress in Organic Coatings*, Vol. 125, pp. 489-499.
- Choi, O.C., Hadje-Ghaffari, H., D., D., and McCabe, S.L. (1991). "Bond of epoxy-coated reinforcement: bar parameters", *ACI Materials Journal*, Vol. 88, No. 2, pp. 207-217.
- Clear, K.C. (1992). *Effectiveness of Epoxy-Coated Reinforcing Steel-Final Report*, Canadian Strategic Highway Research Program, Ottawa, Ontario, Canada 1-128.
- Clifton, J.R., Beeghly, H.F. and Mathey, R.G. (1974). *Nonmetallic Coatings for Concrete Reinforcing Bars*, Federal Highway Administration Offices of Research and Development, Washington, United States.
- Cramer, S.D., Covino Jr, B.S., Bullard, S.J., Holcomb, G.R., Russell, J.H., Nelson, F.J. and Soltesz, S.M. (2002). "Corrosion prevention and remediation strategies for reinforced concrete coastal bridges", *Cement and Concrete Composites*, Vol. 24, No. 1, pp. 101-117.

- Deitz, D.H., Harik, I.E. and Gesund, H. (2003). “Physical properties of glass fiber reinforced polymer rebars in compression”, *Journal of Composites for Construction*, Vol. 7, No. 4, pp. 363-366.
- Ding, L., Lei, M., Wang, X., Shi, Y., Zhu, Z., Yu, P. and Wu, Z. (2021). “Durability of concrete members reinforced with steel-FRP composite bars under dry-wet cycles of seawater”, *Structures*, Vol. 33, pp. 2273-2283.
- Dong, Z., Wu, G. and Xu, Y. (2016). “Experimental study on the bond durability between steel-FRP composite bars (SFCBs) and sea sand concrete in ocean environment”, *Construction and Building Materials*, Vol. 115, pp. 277-284.
- Dong, Z., Wu, G., Zhao, X.-L., Zhu, H. and Lian, J. (2018). “Bond durability of steel-FRP composite bars embedded in seawater sea-sand concrete under constant bending and shearing stress”, *Construction and Building Materials*, Vol. 192, pp. 808-817.
- Dong, Z.Q., Wu, G. and Xu, Y.Q. (2017). “Bond and flexural behavior of sea sand concrete members reinforced with hybrid steel-composite bars presubjected to wet–dry cycles”, *Journal of Composites for Construction*, Vol. 21, No. 2, pp. 04016095.
- Du, Z., Wen, S., Wang, J., Yin, C., Yu, D. and Luo, J. (2016). “The review of powder coatings”, *Journal of Materials Science and Chemical Engineering*, Vol. 4, No. 3, pp. 54-59.
- Duarte, R.G., Castela, A.S., Neves, R., Freire, L. and Montemor, M.F. (2014). “Corrosion Behavior of Stainless Steel Rebars Embedded in Concrete: an Electrochemical Impedance Spectroscopy Study”, *Electrochimica Acta*, Vol. 124, pp. 218-224.

- El-Hawary, M.M. (1999). "Evaluation of bond strength of epoxy-coated bars in concrete exposed to marine environment", *Construction and Building Materials*, Vol. 13, No. 7, pp. 357-362.
- El Refai, A., Ammar, M.A. and Masmoudi, R. (2015). "Bond performance of basalt fiber-reinforced polymer bars to concrete", *Journal of Composites for Construction*, Vol. 19, No. 3, pp. 04014050.
- Elsener, B., Addari, D., Coray, S. and Rossi, A. (2011). "Stainless steel reinforcing bars-reason for their high pitting corrosion resistance", *Materials and Corrosion*, Vol. 62, No. 2, pp. 111-119.
- Eom, I.-H., Oh, S.-K. and Kim, B. (2022). "Bonding performance of steel rebar coated with ultra-high-performance concrete", *Applied Sciences*, Vol. 12, No. 13.
- Fahmy, M.F.M., Wu, Z., Wu, G. and Sun, Z. (2010). "Post-yield stiffnesses and residual deformations of RC bridge columns reinforced with ordinary rebars and steel fiber composite bars", *Engineering Structures*, Vol. 32, No. 9, pp. 2969-2983.
- Fang, S., Li, L., Luo, Z., Fang, Z., Huang, D., Liu, F., Wang, H. and Xiong, Z. (2023). "Novel FRP interlocking multi-spiral reinforced-seawater sea-sand concrete square columns with longitudinal hybrid FRP-steel bars: Monotonic and cyclic axial compressive behaviours", *Composite Structures*, Vol. 305, No. 116487.
- Feng, G., Zhu, D., Guo, S., Rahman, M.Z., Jin, Z. and Shi, C. (2022a). "A review on mechanical properties and deterioration mechanisms of FRP bars under

- severe environmental and loading conditions”, *Cement and Concrete Composites*, Vol. 134, No. 104758.
- Feng, X., Zhang, T., Zhu, R., Chen, Z. and Lu, X. (2022b). “Pitting initiation on 304 stainless steel in a chloride-contaminated pore solution under alternating temperature conditions”, *Corrosion Reviews*, Vol. 40, No. 3, pp. 247-262.
- Ge, W., Han, M., Guan, Z., Zhang, P., Ashour, A., Li, W., Lu, W., Cao, D. and Yao, S. (2021). “Tension and bonding behaviour of steel-FRP composite bars subjected to the coupling effects of chloride corrosion and load”, *Construction and Building Materials*, Vol. 296, No. 123641.
- Gooranorimi, O. and Nanni, A. (2017). “GFRP reinforcement in concrete after 15 Years of Service”, *Journal of Composites for Construction*, Vol. 21, No. 5, pp. 04017024.
- Hasan, M.A., Yan, K., Lim, S., Akiyama, M. and Frangopol, D.M. (2019). “LCC-based identification of geographical locations suitable for using stainless steel rebars in reinforced concrete girder bridges”, *Structure and Infrastructure Engineering*, Vol. 16, No. 9, pp. 1201-1227.
- Hock, V.F., Morefield, S.W., Day, D.C., Weiss, C.A., Malone, P.G. and Hackler, C.L. (2008). “The use of vitreous enamel coatings to improve bonding and reduce corrosion in concrete reinforcing steel”, *Proc., Corrosion Conference and Expo (Corrosion 2008)*, NACE International.
- Hojo, H., Tsuda, K. and Ogasawara, K. (1991). “Form and rate of corrosion of corrosion-resistant FRP resins”, *Advanced Composite Materials*, Vol. 1, No. 1, pp. 55-67.

- Huang, Y., Zhang, Y., Li, X. and Ying, J. (2021). “Bond of epoxy-coated steel bars to seawater sea sand recycled concrete”, *Structures*, Vol. 30, pp. 866-876.
- Khorrarnian, K. and Sadeghian, P. (2021). “Material characterization of GFRP bars in compression using a new test method”, *Journal of Testing and Evaluation*, Vol. 49, No. 2, pp. 1037-1052.
- Kim, K.-H.E. and Andrawes, B. (2019). “Exploratory study on bond behavior of textured epoxy-coated reinforcing bars”, *Journal of Materials in Civil Engineering*, Vol. 31, No. 8, pp. 04019151.
- Kumar, S.V. and GangaRao, H.V. (1998). “Fatigue response of concrete decks reinforced with FRP rebars”, *Journal of Structural Engineering*, Vol. 124, No. 1, pp. 11-16.
- Manning, D.G. (1996). “Corrosion performance of epoxy-coated reinforcing steel: North American experience”, *Construction and Building Materials*, Vol. 10, No. 5, pp. 349-365.
- Manoj Prabhakar, M., Rajini, N., Ayrilmis, N., Mayandi, K., Siengchin, S., Senthilkumar, K., Karthikeyan, S. and Ismail, S.O. (2019). “An overview of burst, buckling, durability and corrosion analysis of lightweight FRP composite pipes and their applicability”, *Composite Structures*, Vol. 230, No. 111419.
- Maranan, G.B., Manalo, A.C., Benmokrane, B., Karunasena, W. and Mendis, P. (2015). “Evaluation of the flexural strength and serviceability of geopolymer concrete beams reinforced with glass-fibre-reinforced polymer (GFRP) bars”, *Engineering Structures*, Vol. 101, pp. 529-541.

- Martin, U., Ress, J., Bosch, J. and Bastidas, D.M. (2020). “Stress corrosion cracking mechanism of AISI 316LN stainless steel rebars in chloride contaminated concrete pore solution using the slow strain rate technique”, *Electrochimica Acta*, Vol. 335.
- McGurn, J.F. (1998). “Stainless steel reinforcing bars in concrete”, in: *Proceedings of International Conference on Corrosion and Rehabilitation of Reinforced Concrete Structures*,
- Montes, P., Bremner, T.W. and Kondratova, I. (2004). “Eighteen-year performance of epoxy-coated rebar in a tunnel structure subjected to a very aggressive chloride-contaminated environment”, *Corrosion*, Vol. 60, No. 10, pp. 04100974.
- Murphy, A.J. (2021). *Comparison of flexural cracking in reinforced concrete beams with different rebar coatings*. Doctoral dissertation Clemson University.
- Nanni, A. (1993). “Flexural behavior and design of RC members using FRP reinforcement”, *Journal of Structural Engineering*, Vol. 119, No. 11, pp. 3344-3359.
- Okelo, R. and Yuan, R.L. (2005). “Bond strength of fiber reinforced polymer rebars in normal strength concrete”, *Journal of Composites for Construction*, Vol. 9, No. 3, pp. 203-213.
- Pauletta, M., Rovere, N., Randl, N. and Russo, G. (2020). “Bond-slip behavior between stainless steel rebars and concrete”, *Materials*, Vol. 13, No. 4, pp. 979.
- Pérez-Quiroz, J.T., Terán, J., Herrera, M.J., Martínez, M. and Genescá, J. (2008). “Assessment of stainless steel reinforcement for concrete structures

- rehabilitation”, *Journal of Constructional Steel Research*, Vol. 64, No. 11, pp. 1317-1324.
- Riazaty, P., Naderi, R. and Ramezanzadeh, B. (2019). “Enhancement of the epoxy coating corrosion/cathodic delamination resistances on steel by a samarium based conversion coating”, *Journal of The Electrochemical Society*, Vol. 166, No. 13, pp. C353-C364.
- Sen, R. (2003). “Advances in the application of FRP for repairing corrosion damage”, *Progress in Structural Engineering and Materials*, Vol. 5, No. 2, pp. 99-113.
- Smith, L.L., Kessler, R.J. and Powers, R.G. (1993). " Corrosion of epoxy-coated rebar in a marine environment." *Epoxy-Coated Reinforcement in Highway Structures*, Transportation Research Circular, Washington, DC, 36-45.
- Sun, Z.-Y., Wu, G., Wu, Z.-S. and Zhang, M. (2011a). “Seismic behavior of concrete columns reinforced by steel-FRP composite bars”, *Journal of Composites for Construction*, Vol. 15, No. 5, pp. 696-706.
- Sun, Z., Tang, Y., Luo, Y., Wu, G. and He, X. (2017). “Mechanical properties of steel-FRP composite bars under tensile and compressive loading”, *International Journal of Polymer Science*, Vol. 2017, No. 5691278, pp. 1-11.
- Sun, Z.Y., Wu, G., Wu, Z.S. and Luo, Y.B. (2011b). “Flexural strengthening of concrete beams with near-surface mounted steel–fiber-reinforced polymer composite bars”, *Journal of Reinforced Plastics and Composites*, Vol. 30, No. 18, pp. 1529-1537.
- Tang, F., Chen, G., Brow, R.K., Volz, J.S. and Koenigstein, M.L. (2012). “Corrosion resistance and mechanism of steel rebar coated with three types of enamel”, *Corrosion Science*, Vol. 59, pp. 157-168.

- Tang, Y., Sun, Z. and Wu, G. (2019). “Compressive behavior of sustainable steel-FRP composite bars with different slenderness ratios”, *Sustainability*, Vol. 11, No. 1118, pp. 1-16.
- Tighiouart, B., Benmokrane, B. and Gao, D. (1998). “Investigation of bond in concrete member with fibre reinforced polymer (FRP) bars”, *Construction and Building Materials*, Vol. 12, No. 8, pp. 453-462.
- Treece, R.A. and Jirsa, J.O. (1987). *Bond strength of epoxy-coated reinforcing bars*. Master's thesis University of Texas at Austin.
- Wang, H. and Belarbi, A. (2005). “Flexural behavior of fiber-reinforced-concrete beams reinforced with FRP rebars”, *ACI Structural Journal*, Vol. 51, No. 230, pp. 895-914.
- Wang, X.-H., Chen, B. and Tang, P. (2018). “Experimental and analytical study on bond strength of normal uncoated and epoxy-coated reinforcing bars”, *Construction and Building Materials*, Vol. 189, pp. 612-628.
- Wei, H., Xia, J., Zhou, W., Zhou, L., Hussain, G., Li, Q. and Ostrikov, K. (2020). “Adhesion and cohesion of epoxy-based industrial composite coatings”, *Composites Part B: Engineering*, Vol. 193, No. 108035.
- Won, J.-P., Lee, S.-J., Kim, Y.-J., Jang, C.-I. and Lee, S.-W. (2008). “The effect of exposure to alkaline solution and water on the strength–porosity relationship of GFRP rebar”, *Composites Part B: Engineering*, Vol. 39, No. 5, pp. 764-772.
- Wu, G., Sun, Z.Y., Wu, Z.S. and Luo, Y.B. (2012). “Mechanical properties of steel-FRP composite bars (SFCBs) and performance of SFCB reinforced concrete structures”, *Advances in Structural Engineering*, Vol. 15, No. 4, pp. 625-635.

- Wu, G., Wu, Z., Luo, Y. and Wei, H. (2009). “A new reinforcement material of steel fiber composite bar (SFCB) and its mechanics properties”, *Proc., 9th International Symposium on Fiber Reinforced Polymer Reinforcement for Reinforced Concrete Structures (FRPRCS-9)*.
- Wu, G., Wu, Z.S., Luo, Y.B., Sun, Z.Y. and Hu, X.Q. (2010). “Mechanical properties of steel-FRP composite bar under uniaxial and cyclic tensile loads”, *Journal of Materials in Civil Engineering*, Vol. 22, No. 10, pp. 1056-1066.
- Yang, Y., Sun, Z.-y., Wu, G., Cao, D.-f. and Pan, D. (2020). “Experimental study of concrete beams reinforced with hybrid bars (SFCBs and BFRP bars)”, *Materials and Structures*, Vol. 53, No. 77, pp. 1-15.
- Yang, Y., Sun, Z.-Y., Wu, G., Cao, D.-F. and Zhang, Z.-Q. (2019). “Flexural capacity and design of hybrid FRP-steel-reinforced concrete beams”, *Advances in Structural Engineering*, Vol. 23, No. 7, pp. 1290-1304.
- Yeih, W., Chang, J.J. and Tsai, C.L. (2004). “Enhancement of the bond strength of epoxy coated steel by the addition of fly ash”, *Cement and Concrete Composites*, Vol. 26, No. 4, pp. 315-321.
- Yeomans, S.R. (1994). “Performance of black, galvanized, and epoxy-coated reinforcing steels in chloride-contaminated concrete”, *Corrosion*, Vol. 50, No. 1, pp. 72-81.
- Yeomans, S.R. (2004). *Galvanized Steel Reinforcement in Concrete*, Elsevier, Amsterdam, Netherlands.
- Zhao, D., Pan, J., Zhou, Y., Sui, L. and Ye, Z. (2020). “New types of steel-FRP composite bar with round steel bar inner core: Mechanical properties and

bonding performances in concrete”, *Construction and Building Materials*, Vol. 242, No. 118062.

Zhou, Y., Zheng, X., Xing, F., Sui, L., Zheng, Y. and Huang, X. (2020). “Investigation on the electrochemical and mechanical performance of CFRP and steel-fiber composite bar used for impressed current cathodic protection anode”, *Construction and Building Materials*, Vol. 255.

Zhou, Y., Zheng, Y., Pan, J., Sui, L., Xing, F., Sun, H. and Li, P. (2019). “Experimental investigations on corrosion resistance of innovative steel-FRP composite bars using X-ray microcomputed tomography”, *Composites Part B: Engineering*, Vol. 161, pp. 272-284.

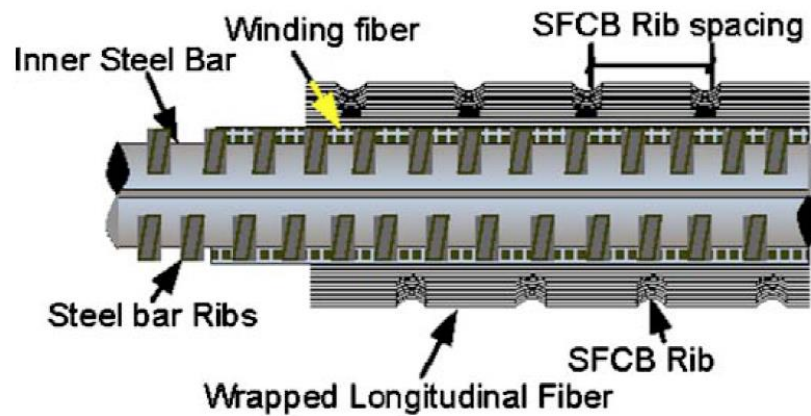


Figure 2.1 Configuration of Steel-FRP composite bars (SFCBs) [Extracted from Wu *et al.* (2010)]

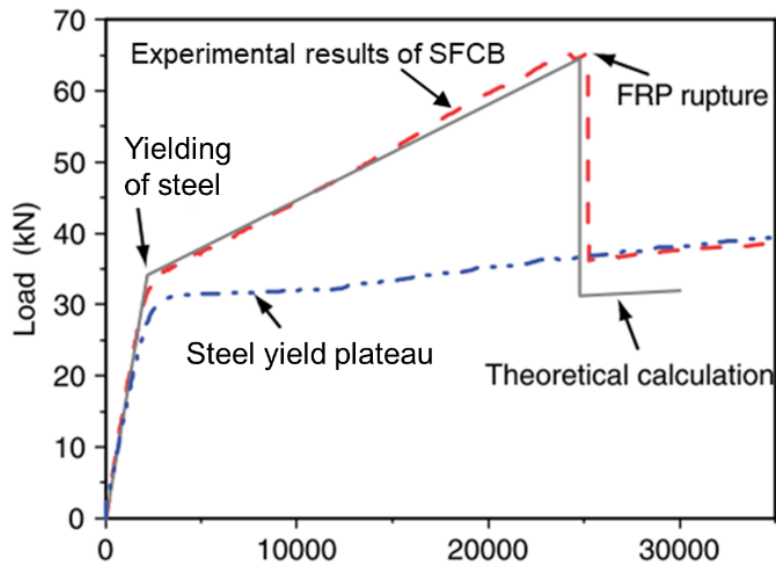


Figure 2.2 Load-strain relationship of SFCBs in tension [Extracted from Wu *et al.* (2012) with modifications]

CHAPTER 3

MANUFACTURING PROCESS AND PROPERTIES OF FRP-COATED STEEL REBARS

3.1 INTRODUCTION

This chapter presents a series of experiments for developing manufacturing methods and examining the material properties of FRP-coated steel rebars (FCSRs). Filament winding is a technology for manufacturing fibre-reinforced polymer (FRP) composites. It was developed in the early 1940s (Abdalla *et al.* 2007) and has now been widely used for the fabrication of FRP tubes, pressure vessels, and other axisymmetric or non-axisymmetric components. Filament winding winds continuous filaments under tension over a rotating mandrel with designed winding angle(s) ranging from the hoop direction, which is perpendicular to the longitudinal axis of the mandrel, to aligned closely parallel to the longitudinal axis of the mandrel (Abdalla *et al.* 2007; Frketic *et al.* 2017). As the most economical and most potent form of fibre reinforcement, continuous fibres can be wound with the designed angles and plies to conform to the stress direction and magnitude in the structures. Apart from these advantages, filament winding also requires a low labour cost in the manufacturing operation (Shen 1995).

The process of filament winding includes three steps (Gutowski 1997). First, to select winding configurations (including the winding angles and the number of fibre plies) and raw materials, including resins and continuous fibre materials (in the forms of filaments, wires, yarns, tapes or others) or prepregs; second, to wind the fibre-reinforced polymer composite; third, to cure the wound product. Based on the raw materials used, i.e., prepregs or resins and continuous fibre materials, filament winding can be recognized as “dry winding” or “wet winding” correspondingly (Frketic *et al.* 2017). Compared with “dry winding”, “wet winding” is less time and cost-consuming (Abdalla *et al.* 2007).

The present study utilises filament winding to produce the FRP coating layer of FCSRs. It is expected that continuous fibres in suitable orientations (typically in orientations close to the hoop direction) may reinforce and hence enhance the performance of an epoxy coating layer so that the coating layer will retain its integrity as a protective layer despite the unavoidable impact forces exerted on the FCSRs during the construction process. Moreover, a small tensile force is always applied to the fibres during a typical filament winding process, which will help produce a thin layer of FRP to minimize its effect on the surface geometry of the steel rebars (i.e., with the shapes of the rebar ribs being properly reflected through the coating layer) and to ensure tight contact between the FRP coating layer and the core steel rebar.

In this Chapter, two manufacturing processes for the production of FCSRs, i.e., filament winding with in-line impregnation (referred to as FWII) and filament winding with vacuum-assisted resin infusion (referred to as FWVARI), are briefly introduced. The mechanical, thermal and physical properties of the FCSRs that were produced with the first method are presented.

3.2 MANUFACTURING PROCESSES

3.2.1 *Filament Winding with In-line Impregnation (FWII)*

FWII involves the in-line impregnation of fibre filaments followed by filament winding. In the present study, a 2-axis filament winding machine was used, as shown in Figure 3.1. The filament winding machine is mainly composed of two parts: one is a movable carriage, which contains a resin bath and fibre delivery system; the other is a mandrel. During a typical winding process, a fibre filament is led through the resin bath for impregnation and then led to the delivery head, which is close to the mandrel. The delivery head will deliver the fibre filament onto the rotating mandrel. The horizontal moving speed of the carriage system must be adjusted together with the rotation speed of the mandrel to achieve the designed winding angle(s). All these are controlled by a computer-based system. It must be noted that, unlike the winding of pipes, vessels, or tanks, during which the mandrel must be removed after winding to obtain the wound products, the manufacturing of FCSRs uses the core steel rebar itself as the mandrel and the wound FRP coating layer will not need to be removed after winding and curing. Figure 3.2 depicts the entire manufacturing process of FCSRs with FWII, which includes the following ten steps:

- (1) De-rust steel rebars that are used to produce FCSRs. The de-rusting methods are not limited to mechanical ways (e.g., rolling and sandblasting), chemical ways (e.g., pickling), etc.
- (2) Lead the glass fibre filament to pass through the reel holders to reach the mandrel surface.

- (3) Set the winding patterns by inputting the winding angle(s) into the computer system and set the winding speed according to the wetting ability of the resin used.
- (4) Prepare the epoxy resin according to the required proportion and pour it into the resin bath to impregnate the fibre filaments.
- (5) Fix the impregnated fibre filament onto the “mandrel”, which is the steel rebar in the current study.
- (6) Start the winding programme until the designated layers are achieved.
- (7) Cure FCSRs on a rotation machine at room temperature.
- (8) Post-cure FCSRs under high temperatures (Optional).
- (9) Cut FCSRs into the required length.
- (10) Seal the two ends of each rebar by spraying or brushing a layer of waterproof material or wrapping FRP covers.

It should be noted that the curing conditions in Steps (7) and (8) can be adjusted in accordance with the curing requirement of the utilised resin.

3.2.2 Filament Winding with Vacuum-Assisted Resin Infusion (FWVARI)

Vacuum-assisted resin infusion (VARI) refers to the process of impregnating dry fibres with liquid resins under a vacuum to help eliminate air bubbles and improve the quality of composites (Goren and Atas 2008). VARI is also called vacuum-assisted resin infusion moulding (VARIM) or vacuum-assisted resin transfer moulding (VARTM). By utilising the pressure exerted by a vacuum bag, VARI is suitable for the fabrication of composites with a higher fibre content as more resins could be removed by applied pressure. For instance, Abdullah *et al.* (2020) produced

kenaf-cotton yarn-reinforced polymer tubes via a combination of dry filament winding and VARI. The composites produced by this method possessed a thinner thickness when compared with those produced through heat-shrink tubes after winding dry filaments.

As inspired by the advantages of VARI, the present study used VARI in combination with filament winding, forming the FWVARI. Different from FWII, which winds impregnated fibre filaments to produce the FRP coating layer, FWVARI winds a dry fibre filament onto the steel rebar first, followed by the VARI process to impregnate the wound steel rebar. As steel rebars generally have ribs, it is thus expected that FWVARI may further densify the contact between the coating layer and the steel rebar. Figure 3.3 depicts the entire manufacturing process of FCSRs with FWVARI, which includes the following ten steps:

- (1) De-rust the steel rebars by the ways mentioned in *section 3.2.1* and fix the steel rebars onto the “mandrel system”.
- (2) Lead the glass fibre filament to pass through the reel holders to reach the mandrel surface.
- (3) Set the winding patterns and set the winding speed.
- (4) Fix the glass fibre filament onto the steel rebar and start winding.
- (5) Remove the steel rebars with wound glass fibres until the designed layers are achieved.
- (6) Prepare the vacuum bag adapted to the length of steel rebars with wound dry fibres for the VARI process.
- (7) Prepare the resins used in the VARI process.
- (8) Start the VARI until dry fibres are fully impregnated.
- (9) Cure the impregnated FCSRs in the required conditions with the vacuum bag.

(10) Take out the cured FCSRs and cut them into the required length.

(11) Seal the ends of cut rebars by spraying or brushing a layer of waterproof material.

In step (7), the resin and hardener that are kept in a container are put into a de-gas chamber sequentially, then vacuum the chamber until the bubbles in the resin and hardener are de-gassed out, then mix the resin and hardener for infusion. To prepare the vacuum bags, several consumable materials, such as flow media, peel ply, and spiral tubes, are placed on the plastic sheet, which aims to lead the resin flow over the whole fibres evenly, and materials on another side are used for buffering purposes, the steel rebars with wound dry fibre in the middle of the consumable materials. Last, fold the plastic sheet and seal the edges using sealant tapes to form a vacuum bag. Then, a vacuum bag is prepared for the vacuum process. In the vacuum-assisted resin infusion (VARI) process, a vacuum pump is used to assist in transporting the resin from the inlets of the vacuum bag to the other side. During the process, dry fibre filaments will be thoroughly impregnated because the air inside the filaments will be expelled and the space will be filled by resin. The details of the placement of materials in the vacuum bag and the VARI process are shown in Figure 3.4.

3.2.3 Raw Materials

The 10 mm GR.500B steel rebars conforming to standard BS4449:2005 were used. The Sika EPOLAM 2031/2031 resin and the ECT 469L-1200 glass fibre provided by Chongqing Polycomp International Corp. (CIPC) were used to make the FRP layer. Carbon fibres are conductive, so carbon fibres in contact with steel may lead to electrochemical corrosion of the core steel rebar (Zhou *et al.* 2019); basalt fibres are

not as durable as glass fibres in combined saline and alkali environments (e.g., in concrete made with seawater and sea-sand) (Wang *et al.* 2017). In addition, both carbon and basalt fibres are more expensive than glass fibres. Therefore, glass fibres were the only material considered in the present study to manufacture FCSRs. The properties of the raw materials are shown in Tables 3.1-3.3.

3.2.4 Specimen Preparation

Two-ply FCSRs were fabricated with FWII and FWVARI with a winding angle of $+86.5^\circ/-86.5^\circ$ following the aforementioned procedures with a length of one meter.

Generally, a critical winding angle exists for FCSRs based on the width of fibre filaments and the diameter of the core steel rebar, which ensures the full coverage by fibre filaments of the core steel rebar with the least material consumption. This critical winding angle can be determined with the following equation:

$$\theta > \cos^{-1}\left(\frac{w}{\pi D}\right) = \cos^{-1}\left(\frac{2}{\pi \times 10}\right) \times \frac{180^\circ}{\pi} = 86.35^\circ$$

where D is the diameter of the steel rebar, and w is the filament width. In the present study, a winding angle of 86.5° was selected as an approximation for FCSRs with a 2 mm filament width and 10 mm rebar diameter.

Epoxy-coated steel rebars (ECSRs) were also prepared by brushing the epoxy on cleaned steel rebars as the reference group. After curing all FCSRs and ECSRs, three 5 mm thick sections were cut from the rebars using a precision saw (Buehler IsoMet High-Speed Pro) with a moving speed of 1mm/min to minimize the damage to the cutting surface. Specimens were fixed in the epoxy to polish the observation surface. Surface polishing was conducted with a sequence of 300-, 800-, 1200-, and 2000-grit

sandpapers and 0.9- μm suspended diamond past at the end. Each grit keeps a polish for two minutes. After polishing, the specimens were dried in a vacuum oven for 24 hours after ultrasonic cleaning to eliminate the water in the specimens.

3.2.5 Scanning Electron Microscope (SEM)

SEM tests were performed on a TESCAN MIRA microscope to compare, at the microscopic level, the difference between FCSRs made with FWII and FWARI. One hour before the SEM tests, all specimens were coated with a thin film of gold-palladium by a vapour-deposit process.

Figures 3.5 and 3.6 show the cross-sectional images of the FRP coating layer and FRP-to-steel interface, respectively. The images of ECSRs are also given in these two figures for comparison purposes. It is seen in Figure 3.5(a) that there were some voids in the FRP coating layer produced with FWII, whereas the coating layer produced with FWVARI has almost no apparent voids, suggesting the quality of the latter was better. Rousseau *et al.* (1999) thought the undulations induced by overlapping bands were a vital reason resulting in the formation of the voids. However, the voids formed in the FRP coating layer should also be related to the high winding speed set during the winding process, which results in an unsaturated impregnation of the fibres in the extreme centre of fibre filaments and thus had not been wetting entirely. This issue can be solved or at least mitigated by lowering the winding speed or using resins that have a better wetting ability with fibres.

The microstructure FRP/steel rebar interface, which is related to the adhesion property of the coating layer to the steel substrate, indicates that adhesion between the FRP layer and steel rebars was better than that of epoxy and steel. Small cracks

were observed in the ECSRs specimens, as pointed out by red arrows, while the interface for FCSRs was kept intact. The microstructure observation reveals that the wound FRP coating layer of FCSRs manufactured by both methods exhibits a better bond ability to steel rebars than that of the epoxy coating. This is because when the coating layer was forced to “peel off” from the steel substrate, the circumferential fibre filaments on the other side would produce a force in the opposite direction to “pull back” the coating layer. The tensile strength of the fibre-reinforced polymer is much larger than the epoxy, which is why the interface of the ECSRs was disturbed while the FCSRs seemed not affected.

Conclusively, FWII helps enhance the contact between the FRP coating layer and the steel rebar. Although the porosity of the FRP coating layer made by FWII is a bit higher than that made by FWVARI, it can be refined by many measures, e.g., utilising a lower winding speed to improve the wetting quality of filaments, utilising filaments possess a higher wetting ability. Moreover, it is difficult to control the vacuum time when using the VARI method. Abdullah *et al.* (2020) reported that the mechanical behaviour of FRP composites was weakened due to the resin-starved regions formed during the VARI process, which resulted in insufficient resin to transfer the load to fibres. Considering the simplicity of FWII, it was adopted in the following works of this thesis.

The optimal winding speed represents a speed at which the production rate can be maximised, while ensuring product quality. The optimal winding speed is dictated by many factors, e.g., the viscosity of the resin, the wettability of the fibre filaments, etc. Therefore, the optimal winding speed differs for each product. In the pilot study, many speed values were trialled, and the voids in the FRP coating layer were

examined with a scanning electron microscope (SEM). Based on the pilot study findings, a speed of 15 rounds/min was selected as an appropriate winding speed to reduce voids formed in the FRP coating layer by reducing the amount of air being entrapped in the fibre filament during the manufacturing process.

3.3 MECHANICAL PROPERTIES

3.3.1 Test Matrix

Tensile and compressive tests were conducted to study the mechanical properties of FCSRs. Three groups of steel rebars with two identical specimens in each group were prepared for tensile test, and two groups of FCSRs were manufactured with two plies glass fibre and a winding angle combination of $+86.5^\circ/-86.5^\circ$ by utilising FWII and FWVARI methods, respectively. One group of uncoated steel rebars (UCSRs) was prepared as the reference group. Each specimen had a total length of 700 mm and a free length of 400 mm. The two ends of each tensile specimen were anchored by centralizing the FCSRs in steel tubes of a length of 150 mm and filling the spare space with epoxy resin.

Two FCSRs manufactured with two plies of glass fibre and a winding angle combination of $+86.5^\circ/-86.5^\circ$ by utilising FWII were prepared for compressive tests. Each compressive specimen had a total length of 200 mm and a free length of 60 mm. The two ends of each FCSR specimen were strengthened with 70 mm long plastic tubes, which were filled with epoxy resin to increase the contact surface with the loading plates of the compression machine. The surface of the two ends was levelled with gypsum to make sure the tested rebars were vertically loaded.

The schematic diagrams of tensile specimens and compressive specimens are exhibited in Figure 3.7.

3.3.2 Experimental Programme

The tensile tests were conducted on an electromechanical universal testing machine (UTM), INSTRON 5982, with reference to ASTM E8 (ASTM 2013). The tensile strain was measured with an advanced video extensometer device. The frequency of data collection was 1 Hz. The uniaxial tensile loading was applied with a displacement control rate of 2 mm/min until the tensile fracture of the core steel rebar. The whole test process of each specimen was monitored from the beginning to the fracture failure of the core steel rebar.

The compressive tests were carried out on an automatic compression testing machine (MATEST) with a loading rate of 0.2 mm/min. The compressive strain was measured by two strain gauges attached to the rebar surface and recorded by data from a logger (KYOWA UCAM-60) with a frequency of 1 Hz. The test was stopped when the load decreased to 60% of the maximum load.

The tensile testing machine and compressive testing setups are shown in Figure 3.8.

3.3.3 Tensile Test Results and Discussions

Table 3.4 shows the tensile strength and tensile modulus of the tested specimens. Figure 3.9 displays the tensile stress-strain responses of all tested rebars. The stress-strain behaviour of FCSRs is almost the same as that of UCSRs, suggesting that an FCSR retains almost all the ductility of the core steel rebar.

Figure 3.10 shows in detail the debonding process of the FRP coating layer on an FCSR. It is seen that white patches initiated from one end of the free-length region, which then propagated with increasing tensile stress. The white patches were caused by the debonding of the FRP coating layer from the core steel rebar. Most importantly, the video record indicates that the white patches emerged after the yielding of the core steel rebar. As the existing structural design codes limit the stress of steel rebars below the yield stress even at the ultimate limit state, the FRP coating layer will not debond when FCSRs are utilised as reinforcement of concrete structures. A failed tensile FCSR specimen was displayed in Figure 3.11(a)

3.3.4 Compressive Test Results and Discussions

Figure 3.11(b) displays a failed compressive FCSR specimen. Table 3.5 shows the key results of compressive tests. Since the specimens failed by buckling after the yielding of the inner steel core, the buckling strength would be greatly influenced by the free length of the tested specimens. Although the designed free length was set as six times the diameter of the FCSRs, the actual values vary from 59mm to 65mm. Therefore, only the yielding compressive strength and the elastic were recorded. Both the yielding strength and the elastic modulus were a little higher than that measured by the tensile test. These differences might be attributed to the different testing systems. Nevertheless, the compressive test preliminary reveals that the two manufacturing methods for FCSRs will not influence the compressive behaviour of the steel rebars, either.

3.4 THERMAL PROPERTIES

3.4.1 Coefficient of Thermal Expansion

The coefficient of thermal expansion (CTE) of the FRP coating layer and the core steel rebar were determined using a thermal-mechanical analyser (Mettler Toledo TMA/SDTA1). Steel rebars and FRP specimens were cut into small pieces of 5 mm x 5 mm x 5 mm. Since FRP is a type of anisotropic material, the dimensional change was measured along the transverse direction of the fibre alignment. The heating rates were set as 10 °C/min from an initial temperature of 30 °C to 150 °C for FRP coating specimens and 20 °C/min from an initial temperature of 40 °C to 600 °C for steel specimens.

Figure 3.12 shows the dimensional changes of FRP and steel specimens as a function of temperature. It can be estimated based on the measured curves that the CTEs were 13.87 $\mu\text{m}/\text{m}\cdot^\circ\text{C}$ and 70.55 $\mu\text{m}/\text{m}\cdot^\circ\text{C}$ for steel and FRP, respectively. The CTE value of steel in the present study is close to the available literature values (Guo *et al.* 2022). Since the CTE value of FRP varies from product to product, depending on the material used, fibre content, and the measured directions (Masmoudi *et al.* 2005), the CTE value tested in the present study is in the range of the reported literature values.

3.4.2 Glass Transition Temperature

Differential scanning calorimeter (DSC) tests were conducted with a thermal analysis system (Mettler Toledo DSC3) under a nitrogen atmosphere to measure the glass transition temperature (T_g) of the FRP coating layer. The specimen was prepared by grinding the FRP coating layer into powder and then kept in an alumina crucible for glass transition temperature measurement, with a heating rate of 5 °C/min from 25 °C to 150 °C. Figure 3.13 shows the DSC curves of all specimens. The T_g values were

estimated to be in the range of 105 °C to 115 °C following the ASTM D3418 standard (ASTM 2021). As the service temperature of FCSRs in concrete structures is usually below 60 °C, the durability of the FRP coating layer should be satisfactory in accordance with the recommendation made by the Canadian Standard Association that the working temperature of an FRP product must be 15 °C lower than its T_g (CSA 2012).

3.5 PHYSICAL PROPERTIES

3.5.1 Coating Thickness

The bond performance of coated steel rebars to concrete is greatly influenced by the coating thickness. It has been a key performance index for other corrosion-resistant steel rebars, e.g., ECSRs and galvanized steel rebars. ASTM A775 (2019) specifies that the coating thickness measurements for ECSRs after curing shall range from 175 to 300 μm and from 175 to 400 μm for Nos. 10 to 16 rebars and Nos. 19 to 57 rebars, respectively.

In the present study, three groups of rebars were manufactured for thickness measurements: (i) ECSRs; (ii) one-ply FCSRs (fibre winding angle: $+86.5^\circ$); and (iii) two-ply FCSRs (fibre winding angles: $+86.5^\circ/-86.5^\circ$). Each group contains one specimen cut from one-meter-long specimens with a segmental length of 100 mm. The coating thickness of each specimen was measured from 9 locations on its cross-section with a stereomicroscope (Model: SMZ1270, Brand: Nikon), as shown in Figure 3.14. Table 3.6 shows the mean thicknesses of all groups. It is seen that the coating thicknesses of Groups 2 and 3 specimens were about 576 μm and 1087 μm ,

respectively. As expected, the coating thickness increased with the increasing number of fibre plies. In general, for polymer products or composites, the thicker, the longer penetrating time is needed for solutions to reach the surface of the core steel rebar. Therefore, the coating thicknesses of FCSRs were much larger than those of ECSRs, suggesting that the corrosion resistance of FCSRs will be better than that of ECSRs.

3.5.2 Surface Roughness

The surface roughness of the coated steel rebars was measured by a 3D laser scanning microscope (KEYENCE VK-X200). The most relevant parameters in describing the relationship between the rebar roughness and its bond performance in concrete are the amplitude parameters, as they accurately depict the surface irregularities perpendicular to the bar surface (Zhang *et al.* 2020). R_a and R_z are two linear amplitude parameters to characterize the linear surface profile of the rebars, as shown in Figure 3.15. R_a is the arithmetic average height calculated by averaging the absolute deviations from the reference line along a specified length, and R_z is the maximum height that quantifies the height difference between the highest and the lowest points over a specified length (Gadelmawla *et al.* 2002).

Figure 3.16 shows the results of surface roughness tests. The results from both the average height and maximum height of tested rebars illustrate the surface roughness will increase after adopting the FRP coating layer when compared with the ECSRs. However, the surface roughness will decrease with the FRP coating layer increasing. This is because the wound fibre on the steel surface will form many “corrugations”, which are much smaller than the original steel ribs on the rebars, leading to a larger “peak-valley” difference. However, with the increase of FRP ply, the later wound

fibres will fill into those “valleys” formed on the former ply and thus decrease the surface roughness of FCSRs.

3.6 CONCLUSIONS

This chapter has elucidated a series of experiments to assess the different manufacturing methods and test the mechanical, thermal and physical properties of FCSRs. FCSRs produced with two different manufacturing processes, one is filament winding with in-line impregnation (FWII) and the other is filament winding with vacuum-assisted resin infusion (FWVARI), were compared. Tensile property, compressive property, glass transition temperature, coefficient of thermal expansion, coating thickness, and surface roughness tests were characterised. The following conclusions to be drawn based on the test results presented in this chapter:

- (1) Both FWVARI and FWII are applicable to produce FCSRs with high quality. The quality of the FCSRs made by FWVARI is slightly better than that made by FWII as evidenced by a lower porosity in the FRP coating layer of the former. However, because of using the vacuum assistance, the manufacturing cost of FWVARI is higher than FWII.
- (2) As the quality of the FCSRs made by FWII could be refined by many costless measures, FWII has higher cost-effectiveness than FWVARI.
- (3) The mechanical behaviour of FCSRs exhibits remarkable similarity to that of the core steel rebars, so FCSRs retain almost all the ductility of the core steel rebars.
- (4) The coating thicknesses of FCSRs with one- and two-ply FRP coating layer(s) were about 576 μm and 1087 μm , respectively, which were thicker than the

values of ECSRs. The test observations suggest that the adhesion ability of the coating layer of an FCSR would be better than that of an ECSR.

- (5) The increased surface roughness of FCSRs will benefit the structurally-related performance of FCSRs in concrete.

3.7 REFERENCES

- Abdalla, F.H., Mutasher, S.A., Khalid, Y.A., Sapuan, S.M., Hamouda, A.M.S., Sahari, B.B. and Hamdan, M.M. (2007). "Design and fabrication of low cost filament winding machine", *Materials & Design*, Vol. 28, No. 1, pp. 234-239.
- Abdullah, S.F.A.S., Zuhudi, N.Z.M., Aris, K.D.M., Roslan, M.N. and Isa, M.D. (2020). "Physical and mechanical characterization of kenaf fiber filament wound composite produced using vacuum-bagging and heat-shrink tube method", *Proc., International Conference of Aerospace and Mechanical Engineering 2019: AeroMech 2019*, Springer, pp. 519-527.
- ASTM (2013). *ASTM E8/E8M*. Standard Test Methods for Tension Testing of Metallic Materials, American Society for Testing and Materials, West Conshohocken, Pennsylvania, USA.
- ASTM (2019). *ASTM A775/A775M*. Standard Specification for Epoxy-Coated Steel Reinforcing Bars, American Society for Testing and Materials, West Conshohocken, Pennsylvania, USA.
- ASTM (2021). *ASTM D3418*. Standard Test Method for Transition Temperatures and Enthalpies of Fusion and Crystallization of Polymers by Differential

Scanning Calorimetry, American Society for Testing and Materials, West Conshohocken, Pennsylvania, USA.

CSA (2012). *CSAS806. Design and Construction of Building Components with Fiber Reinforced Polymers*, Canadian Standard Association, Rexdale, ON, Canada.

Frketic, J., Dickens, T. and Ramakrishnan, S. (2017). "Automated manufacturing and processing of fiber-reinforced polymer (FRP) composites: An additive review of contemporary and modern techniques for advanced materials manufacturing", *Additive Manufacturing*, Vol. 14, pp. 69-86.

Gadelmawla, E.S., Koura, M.M., Maksoud, T.M., Elewa, I.M. and Soliman, H.H. (2002). "Roughness parameters", *Journal of Materials Processing Technology*, Vol. 123, No. 1, pp. 133-145.

Goren, A. and Atas, C. (2008). "Manufacturing of polymer matrix composites using vacuum assisted resin infusion molding", *Archives of Materials Science and Engineering*, Vol. 34, No. 2, pp. 117-120.

Guo, J., Wu, Y., Zhang, X., Zhang, Y., Wang, H., Bai, X. and Lu, H. (2022). "Research on the influence of thermal expansion of steel shaft on dynamic characteristics of full ceramic bearing-rotor system", *Advances in Mechanical Engineering*, Vol. 14, No. 7, pp. 168781322211093.

Gutowski, T.G. (1997). "Filament winding process model for thermosetting matrix composites." *Advanced Composites Manufacturing*, John Wiley & Sons, New York, 373-392.

Masmoudi, R., Zaidi, A. and Gérard, P. (2005). "Transverse thermal expansion of FRP bars embedded in concrete", *Journal of Composites for Construction*, Vol. 9, No. 5, pp. 377-387.

- Rousseau, J., Perreux, D. and Verdiere, N. (1999). "The influence of winding patterns on the damage behaviour of filament-wound pipes", *Composites Science and Technology*, Vol. 59, No. 9, pp. 1439-1449.
- Shen, F.C. (1995). "A filament-wound structure technology overview", *Materials Chemistry and Physics*, Vol. 42, No. 2, pp. 96-100.
- Wang, Z., Zhao, X. L., Xian, G., Wu, G., Raman, R. S., Al-Saadi, S., & Haque, A. (2017). Long-term durability of basalt-and glass-fibre reinforced polymer (BFRP/GFRP) bars in seawater and sea sand concrete environment. *Construction and Building Materials*, Vol 139, 467-489.
- Zhang, Z., Jung, D. and Andrawes, B. (2020). "Evaluation of surface roughness and bond-slip behavior of new textured epoxy-coated reinforcing bars", *Construction and Building Materials*, Vol. 262, No. 120762.
- Zhou, Y., Zheng, Y., Pan, J., Sui, L., Xing, F., Sun, H. and Li, P. (2019). "Experimental investigations on corrosion resistance of innovative steel-FRP composite bars using X-ray microcomputed tomography", *Composites Part B: Engineering*, Vol. 161, pp. 272-284.

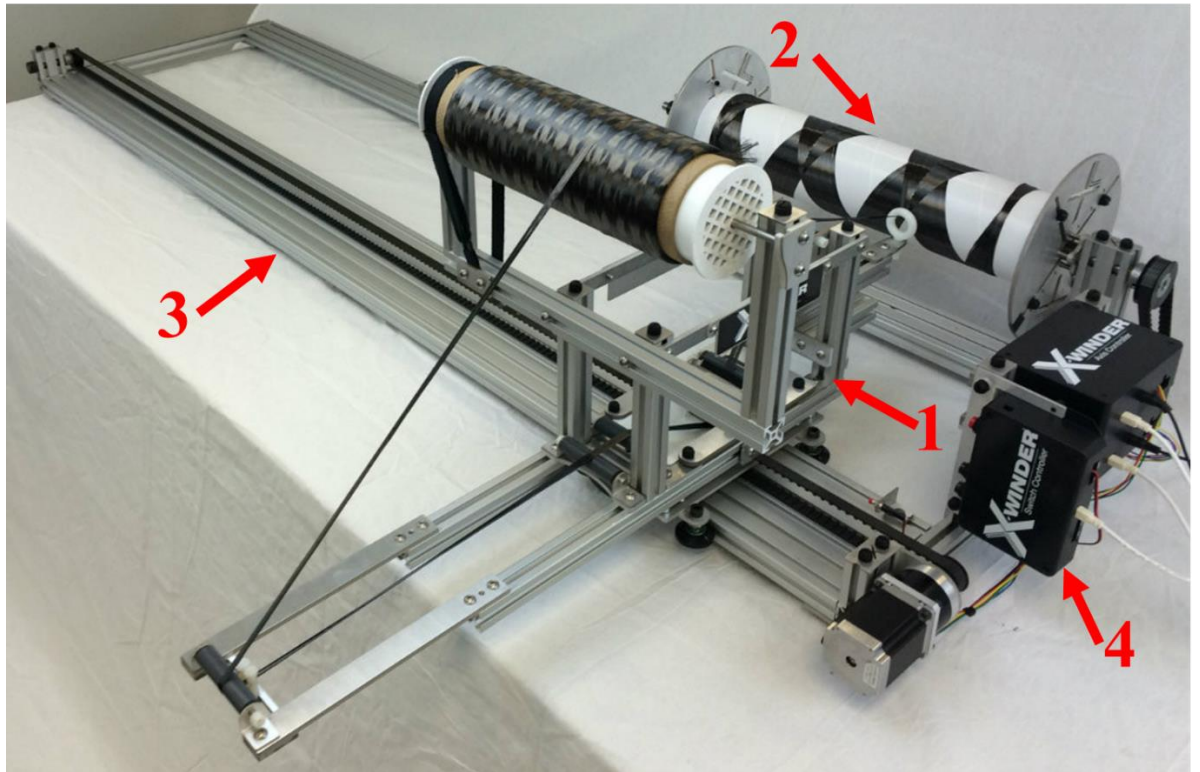


Figure 3.1 Filament winding machine: (1) delivery part; (2) mandrel part; (3) supporting frame; (4) controller.

[Extracted from <https://xwinder.com/2-axis-model-2x-23/>]

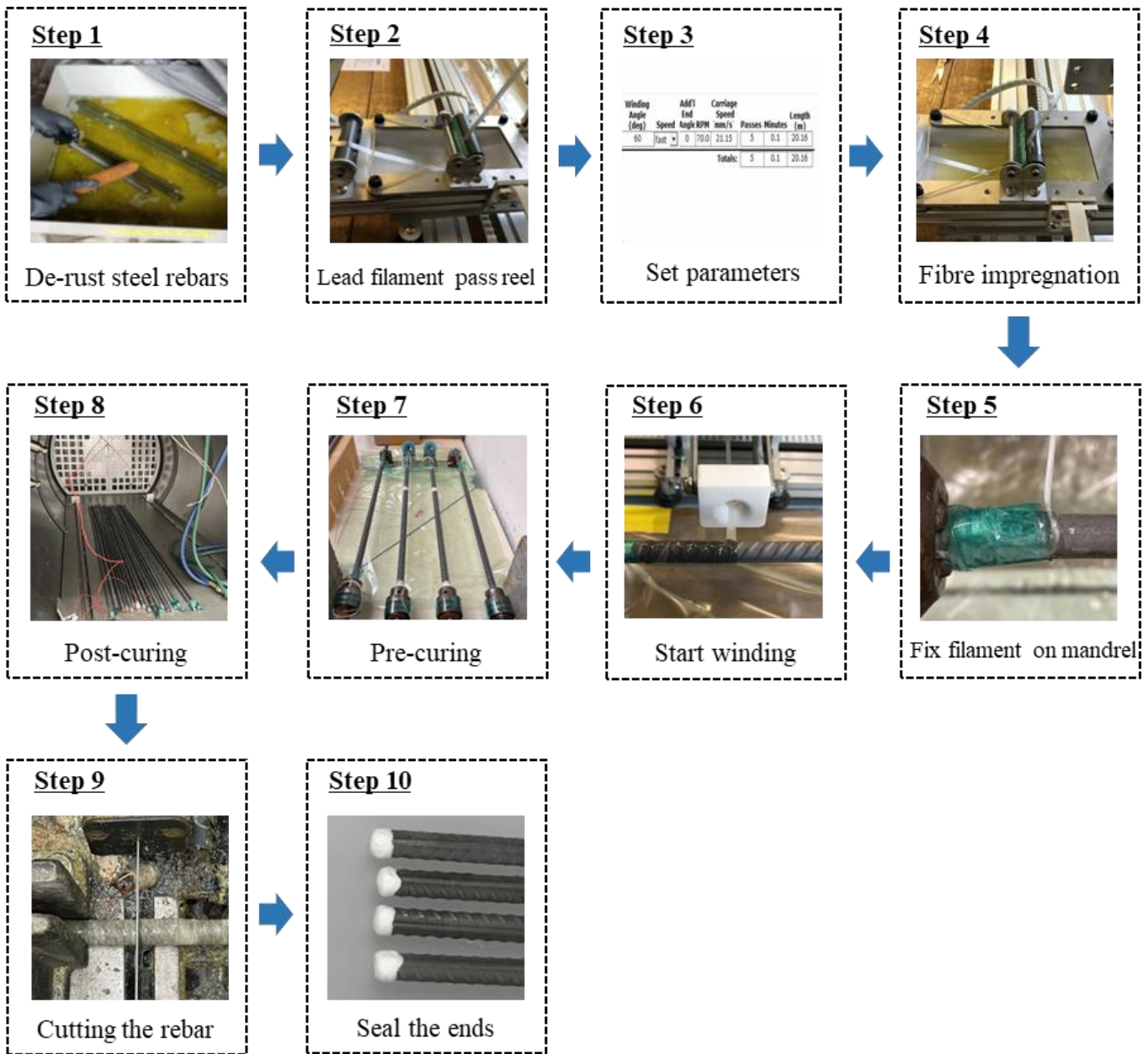


Figure 3.2 Filament winding with in-line impregnation (FWII) for manufacturing FCSRs

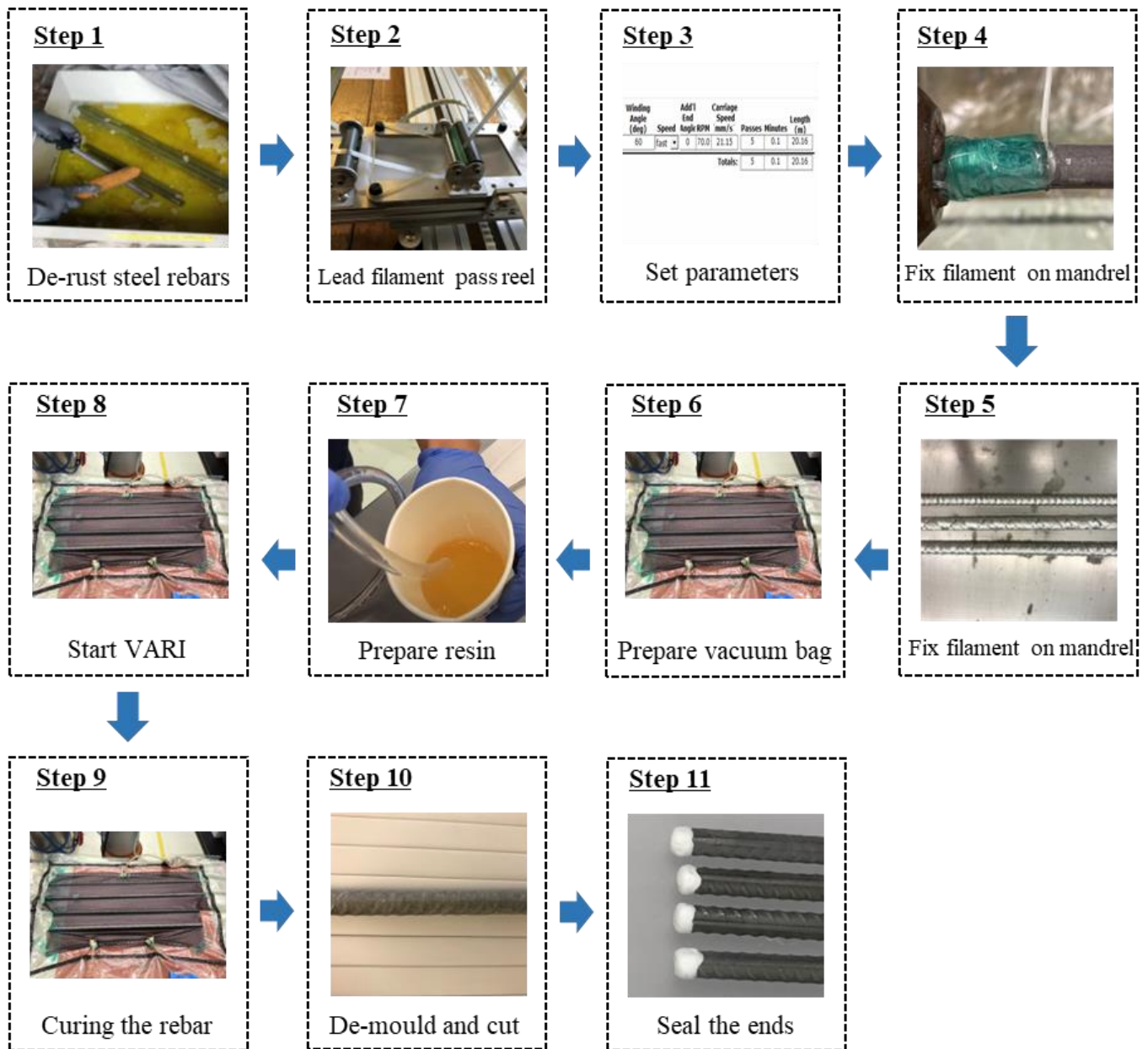
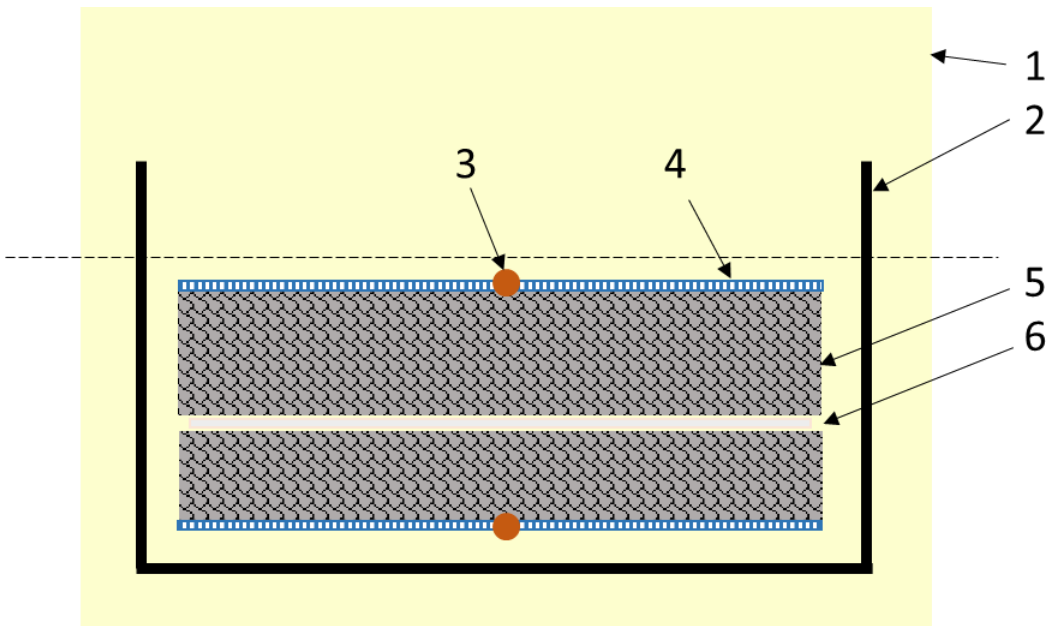
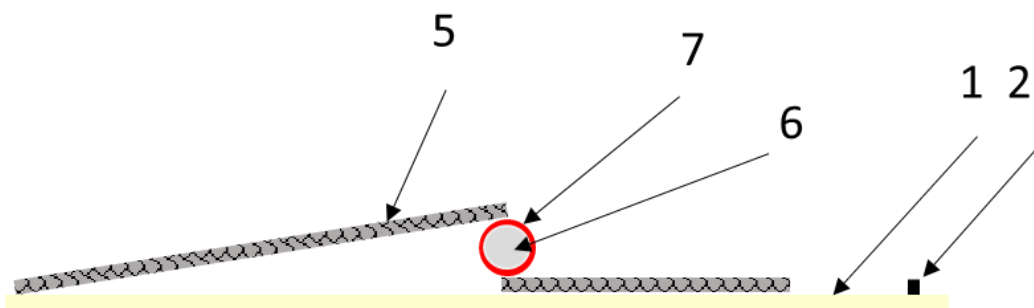


Figure 3.3 Filament winding with vacuum-assisted resin infusion (FWVARI) for manufacturing FCSRs

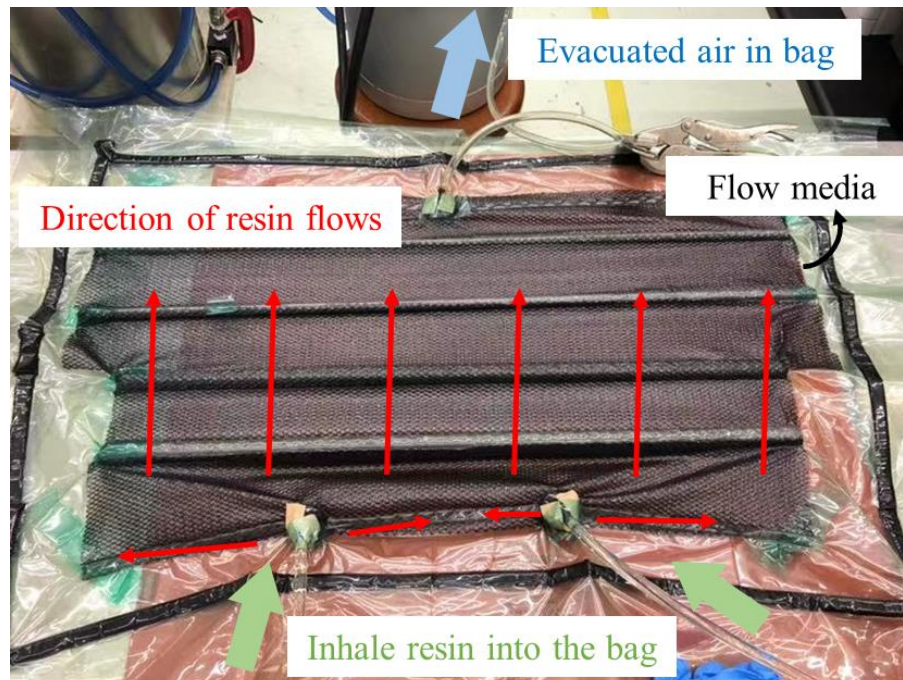


(a) Top view



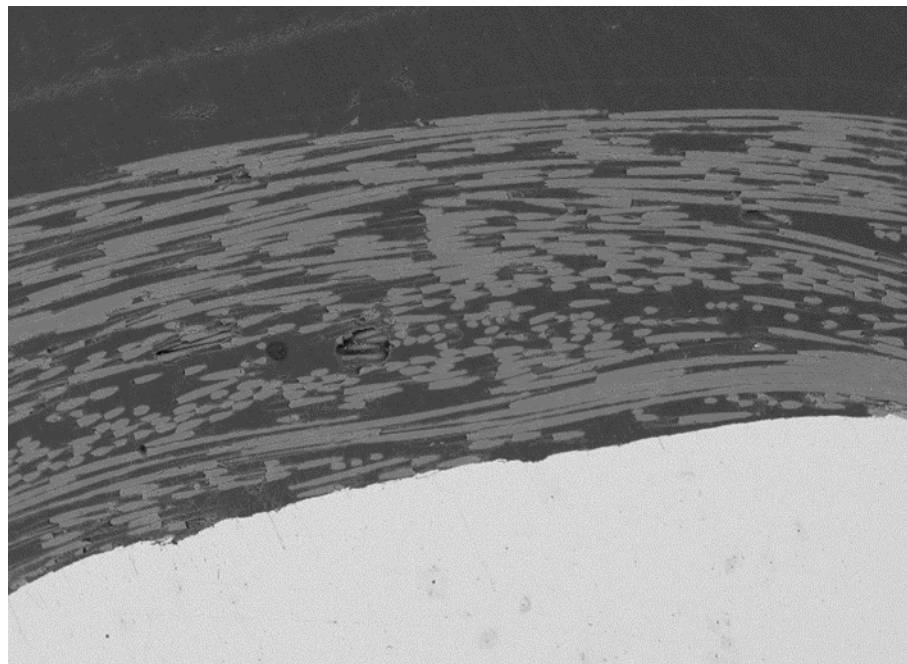
(b) Side view

1 - plastic sheet; 2 – seal tape; 3 – resin infusion connector; 4 – spiral wraps;
 5 – flow medium; 6 – the steel rebar wound with dry filaments; 7 – peel ply.

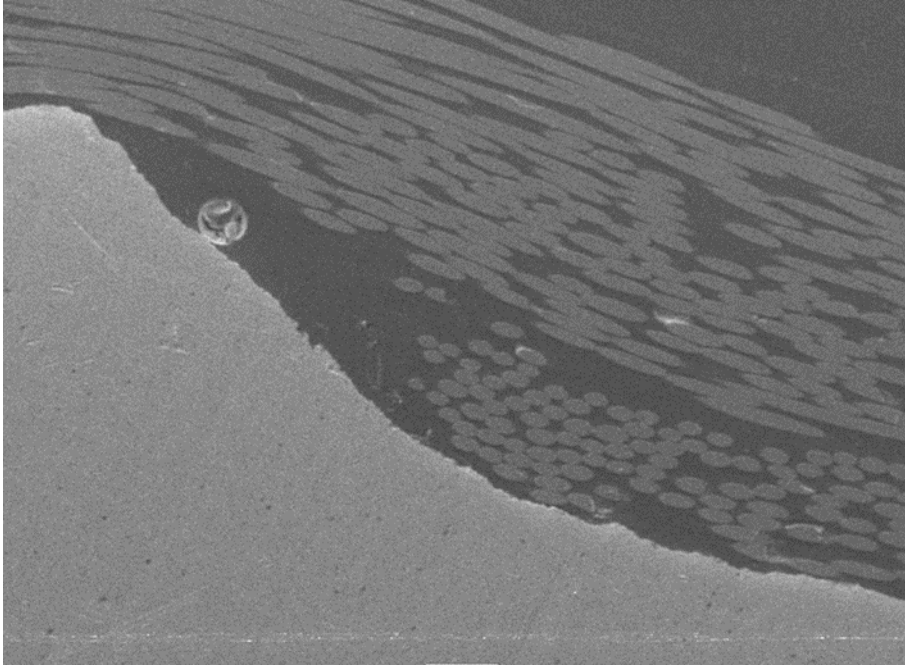


(c) Vacuum-assisted resin infusion process.

Figure 3.4 Details of the (a) vacuum bag from top views; (b) vacuum bag from side view; (c) vacuum-assisted resin infusion process.

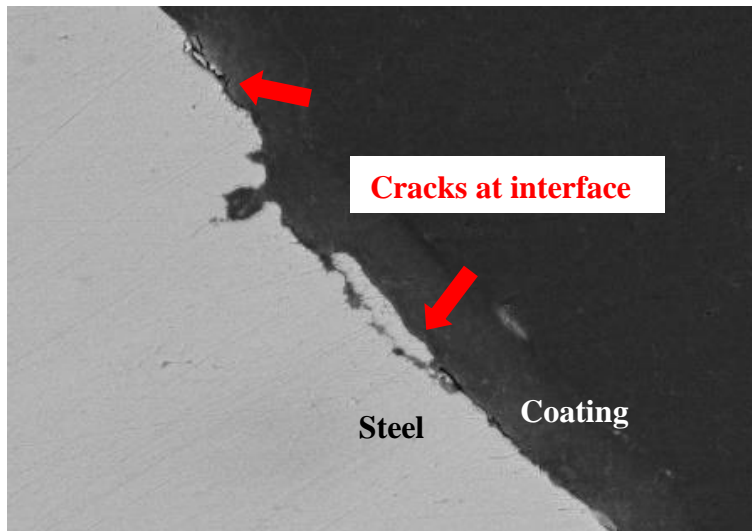


(a) FWII method

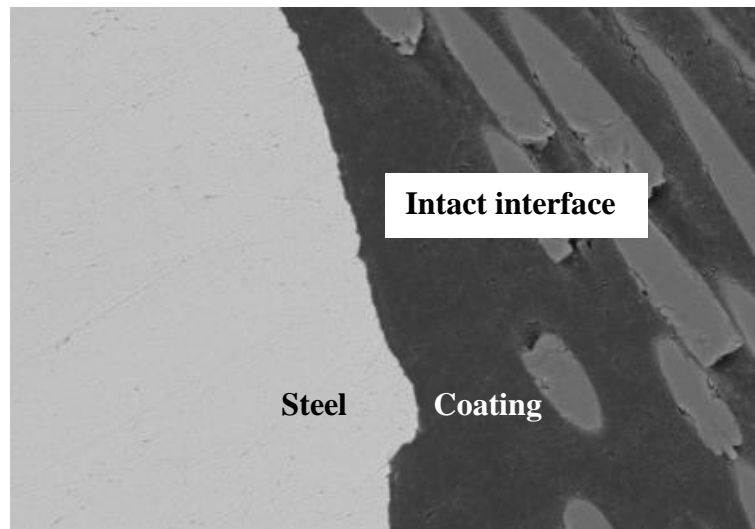


(b) FWVARI method

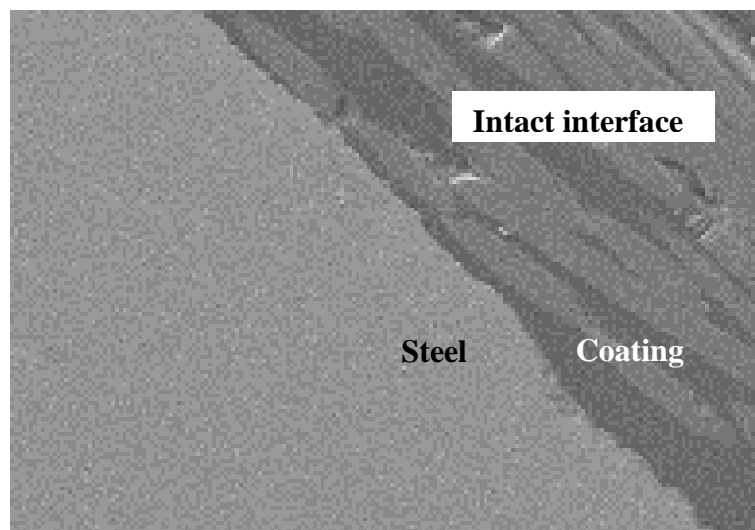
Figure 3.5 FRP coating layers of FCSRs manufactured by two different methods



(a) Epoxy-coated steel rebar



(b) FRP-coated steel rebars by the FWVARI method

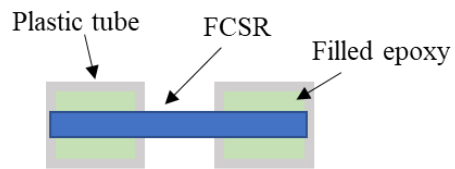


(c) FRP-coated steel rebars by the FWVARI method

Figure 3.6 Coating-to-steel interfaces of different types of rebars

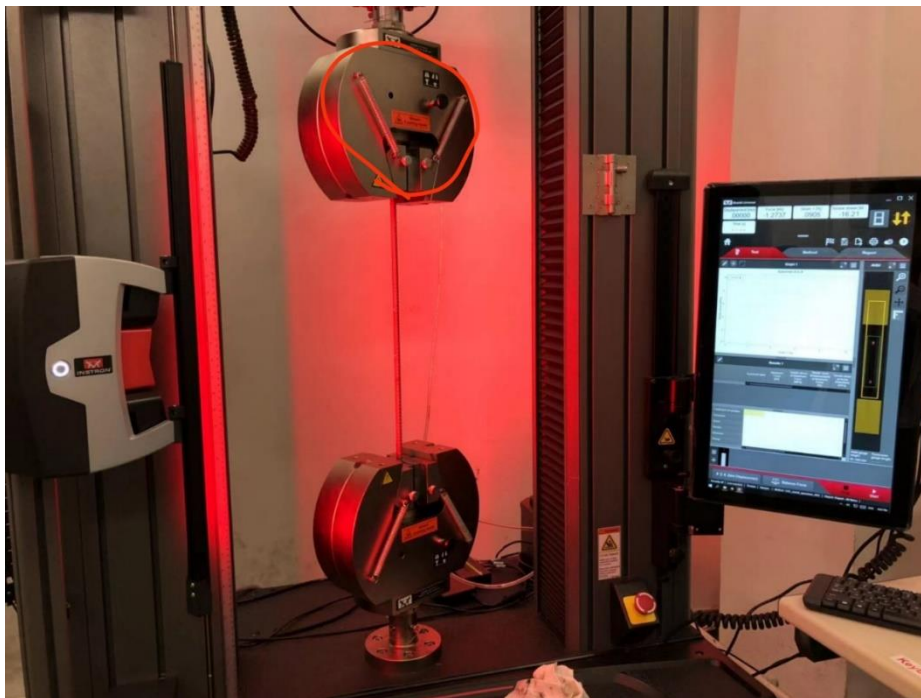


(a) Tensile specimen



(b) Compressive specimen

Figure 3.7 Schematic diagrams of specimens for material property tests



(a) Setup for tensile tests



(b) Setup for compressive tests

Figure 3.8 Setups for material property tests

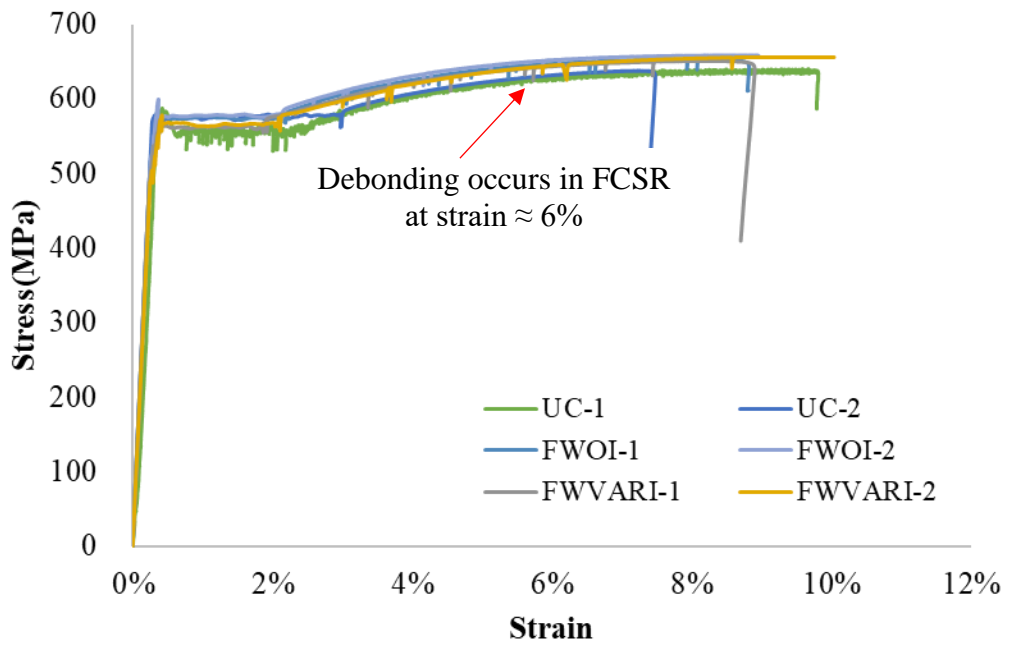


Figure 3.9 Tensile stress-strain curves of uncoated steel rebars (UC), FCSRs (FWOI), and FCSRs (FWVARI)

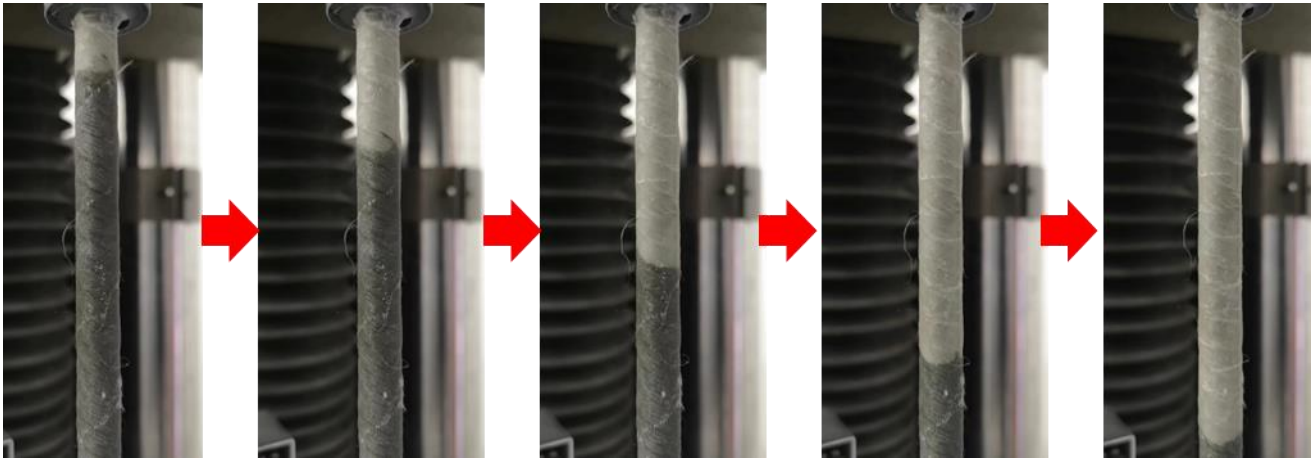


Figure 3.10 Development of coating peeling during a tensile test



(a) A failed FCSR under tension



(b) Failed FCSRs under compression

Figure 3.11 Failed specimens

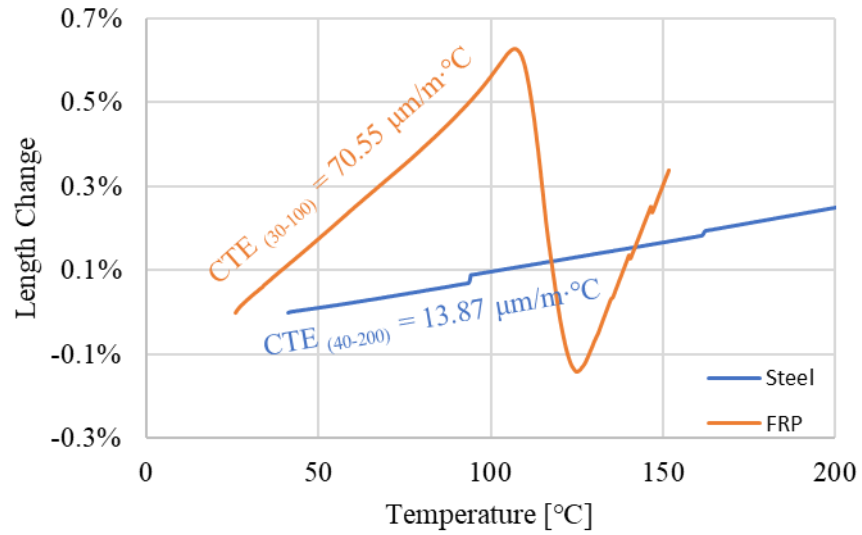


Figure 3.12 Dimensional change of the FRP coating layer and the steel rebar as a function of temperature

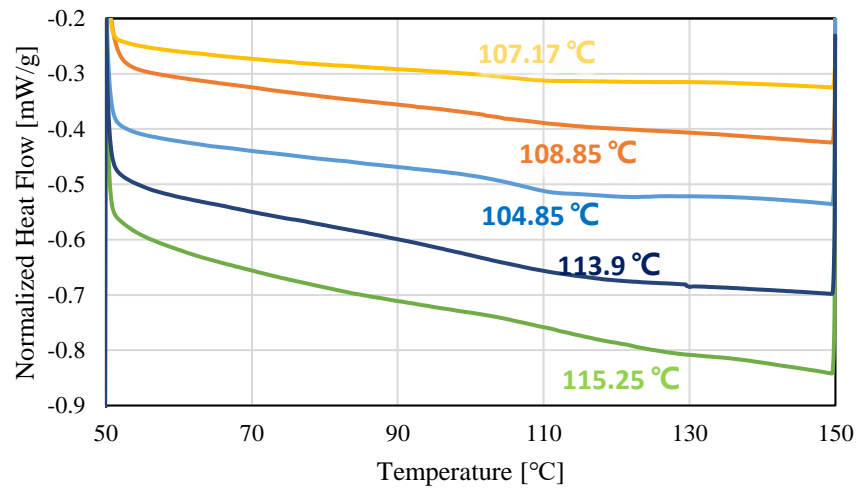


Figure 3.13 The results of differential scanning calorimeter (DSC) tests on the FRP coating layer of five parallel specimens

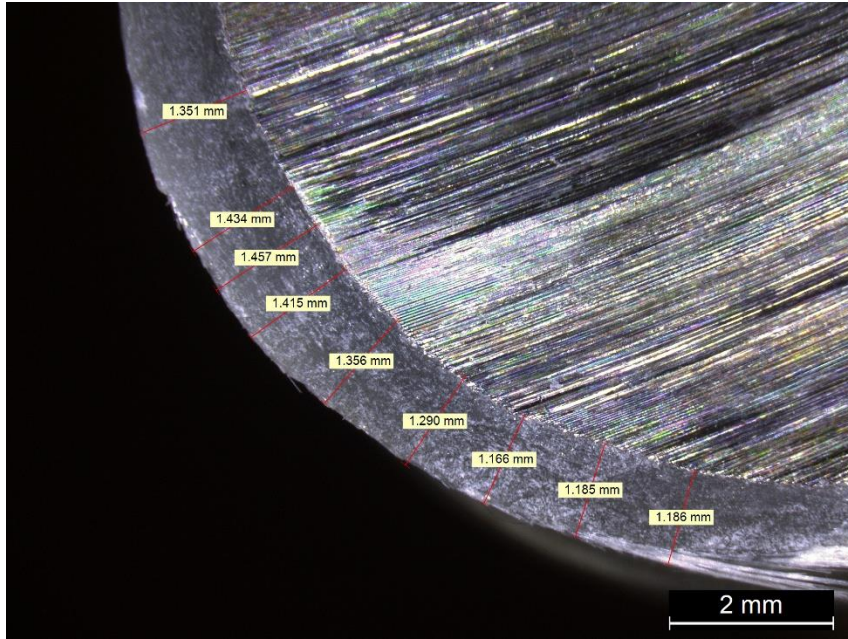
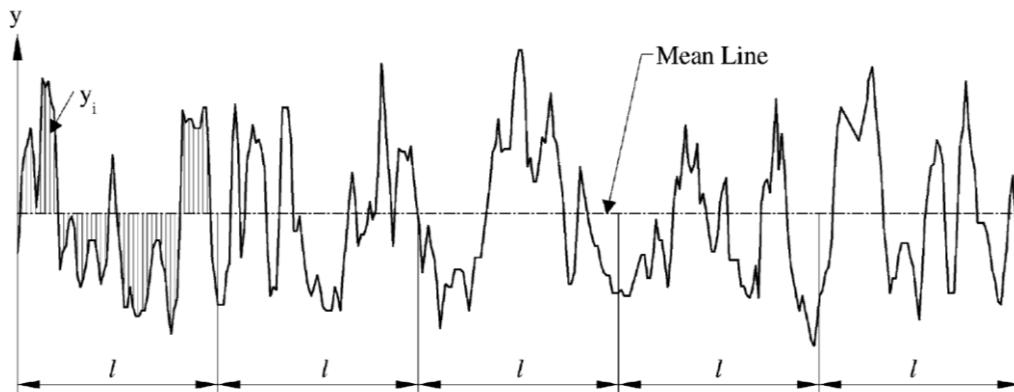
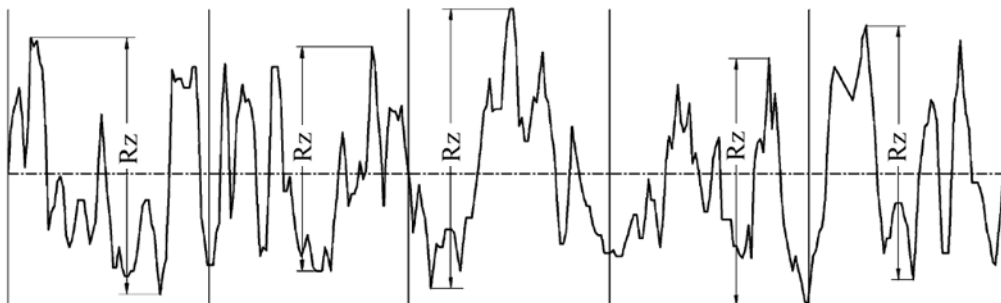


Figure 3.14 Measurement of coating thickness



(a) Arithmetic average height difference parameter, R_a



(b) Maximum height difference parameter, R_z

Figure 3.15 Definition of the roughness-related parameters [Extracted from Gadelmawla et al. (2002)]

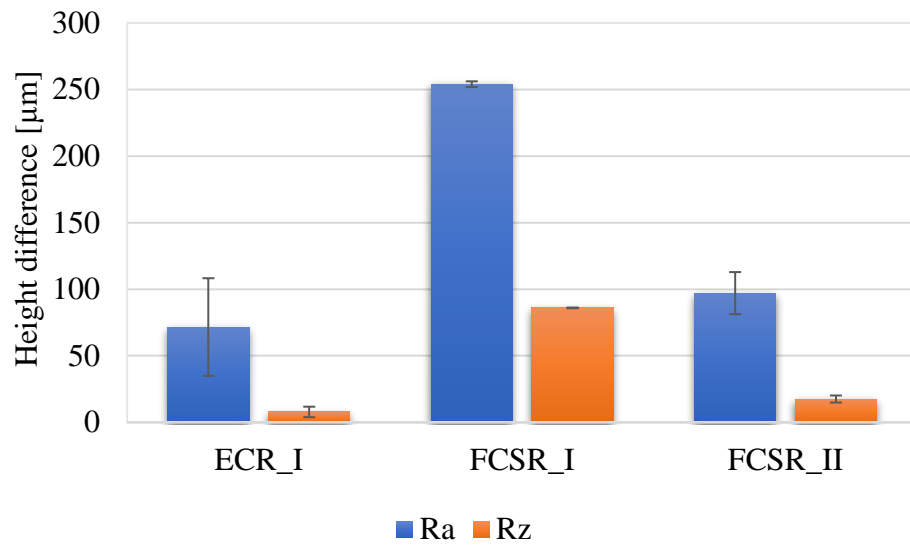


Figure 3.16 Surface roughness values of ECSRs and FCSRs

Table 3.1 Mechanical properties of core steel rebars

Grade	Cross-sectional area	Density	Yield stress	Tensile strength	Coefficient of thermal expansion
B	78.5 mm ²	0.615 kg/m	567 MPa	636 MPa	13.9 μm/m·°C

Table 3.2 Mechanical properties of Sika EPOLAM 2031/2031 epoxy resin

Tensile strength	Tensile modulus	Fracture strain	Glass transition temperature	Coefficient of thermal expansion
80 MPa	3600 MPa	6%	105 °C	70.6 μm/m·°C

Table 3.3 Mechanical properties of glass fibre filaments

Glass type	Sizing agent	Fibre diameter	Linear density	Tensile strength
ECR-Glass	Silane	17 to 22 μm	1200 tex	≥ 0.3 N/Tex

Table 3.4 Key results of tensile tests

Specimen	Yield stress (MPa)	Tensile strength (MPa)	Yield strain (%)	Tensile modulus (GPa)
UC-1	557	620	0.297	188
UC-2	573	638	0.280	205
FWII-1	577	653	0.284	203
FWII-2	578	659	0.300	193
FWVARI-1	563	651	0.272	207
FWVARI-2	564	656	0.280	202

Table 3.5 Key results of compressive tests

Specimen	Yield strength (MPa)	Averaged yield strength (MPa)	Elastic modulus (GPa)	Averaged modulus (GPa)
FWII-1	601.16	593.62	212.867	221.59
FWII-2	608.33		238.183	
FWII-3	571.38		213.719	
FWVARI-1	619.11	627.80	223.53	223.46
FWVARI-2	623.34		223.53	
FWVARI-3	640.94		223.311	

Table 3.6 Thicknesses of all groups

Group	Coating	Number. of FRP plies	Average thickness (μm)
ECSR	Epoxy	-	31.3
FCSR-I	FRP	1	576.0
FCSR-II	FRP	2	1087.0

CHAPTER 4

CORROSION RESISTANCE

4.1 INTRODUCTION

This chapter presents a systematic experimental study on the corrosion resistance of FRP-coated steel rebars (FCSRs). Corrosion resistance is one of the most critical performances of corrosion-resistant steel rebars as they are targeted for concrete structures in aggressive environments. To better understand the entire corrosion evolution of corrosion-resistant steel rebars in a short period, the accelerated corrosion tests (e.g., salt spray, immersion tests, galvanic cell, glass pressure, thermal cycle, etc.) were utilised by numerous researchers (Kautek 1988; Forshee 1993; Bierwagen *et al.* 2000). Although salt spray tests, chemical resistance tests, and chloride permeability tests are standard methods for indicating the corrosion resistance of fusion-bonded epoxy (FBE) coated steel rebars (ASTM 2019), the electrochemical methods are more and more widely accepted. Davis *et al.* (2004) utilised the electrochemical impedance spectroscopy (EIS) method to monitor the CFRP-bonded steel-reinforced concrete (referred to as RC hereafter) system and found that the parameters of the capacitor and the constant phase element representing the CFRP layer, both were identified based on the EIS test results, were linearly related to moisture uptake and delamination area. Xiong *et al.* (2007) utilised

the EIS method to study the corrosion mechanism and corrosion evolution of the CFRP-bonded carbon steel system in simulated soil solution. Tang *et al.* (2012) found that FBE coating outperforms enamel coating as the impedance values of FBE-coated steel rebars were several orders higher than those of enamel-coated steel rebars.

Moreover, field exposure tests are also widely used to study the corrosion resistance of corrosion-resistant rebars. Premature corrosion of epoxy-coated steel rebars (ECSRs) in the substructure of the Long Key Bridge that connected the Florida Keys was reported after seven years of construction, which consequently resulted in concrete cracking and spalling (Manning 1996).

The newly developed FCSRs are expected to be superior in corrosion resistance to ECSRs and galvanized steel rebars (GSRs). With multiple plies of fibres at different angles as distributed reinforcement for the coating layer, the thickness and lamination structure of the FRP coating layer can be controlled to minimise permeability and enhance durability. In addition, the ingress of external corrosive agents towards the core steel rebar surface is likely to be intercepted by interlaminar paths in the laminar structure of the FRP coating layer. This chapter aims to understand the corrosion resistance and corrosion evolution of FCSRs via a systematic experimental investigation consisting of electrochemical tests, laboratory exposure tests under different conditions and field exposure tests in typical marine environments.

4.2 EXPERIMENTAL PROGRAMME

4.2.1 Test Matrix

Six groups of specimens were manufactured and subjected to testing with three identical specimens in each group, which were cut from the same long rebars at different locations. ECSRs and FBERs were tested as a reference group for the comparison purpose of FCSRs. Moreover, FCFBERs were also manufactured and tested as an additional beneficial application of the winding technology to explore the enhanced corrosion protection effect of wound FRP coating on the existing commercially available coated steel rebars. To investigate the relationship between the corrosion resistance and the number of coating plies, the one-ply, two-ply FCSRs and one-ply, two-ply FCFBERs were fabricated and tested.

Details of the test matrix are provided in Table 4.4.

4.2.2 Raw Materials

The epoxy resin and glass fibres used to produce FCSRs and FCFBERs in this chapter were the same as those used in Chapter 3. The properties of steel rebars, epoxy resin, and glass fibres used to manufacture FCSRs are shown in Tables 4.1-4.3, respectively. The FBERs were provided by Fusteel International Group.

4.2.3 Specimen Preparation

FCSRs and FCFBERs were manufactured with a filament winding machine following the procedure introduced in Chapter 3. The surfaces of the uncoated steel rebars (UCSRs) and FBERs were cleaned with alcohol before the filament winding process.

ECSRs were manufactured by brushing liquid epoxy resin onto the surface of UCSRs. The ECSRs were cured following a procedure the same as that utilised for FCSRs and FCFBERs.

After curing, all rebars were cut into a length of 100 mm as test specimens. A copper wire was soldered to one end of each specimen for an electric connection. Then, both ends of the specimen were sealed with a fast-curing silicone sealant DY-M1210 (DEYI) for waterproofing, as shown in Figure 4.1.

4.2.4 56-Day Electrochemical Corrosion Monitoring

The corrosion of all specimens when immersed in 3.5 wt% sodium chloride (NaCl) solution was monitored by electrochemical tests. The tests were performed with an electrochemical workstation (Autolab PGSTAT302N, Metrohm AG). The Analytical Reagent (AR) grade NaCl powder was dissolved into distilled water to prepare the NaCl solution. A typical three-electrode system was utilised: a saturated calomel electrode (SCE) was employed as the reference electrode, the coated steel specimens served as the working electrode and a platinum bar was used as the counter electrode in this system. The test setup is schematically depicted in Figure 4.2(b).

The electrochemical responses, such as the open circuit potential (OCP) and electrochemical impedance of each specimen, were periodically monitored. The polarisation resistance and corrosion rate of each specimen were analysed based on the monitored results. The first time of measurement was performed once the specimen was immersed in the solution. The subsequent measurements were conducted after 14, 21, 28 and 56 days of immersion.

4.2.4.1 Open circuit potential (OCP)

OCP is the potential difference between the working electrode and the reference electrode in a specific electrolyte at which there is no current since the circuit is not closed. The schematic of the OCP test setup is shown in Figure 4.2(a). OCP can reflect the spontaneity of the reaction and thus be used as a superficial indicator of the tendency to corrode and the ability of the coatings to protect metals from corrosion (Huang *et al.* 2004; Caldoni *et al.* 2020). The OCPs of each specimen were recorded for one hour with a scanning rate of 1 Hz after immersing the working electrode (tested specimens) into the 3.5 wt% NaCl solution. The one-hour continued monitoring is needed until a constant OCP value is reached as a stable OCP value indicates the electrochemical reactions in the investigated system have reached a constant rate, which is regarded as the equilibrium state, and the subsequent electrochemical experiments can be performed (Caldoni *et al.* 2020).

4.2.2.3 Electrochemical impedance spectroscopy (EIS)

All the coated steel rebars were then tested using the typical three-electrode setup at room temperature to perform the electrochemical impedance spectroscopy (EIS) tests. The EIS data were measured at a rate of 10 points per decade with a sinusoidal wave of 10 mV in amplitude around the OCP (E_{ocp}), which was measured in the first hour of immersion, and the frequency of measurement ranging from 100 kHz to 5 mHz.

4.2.4.3 Potentiodynamic polarisation (PP)

A potentiodynamic polarisation (PP) test was carried out following an EIS test. The PP test was performed by applying a potential range from open circuit potential minus 300 mV to open circuit potential plus 1500 mV. The scanning rate was set as 5.0 mV/s.

4.2.4.4 Linear polarisation resistance (LRP)

The linear polarisation resistance (LRP) test was carried out in the same setup as the PP test. The scanning range of the LRP test was from OCP value minus 15 mV to OCP value plus 15 mV. The scanning rate was set as 0.167 mV/s to measure the variation of the polarisation resistance and corrosion rate of specimens after being immersed in the 3.5 wt% sodium chloride solutions for up to 56 days.

The Stern and Geary Method has been widely used in many systems to determine the polarisation resistance R_p and measure the corrosion rate i_{corr} .

The polarisation resistance R_p was determined with the Stern and Geary Method based on the LRP data as suggested by ASTM G59-97:

$$R_p = \left(\frac{\partial E}{\partial i} \right)_{i=0, \frac{dE}{dt} \rightarrow 0} \quad (4-3)$$

The Stern-Geary equation can be used to determine the corresponding corrosion current density:

$$i_{corr} = \frac{B}{R_p} \quad (4-4)$$

The units of R_p , i_{corr} and B are $\Omega \cdot \text{cm}^2$, $\mu\text{A}/\text{cm}^2$ and V, respectively. Andrade and Alonso (1996) analysed numerous metal/electrolyte systems and concluded that a value of 26 mV for B in the Stern-Geary equation was suitable for the case of steel embedded in concrete where steel was in the active state (corrosion). A value of 52 mV for B would be more appropriate for the passive steel.

The penetration corrosion rate, CR , can be determined from i_{corr} as:

$$CR = 3.27 \times 10^3 \frac{i_{corr}EW}{\rho} \quad (4-5)$$

where EW is the equivalent weight of a corroded specimen, and ρ is material density. The unit of CR is mm/yr. The corrosion current density was used in the present study to define the corrosion rate of tested rebars.

4.2.5 Six-Month Outdoor and One-Year Laboratory Exposure

A 6-month exposure to the outdoor atmospheric environment of Hong Kong was also conducted to compare the corrosion state of FCSRs with that of ECSRs and UCSRs.

After the 56 days of electrochemical tests, experimental specimens were continuously immersed in 3.5 wt% sodium chloride solution for up to 12 months. Afterwards, surface observations and cross-section examinations were performed to study the corrosion-induced damage.

4.2.6 Two-Year Marine Exposure

The corrosion resistance of FCSRs in a realistic marine environment is investigated through field exposure tests. A total of 36 specimens were exposed to the splash zone

near the Hong Kong-Zhuhai-Macao Bridge. 12 specimens were sustained to tensile stress, 11 specimens were sustained to compressive stress, and 12 specimens were kept under a no-load state. Their corrosion state after one year of exposure and two years of exposure were observed and compared in this study. The corrosion state of FCSRs with longer exposure time in the field will be present in the later work.

Cross sections of the different coated rebars that experienced the corrosion tests were prepared to investigate the variation of their microstructure using the scanning electron microscopy method. All these specimens were prepared following the procedures introduced in Section 3.2.4.

4.3 RESULTS AND DISCUSSIONS

4.3.1 Open Circuit Potential (OCP)

Figure 4.4 shows the OCP evolution diagrams of all groups. Figure 4.5 further compares the average OCPs of all groups. The average OCPs of three ECSRs demonstrate a gradual decrease from -0.45V/SCE to -0.59V/SCE . Since the specimens were rotated until pre-cured, it is difficult for the epoxy to be gathered at the most convex positions of the rib. Therefore, the ribs on the steel rebars were not well protected by the epoxy, and the condition of some ribs was nearly equal to the UCSRs, which also explained why the initial OPC of the ECSRs was negative, which indicated the corrosion had already occurred in these specimens. The average steady OCP values of FCSRs were 1.64V/SCE and 1.79V/SCE for one- and two-ply FRP coating, respectively. The fluctuations in the figure were attributed to the rough surface of the FCSRs since a homogenous coating usually produces a more steady

trend of OCPs (Huang *et al.* 2004). The level of fluctuation was consistent with the surface roughness results. It is obvious that one-ply FCSRs have severe fluctuation in OCP measurement, which was due to the higher surface roughness of one-ply FCSRs. Compared with ECSRs, higher positive OCP values were observed for FCSRs, which indicates FRP coating possesses a more excellent barrier effect against water penetration. Therefore, it could protect the core steel rebars to be more durable. The initial different trends (some increased from a very negative value while some decreased from a positive value) between specimens can be attributed to the instability of the circuit system. Similar results were reported by Sridhar *et al.* (2003), where the OCP value of uncoated stainless steel specimens shifted towards the active direction with the time increasing while their hydroxyapatite-coated stainless steel specimens shifted towards noble directions due to the insulation effect of the coating material. Chang *et al.* (2008) attributed the initial increase trend of the OCP-time curve to the surface activation of the tested specimens.

For FBERs, the steady OCP value was negative for FBER-2 while positive for both FBER-1 and FBER-3, with an average value of around 0.14V/SCE. The deviation of the FBER-2 specimen can be ascribed to the initial defects that existed in the coating layer. The results indicated that the fusion-bonded epoxy coating layer could keep the core steel rebar from corrosion when the coating has no defects, though the corrosion resistance of the intact fusion-bonded epoxy coating was not as good as the FRP coating. For FCFBERs, the steady average OCP was 1.42V/SCE and 1.22V/SCE for one- and two-ply FCFBERs, respectively. The fluctuation during the measurements of these two groups again approved the one-ply FRP coated specimens have more significant surface roughness.

The variation of the OCP values of each group after being immersed in the 3.5 wt% sodium chloride solution at room temperature for up to 56 days was shown in Figure 4.5. The OCP values of ECSRs decreased from -0.6V/SCE to -0.7V/SCE as the dissolution of the steel continued occurring from the weakest rib edge area to a larger penetrated portion. The OCP values of both FCSRs and FCFBERs decreased from the very positive values at the beginning stage, which illustrates the core steel rebar was protected from corrosion and gradually approached 0 V/SCE with the increasing immersion time. After 56 days of immersion in 3.5 wt% sodium chloride solution, the OCP values of all the coated specimens were still far higher than the threshold -0.2 V/SCE, which represents a 90% probability that steel corrosion is not occurring (ASTM 2009). The decreased OPC values of the coated specimens can be attributed to the wetting effect of the coating layers after being immersed in the solutions. The OCP values of the FRP-coated specimens (including FCSRs and FCFBERs) were higher than those of the FBERs. This might be attributed to the fact that organic coating materials were different from the two categories of specimens, as the FBERs utilised powder epoxy while FCSRs employed liquid epoxy to form the coating layer. However, according to the present study, there is no clear relationship between the FRP coating thickness and the OCP values of FRP-coated specimens. Nevertheless, the higher OCP values of FRP-coated specimens than epoxy-coated specimens indicated the good anodic protection effect of the FRP coating layers on steel rebars.

4.3.2 Electrochemical Impedance Spectroscopy (EIS)

The initial electrochemical impedance of the ECSRs, one-ply FCSRs, and two-ply FCSRs, as well as FBERs, one-ply FBERs, and two-ply FBERs, are displayed in

Figure 4.6. The impedances and phase angles of each group, as shown in Bode plots, are quite consistent except the specimen FBER-2, which has a relatively lower resistance than the other two specimens in the same group. The difference might be due to the initial existing damaged point on this specimen. The parameters in the electrical equivalent circuit (EEC) model were determined by fitting the recorded EIS data using ZSimpWin software. The satisfactory fitting results were obtained for the proposed EEC model as the chi-squared values ranged from 10^{-3} to 10^{-2} for all the specimens. Table 4.5 lists the parameters obtained from data fitting.

Figure 4.3 shows the EEC model, which was usually chosen to fit the experimental data of the coated specimens. R_s refers to the solution resistance in the tested system, the pore resistance of the coating layer is represented by R_c , R_{ct} is the charge transfer resistance due to the electrochemical reaction occurring at the metal surface. The constant phase element (CPE) was often incorporated into the model to represent the element that exhibits the electrical property between a capacitor and a resistor. CPE_{dl} and CPE_c are the capacitance contributed by the double-layer and the coating layer, respectively. The electrochemical response occurs at the electrode/electrolyte interface, which depends on the charge species and microstructure of electrodes, which makes a double-layer element away from a pure capacitor (Macdonald and Johnson 2018). The heterogeneous thickness and roughness of the coating layer prevent it from behaving like a pure capacitor, either. The mathematical definition of a CPE is represented by the following equation:

$$Z_{CPE} = Y^{-1}(j\omega)^{-n} \quad (4-1)$$

where Y is a constant, j is the imaginary unit, ω represents the angular frequency, and the exponent n varies between 0 and 1. It can reflect the deviation of an

electrochemical element from a pure capacitor (Kong *et al.* 2016). The CPE is regarded as an ideal capacitor when $n=1$ and an ideal resistor when $n=0$. Y and n can be obtained by data fitting using the selected EEC model. The effective capacitance of a CPE can be calculated using the index Y , n and the resistance R by the following equation:

$$C = Y^{1/n} R^{(1-n)/n} \quad (4-2)$$

For FRP-coated specimens, two time constants, which are related to the dielectric property of the FRP coating layer and the electrochemical reactions at the interfacial zone (Zoltowski 1998), respectively, are established in the electrochemical analysis.

Generally, the coating resistance R_c demonstrates the resistance of the coating layer against the intrusion of electrolyte, which depends on the pore structures and the bonded area of the coating; the coating capacitance, C_c , basically illustrate the diffusivity of solutions into the coating layer (Mansfeld 1995). These two parameters were determined by the dielectricity and microstructure properties of the FRP coating layer. The coating resistances, as presented in Table 4.5, are nearly 10^9 and $10^{13} \Omega \text{ cm}^2$ for the one- and two-ply FCSRs, respectively, and the coating capacitances of those specimens were in the range of $10^{-13} \sim 10^{-11} \text{ F/cm}^2$. The results indicate that FRP coatings have excellent performance in resisting the intrusion of the solution. The value of n_c is close to 1 for all the FRP-coated specimens, which implies that the FRP coatings can be regarded as pure capacitors.

The double-layer capacitance (C_{dl}) describes the ability to store electrical energy through the double-layer effect. The double-layer capacitances of all the FRP-coated specimens were in the range of $10^{-13} \sim 10^{-10} \text{ F/cm}^2$, which are smaller than those of

the epoxy-coated specimens (10^{-9} to 10^{-3} F/cm²). The charge transfer resistance (R_{ct}) of the specimens illustrates the corrosion rate at the metal surface, which represents the resistance when electrons transfer from the ions in the electrolyte to the metal. ECSRs have the lowest R_c of 248-1340 $\Omega \text{ cm}^2$ among all the specimens. The R_c of all the FRP-coated specimens was in the range of $10^{10} \sim 10^{13} \Omega \text{ cm}^2$, which is approximately eight orders of magnitude larger than those of the epoxy-coated specimens. All the coated specimens have exhibited low double-layer capacitance and high charge transfer resistance, which illustrate the exceptional ability of the FRP coating layer to resist the flow of electrons across the steel surface.

The impedance spectrum of the example specimen in each group after being immersed in the 3.5 wt% sodium chloride solutions for 0, 14, 21, 28, and 56 days was drawn and compared in Figure 4.7. Overall, the diagram of the ECSRs shows a quick small impedance, which varied between 20~60 $\Omega \cdot \text{cm}^2$. The slight increase in the impedance values after 28 days and 56 days of immersion might be due to the accumulation of the rust formed on the rebar's surface, with that retard the process of corrosion. A similar development could be observed in the FBERs. They had a higher impedance value than that of ECSRs but a lower value than that of FRP-coated specimens because the defects on the FBERs would corrode once exposed to aggressive environments. Since the defect area is quickly small, another area can still be protected at the initial stage. FBERs showed a better resistance than ECSRs but a worse performance than FRP-coated specimens. This also explained why the resistance increased after two weeks of immersion. The impedance spectrum of FCSRs (both one- and two-ply) and FCFBERs showed a similar trend. Specifically, the impedance values of two-ply FCSRs, one-ply FCFBERs, and two-ply FCFBERs decreased slightly from $10^{11} \Omega \cdot \text{cm}^2$ after two weeks of immersion in the low-

frequency ranges, while the impedance values of the one-ply FCSRs decreased from $10^{11} \Omega \cdot cm^2$ to $10^{10} \Omega \cdot cm^2$, indicating a sharp decrease in the resistance of the FRP coating layers. The impedance values of all the coated specimens decreased rapidly in the third week of immersion to around $10^9 \Omega \cdot cm^2$, and then became steady in the following two weeks, decreasing slightly to $10^8 \sim 10^9 \Omega \cdot cm^2$. The decrease of the impedance was associated with the moisture uptake of the FRP-coating layer, as Davis *et al.* (2004) discovered that the impedance of the FRP-confined steel-reinforced concrete specimens was associated with the moisture uptake of the FRP layers. A similar observation was also found by Hinderliter *et al.* (2006) according to the theoretical calculation. The more readily decrease of the one-ply FCSRs could be attributed to the smaller effective thickness of the one-ply coating. The steady variation during the 3-8 weeks might be attributed to the saturation state of the FRP coating layers, which needs further investigation in the later work.

4.3.3 Potentiodynamic Polarisation (PP)

Figure 4.8 exhibits the corrosion potential (E_{corr}) derived from the PP tests, which is the average value of three identical specimens in each group. All FCSRs and FCFBERs exhibited positive corrosion potentials, while the ECSRs and one FBER with defects showed negative potentials, which is in line with the OCP results, as displayed in Figure 4.4. It is noteworthy that the corrosion potential of the ECSRs group derived from PP tests is around -0.88 V, more negative than their open circuit potentials. Therefore, ECSRs are more prone to the disturbance of charging currents compared to the FRP-coated specimens. The aforementioned phenomenon can be

attributed to the varied polarisation, which results in a constant fluctuation of the charges retained at the steel-electrolyte interface, making it challenging to directly distinguish the small faradaic current from the distortion of the potentiodynamic near the corrosion potential. (Zhang *et al.* 2009). All FCSRs and FCFBERs have an averaged corrosion current of around 10^{-12} A, which is about nine orders of magnitude smaller than that of the epoxy-coated specimens. Therefore, the potentiodynamic polarisation test results also proved that all the FRP-coated specimens could protect the core steel rebar from corrosion.

4.3.4 Linear Polarisation Resistance (LRP)

Figures 4.9 and 4.10 show the evolution diagrams of the average polarisation resistance (R_p) and corrosion current density (i_{corr}) of all groups, respectively. The absence of data at the beginning and after 14 days of immersion for FRP-coated specimens (both one- and two-ply) was due to the large resistance of the FRP coating layer (Gonzalez *et al.* 1985), the induced corrosion current density too small to be measured by the apparatus (the measurement limit of the equipment is 10^{-12} A). It is seen that for each type of rebar, R_p generally increased, whereas i_{corr} generally decreased with increasing immersion time. This could be understood by the gradual ingress of water through the coating layer of all types of coated steel rebars. After 56 days of immersion, the average i_{corr} of ECSRs, one-ply FCSRs and two-ply FCSRs increased to 9.04×10^{-6} , 1.35×10^{-12} and 1.64×10^{-12} A /cm², respectively, which suggests that the i_{corr} values of FCSRs were many orders of magnitude lower than those of the ECSRs and the UCSRs. A lower corrosion current density represents fewer defects and voids in the coating layer (Castro *et al.* 2005). Moreover, in

accordance with Andrade and Alonso (2004), the corrosion state of steel rebars is “*Negligible*” when the corrosion current density is lower than $0.1 \mu\text{A}/\text{cm}^2$; “*Low*” when the corrosion current density is between $0.1 \mu\text{A}/\text{cm}^2$ and $0.5 \mu\text{A}/\text{cm}^2$; “*Moderate*” when the corrosion current density is between $0.5 \mu\text{A}/\text{cm}^2$ and $1 \mu\text{A}/\text{cm}^2$; and “*High*” when the corrosion current density is higher than $1 \mu\text{A}/\text{cm}^2$. The corrosion level of the UCSRs, ECSRs and FCSRs after 56 days of immersion in 3.5 wt% NaCl solution are *High*, *High* and *Negligible*, respectively, further suggesting that the corrosion resistance of FCSRs are superior to that of ECSRs when subjected to saltwater immersion.

4.3.5 Six-Months Outdoor and One-Year Laboratory Exposure

Figures 4.11(a)-(c) and Figures 4.11(d)-(f) show the typical corrosion patterns of three types of rebars after exposure to the outdoor atmospheric environments of Hong Kong for six months and after immersion in 3.5 wt% NaCl solution for 12 months, respectively. It is seen that the FCSR still maintained a good state, whereas the UCSRs and ECSRs showed very severe corrosion. It should be noted that the epoxy coating layer at the edges of the ribs of the present ECSRs was thinner than that of commercial ECSRs produced with the fusion bonding process, but the rib regions of the latter are also, in general, the weak regions against steel corrosion. The above observations further confirm the superior corrosion resistance of the FCSRs.

Figure 4.13 (c) to Figure 4.13 (f) compare the interface morphology of ECRRs, one-ply FCSRs, FBERs and the one-ply FCFBERs, respectively. The corrosive product, which is in medium grey as shown in the SEM images, can be seen in Figure 4.13 (c) and Figure 4.13 (e), which indicates that both ECSRs and FBERs with the initial

defects were easily corroded, and the corrosion would continue to occur under the epoxy coating, the same results have been reported by Wu *et al.* (Wu *et al.* 2019). On the contrary, Figure 4.13 (d) and Figure 4.13 (f) further prove that FRP coating can protect the UCSRs as well as provide additional protection for the coated steel rebars whose coating layer is prone to be damaged, thus causing more pinholes.

4.3.6 Two-Year Marine Exposure

The corrosion state of the FCSRs after being exposed to the splash zone in the Hong Kong-Zhuhai-Macao Bridge Exposure Test Station for one year and two years were presented in Figure 4.12 and compared with the galvanized steel and stainless steel materials as the load frame were galvanized and the screw bars were stainless. It is clear that the galvanized steel corroded more severely with the exposure time increasing, while the stainless screw bars and nuts were not corroded. For FCSRs, the FRP coating layer was kept intact after two years' exposure, and no corrosion sign was found in the FCSRs (the yellow area at the two ends was dyed by the rust produced by galvanized steel frames).

The interface of the coating and steel substrate of the different types of rebars was observed by SEM technology. Figures 4.13 (a) and 4.13(b) show the details of the one-year field exposure specimen and two-year field exposure specimen, respectively. Both the interface and the coating layer were kept intact for both types of specimens, which was consistent with the surface observation results.

4.4 CONCLUSIONS

In this chapter, a series of electrochemical tests were utilised to understand the corrosion state and evolution of FRP-coated steel rebars (FCSRs). The test results were compared with those of uncoated steel rebars (UCSRs) and epoxy-coated steel rebars (ECSRs). The following exposure tests were conducted on FCSRs to evaluate their corrosion resistance: (a) 6-month exposure to the outdoor atmospheric environment of Hong Kong; (b) 12-month immersion in 3.5 wt% NaCl solution; and (c) 2-year field exposure at a marine site near the Hong Kong-Zhuhai-Macao bridge. The following conclusions were drawn based on the test results:

- (1) The corrosion rates of FCSRs are many orders of magnitude lower than those of UCSRs and ECSRs when immersed in 3.5% NaCl solution under ambient conditions.
- (2) The results of the EIS tests showed that the FRP coating layer protects the core steel rebar against electrochemical corrosion.
- (3) The OCP values of ECSRs decreased to an average value of around -0.6 V after the electrochemical system became steady, while those of FCSRs kept positive. This suggests that the FRP coating layer performs well in corrosion protection.
- (4) The observations of exposure tests also suggested that the FRP coating layer protects the core steel rebar against electrochemical corrosion. After half a year of exposure to the outdoor atmospheric environment of Hong Kong, or one year of immersion in 3.5 wt% NaCl solution or two years of exposure in the splash zone at an artificial island of the Hong Kong-Zhuhai-Macao Bridge, FCSRs maintained a good state.

4.5 REFERENCES

- Andrade, C. and Alonso, C. (1996). “Corrosion rate monitoring in the laboratory and on-site”, *Construction and Building Materials*, Vol. 10, No. 5, pp. 315-328.
- Andrade, C. and Alonso, C. (2004). “Test methods for on-site corrosion rate measurement of steel reinforcement in concrete by means of the polarization resistance method”, *Materials and Structures*, Vol. 37, No. 9, pp. 623-643.
- ASTM (2009). *ASTM C876-09*. Standard Test Method for Corrosion Potentials of Uncoated Reinforcing Steel in Concrete, American Society for Testing and Materials, West Conshohocken, Pennsylvania, USA.
- ASTM (2019). *ASTM A934/A934M*. Standard Specification for Epoxy-Coated Prefabricated Steel Reinforcing Bars, American Society for Testing and Materials, West Conshohocken, Pennsylvania, USA.
- Bierwagen, G.P., He, L., Li, J., Ellingson, L. and Tallman, D.E. (2000). “Studies of a new accelerated evaluation method for coating corrosion resistance—thermal cycling testing”, *Progress in Organic Coatings*, Vol. 39, No. 1, pp. 67-78.
- Caldona, E.B., Smith, D.W. and Wipf, D.O. (2020). “Surface electroanalytical approaches to organic polymeric coatings”, *Polymer International*, Vol. 70, No. 7, pp. 927-937.
- Chang, Y.-T., Wen, N.-T., Chen, W.-K., Ger, M.-D., Pan, G.-T. and C.-K. Yang, T. (2008). “The effects of immersion time on morphology and electrochemical properties of the Cr(III)-based conversion coatings on zinc coated steel surface”, *Corrosion Science*, Vol. 50, No. 12, pp. 3494-3499.

- Davis, G.D., Rich, M.J. and Drzal, L.T. (2004). “Monitoring moisture uptake and delamination in CFRP-reinforced concrete structures with electrochemical impedance sensors”, *Journal of Nondestructive Evaluation*, Vol. 23, No. 1, pp. 1-9.
- Forshee, A.G. (1993). “Accelerated corrosion testing, part I: An overview of 20 possible accelerated corrosion tests”, *Metal Finishing*, Vol. 91, No. 9, pp. 50-54.
- Gonzalez, J.A., Molina, A., Escudero, M.L. and Andrade, C. (1985). “Errors in the electrochemical evaluation of very small corrosion rates—I. polarization resistance method applied to corrosion of steel in concrete”, *Corrosion science*, Vol. 25, No. 10, pp. 917-930.
- Hinderliter, B.R., Croll, S.G., Tallman, D.E., Su, Q. and Bierwagen, G.P. (2006). “Interpretation of EIS data from accelerated exposure of coated metals based on modeling of coating physical properties”, *Electrochimica Acta*, Vol. 51, No. 21, pp. 4505-4515.
- Huang, Y., Zeng, X., Hu, X. and Liu, F. (2004). “Corrosion resistance properties of electroless nickel composite coatings”, *Electrochimica Acta*, Vol. 49, No. 25, pp. 4313-4319.
- Kautek, W. (1988). “The galvanic corrosion of steel coatings: aluminum in comparison to cadmium and zinc”, *Corrosion Science*, Vol. 28, No. 2, pp. 173-199.
- Kong, J.-Z., Hou, T.-J., Wang, Q.-Z., Yin, L., Zhou, F., Zhou, Z.-F. and Li, L.K.-Y. (2016). “Influence of titanium or aluminum doping on the electrochemical

- properties of CrN coatings in artificial seawater”, *Surface and Coatings Technology*, Vol. 307, Part A, pp. 118-124.
- Liang, H., Li, S., Lu, Y., Hu, J. and Liu, Z. (2019). “Electrochemical performance of corroded reinforced concrete columns strengthened with fiber reinforced polymer”, *Composite Structures*, Vol. 207, pp. 576-588.
- Macdonald, J.R. and Johnson, W.B. (2018). "Fundamentals of impedance spectroscopy." *Impedance Spectroscopy: Theory, Experiment, and Applications*, 1-20.
- Manning, D.G. (1996). “Corrosion performance of epoxy-coated reinforcing steel: North American experience”, *Construction and Building Materials*, Vol. 10, No. 5, pp. 349-365.
- Mansfeld, F. (1995). “Use of electrochemical impedance spectroscopy for the study of corrosion protection by polymer coatings”, *Journal of Applied Electrochemistry*, Vol. 25, No. 3, pp. 187-202.
- Sridhar, T., Mudali, U.K. and Subbaiyan, M. (2003). “Preparation and characterisation of electrophoretically deposited hydroxyapatite coatings on type 316L stainless steel”, *Corrosion Science*, Vol. 45, No. 2, pp. 237-252.
- Tang, F., Chen, G., Brow, R.K., Volz, J.S. and Koenigstein, M.L. (2012). “Corrosion resistance and mechanism of steel rebar coated with three types of enamel”, *Corrosion Science*, Vol. 59, pp. 157-168.
- Wu, T., Yan, M., Yu, L., Zhao, H., Sun, C., Yin, F. and Ke, W. (2019). “Stress corrosion of pipeline steel under disbonded coating in a SRB-containing environment”, *Corrosion Science*, Vol. 157, pp. 518-530.

- Xiong, W.B., Chen, Y.F. and Lu, M.X. (2007). “Corrosion behavior of CFRP/carbon steel system in a simulated soil solution studied by electrochemical impedance spectroscopy”, *Corrosion and Protection*, Vol. 28, No. 10, pp. 503-508.
- Zhang, X.L., Jiang, Z.H., Yao, Z.P., Song, Y. and Wu, Z.D. (2009). “Effects of scan rate on the potentiodynamic polarization curve obtained to determine the Tafel slopes and corrosion current density”, *Corrosion Science*, Vol. 51, No. 3, pp. 581-587.
- Zoltowski, P. (1998). “On the electrical capacitance of interfaces exhibiting constant phase element behaviour”, *Journal of Electroanalytical Chemistry*, Vol. 443, No. 1, pp. 149-154.

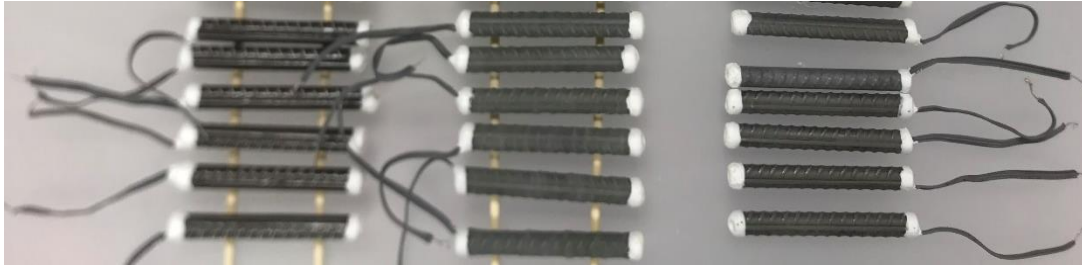
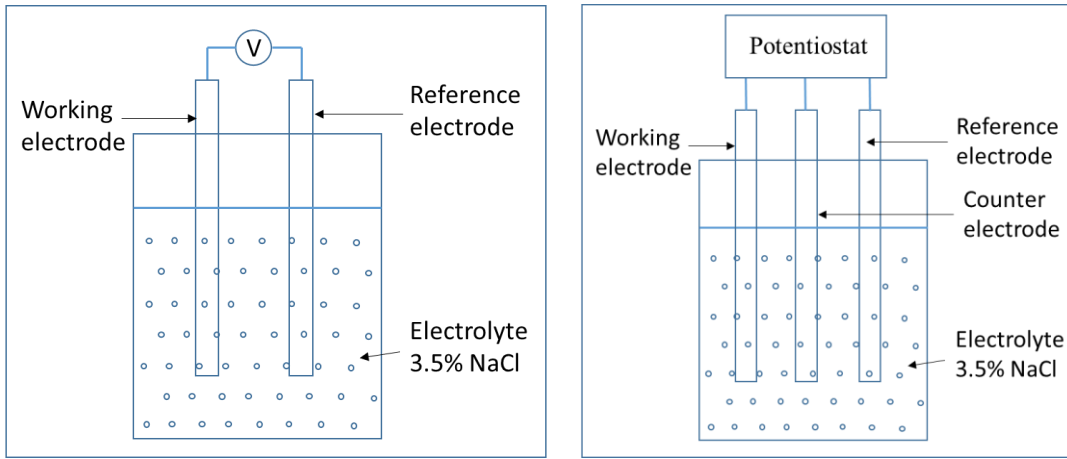


Figure 4.1 Examples of FRP-coated steel rebars for electrochemical tests



(a) OCP tests

(b) EIS, PP and LPR tests

Figure 4.2 Test setups for electrochemical tests

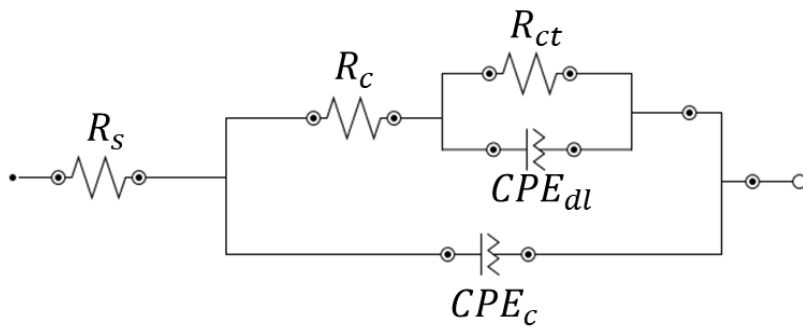
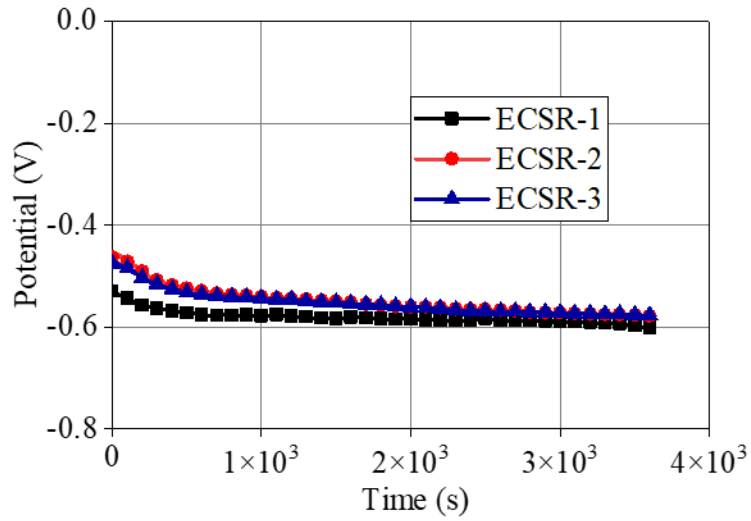
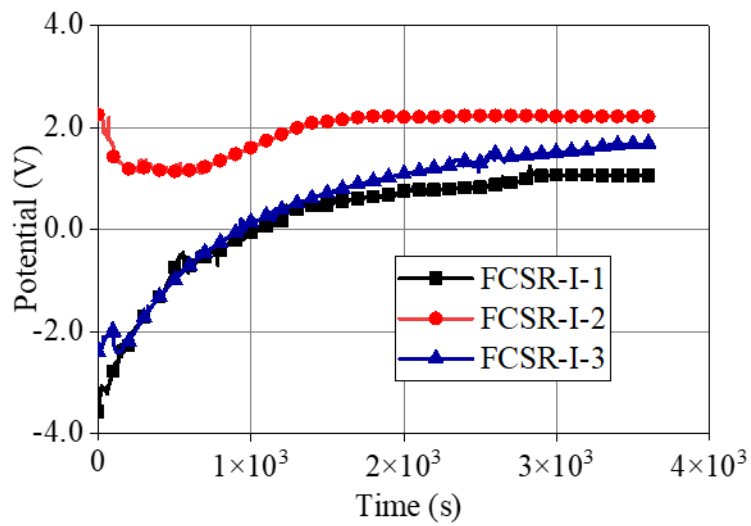


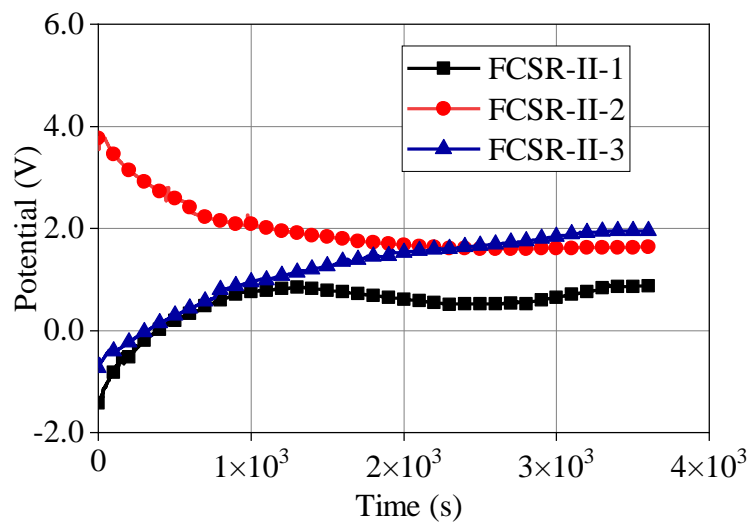
Figure 4.3 Electrical equivalent circuit (EEC) model for data fitting



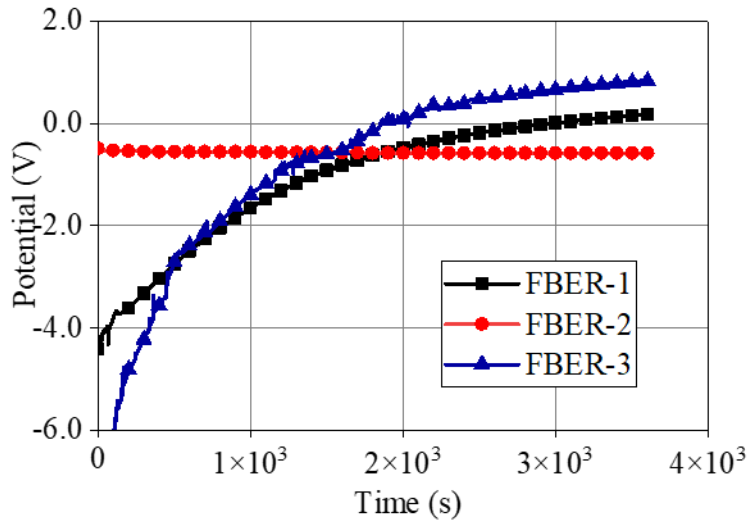
(a) OCP evolutions of epoxy-coated steel rebars



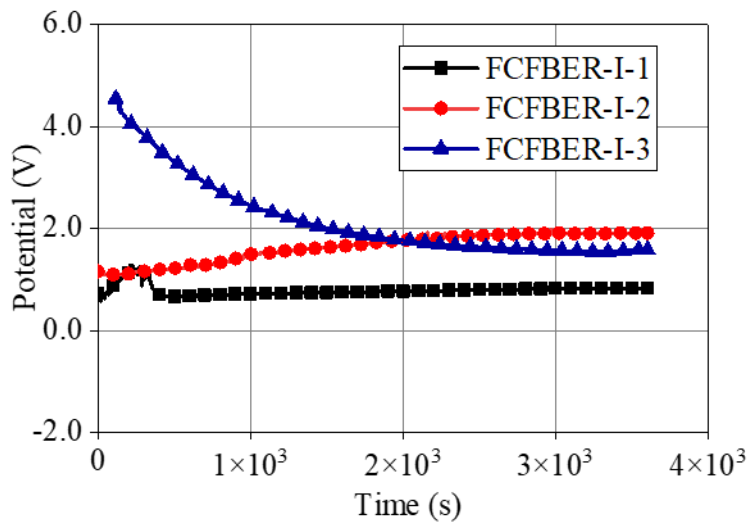
(b) OCP evolutions of one-ply FRP-coated steel rebars



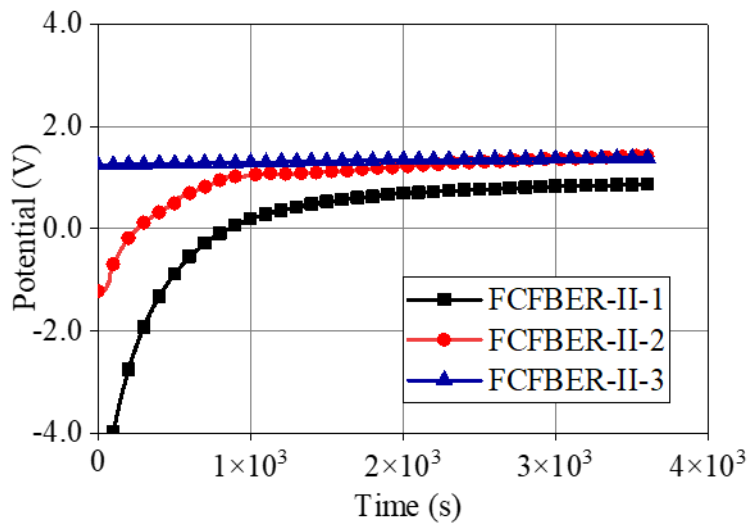
(c) OCP evolutions of two-ply FRP-coated steel rebars



(d) OCP evolutions of fusion-bonded epoxy-coated steel rebars (FBERs)



(e) OCP evolutions of one-ply FRP-coated FBERs



(f) OCP evolutions of two-ply FRP-coated FBERs

Figure 4.4 OCP evolution diagrams for different types of steel rebars

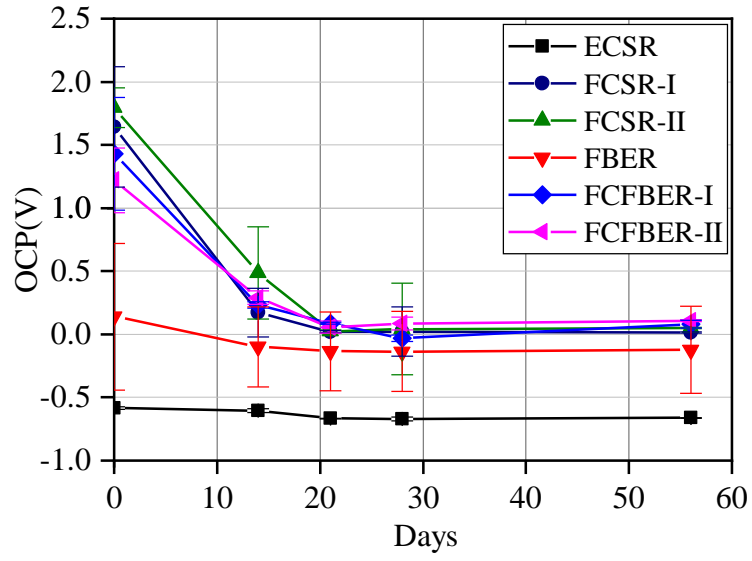
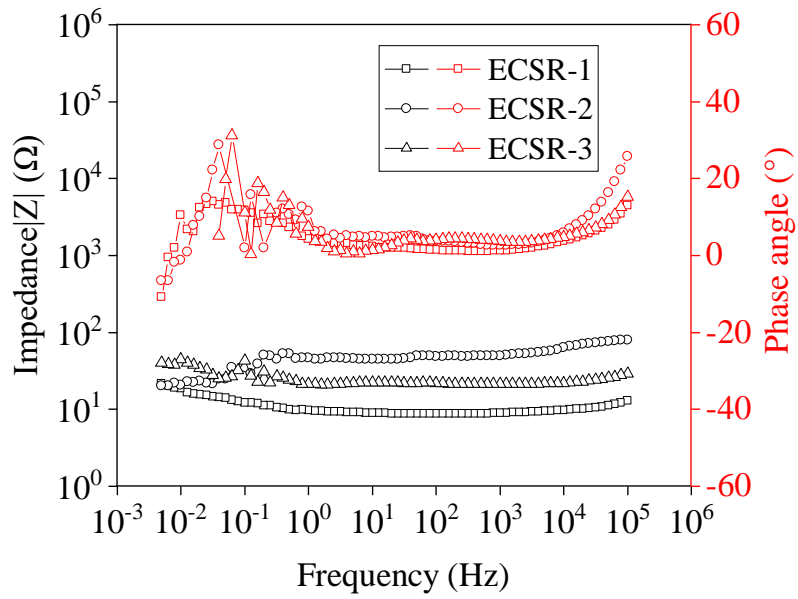
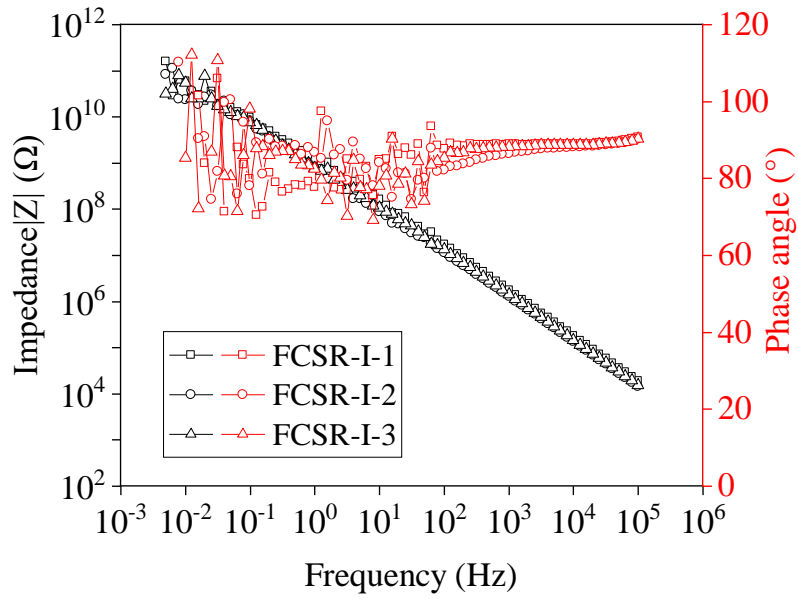


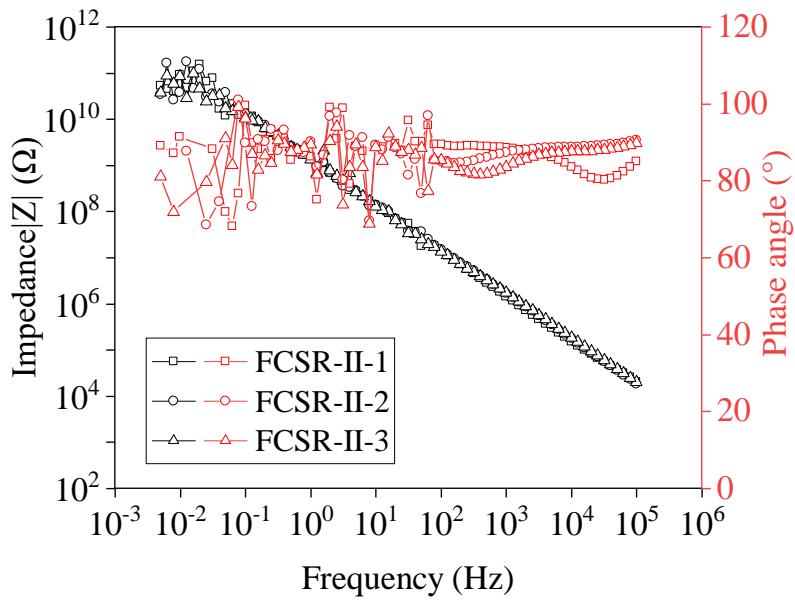
Figure 4.5 Variation of average OCP values of all groups



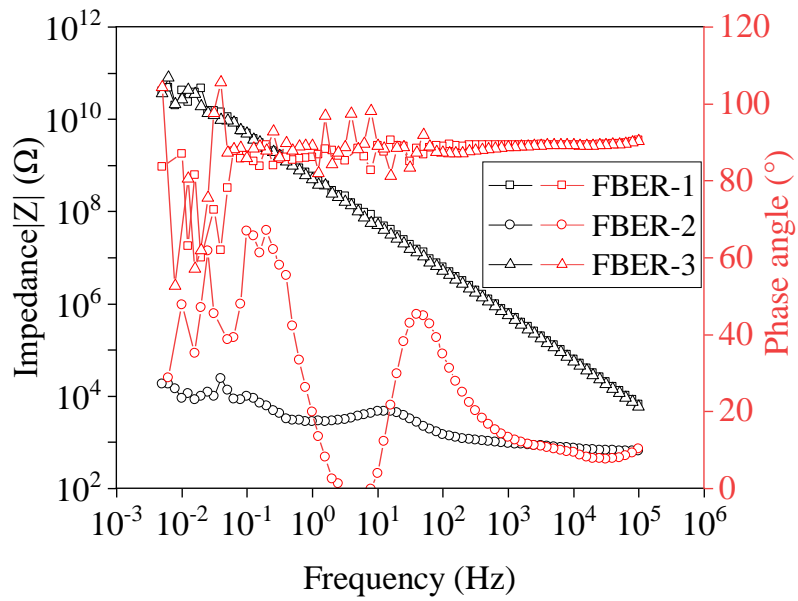
(a) Bode plot of epoxy-coated steel rebars



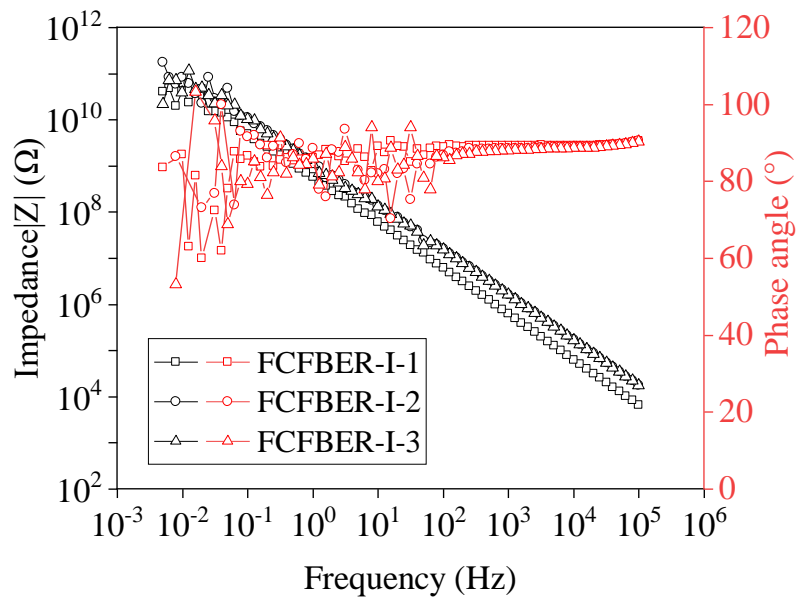
(b) Bode plot of one-ply FRP-coated steel rebars



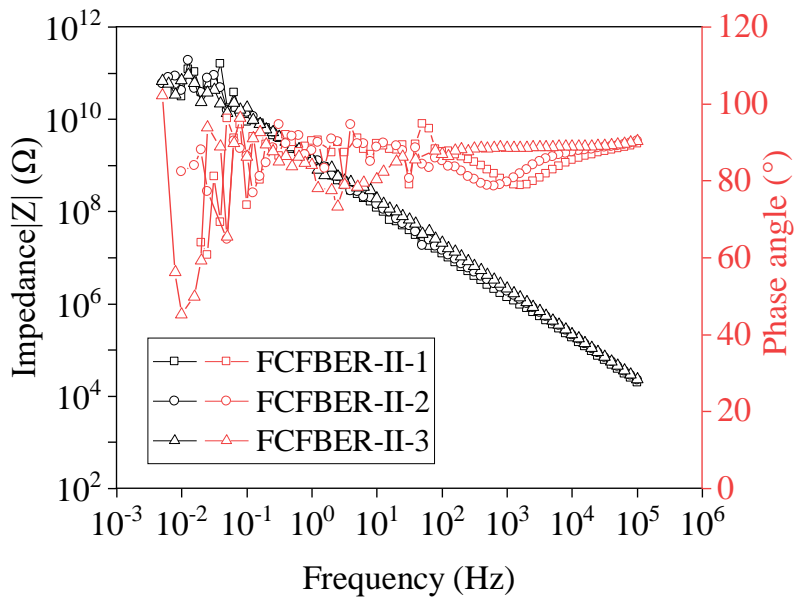
(c) Bode plot of two-ply FRP-coated steel rebars



(d) Bode plot of fusion-bonded epoxy-coated steel rebars (FBERs)

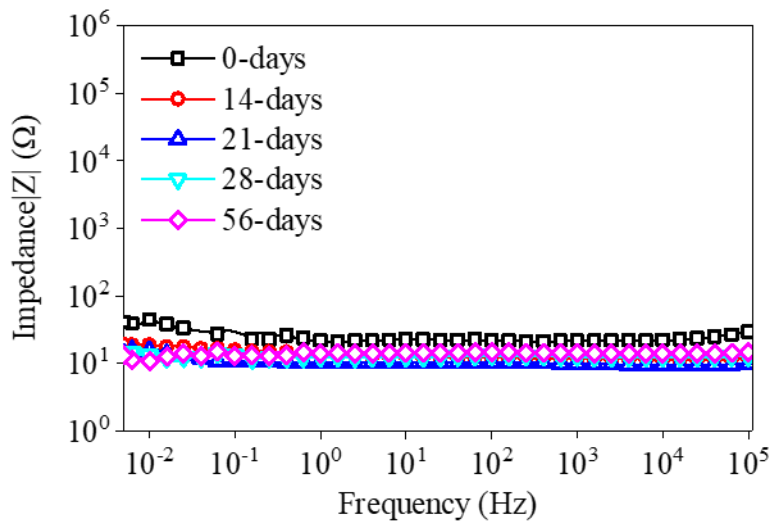


(e) Bode plot of one-ply FRP-coated FBERs

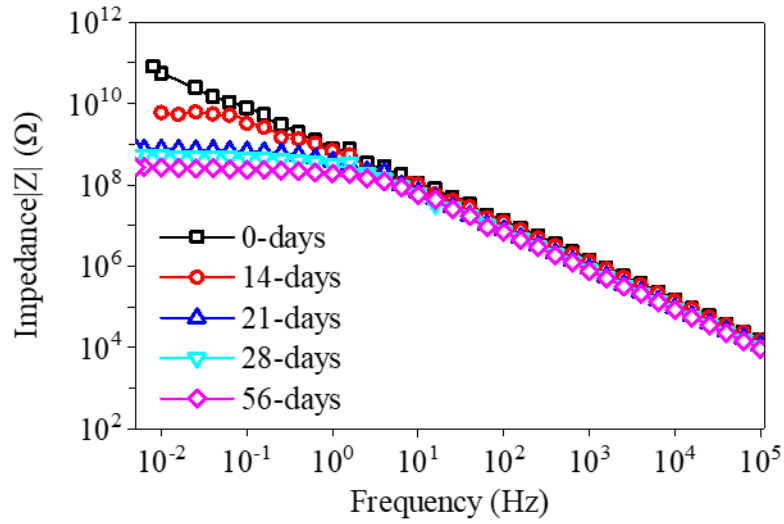


(f) Bode plot of two-ply FRP-coated FBERs

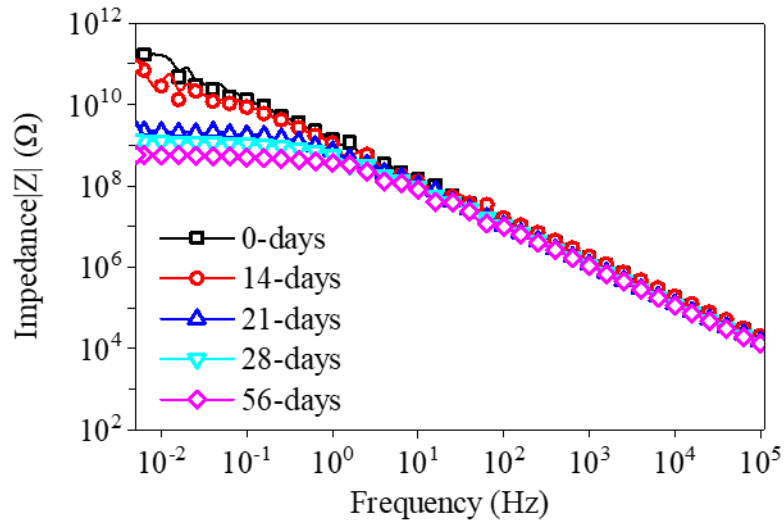
Figure 4.6 Bode plots of different types of steel rebars



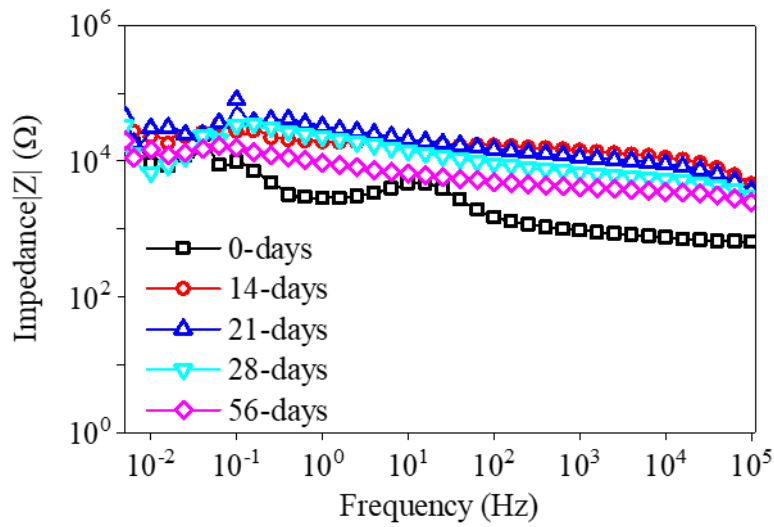
(a) Epoxy-coated steel rebars



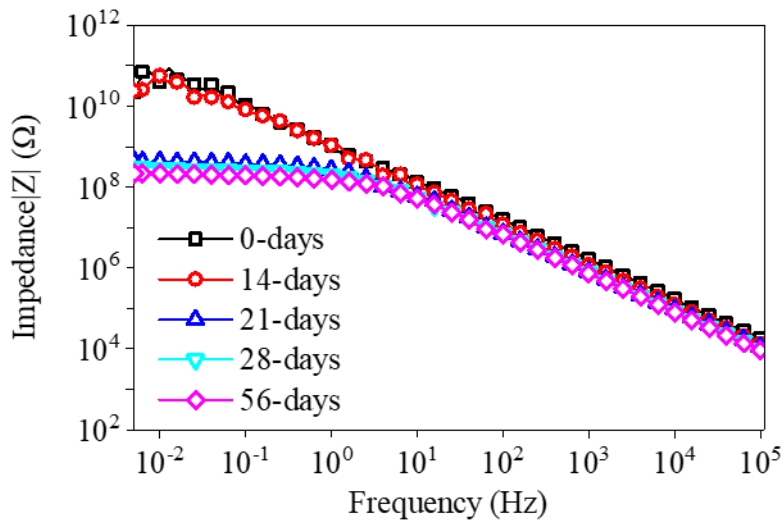
(b) One-ply FRP-coated steel rebars



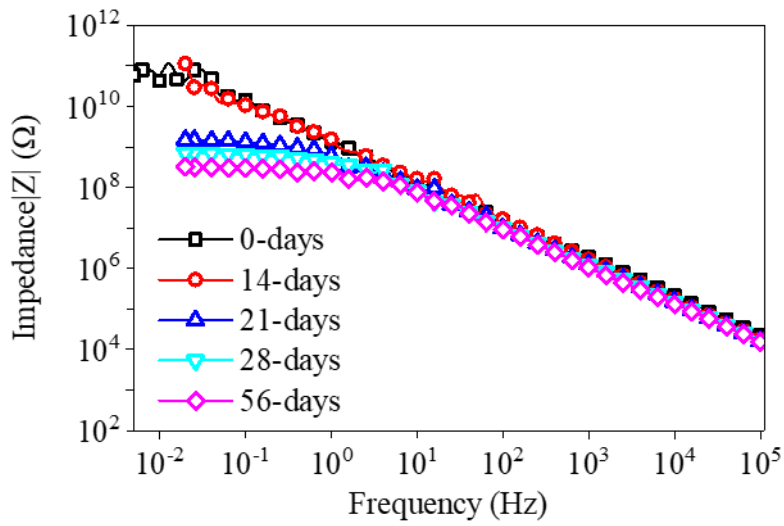
(c) Two-ply FRP-coated steel rebars



(d) Fusion-bonded epoxy-coated steel rebars (FBERs)



(e) One-ply FRP-coated FBERs



(f) Two-ply FRP-coated FBERs

Figure 4.7 Impedance spectra for specimens after being immersed in 3.5 wt% NaCl solution for up to 56 days

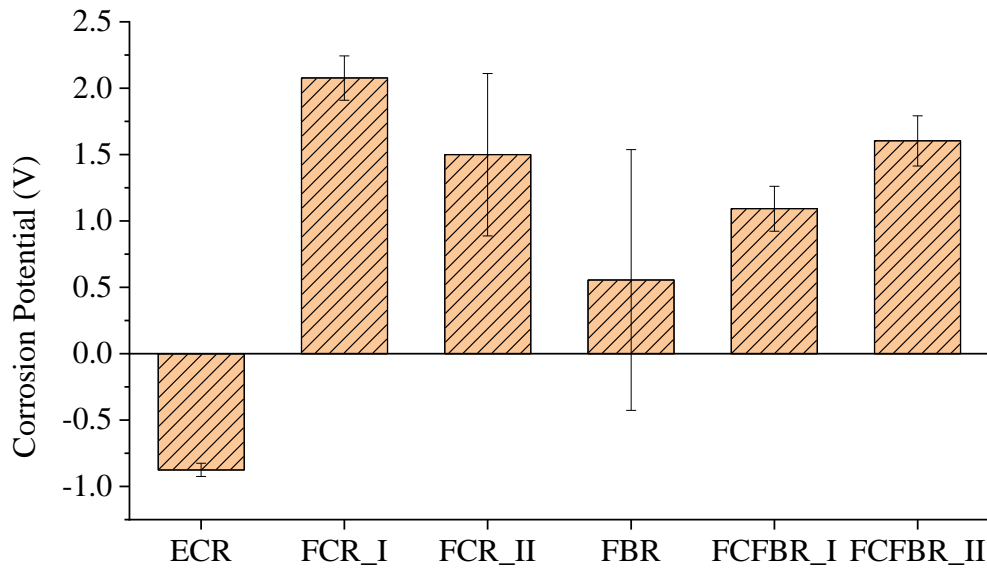


Figure 4.8 Corrosion potential extracted from potentiodynamic polarisation tests

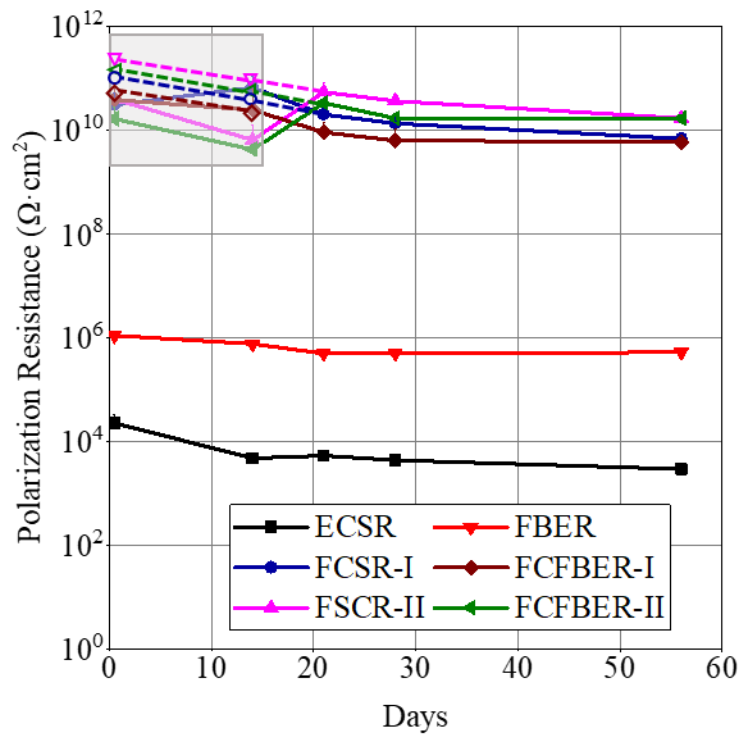


Figure 4.9 Polarisation resistance evolutions of specimens immersed in 3.5 wt% NaCl solution for up to 56 days

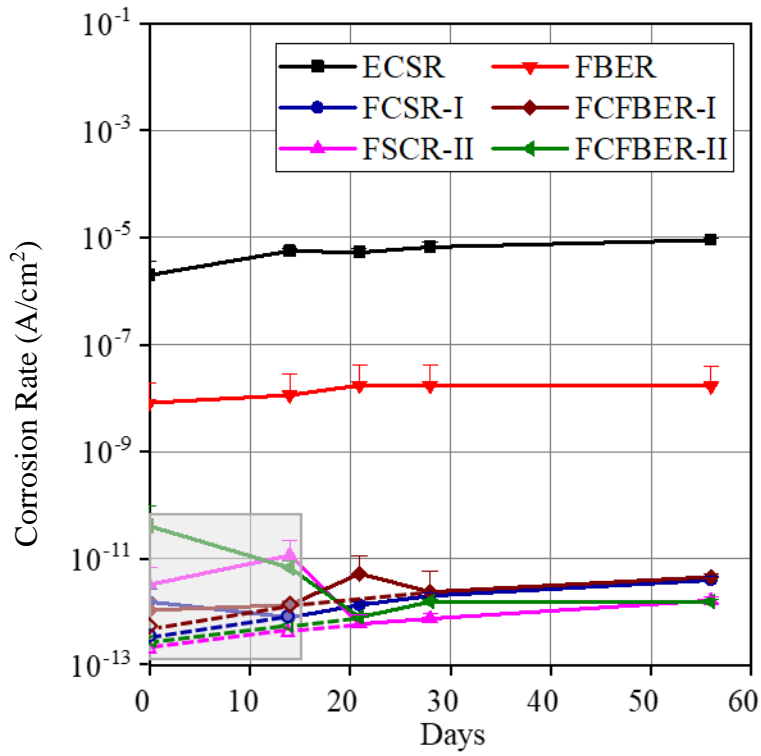


Figure 4.10 Corrosion rate evolutions of specimens immersed in 3.5 wt% NaCl solution for up to 56 days

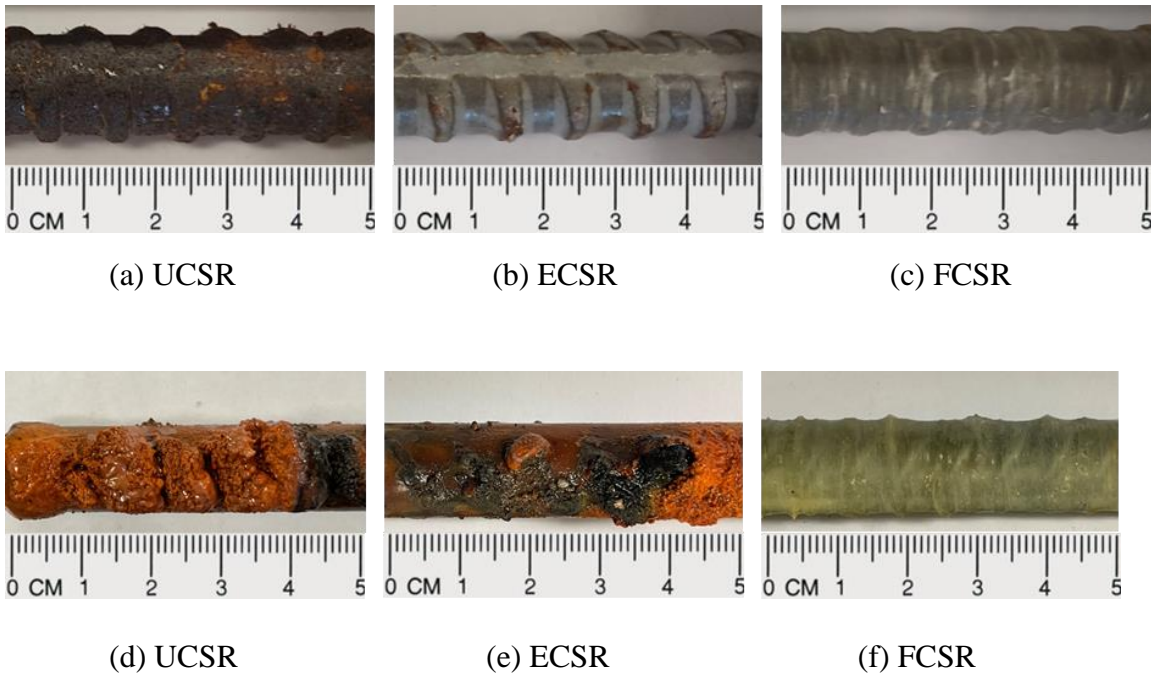
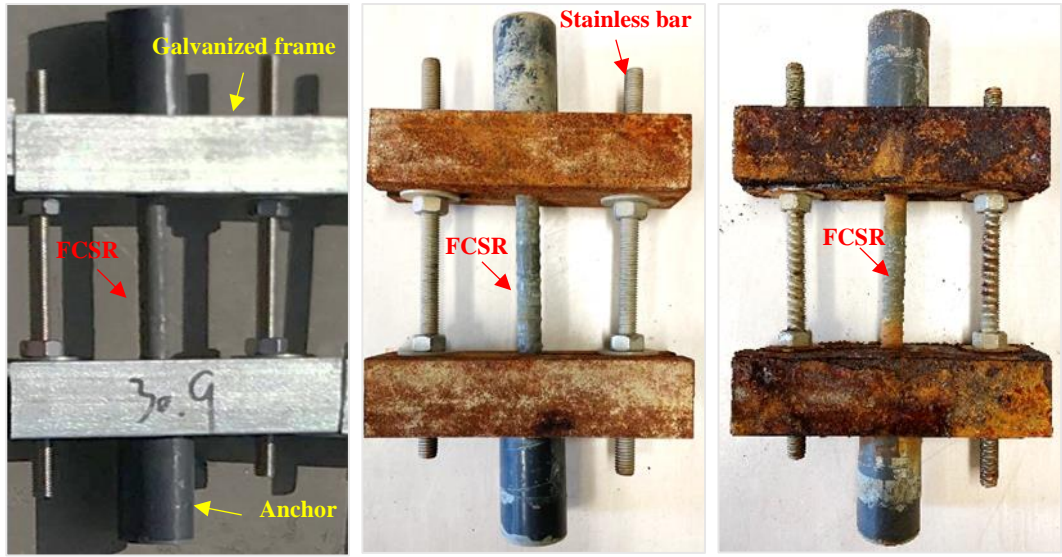


Figure 4.11 Corrosion state of rebars after exposure to the outdoor atmospheric environment for six months [(a)-(c)] and after immersion in 3.5 wt% NaCl solution for 12 months [(d)-(f)]

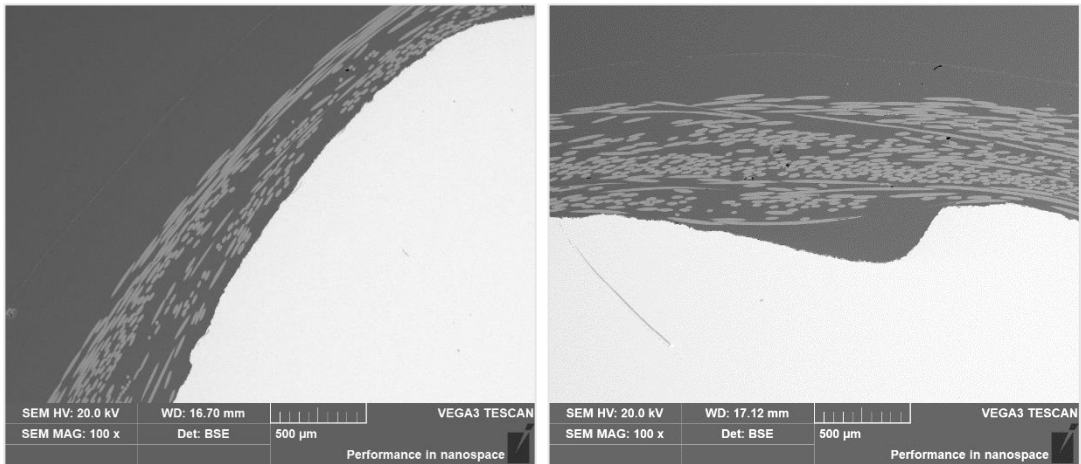


(a) 0 year

(b) 1 year

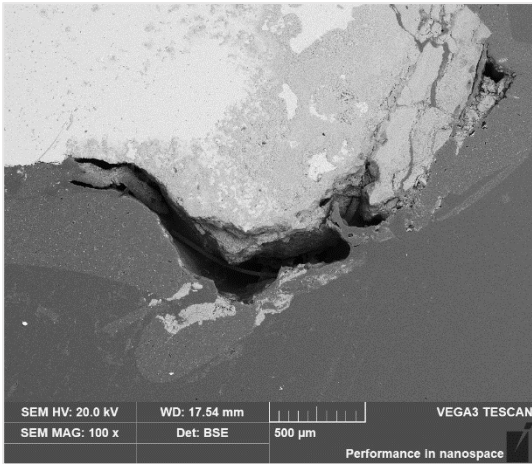
(c) 2 years

Figure 4.12 Corrosion state of specimens after exposure to the splash zone near the Hong Kong-Zhuhai-Macao Bridge for different periods

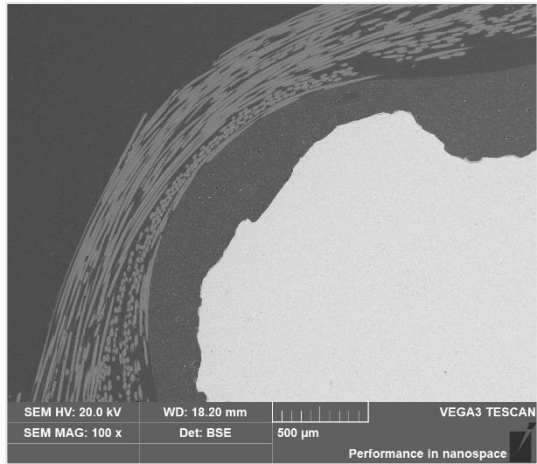


(a) 1-year field exposure

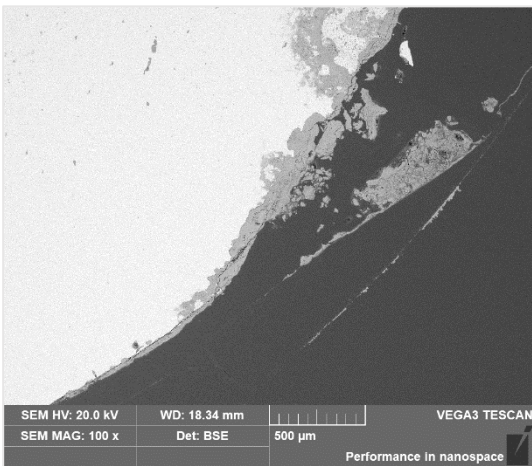
(b) 2-year field exposure



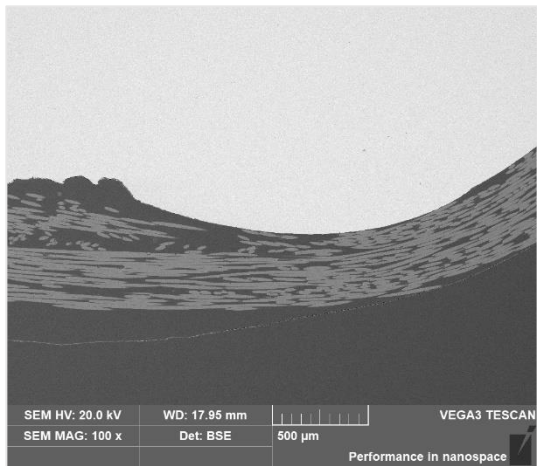
(c) FBER



(d) FCFBER-I



(e) ECSR



(f) FCSR-I

Figure 4.13 SEM images of the cross-sections of different types of steel rebars

Table 4.1 Mechanical properties of crescent-ribbed steel rebars

Grade	Diameter	Mass	Yield stress	Tensile strength
B	10 mm	0.615 kg/m	567 MPa	636 MPa

Table 4.2 Mechanical properties of epoxy resin

Tensile strength	Tensile modulus	Fracture strain	Glass transition temperature
80 MPa	3600 MPa	6%	105 °C

Table 4.3 Mechanical properties of glass fibres filaments

Glass type	Sizing agent	Fibre diameter	Linear density	Tensile strength
ECR-Glass	Silane	17 to 22 μm	1200 tex	≥ 0.3 N/Text

Table 4.4 Test matrix for experiments

Specimen	Coating	Number of fibre plies	Average thickness (μm)
ECSR	Epoxy	-	31.3
FCSR-I	FRP	1	576
FCSR-II	FRP	2	1087
FBER	Epoxy	-	425
FCFBER-I	Epoxy + FRP	1	1010
FCFBER-II	Epoxy + FRP	2	1598

Note:

- a) ECSR is epoxy-coated steel rebar;
- b) FCSR is FRP-coated steel rebar;
- c) FBER is fusion-bonded epoxy-coated steel rebar;
- d) FCFBER is FRP-coated fusion-bonded epoxy-coated steel rebar.

Table 4.5 Parameters of the EEC model obtained by experimental data fitting

Specimen	$Y_c(\Omega - sec^n / cm^2)$	n_c	$R_c(\Omega cm^2)$	$C_c(F/cm^2)$	$Y_{dl}(\Omega - sec^n / cm^2)$	n_{dl}	$R_{ct}(\Omega cm^2)$	$C_{dl}(F / cm^2)$
ECR-I-1	1.39E-09	1.00	237	1.39E-09	1.22E-03	0.76	248	8.30E-04
ECR-I-2	4.16E-11	1.00	0.01	4.16E-11	6.67E-17	0.80	1340	3.64E-20
ECR-I-3	0.00309	1.00	358	3.09E-03	6.23E-13	1.00	355	5.51E-13
FCSR-I-1	5.70E-12	0.95	3.09E+19	1.54E-11	1.03E+10	0.81	7.40E+10	6.09E+14
FCSR-I-2	5.94E-12	0.98	2.30E+09	5.41E-12	2.70E-12	0.90	1.11E+13	3.87E-12
FCSR-I-3	5.15E-12	0.98	9.05E+09	4.90E-12	3.29E-12	0.88	1.53E+13	5.52E-12
FCSR-II-1	1.23E-13	1.00	1.28E+08	1.23E-13	6.41E-14	0.98	4.19E+13	6.51E-14
FCSR-II-2	1.89E-13	0.98	9.05E+13	2.02E-13	1.00E-20	0.80	2.07E+07	6.75E-24
FCSR-II-3	1.79E-13	0.98	1.89E+13	1.84E-13	1.00E-20	0.80	3.32E+05	2.40E-24
FBER-1	1.09E-11	0.99	2.55E+12	1.12E-11	1.61E-11	1.00	3.40E+19	1.61E-11

FBER-2	5.14E-08	1.00	7.08E+04	5.14E-08	7.76E-06	1.00	4.90E+05	7.76E-06
FBER-3	1.30E-11	0.99	4.50E+11	1.33E-11	5.19E-12	1.00	5.17E+15	5.19E-12
FCFBER-I-1	5.50E-12	0.96	2.15E+19	1.13E-11	6.82E+09	0.89	9.38E+13	6.44E+12
FCFBER-I-2	4.94E-12	0.97	1.00E+22	9.46E-12	4.76E-10	0.80	5.56E+10	1.09E-09
FCFBER-I-3	5.44E-12	0.97	1.93E+12	5.90E-12	6.96E-06	0.80	8.09E+00	6.03E-07
FCFBER-II-1	5.80E-12	0.96	1.04E+19	1.22E-11	3.77E-07	0.84	9.63E+17	6.94E-05
FCFBER-II-2	5.17E-12	0.95	7.15E+10	4.92E-12	3.59E+05	0.80	1.15E+13	1.62E+10
FCFBER-II-3	4.41E-12	0.95	1.16E+19	1.04E-11	1.13E-20	0.83	2.22E+11	2.02E-22

CHAPTER 5

IMPACT RESISTANCE

5.1 INTRODUCTION

Impact resistance is a key performance indicator of corrosion-resistant steel rebars with protective coating layers, e.g., epoxy-coated steel rebars (ECSRs), galvanized steel rebars, enamel-coated steel rebars, etc. Steel rebars are frequently subjected to impacts caused by impact and dropping during transportation and installation. These impacts are neutral for uncoated steel rebars (UCSRs) but may be fatal for coated steel rebars as the resulting impact damages on the coating layer would ease the diffusion of aggressive ingredients.

ECSRs have been recognized to have poor impact resistance, which may be attributed to the brittleness of epoxy resin (Chen *et al.* 2021). When ECSRs are used in field applications, their poor impact resistance dramatically weakens their corrosion resistance as pitting corrosion easily occurs at the damaged regions and then propagates underneath the coating layer. Many attempts have been made to improve the impact resistance of ECSRs, one of which is by adding reinforcing materials into the epoxy coating layer to enhance its impact ductility. For instance, Chen *et al.* (2021) added multi-walled carbon nanotubes into epoxy resin, producing a new type of fusion-bonded epoxy coating with enhanced tensile strength and impact resistance.

They attributed the enhanced mechanical properties to a good distribution of multi-walled carbon nanotubes in epoxy, which resulted in an excellent interfacial bond between the two materials. Ye *et al.* (2007) concluded that the dominant mechanism for the improved impact resistance of nanotubes-blended epoxy could be attributed to the bridging-pull-out-breaking effect of nanotubes, which dissipate extensive impact energy by forming massive micro-cracking in front of the main crack. Miao *et al.* (2023) developed a gradient polyurethane silica coating consisting of several layers mixed with different silica particle sizes and concentrations. This new coating exhibited excellent impact resistance. The multiphase microstructure of the modified epoxy was verified to possess a significantly improved impact behaviour as compared to the unmodified epoxy polymers (Kinloch *et al.* 1987).

Compared with nanomaterials, continuous fibres, e.g., glass and basalt fibres, are a type of more economical reinforcement for epoxy resins. Panciroli and Giannini (2021) found that glass fibre-reinforced epoxy composites have drastically higher impact resistance than flax fibre-reinforced epoxy composites, which is attributed to the higher strength of the glass fibres than flex fibres. The energy absorption of FRP composites would not only increase with the increasing thickness of FRP composites (Chinnarasu and Ramajeyathilagam 2023) but also be influenced by the configuration of the reinforcing materials. The impact energy towards FRP composites may be dissipated as heat as it is spent in generating microcracks in the matrix, occurrence of delamination, and rupturing of fibres (Meola and Carlomagno 2010). Muhi *et al.* (2009) found that the hybridization layout of the fibres enhanced the penetration resistance of the composite laminates since the splitting easily occurred in the unidirectional composites even at low energies (Cantwell and Morton 1991) while composites with two fibre plies of $+45^\circ/-45^\circ$ showed higher impact resistance and

residual strength (Morton and Godwin 1989). Li *et al.* (2000) reported similar observations and concluded that cross-ply FRP composites have higher impact resistance than unidirectional ones.

Based on the knowledge gained on the impact resistance of continuous fibre-reinforced polymer composites, it is expected that the FRP coating layer of FCSRs may have better impact and peel resistance than an epoxy coating layer. Because the use of continuous fibres as reinforcement can minimise/constrain cracks and avoid through-cracks in the coating layer, and the use of the filament winding technique can ensure tight contact between the FRP coating layer and the core steel rebar. This chapter therefore presents an experimental study to demonstrate the impact resistance, which refers to the drop-weight impact resistance in the present study, of the FCSRs. The research parameters include the number and the fibre winding angle(s) of fibre plies in the FRP coating layer.

5.2 EXPERIMENTAL PROGRAMME

5.2.1 Test Matrix

Ten groups of rebar specimens were prepared and tested, including eight groups of FCSRs and one group of ECSRs with three levels of impact energy, and one group of UCSRs served as controls. Each group with different impact energy levels consisted of three identical rebar specimens.

Each specimen was given a name in the format of “ $M - I - L$ ” where M stands for coating materials (e.g., “UCSR” represents uncoated steel rebars, “ECSR” represents epoxy-coated steel rebars, “FCSR” represent the FRP-coated steel rebars), the letter

I represents the wound fibre angles of each coating ply, for example, “A” represents a fibre ply with the winding angle of +86.5 °, “C” represents a fibre ply with the winding angle of -86.5°, and “FFA” represents three plies fibres with the combinations of +45°/-45°/+86.5°, *L* stands for the level of impact energies, “L1-L5” corresponding to the level 1 to level 5 as listed in Table 5.1, respectively.

5.2.2 Specimens Preparation

FCSRs were prepared with the manufacturing procedure that has been introduced in Chapter 3. The key properties of the epoxy resin, glass fibre and steel rebars that are used to produce the FCSRs are given in Table 5.1-5.3, respectively. ECSRs were prepared by brushing epoxy resin on cleaned steel rebars. The epoxy resin, steel rebars and curing conditions (i.e., temperature and humidity) were the same as those used for FCSRs. Each rebar specimen was cut into 100 mm in length, and then both ends sealed with silicone sealant DY-M1210 (DEYI) for waterproofing, with one end was connected to a piece of copper wire before being sealed with silicone sealant. After the impact, the sealed ends of each specimen were brushed with another layer of the silicone sealant to repair the damages on the sealed ends caused by the impact and thus to ensure the waterproofing for two ends during the following electrochemical tests., as shown in Figure 5.2. The sealed end cover was thicker than the FRP coating layer to reduce the influence of the sealant on the electrochemical response of the tested specimens (Fan *et al.*, 2018).

5.2.3 Impact Tests

Impact tests were performed with reference to ASTM D7136 (ASTM 2020) on a drop-weight testing machine, as shown in Figure 5.1. The impact energy for each group of FCSRs and ECSRs was determined in accordance with the coating thickness,

$$E = C_E h \quad (5-1)$$

E represents the potential energy of the impactor before the drop (unit: J), and C_E denotes the specific impact energy ratio to the thickness of the impact target, which is taken as 6.7 J/mm as per ASTM D7136 (ASTM 2020); h is the nominal coating thickness. The drop height of the impactor required to achieve the impact energy is calculated by,

$$H = \frac{E}{m_d g} \quad (5-2)$$

where H is the drop height of the impactor (unit: m), m_d is the mass of the impactor to produce impact damage, and g is the acceleration due to gravity, which is taken as 9.81 m/s². Based on the measured coating thicknesses, the designed three levels of impact energy were 2.8 J, 6.7 J and 10.7 J for ECSRs and one-ply FCSRs; were 6.7 J, 10.7 J and 17.1 J for two-ply ECSRs, were 10.7 J, 17.1 J and 27.4 J for three-ply FCSRs. Due to the limited height (i.e., 1.6 meters for the drop-weight machine), the minimum mass of the impactor is equal to 1.75 kg to create an impact energy of 27.4 J. Therefore, a mass of 1.8 kg was chosen in the present study to create impact damage to the test specimen. The lower impact energies were achieved by adjusting the drop height of the impactor. UCSRs were not subjected to impact as they were not sensitive to impact damages. A total of 84 specimens that uncoated/coated with different fibre plies (one-ply, two-ply, and three-ply FRP coating, epoxy coating) and winding

angle(s) (combination of different winding angles $\pm 45^\circ$, $\pm 60^\circ$, $\pm 86.5^\circ$, and different layup sequences) were prepared and tested, the details of each type of rebar were displayed in Table 5.5.

5.2.4 Coating Damage Observations

Scanning electron microscopy (SEM) was conducted to observe the impact-induced damages on the coating layer at microscopic levels on a scanning electron microscope (TESCAN VEGA3).

The specimen was cut into a five mm-long section from a rebar at the impact location. When cutting the small section from a rebar, the moving speed of the cutter was fixed at 1 mm/min perpendicular to the longitudinal axis of the rebar to minimize extra cutting damage, as shown in Figure 5.3. After cutting, the specimen was cold-mounted into a mould with liquid epoxy before the polishing process, as shown in Figure 5.4. Then, the cross-section of the specimen was polished sequentially using 240-, 400-, 800-, 1200-, and 2000-grit sandpapers until it reached mirror quality and followed a 9- μ m diamond suspension polishing process for two minutes, as shown in Figure 5.5.

5.2.5 Post-Impact Electrochemical Tests

The specimens subjected to the impact energies were then immersed in the 3.5 wt.% sodium chloride solution for electrochemical tests at room temperature.

The OCP values between the reference electrode and the working electrode (tested specimens) were recorded for one hour until its trend gradually became steady in

every measurement. The EIS test and potentiodynamic test were then carried out sequentially by utilising a classic three-electrode system, as illustrated in Figure 4.1 in Chapter 4. A saturated calomel electrode was employed as a reference electrode, a carbon rod was used as a counter electrode, and the rebar specimen served as a working electrode in this testing system. The potentiodynamic polarisation test was carried out by scanning over a potential of 300 mV cathodically and anodically from the OCP value with a scanning rate of 2.5 mV/s. The variation of the current under different potentials was then monitored to calculate the polarisation resistance R_p of the working electrode. Which was used to calculate the corrosion current density of the specimens. The absolute value of the monitored current under the corresponding potential is drawn in a logarithmic scale, as shown in Figure 5.6, which is the typical Tafel curve used to extract the corrosion potential E_{corr} and the current density of corrosion i_{corr} . The corrosion potential E_{corr} describes the propensity of the electrochemical reaction to happen at the interface of metal and coatings and the corresponding corrosion current i_{corr} reveals the relevant kinetic behaviours (Caldona *et al.* 2020).

EIS test was taken by applying a sinusoidal wave with an amplitude of 10 mV around the open circuit potential, which ranges from 10^5 Hz to 5×10^{-1} Hz, and the data acquisition frequency is 10 per decade. The EIS data was then logged as a function of frequency, and the equivalent electrical circuit (EEC) models were then used to analyze the coating performance.

All the electrochemical data was acquired through a potentiostat (PGSTAT302N Autolab).

5.3 RESULTS AND DISCUSSIONS

5.3.1 Coating Damage

The typical coating damages on the coated steel rebars caused by the impact are displayed in Figure 5.2. It is seen that the epoxy coating layer was fragmented and peeled off from the steel surface after impact, whereas the FRP coating layer retained its integrity, although penetration occurred to some extent.

Figure 5.7 shows the cross-sectional view of FCSRs after impact. As expected, with increasing impact energy, more cracks were formed and propagated deeper in the thickness direction. It is interesting to note that, unlike the epoxy coating layer, which was damaged at the impact locations, almost no penetrated cracks were formed in the FRP coating layer when the impact energy was at a low level, i.e., Levels I and II. Only when the impact energy increased to Level III, penetrated cracks were observed in the FRP coating layer, which may suggest a failure of the FRP coating layer in protecting the substrate steel rebar against corrosion.

5.3.2 Open Circuit Potential

Figure 5.8 shows the OCP evolution of all groups. In each subfigure of Figure 5.8, an OCP evolution curve is an average of the curves of three identical specimens. It is seen that the OCP for either FCSRs or ECSRs generally decreased with increasing immersion time in 3.5 wt% NaCl solution. This could be understood by the gradual diffusion of electrolyte across the coating layer, which de-passivated the substrate steel rebar.

It is interesting to note that the OCP values of UCSRs almost kept at around -0.8 V/SCE during the immersion, which suggests that the corrosion potential of the screw-thread steel rebars used in this study was around -0.8 V/SCE in this type of electrolyte. Besides, the three curves for ECSRs under three levels of impact energy almost coincide with each other, as shown in Figure 5.2(b); all decreased from an initial value of about -0.4 V/SCE to -0.8 V/SCE after 10 hours of immersion. It may be understood that even the lowest level of impact energy can completely destroy the epoxy coating layer of an ECSR, and a continued increase in impact energy may not lead to more severe impact damage. The more positive initial OCP values of ECSRs (about -0.4 V/SCE) than those of UCSRs (about -0.8 V/SCE) could be understood because the metal area of the former that caused by impact and exposure to the electrolyte was smaller than that of UCSRs.

By contrast, the three curves for each group of FCSRs shifted more negatively with the increasing level of impact energy, as shown in Figures 5.2 (b), (c) and (d). Such differences suggest different degrees of impact-induced coating damage. It is also noted that the average terminal OCP value of FCSRs was more positive than that of ECSRs that experienced the same level of impact energy, which suggests that the impact resistance of FCSRs is superior to that of ECSRs. In addition, as expected, the terminal OCP increased with the increasing number of fibre plies, confirming that the thicker the FRP coating layer, the higher the impact resistance.

Figure 5.9 and Figure 5.10 compared the OCP values of the two- and three-ply FCSRs with different winding angle(s) under the same levels of impact energy, respectively. For two-ply FCSRs, all the groups showed an excellent impact resistance to level II impact energy as the OCP values remained positive even after a long time immersion in the 3.5 wt% NaCl solution. Group AA and CC showed a similar trend under all

three levels of impact energy, while group CA exhibited the best impact resistance, and group AC performed worse among the four winding configurations. In detail, the OCP value of group AC that sustained the level III impact decreased to -0.61 V/SCE after being immersed in the saline solution, and group CC decreased to -0.5 V/SCE after 110 hours of immersion. For those who sustained a level IV impact energy, the OCP value of group CA remained positive for nearly ten hours, while the other three groups were negative from the initial immersion. For three-ply FCSRs, no difference can be seen between the groups that sustained loading of level III and level IV impact energies, as all the groups kept positive even after an immersion period of 300 hours. However, the group FFA that sustained impact energy of level V decreased to -0.4 V/SCE after 50 hours' immersion, which suggests a poor impact resistance of three-ply FCSRs with a winding angle combination of “+45°/-45°/+86.5°” when compared with other winding angle combinations.

In conclusion, the open circuit corrosion values of FCSRs impacted by different levels of energy shifted to a higher value than that of the UCSRs and ECSRs. OCP tests qualitatively proved that FCSRs exhibit excellent impact resistance compared with the ECSRs, and the wound fibres could absorb part of the energies and prevent the epoxy from peeling off the steel, which would cause direct exposure of the steel to aggressive environments. Moreover, the OCP results verified that impact resistance would increase with the fibre plies, and winding angle(s) also have an influence on the impact resistance of FCSRs. The winding configuration with a “cross-over” combination between plies could improve the impact resistance of the coating layer. However, the optimal winding configurations still need to be further investigated.

5.3.3 Potentiodynamic Polarisation

Figure 5.11 shows the evolution of corrosion current density (i_{corr}) and the polarisation resistance (R_p) of UCSRs, ECSRs and FCSRs after an impact of 10.7 J. It is seen that UCSRs had the highest corrosion rate, which was $4.7 \times 10^{-4} \text{ A/cm}^2$ at 40 hours of immersion. The i_{corr} of ECSRs ($4.3 \times 10^{-5} \text{ A/cm}^2$) was very close to that of uncoated steel rebars, suggesting that the epoxy coating layer almost failed after impact. By contrast, the three types of FCSRs had i_{corr} values, which were many orders of magnitude lower than those of UCSRs and ECSRs. The i_{corr} of FCSRs decreased with the increase in the number of fibre plies suggesting that the thicker the coating, the fewer the defects and voids in the coating layer after impact (Castro et al. 2005), which in turn confirms that FCSRs with thicker coating layers have a higher impact resistance. Based on the above observations, the impact resistance of coated steel rebars follows an order: three-ply FCSRs > two-ply FCSRs > one-ply FCSRs > ECSRs.

Figure 5.12 compares the evolution of the i_{corr} of two-ply FCSRs with different winding angles after impact. The fibre angle combinations include $+86.5^\circ/+86.5^\circ$ (A-A), $+86.5^\circ/-86.5^\circ$ (A-C), $-86.5^\circ/+86.5^\circ$ (C-A) and $-86.5^\circ/-86.5^\circ$ (C-C). It is seen from Figures 5.9(a) and (b) that after impact with energy Level II and Level III, the i_{corr} evolution of two-ply FCSRs with four types of winding angle combinations was similar. The corrosion current density of all the impacted two-ply FCSRs increased from initially around 10^{-13} A/cm^2 to 10^{-11} A/cm^2 at 400 hours, which could be attributed to the fact that the impact energy levels are too low to induce substantial damage to the four types of the FRP coating layer. However, after being impacted with a higher energy Level IV, the FCSRs with a winding angle combination of

+86.5°/+86.5° exhibited the highest i_{corr} (around 10^{-9} A/cm²), followed by the FCSRs with a winding angle combination of +86.5°/-86.5° (around 10^{-11} A/cm²), as shown in Figure 5.12(c). The i_{corr} of FCSRs with winding angle combinations of -86.5°/+86.5° and -86.5°/-86.5° remained within a range between 10^{-13} A/cm² to 10^{-11} A/cm² which is similar to the situation for impact energy Level II and Level III. The lower the corrosion rate, i.e., the higher the polarisation resistance, the fewer the defects and voids in the coating layer after impact (Castro *et al.* 2005). The impact resistance of two-ply FCSRs with different winding angles follows an order: -86.5°/+86.5° \approx -86.5°/-86.5° > +86.5°/-86.5° > +86.5°/+86.5°. This order could be understood that for an FCSR with a filament wound FRP coating layer, the first fibre ply with a crossed winding angle to the ribs' direction will greatly benefit the impact resistance of the coating layer.

Figure 5.13 compares the evolution of the i_{corr} of three-ply FCSRs with different winding angles after impact. The fibre angle combinations include +86.5°/-86.5°/+86.5° (A-C-A), +60°/-60°/+86.5° (S-S-A) and +45°/-45°/+86.5° (F-F-A). It is seen from Figure 5.10 that after impact with energy Level 3 to Level 5, the i_{corr} evolutions of three-ply FCSRs with three types of winding angle combinations were similar. The corrosion current density of all the groups increased from initially around 10^{-13} A/cm² to 10^{-11} A/cm² at 150 hours, except the group with a winding angle combination of +60°/-60°/+86.5°, which increased a little bit more to 10^{-10} A/cm² at 150 hours. The impact resistance of three-ply FCSRs with different winding angles follows an order: +86.5°/-86.5°/+86.5° \approx +45°/-45°/+86.5° > +60°/-60°/+86.5°.

5.3.4 Electrochemical Impedance Spectroscopy

Figure 5.14 shows the evolution of impedance spectra of UCSRs, ECSRs, one-ply FCSRs and two-ply FCSRs. The test results of three-ply FCSRs are not presented in Figure 5.14 because their thick coating layers protect them well against impact, resulting in not much difference among their test results. The test results that are presented by scatters in Figure 5.14 are fitted using EEC models that are given in Figure 5.15. The fitting curves are also plotted with continuous lines in Figure 5.14 for comparisons. In the two EEC models, the element R_s represents the resistance of electrolytes of the test system; R_c and R_{ct} represent the resistance provided by the coating layer and the electrochemical charge transfer activity, respectively; CPE_c and CPE_{dl} represent the capacitive behaviour of the coating layer and the double-layer capacitive effect of the electrode-electrolyte interface, respectively. Here, constant phase elements (CPE_c and CPE_{dl}) instead of pure capacitors were used to describe the dielectric properties of the coating layer and the electrode-electrolyte interface due to the material non-homogeneity and the non-ideal diffusion of aggressive ingredients ((Tang *et al.* 2016).

According to Akbarinezhad *et al.* (2009), the area under the bode plots can be used as an index to assess the protective behaviour of the coating specimens, which considers the EIS data under all regions of frequency, and Kouhi *et al.* (2012) also found the change of the area under bode plots can capture the degradation behaviour of the polymeric coatings. The area method essentially still compares the value of the impedance moduli and the phase angle. Therefore, the impedance moduli and phased angle were used to analyse the EIS results in this study.

It is seen in Figures 5.14(a) and (b) that the impedance moduli were around $10^3 \Omega \cdot cm$, and the phase angles were kept near 0° at all frequency regions for both UCSRs and ECSRs. By contrast, as is seen in Figures 5.14 (c) to (k), the impedance moduli varied from $10^6 \Omega \cdot cm$ to $10^{11} \Omega \cdot cm$ and the phase angles varied from 0° to 90° with the varying number of fibre plies and varying levels of impact energy.

Figures 5.14 (c)-(f) and Figures 5.14 (g)-(k) compared the EIS results of one-ply FCSRs and two-ply FCSRs subjected to the different levels of impact energy, respectively. Specifically, after impact with the level I and level II loading energy, the one-ply FCSRs, the slope of logged impedance vs frequency plot was around -1, the impedance value was around $10^{10} \Omega \cdot cm$ at a low frequency, and the phase angle kept around 90 degrees, the results were consistent with the performance of the high-quality coating as reported by Akbarinezhad *et al.* (2009), however, after impacted by level III energy, the impedance value of the one-ply FCSRs decreased to around $10^7 \Omega \cdot cm$ and further decreased to $10^6 \Omega \cdot cm$ after 2 hours' immersion in the 3.5 wt% NaCl solution. The relevant phase angle decreased from 90 degrees at the high frequency to 0 degrees in the low-frequency region. The phase angle at the high frequency also decreased from 90 degrees to around 70 degrees with the immersion time increasing, which was consistent with the study by Mahdavian and Attar (2006), who use the phase angle at the high frequency as an index to illustrate the performance of organic coatings. Although the one-ply FRP coating showed deterioration after level III impact energy, it still behaved better and reserved a certain protection toward the core steel rebar when compared with the UCSRs and the damaged ECSRs.

For two-ply FCSRs with a winding angle of $+86.5^\circ/+86.5^\circ$, the coating performance also decreased with the increase of the impact levels. This can be attributed to the

remaining effective thickness of the coating (undamaged depth) decreased with the impact levels. However, for two-ply FCSRs with a winding angle of $-86.5^\circ/+86.5^\circ$, no difference can be observed between specimens with different impact energies at the initial stage of immersion in the 3.5 wt% sodium chloride solution. They still showed high quality even after the level IV impact energy. This is because the remaining effective thickness of the FRP coating layer can still protect the steel core, which means the impact resistance of the FCSRs with the winding angle combination of $-86.5^\circ/+86.5^\circ$ was higher than the winding angle combination of $+86.5^\circ/+86.5^\circ$. The decreasing of the impedance and the phase angles at the low-frequency region for FCSRs $86.5^\circ/+86.5^\circ$ can be attributed to the diffusion of the electrolytes, as the polymeric coating will deteriorate with the immersion in the salt solutions (Akbarinezhad *et al.* 2009).

The coating resistance of the coated specimens can be calculated according to the applied EEC models. Figure 5.16 displays the coating resistance of the one-ply FCSRs that were subjected to the different levels of the impacted loading, while Figure 5.17 exhibits the coating resistance of the two-ply FRP coated steel rebars with different winding angle(s) subjected to the level IV impact energy since the higher impact energy can more easily distinguish the impact resistance of two-ply FCSRs. It is clear from Figure 5.16 that the initial coating resistance would decrease with impact levels as the coating resistance decreased from $10^{11} \Omega$ to $10^6 \Omega$. After being impacted with the level IV loading energy, the specimen with a winding angle combination of $+86.5^\circ/+86.5^\circ$ exhibited the lowest coating resistance of around $10^7 \Omega$, followed by specimens with $+86.5^\circ/-86.5^\circ$, $-86.5^\circ/-86.5^\circ$ winding angle(s), and the specimens with $-86.5^\circ/+86.5^\circ$ winding angle(s) showed the highest coating

resistance of around $10^9 \Omega$, the results again proved that the specimen with a winding angle combination of $-86.5^\circ/+86.5^\circ$ possesses the highest impact resistance.

5.4 CONCLUSIONS

In this chapter, ten groups of specimens were meticulously prepared and tested to evaluate the impact resistance of FRP-coated steel rebars (FCSRs). The research parameters included the number of fibre plies and the fibre winding angle(s). Apart from the conventional impact damage assessment methods, a novel method that indirectly quantifies impact-induced coating damage by testing the post-impact electrochemical behaviour of coated steel rebars was developed and utilised. The test results and discussions presented in this chapter enable the following conclusions to be drawn:

- (1) FCSRs possess better impact resistance than epoxy-coated steel rebars (ECSRs).
- (2) An FRP coating layer is much superior to an epoxy coating layer in terms of impact resistance and peel resistance during the construction process.
- (3) The impact resistance of an FRP coating improves with the increasing number of fibre plies.
- (4) The fibre angle combination of an FRP coating significantly affects its impact resistance as fibres crossing instead of along the direction of steel ribs can provide a higher impact resistance for the FRP coating layer.
- (5) By measuring the post-impact electrochemical behaviour of coated steel rebars, the impact-induced coating damage was indirectly quantified.

The novel method is an alternative to the existing visual inspection-based impact damage assessment methods for coated steel rebars.

However, it should be noted that the quantitative relationship between the impact resistance and both winding angle(s) and the number of fibre plies in the FRP coating layer needs further investigation. Moreover, the influence of different types of damage on the corrosion resistance of FCSRs is worth to be studied.

5.5 REFERENCES

Akbarinezhad, E., Bahremandi, M., Faridi, H.R. and Rezaei, F. (2009). “Another approach for ranking and evaluating organic paint coatings via electrochemical impedance spectroscopy”, *Corrosion Science*, Vol. 51, No. 2, pp. 356-363.

ASTM (2019a). *ASTM A775/A775M*. Standard Specification for Epoxy-Coated Steel Reinforcing Bars, American Society for Testing and Materials, West Conshohocken, Pennsylvania, USA.

ASTM (2019b). *ASTM A934/A934M*. Standard Specification for Epoxy-Coated Prefabricated Steel Reinforcing Bars, American Society for Testing and Materials, West Conshohocken, Pennsylvania, USA.

ASTM (2020). *ASTM D7136/D7136M*. Standard Test Method for measuring the Damage Resistance of a Fiber-Reinforced Polymer Matrix Composite to a Drop-Weight Impact Event, American Society for Testing and Materials, West Conshohocken, Pennsylvania, USA.

- Caldona, E.B., Smith, D.W. and Wipf, D.O. (2020). “Surface electroanalytical approaches to organic polymeric coatings”, *Polymer International*, Vol. 70, No. 7, pp. 927-937.
- Cantwell, W.J. and Morton, J. (1991). “The impact resistance of composite materials—a review”, *Composites*, Vol. 22, No. 5, pp. 347-362.
- Castro, Y., Ferrari, B., Moreno, R. and Durán, A. (2005). “Corrosion behaviour of silica hybrid coatings produced from basic catalysed particulate sols by dipping and EPD”, *Surface and Coatings Technology*, Vol. 191, No. 2-3, pp. 228-235.
- Chen, S., Wang, X., Zhu, G., Lu, Z., Zhang, Y., Zhao, X. and Hou, B. (2021). “Developing multi-wall carbon nanotubes/Fusion-bonded epoxy powder nanocomposite coatings with superior anti-corrosion and mechanical properties”, *Colloids and Surfaces A: Physicochemical and Engineering Aspects*, Vol. 628, No. 127309.
- Chinnarasu, A. and Ramajeyathilagam, K. (2023). “Numerical study on influence of target thickness on impact response of GFRP composites”, *Materials Today: Proceedings*, Vol. pp.
- Kinloch, A.J., Kodokian, G.A. and Jamarani, M.B. (1987). “Impact properties of epoxy polymers”, *Journal of Materials Science*, Vol. 22, pp. 4111-4120.
- Kouhi, M., Mohebbi, A. and Mirzaei, M. (2012). “Evaluation of the corrosion inhibition effect of micro/nanocapsulated polymeric coatings: a comparative study by use of EIS and Tafel experiments and the area under the Bode plot”, *Research on Chemical Intermediates*, Vol. 39, No. 5, pp. 2049-2062.

- Li, G., Pang, S.-S., Helms, J.E. and Ibekwe, S.I. (2000). “Low velocity impact response of GFRP laminates subjected to cycling moistures”, *Polymer Composites*, Vol. 21, No. 5, pp. 686-695.
- Mahdavian, M. and Attar, M.M. (2006). “Another approach in analysis of paint coatings with EIS measurement: Phase angle at high frequencies”, *Corrosion Science*, Vol. 48, No. 12, pp. 4152-4157.
- Meola, C. and Carlomagno, G.M. (2010). “Impact damage in GFRP: New insights with infrared thermography”, *Composites Part A: Applied Science and Manufacturing*, Vol. 41, No. 12, pp. 1839-1847.
- Miao, J., Shen, Y., Tao, J., Zeng, X., Liu, S. and Wang, Z. (2023). “Design and spraying-preparation of the gradient coatings with various diameters and contents of SiO₂ nano-particles for the enhanced anti-impact and thermal insulation performance”, *Progress in Organic Coatings*, Vol. 179, No. 107491.
- Morton, J. and Godwin, E.W. (1989). “Impact response of tough carbon fibre composites”, *Composite Structures*, Vol. 1, No. 1, pp. 1-19.
- Muhi, R.J., Najim, F. and de Moura, M.F.S.F. (2009). “The effect of hybridization on the GFRP behavior under high velocity impact”, *Composites Part B: Engineering*, Vol. 40, No. 8, pp. 798-803.
- Panciroli, R. and Giannini, O. (2021). “Comparing the impact resistance of flax/epoxy and glass/epoxy composites through experiments and numerical simulations”, *Composite Structures*, Vol. 264, No. 113750.

- Rousseau, J., Perreux, D. and Verdiere, N. (1999). “The influence of winding patterns on the damage behaviour of filament-wound pipes”, *Composites Science and Technology*, Vol. 59, No. 9, pp. 1439-1449.
- Tang, F., Chen, G. and Brow, R.K. (2016). “Chloride-induced corrosion mechanism and rate of enamel- and epoxy-coated deformed steel bars embedded in mortar”, *Cement and Concrete Research*, Vol. 82, pp. 58-73.
- Ye, Y., Chen, H., Wu, J. and Ye, L. (2007). “High impact strength epoxy nanocomposites with natural nanotubes”, *Polymer*, Vol. 48, No. 21, pp. 6426-6433.

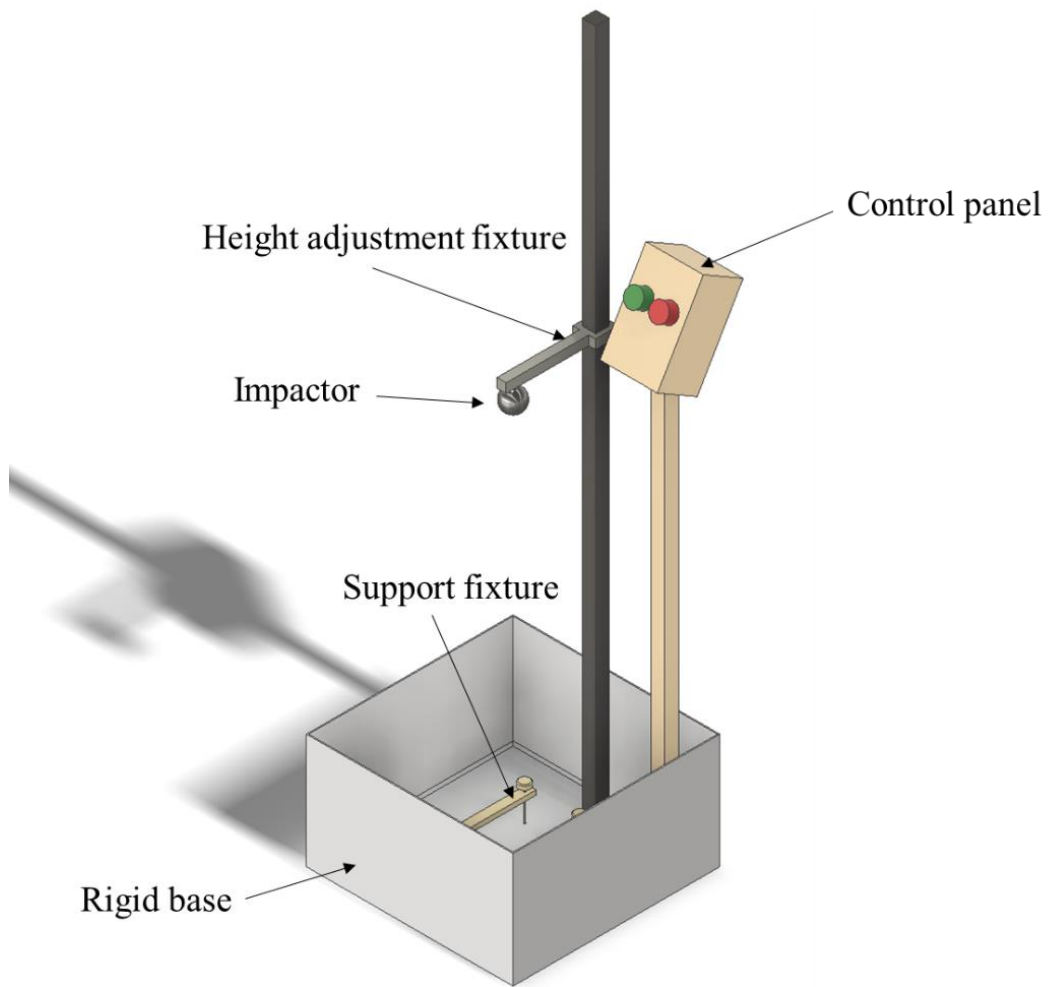


Figure 5.1 Facility used to induce impact damage

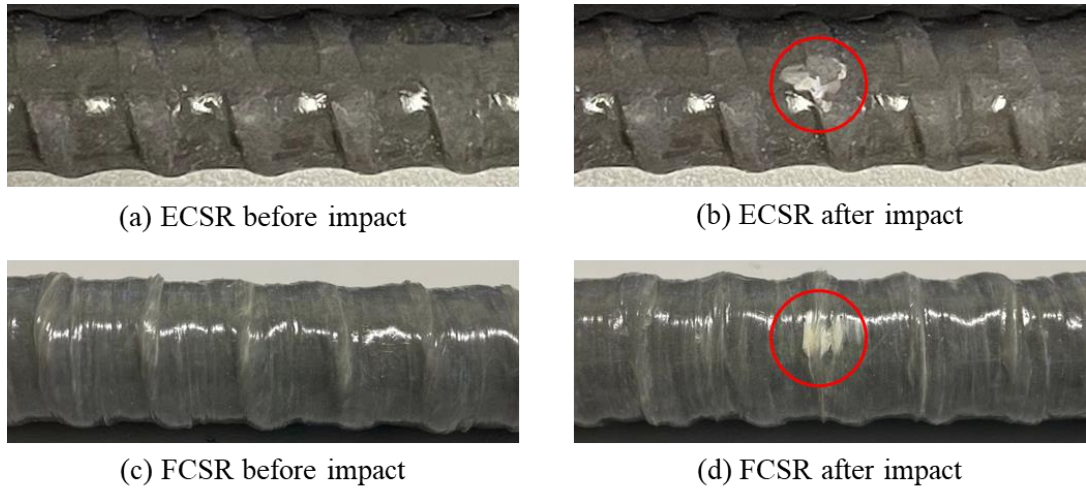


Figure 5.2 Comparison of coated steel rebars before and after impact

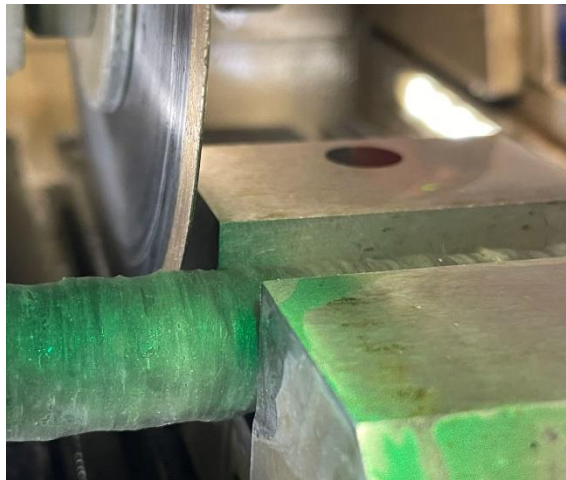


Figure 5.3 Cutting a rebar for SEM observation



Figure 5.4 Cold mounting of specimens in a plastic mould



Figure 5.5 Polishing the observation surface of cold-mounted specimens

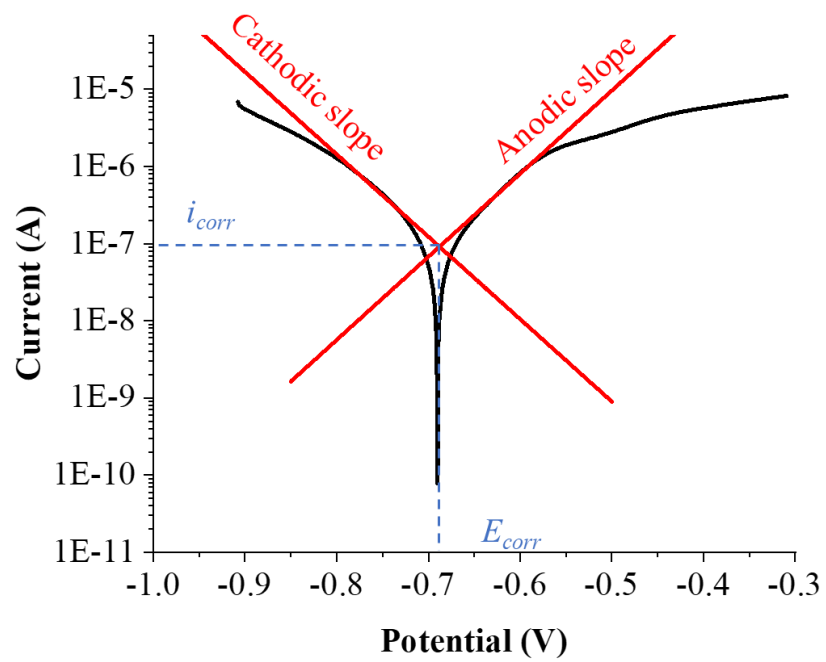
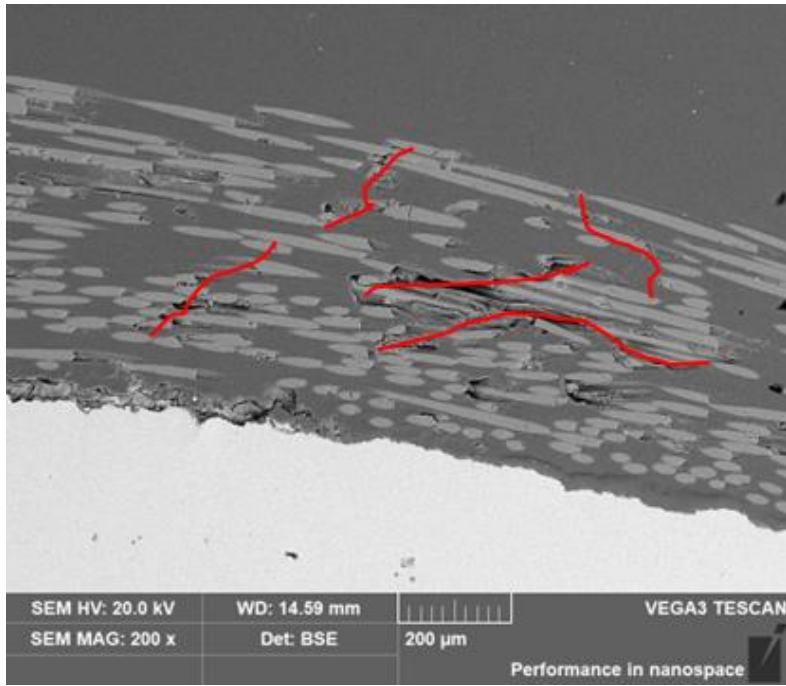
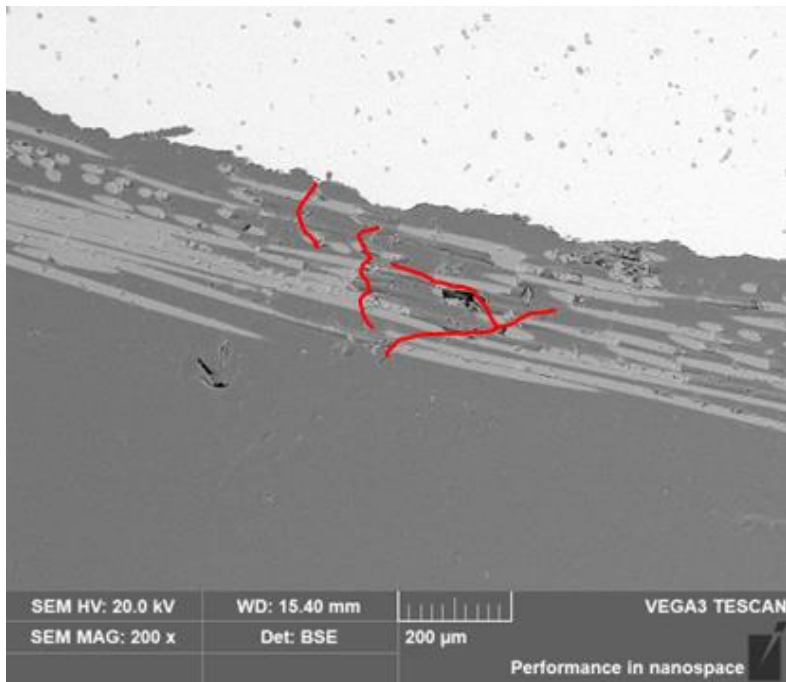


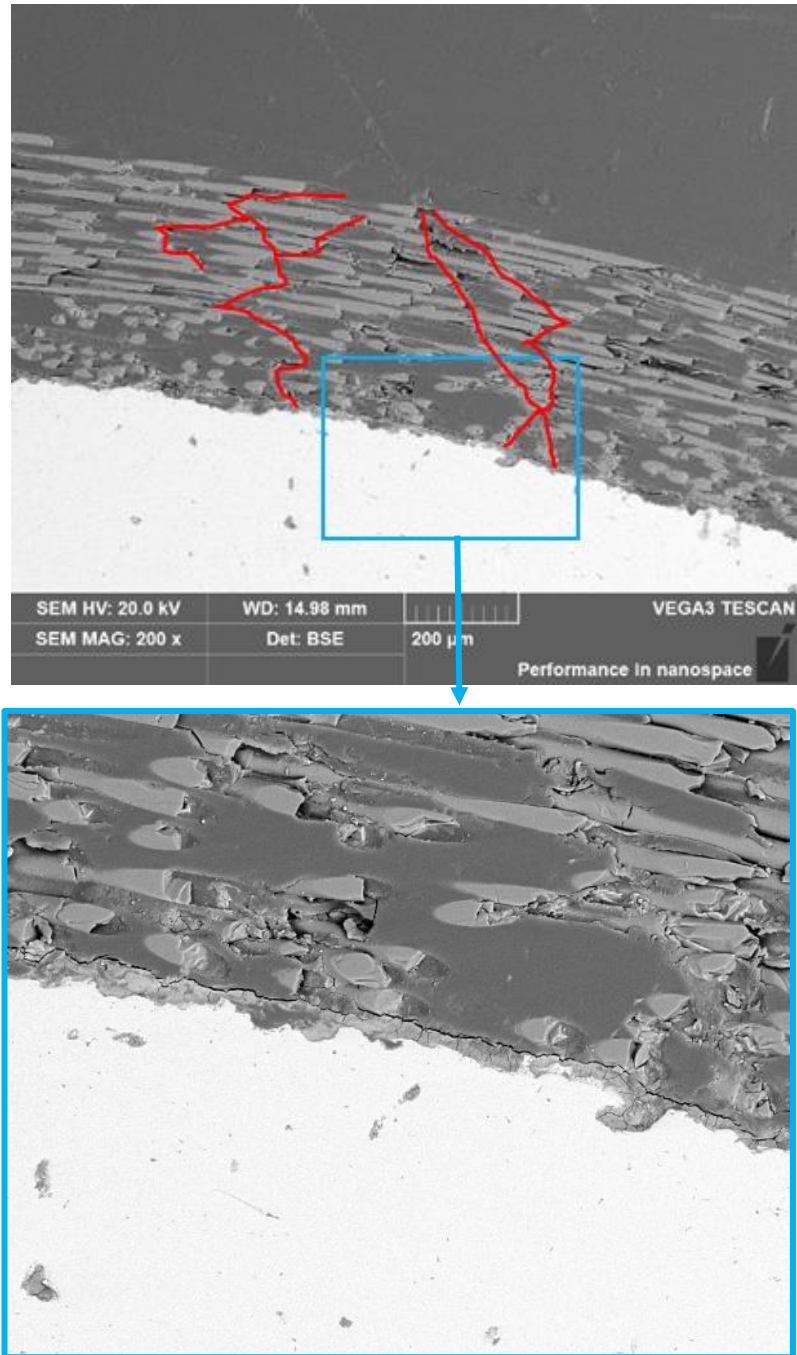
Figure 5.6 Typical Tafel curve for potentiodynamic analysis



(a) Level-I impact

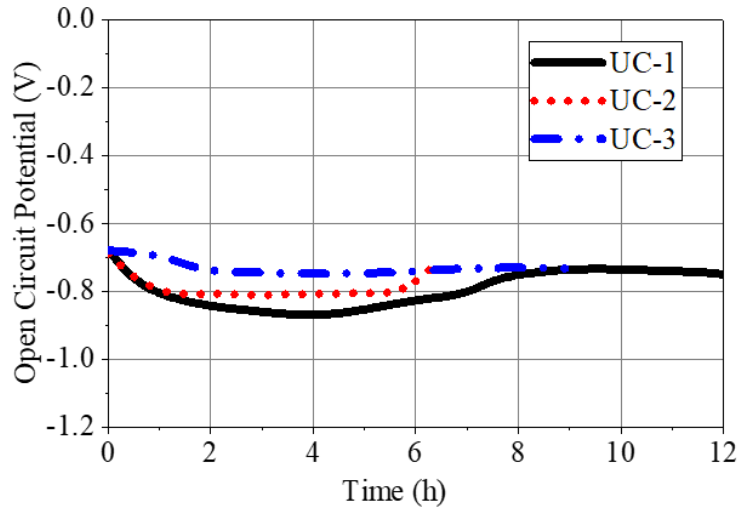


(b) Level-II impact

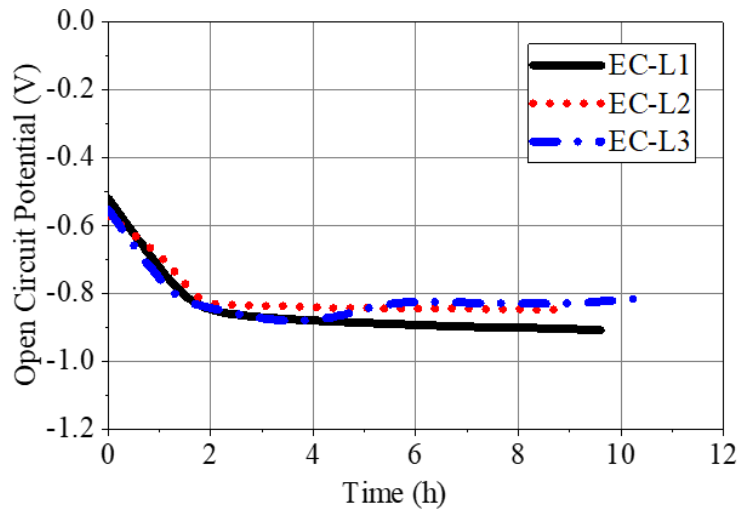


(c) Level-III impact

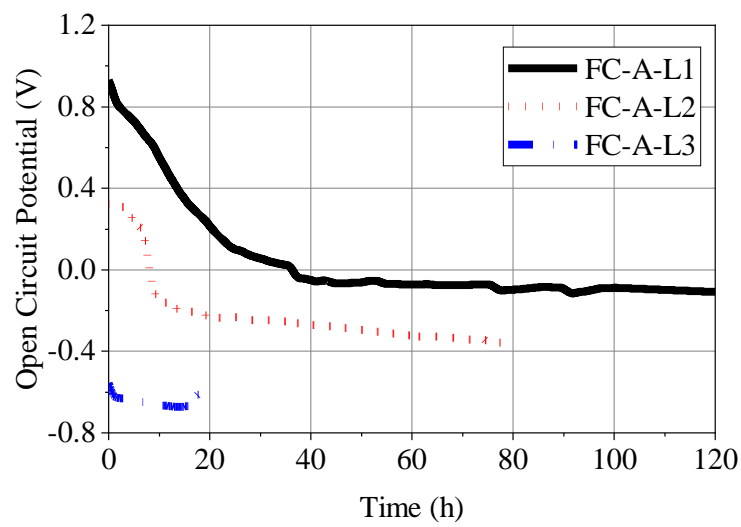
Figure 5.7 Microstructures of FCSRs impacted with different levels of energy.



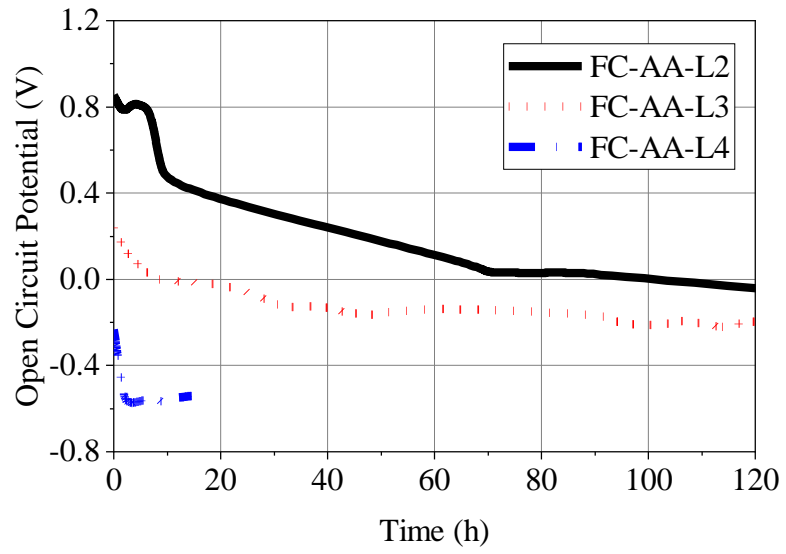
(a) Uncoated steel rebars



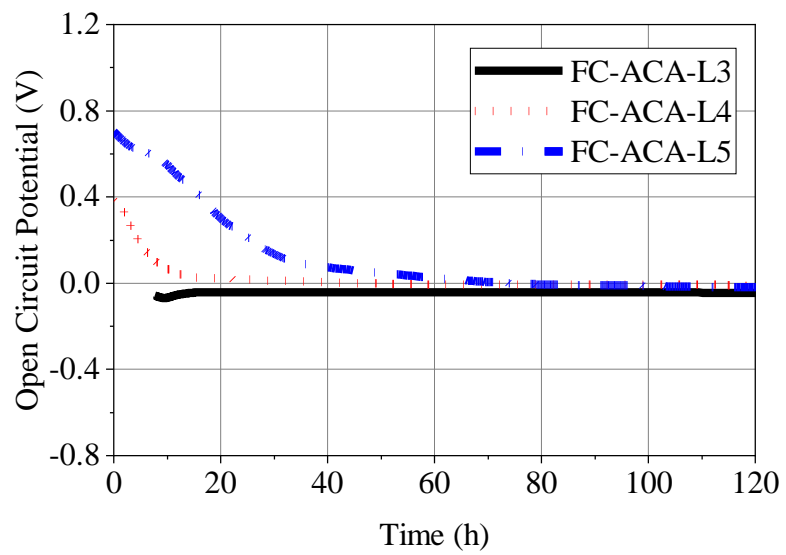
(b) Epoxy-coated steel rebars



(c) One-ply FRP-coated steel rebars

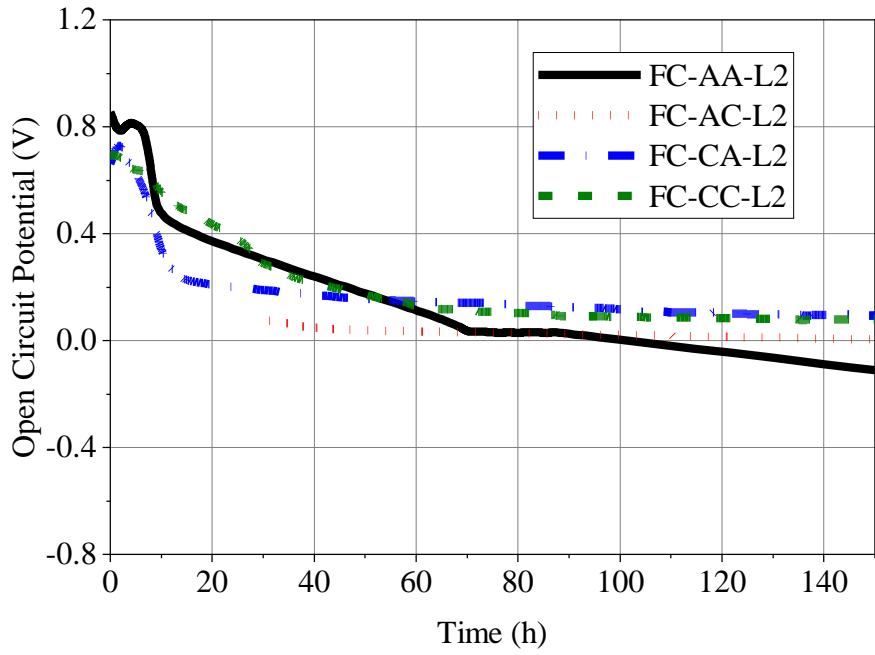


(d) Two-ply FRP-coated steel rebars

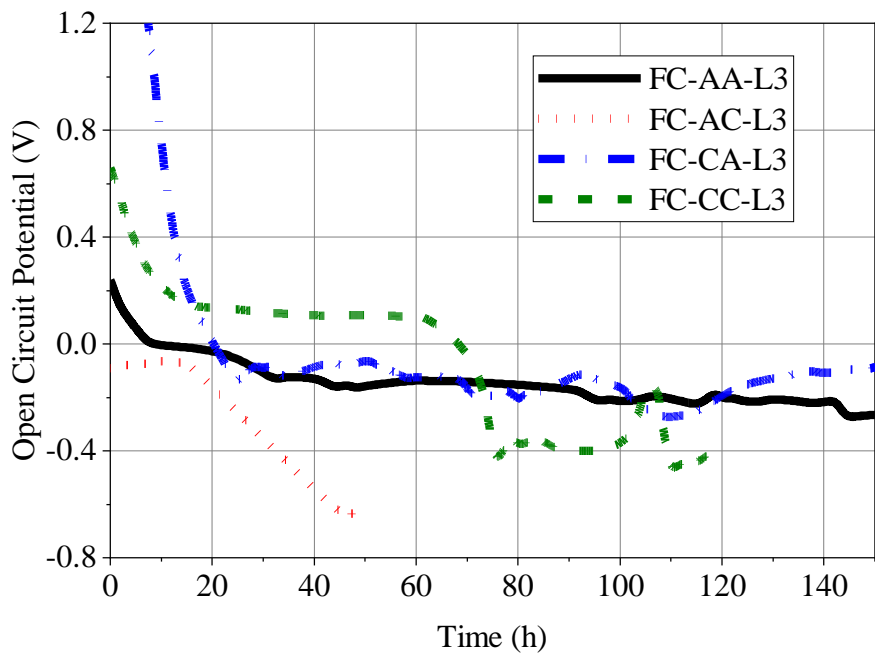


(e) Three-ply FRP-coated steel rebars

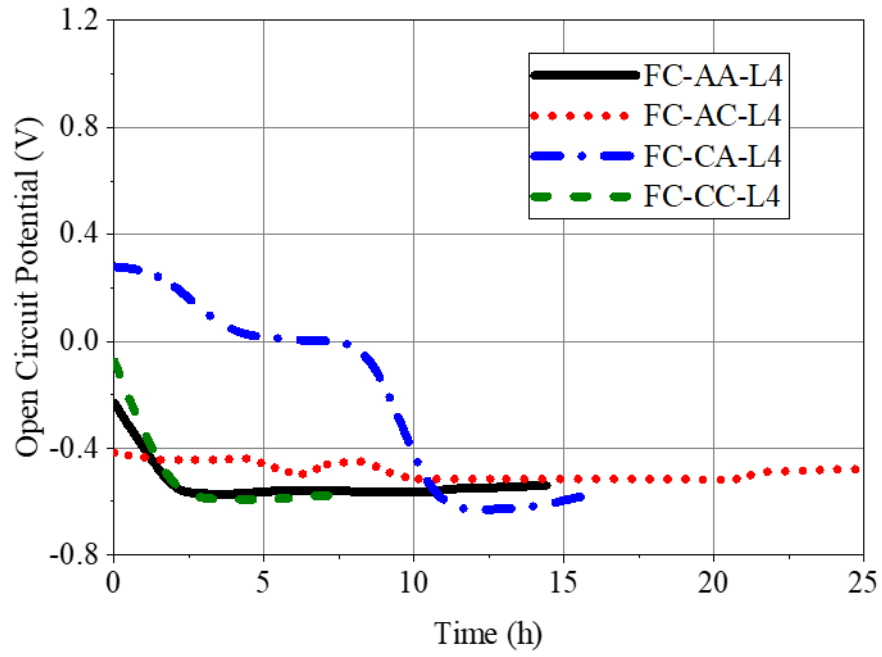
Figure 5.8 OCP values of specimens with different numbers of fibre plies after impact with different levels of energy



(a) Level 2: L2=6.7 J

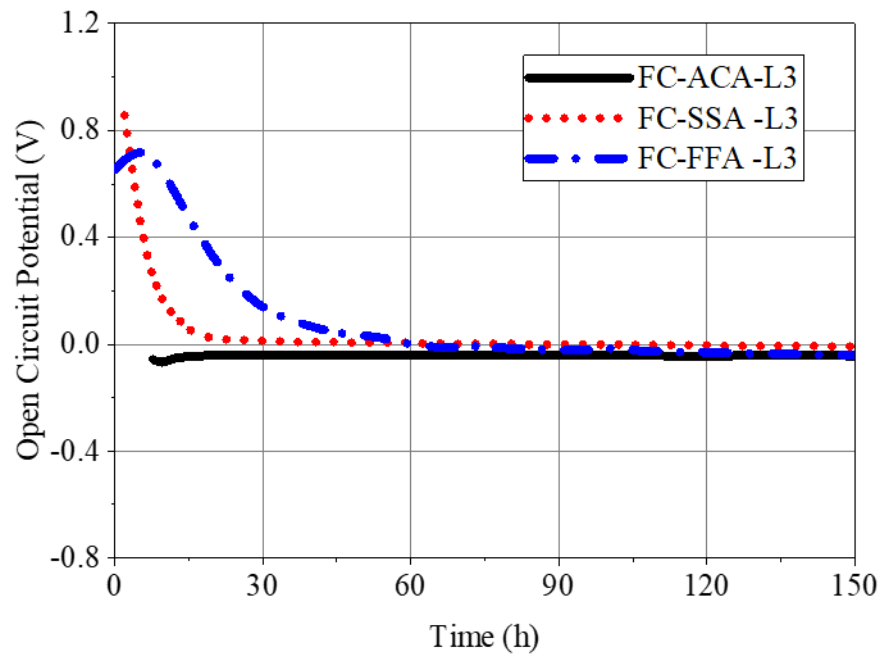


(b) Level 3: L3 = 10.7 J

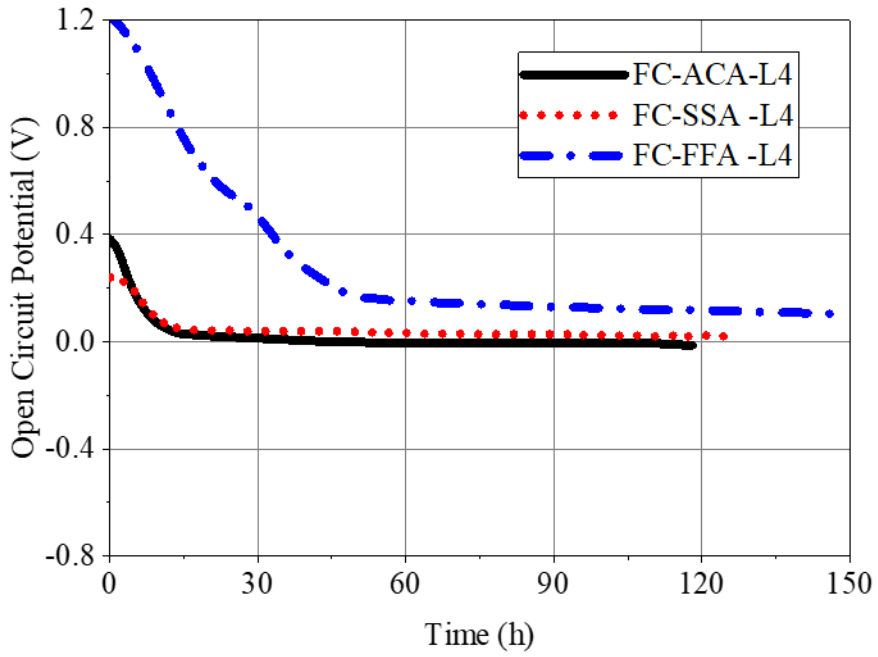


(c) Level 4: L4 =17.1 J

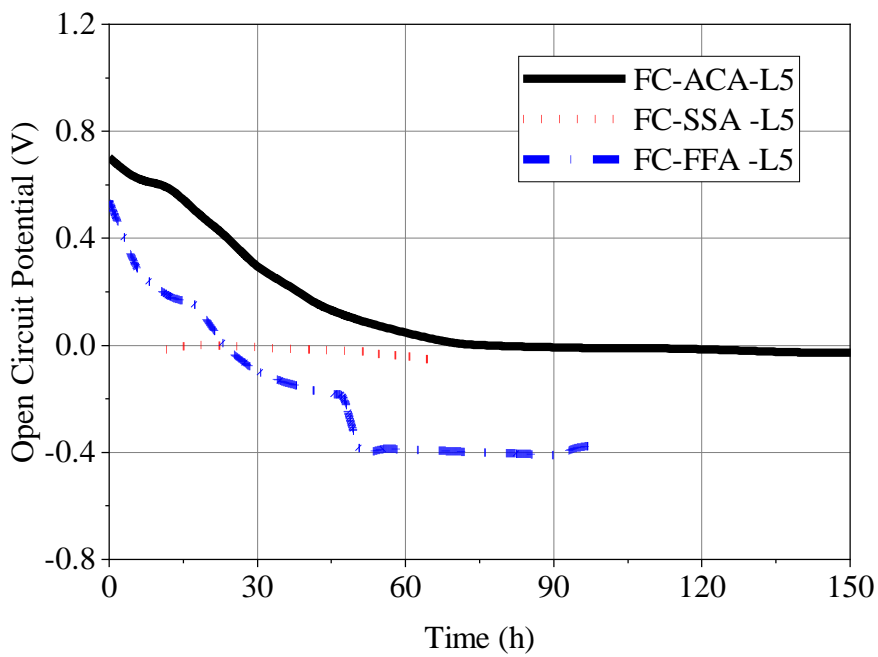
Figure 5.9 OCP values of two-ply FCSRs with different winding angle(s) after impact with different levels of energy



(a) Level 3: L3=10.7 J

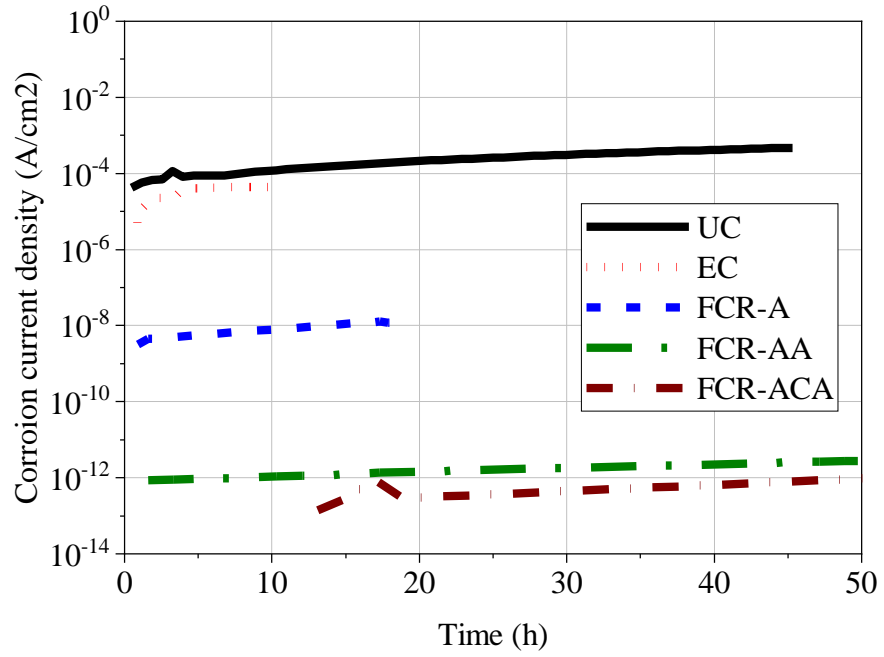


(b) Level 4: L4=17.1 J

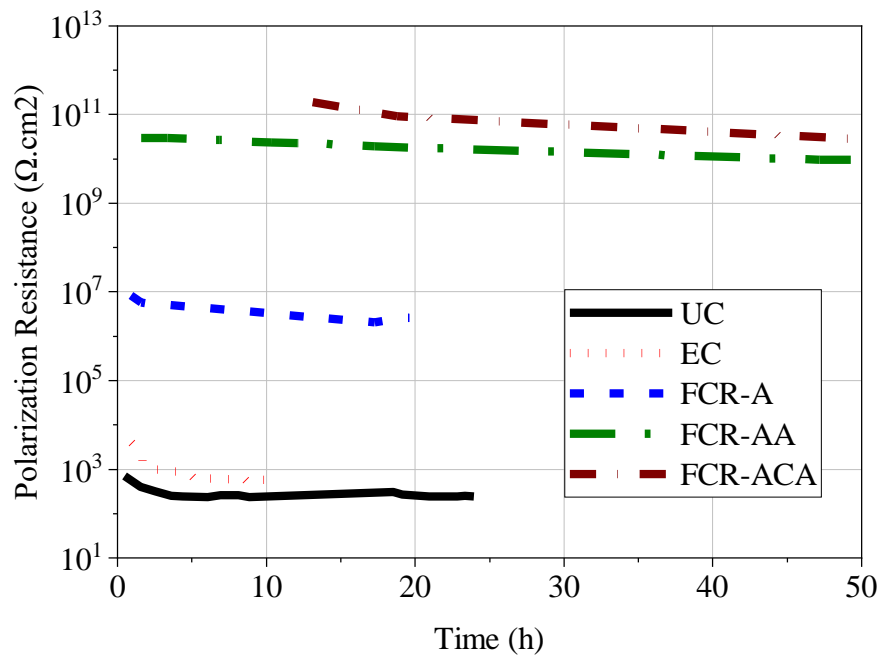


(c) Level 5: L5=27.4 J

Figure 5.10 OCP values of three-ply FCSRs with different winding angle(s) after impact with different levels of energy

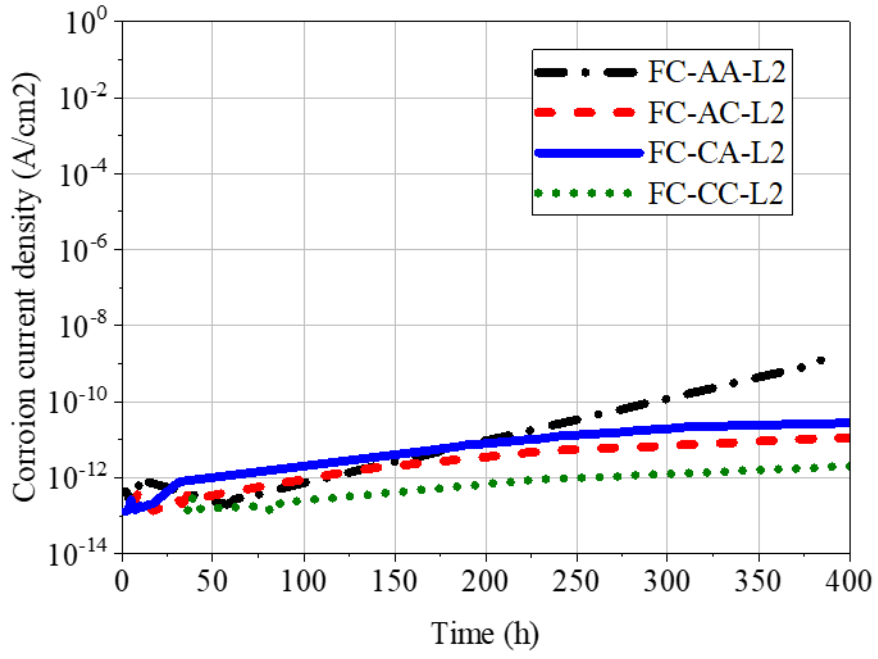


(a) Corrosion current density (i_{corr})

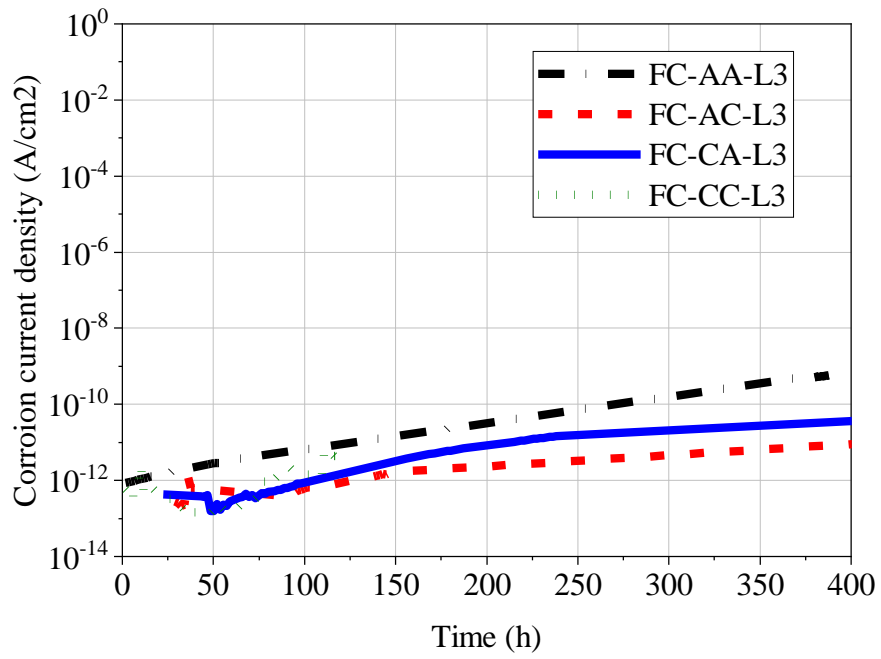


(b) Polarisation resistance (R_p)

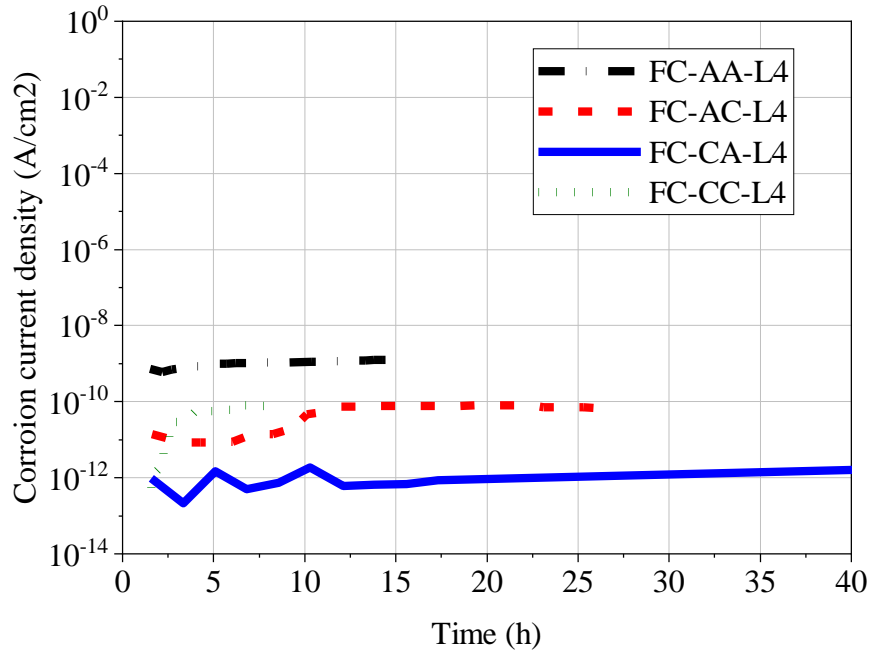
Figure 5.11 Evolutions of the corrosion current density and polarisation resistance of different types of steel rebars after impact with energy of 10.7 J



(a) Level 2: L2=6.7 J

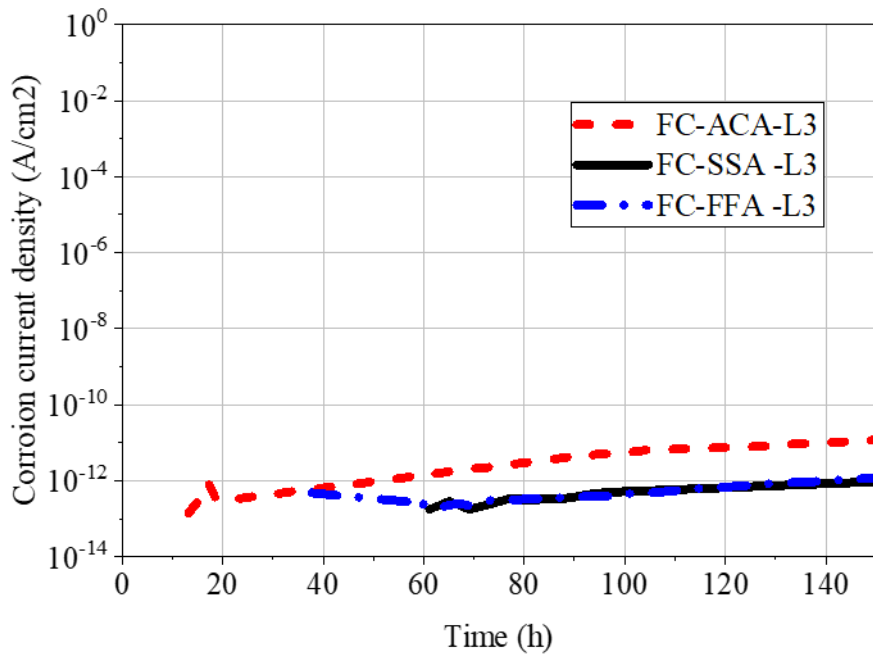


(b) Level 3: L3=10.7J

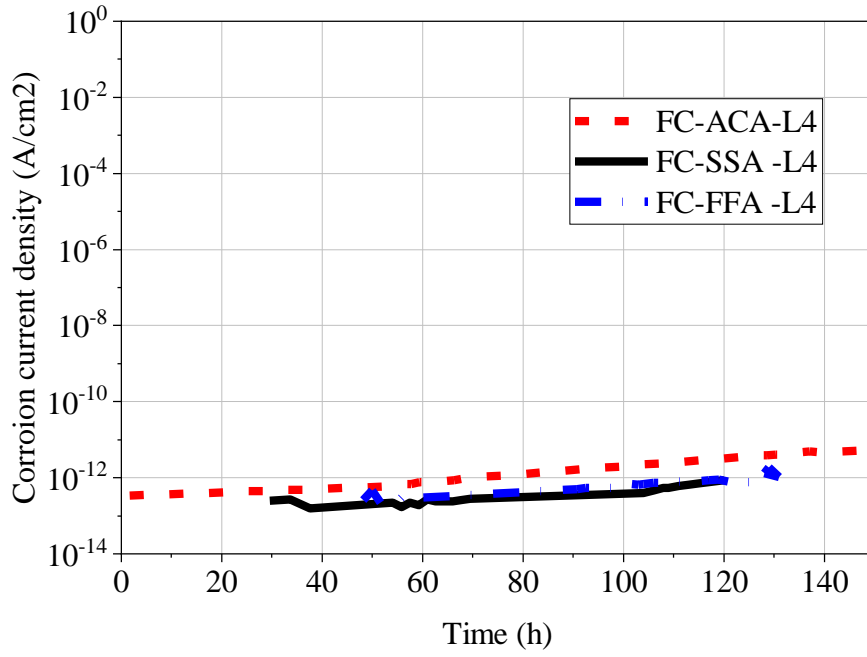


(c) Level 4: L4=17.1 J

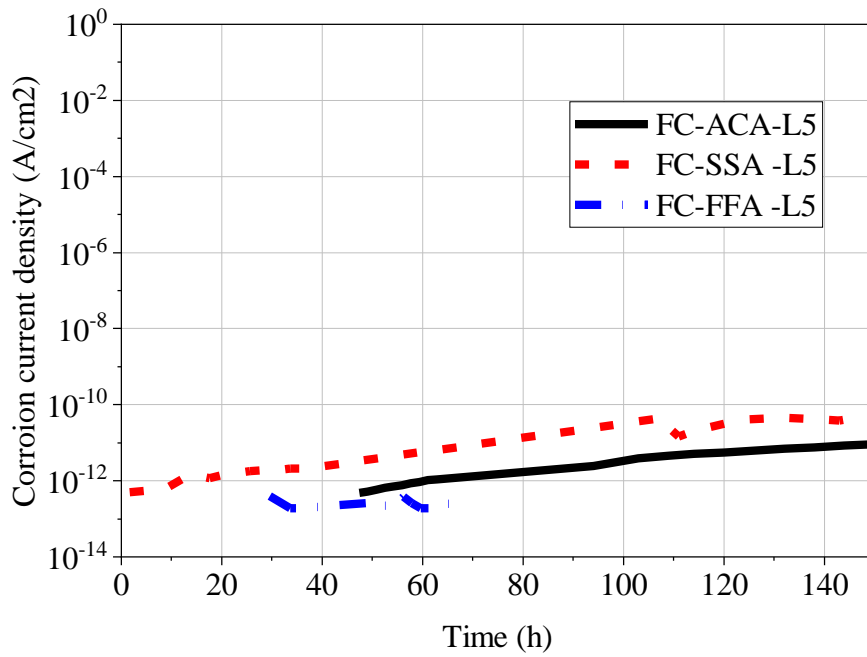
Figure 5.12 Corrosion current density (i_{corr}) evolutions of FCSRs with two fibre plies of different winding angle combinations after impact with different levels of energy



(a) Level 3: L3=10.7 J

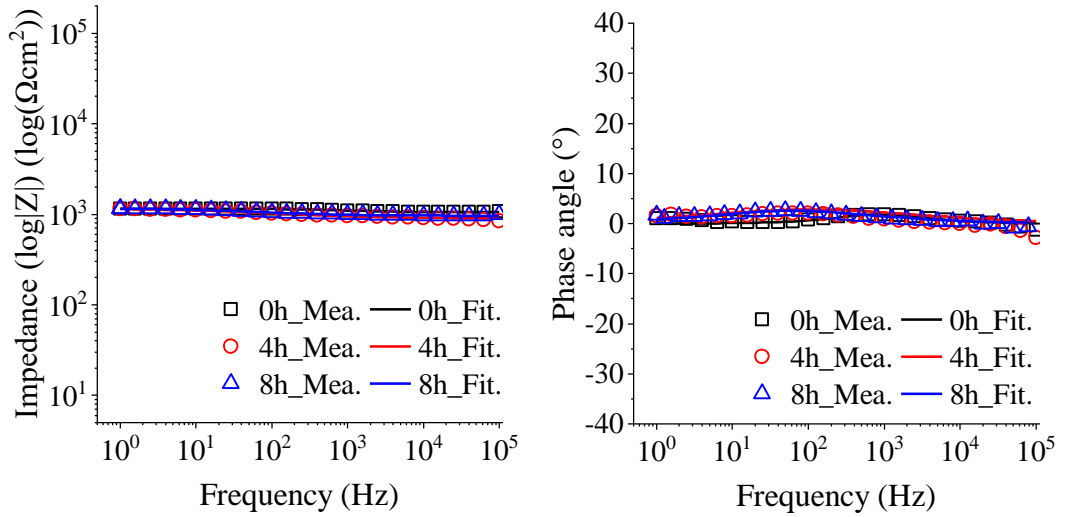


(b) Level 4: L4=17.1 J

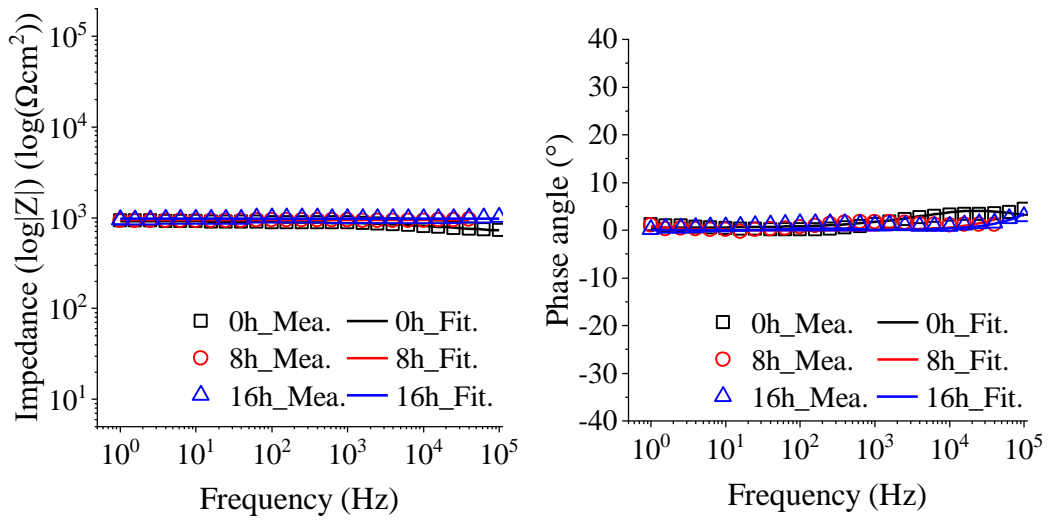


(c) Level 5: L5=27.4 J

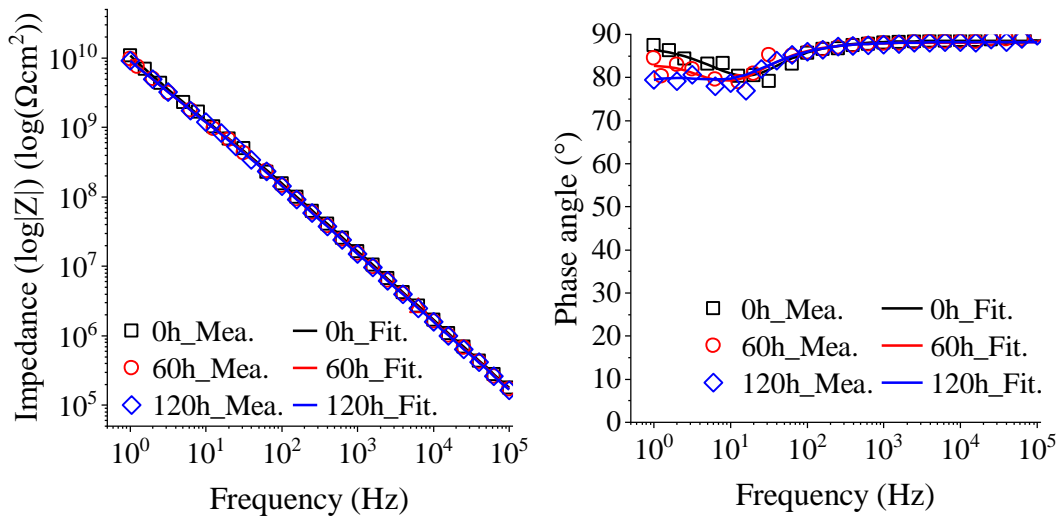
Figure 5.13 Corrosion current density (i_{corr}) evolutions of three-ply FCSRs with different winding angle combinations after impact with different levels of energy



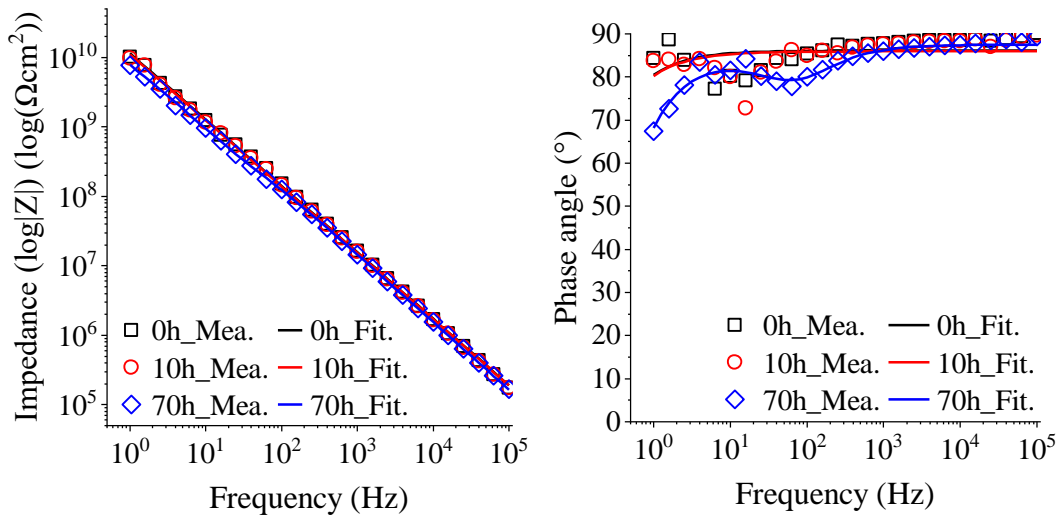
(a) Uncoated steel rebars (UCSRs)



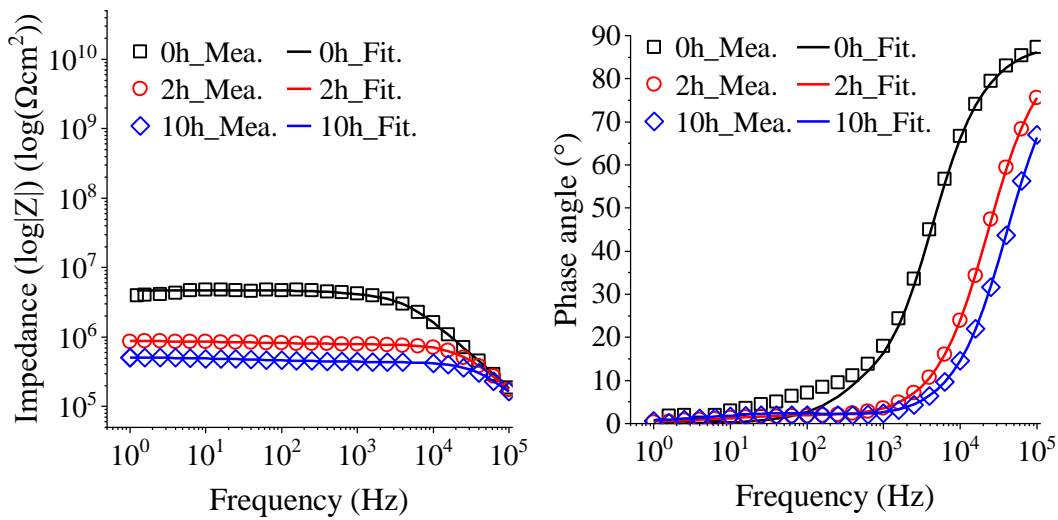
(b) ECSRs after impact with energy of 2.8 J



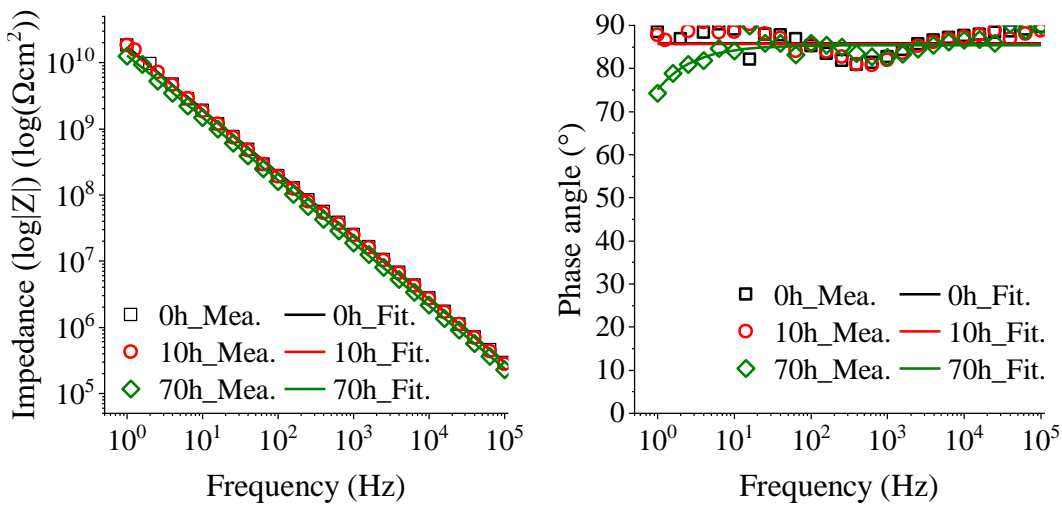
(c) One-ply FCSRs after impact with energy of 2.8 J



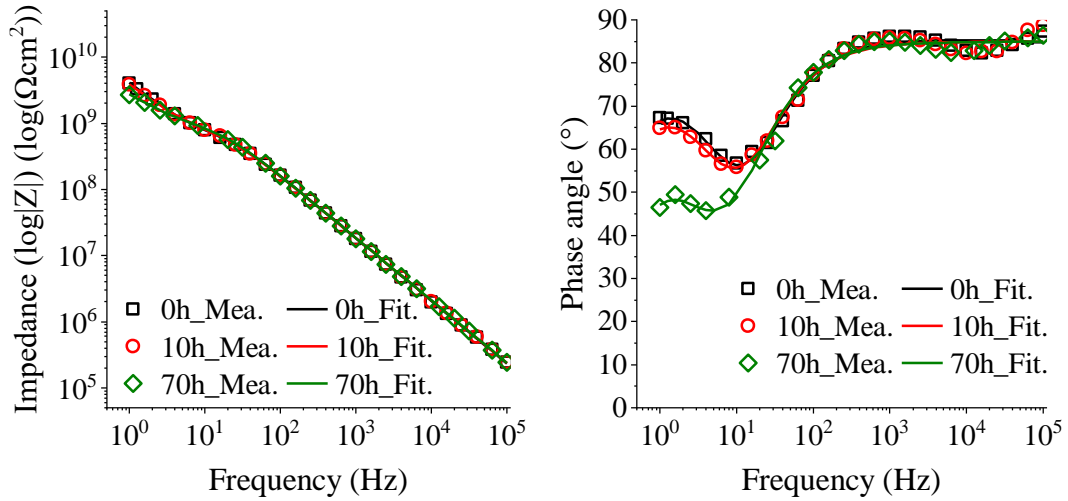
(d) One-ply FCSRs after impact with energy of 6.7 J



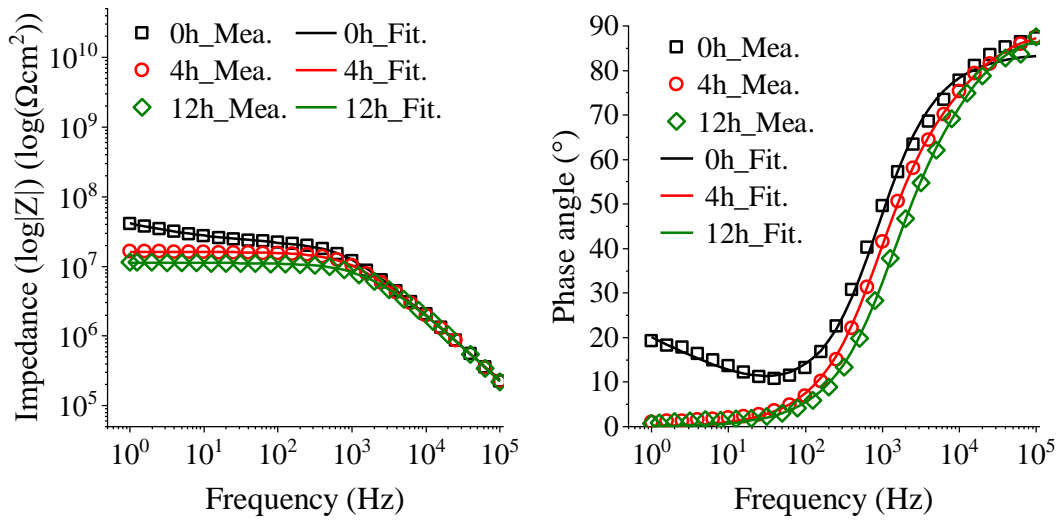
(e) One-ply FCSRs after impact with energy of 10.7 J



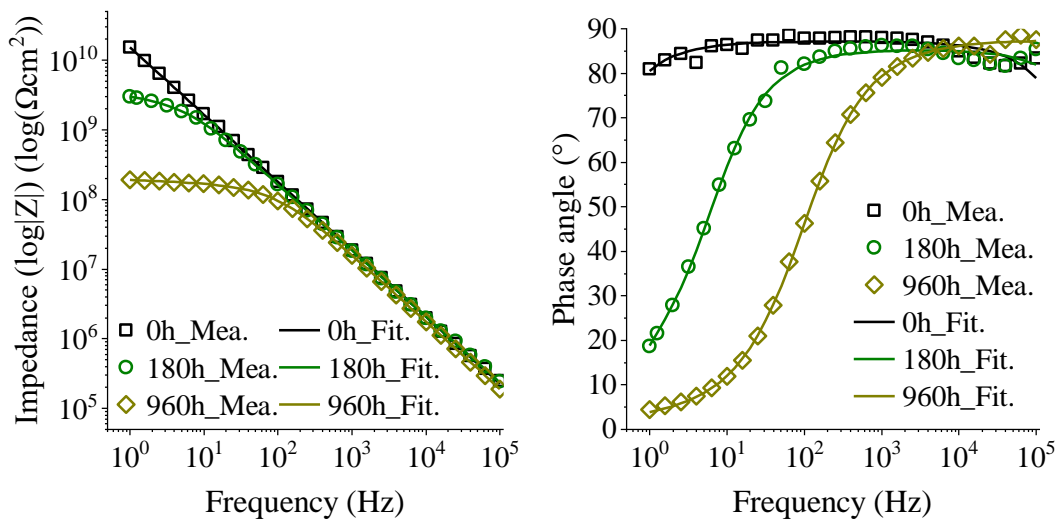
(f) Two-ply (+86.5° / +86.5°) FCSRs after impact with energy of 6.7 J



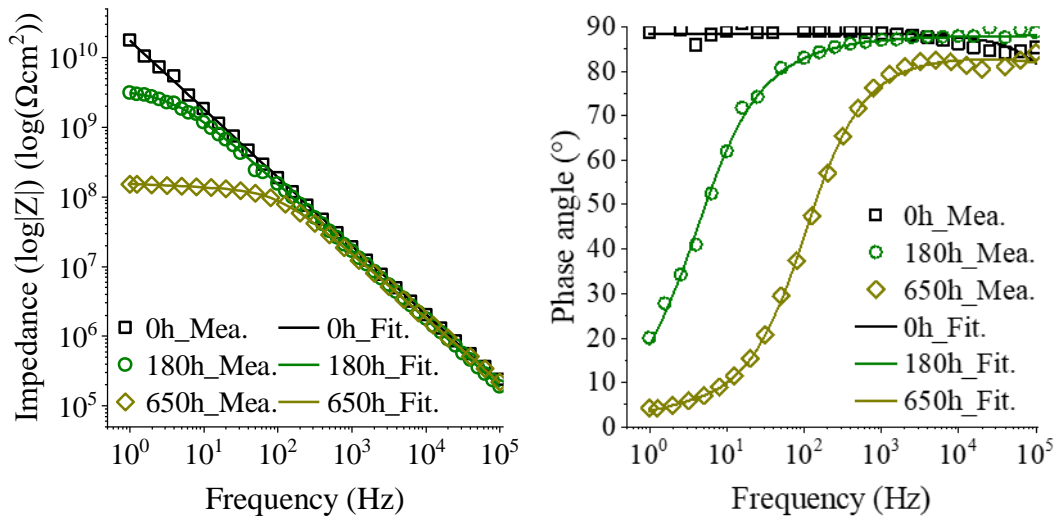
(g) Two-ply ($+86.5^\circ / +86.5^\circ$) FCSRs after impact with energy of 10.7 J



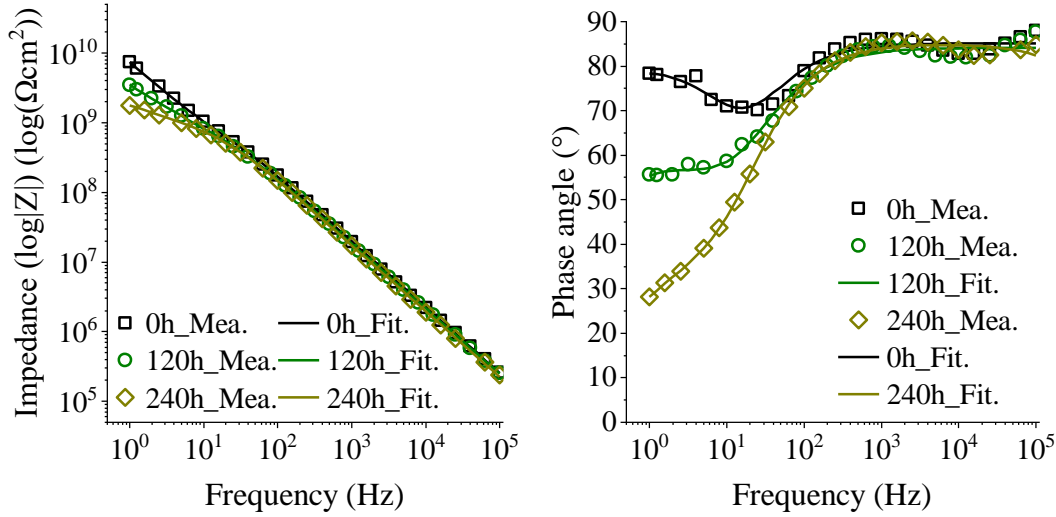
(h) Two-ply ($+86.5^\circ / +86.5^\circ$) FCSRs after impact with energy of 17.1 J



(i) Two-ply ($-86.5^\circ / +86.5^\circ$) FCSRs after impact with energy of 6.7 J

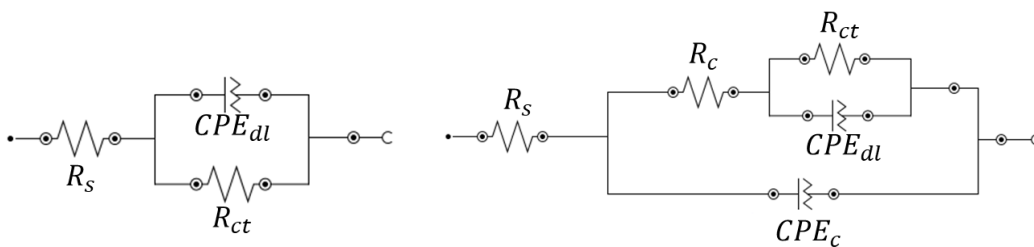


(j) Two-ply (-86.5° / +86.5°) FCSRs after impact with energy of 10.1 J



(k) Two-ply (-86.5° / +86.5°) FCSRs after impact with energy of 17.1 J

Figure 5.14 Bode plots of different groups of impacted specimens after being immersed in NaCl solution for different periods



(a) Uncoated steel rebars

(b) Epoxy-coated and FRP-coated steel rebars

Figure 5.15 Equivalent electrical circuit (EEC) models for different types of steel rebars

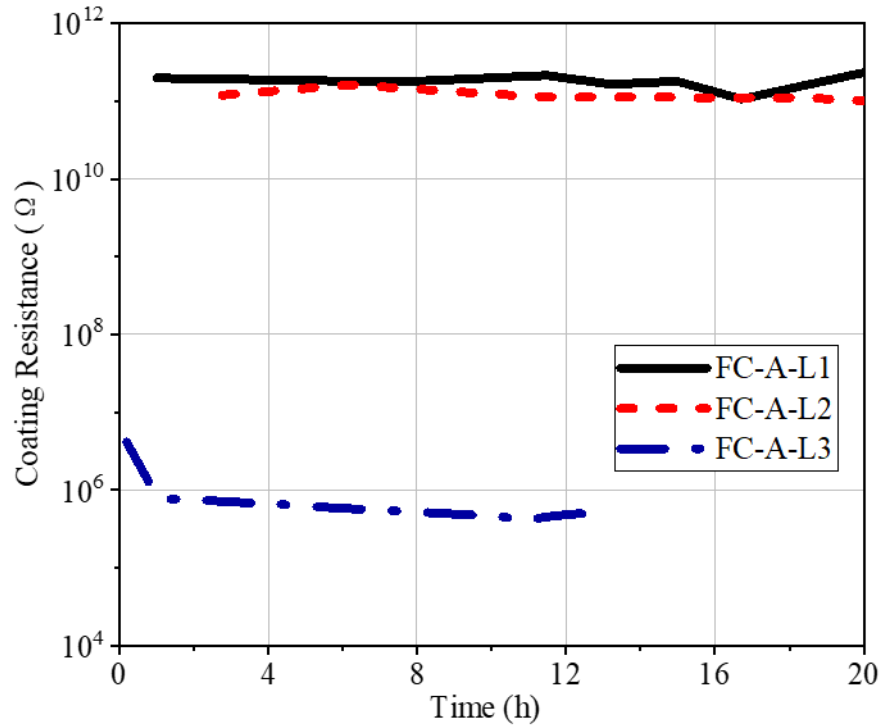


Figure 5.16 Resistance of coating layer after impact with different levels of energy
(L1=2.8 J; L2=6.7 J; L3=10.7 J)

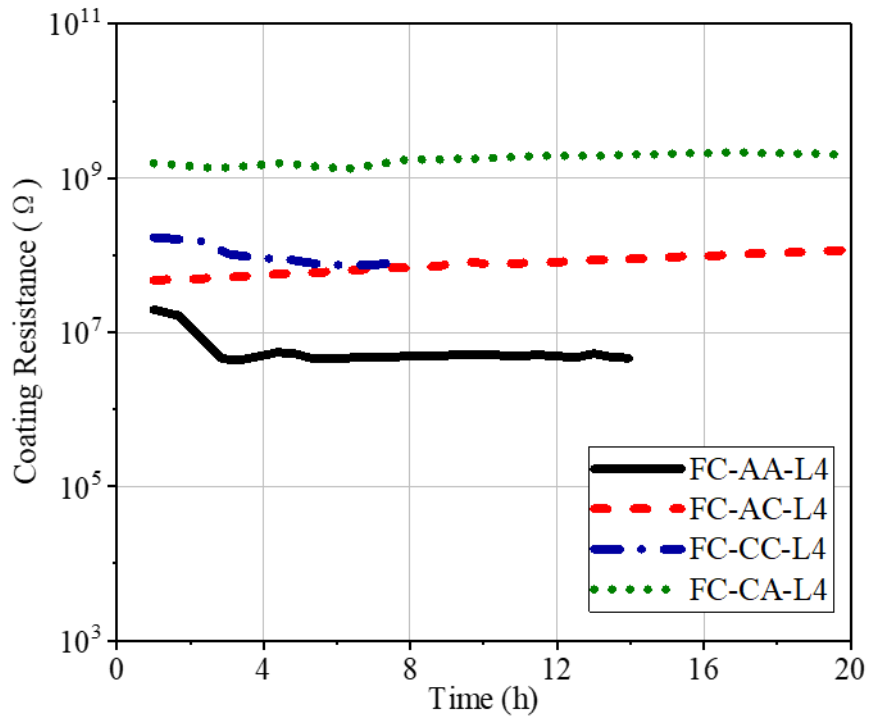


Figure 5.17 Coating resistance of two-ply FCSRs with different winding angle(s) after impact with energy of 17.1 J

Table 5.1 Mechanical properties of core steel rebars

Grade	Diameter	Yield stress	Tensile strength
PSB830	15 mm	996 MPa	1120 MPa

Table 5.2 Mechanical properties of epoxy resin

Tensile strength	Tensile modulus	Fracture strain	Glass transition temperature
79 MPa	2900 MPa	4.5%	120 °C

Table 5.3 Mechanical properties of glass fibre filaments

Glass type	Sizing agent	Fibre diameter	Linear density	Tensile strength
ECR-Glass	Silane	17 to 22 μm	1200 tex	≥ 0.3 N/Tex

Table 5.4 Impact energy levels for different types of steel rebars

Rebar type	Energy level I	Energy level II	Energy level III	Energy level IV	Energy level V
ECSR	2.8J	6.7J	10.7J	-	-
One-ply FCSR	2.8J	6.7J	10.7J	-	-
Two-ply FCSR	-	6.7J	10.7J	17.1J	-
Three-ply FCSR	-	-	10.7J	17.1J	27.4 J

Note:

- a) "ECSR" represents epoxy-coated steel rebars;
- b) "FCSR" represents FRP-coated steel rebars.

Table 5.5 Test matrix for impact tests

Group	Coating material	Number of coating layers	Winding angle(s)
UCSR	--	--	--
ECSR	Epoxy	1	--
FCSR-A	FRP	1	+86.5°
FCSR-AA	FRP	2	+86.5° / + 86.5°
FCSR-AC	FRP	2	+86.5° / -86.5°
FCSR-CA	FRP	2	-86.5° / +86.5°
FCSR-CC	FRP	2	-86.5° / -86.5°
FCSR-FFA	FRP	3	+45°/-45° /+86.5°
FCSR-SSA	FRP	3	+60° /-60° /+86.5°
FCSR-ACA	FRP	3	+86.5°/-86.5°/+86.5°

Note:

- a) “UCSR” represents uncoated steel rebars;
- b) “ECSR” represents epoxy-coated steel rebars;
- c) “FCSR” represents FRP-coated steel rebars;
- d) The letter(s) following “-” represents the winding angle(s) of the fibre plies in the FRP coating layer, for example:
 - i) “A” represents one layer of fibre ply with a winding angle of +86.5°;
 - ii) “C” represents one layer of fibre ply with a winding angle of -86.5°;
 - iii) “FFA” represents three layers of fibre plies with winding angles of +45°/-45°/+86.5°;
 - iv) “SSA” represents three layers of fibre plies with winding angles of +60° /-60° /+86.5°.

CHAPTER 6

BOND PERFORMANCE OF FRP-COATED STEEL REBARS IN CONCRETE

6.1 INTRODUCTION

This chapter presents an experimental study on the bond performance of FRP-coated steel rebars (FCSRs) to concrete. The bond performance of reinforcement in concrete plays a significant role in governing the performance of reinforced-concrete (RC) structures, as sufficient bond strength ensures the stress transfer between steel rebars and concrete (Cosenza *et al.* 1995). When a novel type of steel rebar is developed, the bond performance to concrete is usually a major concern for engineers in the construction industry before practical implementation.

The bond performance of epoxy-coated steel rebars (ECSRs) to concrete has been extensively studied for decades. It has been well-acknowledged that the bond performance of ECSRs to concrete is worse than that of uncoated steel rebars (UCSRs) because the epoxy coating decreases the friction between the effective rib-bearing areas and concrete (Grundhoffer *et al.* 1992). In order to compensate for this performance gap, Chinese engineers introduce a reduction factor of 0.8 as the relative bond characteristic coefficient for estimation of the maximum crack width of reinforced concrete (RC) structures when ECSRs are used (GB50010 2015). In

addition, it has been found by Choi *et al.* (1991) that the maximum bond stress of ECSRs decreases with increasing thickness once the thickness exceeds a certain value, which is often referred to as the allowable maximum coating thickness for ECSRs. For example, Miller *et al.* (2003) suggested the maximum allowable coating thickness to be 420 μm for rebars with a diameter larger than 19 mm.

As a novel type of corrosion-resistant steel rebars, FRP-coated steel rebars (FCSRs) have been found to have outstanding durability and corrosion resistance in previous chapters. However, as the thicknesses of FCSRs are in the range of 500 μm to 1500 μm , which are far beyond the thickness range of ECSRs (i.e., 175 to 300 μm), the bond performance of FCSRs to concrete is not clear. The study presented in this chapter therefore focused on the bond performance of FCSRs to concrete. A total of 48 pull-out specimens were cast and tested. The influence of winding configurations, i.e., the number and the winding angle(s) of fibre plies in the FRP coating layer and the rib patterns of the core steel rebar, on the bond performance of FCSRs to concrete were investigated and compared with those of USRs and ECSRs.

6.2 EXPERIMENTAL PROGRAMME

6.2.1 Test Matrix

A total of 16 groups of specimens for pull-out tests were prepared and tested. The test parameters included the rib patterns of the core steel rebar and the number and the winding angle(s) of the fibre plies in the FRP coating layer. Each group had three identical specimens. A group of UCSRs and a group of ECSRs were also tested for comparison purposes. The test matrix is shown in Table 6.1.

6.2.2 Materials

(1) Steel rebars

The steel rebars used in the present study were two types of conventional steel rebars: one was a type of deformed steel rebars with crescent ribs of 14 mm in the nominal diameter conforming to GB/T 1499.2 (GB/T-1499.2 2018) standard; the other was a type of screw-thread steel rebars with spiral ribs and of 15 mm in the nominal diameter conforming to GB/T 20065 (GB/T 20065 2016) standard. The nominal diameters of the two types of steel rebars are close but not strictly the same because of the availability of the products in the market. The properties of the steel rebars provided by the manufacturers are shown in Table 6.2, and the steel rebars used in this experiment are displayed in Figure 6.1.

(2) Resin

The resin used in the present study was AM-8910 epoxy resin produced by Wells Advanced Materials Co., Ltd. The supplier suggested a curing procedure to achieve a near-excellent material performance, i.e., 60°C curing for 4 hours followed by 110°C curing for 3 hours. The glass transition temperature was 108°C after the curing procedure, which was measured by *Differential Scanning Calorimetry* tests following the process introduced in Chapter 3.

(3) Fibre

ECT469L-1200 glass fibre filaments provided by Chongqing Polycomp International Corp. (CPIC) with a linear density of 1200 tex were used in the present study. The properties of glass fibre filaments are displayed in Table 6.3.

(4) Concrete

The 50 MPa concrete was used to cast the pull-out specimens. Table 6.4 shows the mix proportion of utilized concrete. The compressive strength was tested using standard cylinder specimens with a dimension of " $\Phi 150 \text{ mm} \times 300 \text{ mm}$ "; all the specimens were cured in the condition of standard temperature and standard humidity for 28 days and then tested by MATEST concrete compression testing machine, as shown in Figure 6.2. Each batch contains three cylinder specimens, and the average concrete compressive strength was measured from 52.1 MPa to 59.4 MPa for the 1st to 4th batch of the specimens.

6.2.3 Specimen Preparation

All FCSRs were manufactured following a production process, which has been introduced in Chapter 3 of this thesis.

Since it is the FRP coating layer that makes direct contact with the concrete, the pull-out tests were performed in reference to ASTM D7913 (ASTM 2020), a standard test method for the bond strength of FRP rebars to concrete. As shown in Figure 6.3, the size of the concrete cubic was 150 mm^3 , and the embedded length of the specimens was four times the rebar diameter. The wood framework with two drilled holes in the middle of two sides was used to cast pull-out specimens. The PVC tube was fixed in

the framework in the unbound zone to ensure the bond length of the steel rebars. The rubber tape was bound onto the rebar at the PVC tube sections to fill the gap between rebars and PVC tubes and thus prevent the outflow of slurry concrete. The 6 mm diameter steel cages were put in the middle of the concrete specimens as stirrups to enhance the crack resistance of the concrete cubic, thus avoiding the splitting failure in the pull-out test. The length of the rebars was 700 mm, while half of the length was covered with coating materials for FCSRs to avoid the damages caused by gripping at the loaded end. The framework was taken apart after 24 hours of casting. The testing was conducted on the specimens after a 28-day curing period.

6.2.4 Methodology

The pull-out tests were performed in a UTM, as displayed in Figure 6.4, in conformity with ASTM D7913 (ASTM 2020). The specimen was put on a designed steel frame, and a thin layer of polytetrafluoroethylene film was inserted between the concrete block and steel plate to minimise the friction between the contact surface of the specimen and setups that would be induced during the testing.

Displacement-controlled method was employed for the tests. The loading rate was set as 1 mm/min. The displacement at the loading end was measured by three linear variable differential transformers (LVDTs), while the free-end displacement was measured by two LVDTs that were fixed on the rebars. The data logger (KYOWA UCAM-60) was used to record the load and displacement data with a frequency of 1 Hz.

The elongation of the rebars, the installation of the LVDTs at the loaded end of the pull-out specimens, and the deformation of the plastic sheet and steel frame are

factors that need to be considered in the calculation of the load-end slip. Therefore, the free-end slip, which will not be affected by the above factors, was used in the current study for analysis. The average bond strength was calculated through the following equation:

$$\tau = \frac{P}{\pi dl} \quad (6-1)$$

where P is the maximum pull-out load of the specimen, l is the embedment length of the rebars in concrete, and d is the nominal diameter of the rebars, so the thickness of the coating layer was not considered in this experiment.

Since the concrete strength was a little different from each batch of casting, the bond strength of all the pull-out specimens was normalized according to the following equation (Darwin and Graham 1993) to reduce the influence of the concrete strength on the bond strength between steel rebars and concrete:

$$\tau_n = \tau_t \times \sqrt{\frac{\sigma_d}{\sigma_t}} \quad (2)$$

where τ_n is the normalized bond strength, τ_t is the tested bond strength, σ_d is the designed concrete strength and σ_t is the tested concrete strength. As a result, the bond strength in the present study refers to the normalized bond strength hereafter.

6.3 EXPERIMENTAL RESULTS

6.3.1 Failure Modes

Since the steel reinforcement stirrups were used in each concrete block, no sudden splitting failure occurred during the pull-out test. Six specimens failed by the yielding

of the core steel rebars, while the other specimens failed by pulling out of the coated/uncoated steel rebars with several radial cracks developed and observed on the concrete cubic, as shown in Figure 6.5.

6.3.2 Bond Stress-Slip Curves

The bond stress-slip curves of all the tested specimens are displayed in Figures 6.6 and 6.7. In each subfigure, a bold red line represents the average curve of three identical specimens, which was obtained by the curve averaging operation of Origin Pro software (OriginLab Corp.). Table 6.5 gives the key results of the bond tests carried out for each specimen.

6.4 ANALYSIS AND DISCUSSIONS

6.4.1 Failure Modes

Although all the specimens failed by pulling out of the rebars, the details of the failure surface of the specimens were different for each group, as shown in Figure 6.8 and Figure 6.9. The specimens reinforced with UCSRs failed by shearing off the concrete between steel ribs as a UCSR always has a higher effective rib height than those of coated steel rebars. For ECSRs, which have a relatively lower effective rib height and a relatively smooth surface, the debonding occurred at the concrete/rebar interface, and debonding of the coating layer was also observed. Although all the FCSRs failed at the coating layer, similar to the ECSRs, the debonding of the coating layer has not occurred in FCSRs specimens. The enhanced bond performance of the coating layer to the steel substrate is attributed to the existence of the glass fibre and the filament

winding technology of continuing long fibre onto the steel rebars. For FCSRs, the failure mode varies with the number of fibre plies and fibre winding angle(s). For one-ply FCSRs, the failure surface is mainly located at a shallow depth of the FRP coating. However, the failure surface would get deeper with the increase of the FRP coating thickness.

For FCSRs wound with small winding angle(s), that is $+60^{\circ}/-60^{\circ}$ winding combination in this study, the continuous long glass fibre will sustain part of the force in the longitudinal direction when the shear force is transmitted from the steel to concrete. It can be seen from Figure 6.7 (g) that some fibres were broken in the direction perpendicular to the rebar length. Thus, the small angle winding configurations can theoretically increase the bond strength of the FCSRs as the fibres in epoxy increase the in-plane shear capacity of the coating layer. The influence of the winding angle(s) on the bond strength of the FCSRs will be discussed in the later section.

The details of the concrete/rebar interface for the failed specimens are shown in Figure 6.8 and Figure 6.9 for screw-thread steel (STS) rebars and crescent-ribbed steel (CRS) rebars, respectively. A sketch map illustrating the location of failure surfaces for different types of steel rebars embedded in concrete is shown in Figure 6.10.

6.4.2 Effect of Coating Materials

The normalized bond strength of the FRP-coated screw-thread and crescent-ribbed steel rebars to concrete are summarised and compared with those of UCSRs and ECSRs in Figure 6.11 and Figure 6.12, respectively. The FCSRs analysed in this

section refer to the one-ply fibre of the FRP coating layer with a winding angle of 86.5°.

The epoxy coating decreased the bond strength of both types of steel rebars in concrete, as clearly illustrated in Figure 6.10 and Figure 6.11, which coincides with the previous studies (De Anda *et al.* 2006; Wang *et al.* 2018; Naha *et al.* 2021; Shang *et al.* 2021). The bond strength of epoxy-coated crescent-ribbed steel rebars decreased by 17.4%, while the screw-thread steel rebars decreased by 11.5% with epoxy coating. The experimental results proved that FRP coating did not reduce the bond performance when embedded in concrete. Instead, it even enhanced the bond of steel rebars to concrete. The bond strength increased by 7.57% for FRP-coated crescent-ribbed steel rebars and improved by 16.5% for FRP-coated screw-thread steel rebars. The enhanced bond strength can be attributed to the FRP coating layer. The epoxy coating layer has a lower shear strength and a relatively smaller bond strength to the steel substrate than the FRP coating layer. The FRP coating layer can sustain a higher shear force during the pulling-out process due to the existence of the glass fibre, especially the multi-directional fibres (Selmy *et al.* 2012). Moreover, the wound fibres could restrict the peeling of the coating layer off the steel substrate.

6.4.3 Effect of FRP Coating Thickness

The mechanism of the coating layer to prevent the corrosion of the core steel rebar is to keep the water and oxygen from the rebars. Theoretically, the thicker the coating layer, the better the protection effect and the longer the lifetime of the rebars and structure would be. However, as stated by many researchers before (Choi *et al.* 1991; Miller *et al.* 2003), the bond strength of the ECSRs decreases noticeably once the

coating thickness exceeds the threshold value, making the ECSRs unsuitable for structure construction. This is the reason that limits the thickness of the epoxy coating, thus restricting the protective effect of the epoxy coating layer. Although the material cost would increase with the coating thickness, there must be the most satisfactory combination from the lifecycle consideration.

Fig. 6.13 and Fig. 6.14 show the influence of the thickness on the bond strength of FRP-coated screw-thread and FRP-coated crescent-ribbed steel rebars, respectively. Different from the ECSRs, ethylene-vinyl acetate–modified cement slurry-coated rebars, and graphene-modified epoxy-coated steel bars (Darwin and Graham 1993; Jo and Do 2018; Shang *et al.* 2021), FCSRs showed a positive correlation with the coating thickness in bond strength. The thicker coating layer will physically result in better corrosion resistance of the coated steel rebars, as the water and oxygen are more challenging to intrude into the coating layers. Therefore, the thicker FRP coating layers could be adopted in extremely hostile environments to protect the core steel rebars better. If there is a threshold value for FRP coating, as that existed for epoxy coating, it still needs further investigation.

6.4.4 Effect of Winding Configuration

The major problem encountered in manufacturing the FCSRs is that the wound fibres will reduce the relative rib area of the steel rebar, which will theoretically reduce the mechanical interlock force between the steel rebars and concrete (Darwin and Graham 1993). However, according to the previous studies, the winding configurations [e.g., winding angle(s) and number of fibre plies in the FRP coating layer] of the filaments on steel rebars are the primary factors influencing the effective

rib height of the FCSRs. So, this section compares the bond properties of FCSRs with different winding angles.

The bond strength of FCSRs with different winding angles is shown in Figure 6.15 and Figure 6.16 for STS rebars and CRS rebars, respectively. “C” means the winding angle of the fibre ply is -86.5° , and “A” means the winding angle of the fibre ply is “ $+86.5^\circ$ ”. Thus, “CA” means a winding angle combination of $-86.5^\circ/+86.5^\circ$ for the coating layer, and “AA” represents a winding combination of $+86.5^\circ/+86.5^\circ$, “SS” means a winding angle combination of $-60^\circ/+60^\circ$.

Different winding angle combinations have different levels of improvement on the bond strength for two types of steel rebars. For screw-thread steel rebars, the specimens with a $+86.5^\circ/-86.5^\circ$ winding angle combination had the highest bond strength, which increased by 27.0%, while the $60^\circ/+60^\circ$ winding angle configuration improved the bond strength of FCSRs by 14.5% and the $-86.5^\circ/+86.5^\circ$ configuration only enhanced the bond performance of FCSRs for 9.64%. For crescent-ribbed steel rebars, the $60^\circ/+60^\circ$ winding angle combination improved the bond strength of FCSRs more than the $-86.5^\circ/+86.5^\circ$ combination, as the former one increased by 17.5% and the latter improved by 9.43%. As explained before, small winding angle(s) can theoretically improve the bond strength as the continuous long glass fibres will sustain part of the load. The results of CRS rebar groups approved this opinion. However, this explanation does not seem to support the results of STS rebar groups. This could be attributed to the difference in rib patterns. The rib parameters, such as rib distribution, rib height, and rib width, differ from the steel rebars. The higher rib height of the STS rebars has a larger influence on the winding quality of the FRP coating layer, as the fibres are not straight wound onto the steel surface. Instead, they are wavyly distributed on the steel rebars with ribs. Therefore, if the rib height is too

large, the fibres inside the epoxy cannot successfully transfer the force in the longitudinal direction of the steel rebars. This might be the reason that the “60°/+60°” winding configuration for STS rebars did not sustain the largest bond load.

The differences between FCSRs that are manufactured with different types (e.g., rib patterns) of core steel rebars illustrated that rib patterns will affect the coating quality and further the bond properties of the FCSRs.

Model Code 2010 (Taerwe and Matthys 2013) defines $\tau_{max} = 2.5\sqrt{f_{c,m}}$ as the good bond condition for steel reinforcement. It is clear from Figure 6.17 that all the FCSRs tested in the current study have a bond strength more prominent than the maximum value defined in Model Code 2010. By contrast, Sena-Cruz *et al.* (2009) concluded that $\tau_{max} = 0.73\sqrt{f_{c,m}}$ and $\tau_{max} = 1.46\sqrt{f_{c,m}}$ for galvanized/epoxy double-layer coated steel rebars and galvanized steel rebars, respectively, which proved these two types of rebars have poor bond performance in concrete. Only part of the ethylene-vinyl acetate-modified cement slurry-coated rebars tested by Jo and Do (2018) reached the “good bond condition”, as stated in Model Code 2010 (CEB-FIP 2010). Although the bond strength of ECSRs reaches the “good bond condition” requirement for coated steel rebars ($\alpha = 1.25$), their performance was much inferior to that of uncoated deformed steel rebars ($\alpha = 2.5$). Therefore, the bond performance of the FCSRs is quite competitive compared with other coated steel rebars.

6.5 LOCAL BOND STRESS-SLIP MODEL FOR FRP-COATED STEEL REBARS

The bond stress-slip relationship of the steel rebars in concrete structures describes the bond properties between reinforcement and surrounding concrete, which is crucial in the design and analysis of reinforced concrete elements (Lin *et al.* 2019). However, the properties of the bars, such as the rib pattern, rebar diameter, concrete strength, existence of the stirrup, and concrete cover-to-rebar diameter ratio, will affect the bond performance of the steel rebars in concrete (Jin *et al.* 2020).

The mean bond stress-slip relationship for steel rebars in concrete was outlined in Model Code 2010 (CEB-FIP 2010) by the following equations:

$$\tau = \tau_{\max} (s/s_1)^\beta \quad \text{for } s \leq s_1 \quad (6-3)$$

$$\tau = \tau_{\max} \quad \text{for } s_1 \leq s \leq s_2 \quad (6-4)$$

$$\tau = \tau_{\max} - (\tau_{\max} - \tau_f) \cdot \frac{s-s_2}{s_3-s_2} \quad \text{for } s_2 \leq s \leq s_3 \quad (6-5)$$

$$\tau = \tau_f \quad \text{for } s_3 \leq s \quad (6-6)$$

where s is the relative displacement parallel to the bar axis, s_1 is the corresponding slip when bond strength reaches the maximum value, s_2 is the slip when bond strength starts to decrease, s_3 is the slip when bond stress reaches the τ_f , and τ_f is the residual bond stress provided by the frictional force between the rebars and concrete,

Model Code 2010 (CEB-FIP 2010) suggests the value of τ_{\max} as $2.5\sqrt{f_{c,m}}$, s_1 equals 1.0 mm, s_2 equals to 2.0 mm, and s_3 equals to clear distance between ribs, β equals 0.4, and τ_f equals to $0.4 \tau_{\max}$ for deformed steel rebars. The experimental results of each type of rebar are compared with the analytical results obtained by the FIB model for two types of ribbed steel rebars in Figure 6.18, as the crescent-ribbed steel rebars have a clear rib distance of 8.2 mm (GB/T-1499.2 2018) while the screw-thread steel

rebars have a clear rib distance of 5.8 mm (GB/T-20065 2016). It can be seen from the graphs that analytical results calculated from the FIB model underestimate the bond strength as well as the bond stiffness of UCSRs and FCSRs. According to Sena-Cruz *et al.* (2009), new parameters (α, β, s_1) that defines the local bond stress-slip law for new types of rebars can be obtained from the experimental results by inverse analysis.

The parameter α is calculated according to the equation (6-7):

$$\alpha = \frac{\sqrt{f_{c,m}}}{\tau_{max}} \quad (6-7)$$

The value of the α obtained from the experiments is shown in Figure 6.19. The fitting results for α are 3.16 for FRP-coated screw-thread steel rebars and 3.17 for crescent-ribbed steel rebars, which is quite close. It seems that rib type has little effect on the average bond strength of the FCSRs.

The value of the s_1 was obtained by averaging the slip value at the maximum bond stress of each specimen. The fitting result for s_1 was approximated to be 0.5 mm, so s_1 was set as 0.5 mm for the modified model for FCSRs. Similarly, the value of s_2 was set at 1.0 mm according to the experimental results.

The value of β in the FIB model is correlated to the bond stiffness of the rebars. Since FCSRs have an evident improvement in bond stiffness, there should be a modified β for the FCSRs based on the 0.4 as recommended in Model Code 2010 (Taerwe and Matthys 2013).

τ_f is relevant to the friction force of the rebars in concrete after being pull-out, s_3 , which is related to the clear rib distance of rebars, determines the slip value when bond strength almost reaches a plateau. Since the FRP coating changed the surface

texture of the steel rebars, these two parameters should also be modified based on the original FIB model.

The modified value of β , τ_f , and s_3 for FRP-coated screw-thread steel rebars and FRP-coated crescent-ribbed steel rebars were summarised in Table 6.6.

Figure 6.20 displays the modified local bond stress-slip models for FCSRs manufactured with screw-thread and crescent-ribbed steel rebars, and the modified local bond stress-slip models were compared with the average bond stress-slip curve of experimental results. It is obvious that the modified models fit the experimental data better than the original model recommended in Model Code 2010 (Taerwe and Matthys 2013).

Although the local bond stress-slip model suggested in Model Code 2010 (Taerwe and Matthys 2013) underestimated the bond performance of FCSRs in reinforced concrete structures, this model can still be used in the design of FCSR-reinforced concrete structures at the current stage for conservative consideration.

6.6 CONCLUSIONS

In this chapter, a total of 16 groups of pull-out specimens for bond performance tests were prepared and tested. The test parameters included the rib pattern of the core steel rebar, the number of fibre plies and the winding angle(s) of the FRP coating layer. Specimens with uncoated steel rebars (UCSRs) and epoxy-coated steel rebars (ECSRs) were also tested for comparison. The following conclusions were drawn based on the test results and discussions:

- (1) The bond performance of FCSRs to concrete is comparable to or even better than that of UCSRs and is superior to that of ECSRs.
- (2) The bond strength of FCSRs is positively correlated to the number of fibre plies of the FRP coating layer, which is valid for core steel rebars with both screw-thread and crescent rib patterns.
- (3) The winding configuration of the FRP coating layer affects the bond performance of FCSRs to concrete. The failure mechanism of the bond between FCSRs and concrete may change with the fibre winding angle(s) of the FRP coating layer.
- (4) A modified local bond stress-slip model has been proposed for FCSRs with more accurate predictions for bond stress and stiffness. The existing local bond stress-slip models for uncoated steel rebars (UCSRs) are also suitable for FCSRs by providing conservative predictions of the bond performance to concrete.

6.7 REFERENCES

ASTM (2020). *ASTM D7913/D7913M*. Standard Test Method for Bond Strength of Fiber-Reinforced Polymer Matrix Composite Bars to Concrete by Pullout Testing, American Society for Testing and Materials, West Conshohocken, Pennsylvania, USA.

CEB-FIP. (2010). *Model Code for Concrete Structures*. Thomas Telford Services Ltd., London.

- Choi, O.C., Hadje-Ghaffari, H., D., D., and McCabe, S.L. (1991). "Bond of epoxy-coated reinforcement: bar parameters", *ACI Materials Journal*, Vol. 88, No. 2, pp. 207-217.
- Cosenza, E., Manfredi, G. and Realfonzo, R. (1995). "Analytical modelling of bond between FRP reinforcing bars and concrete", *Non-metallic (FRP) Reinforcement for Concrete Structures: Proceedings of the Second International RILEM Symposium*, CRC Press, pp. 164.
- Darwin, D. and Graham, E.K. (1993). *Effect of deformation height and spacing on bond strength of reinforcing bars*, University of Kansas Center for Research, Inc.
- De Anda, L., Courtier, C. and Moehle, J.P. (2006). "Bond strength of prefabricated epoxy-coated reinforcement", *ACI Materials Journal*, Vol. 103, No. 2, pp. 226.
- GB50010 (2015). *GB50010*. Code for Design of Concrete Structures, Ministry of Housing and Urban-Rural Construction of the People's Republic of China, China.
- GB/T-1499.2 (2018). *GB/T 1499.2*. Steel for the Reinforcement of Concrete—Part 2: Hot Rolled Ribbed Bars, China Building Industry Press, Beijing, China.
- GB/T-20065 (2016). *GB/T 20065*. Screw-thread Steel Bars for Prestressing of Concrete, China Academy of Building Research, Beijing.
- Grundhoffer, T.M., French, C.E. and Leon, R.T. (1992). "Bond behavior of uncoated and epoxy-coated reinforcement in concrete." Final report for University of Minnesota, Center of Transportation Studies and National Science Foundation.

- Jin, L., Liu, M., Zhang, R. and Du, X. (2020). “3D meso-scale modelling of the interface behavior between ribbed steel bar and concrete”, *Engineering Fracture Mechanics*, Vol. 239.
- Jo, Y. and Do, J. (2018). “Pull-out bond strength and flexural load test of concrete beam with ethylene-vinyl acetate–modified cement slurry-coated rebar”, *Advances in Structural Engineering*, Vol. 21, No. 14, pp. 2130-2142.
- Lin, H., Zhao, Y., Ozbolt, J., Feng, P., Jiang, C. and Eligehausen, R. (2019). “Analytical model for the bond stress-slip relationship of deformed bars in normal strength concrete”, *Construction and Building Materials*, Vol. 198, pp. 570-586.
- Miller, G.G., Kepler, J.L. and Darwin, D. (2003). “Effect of epoxy coating thickness on bond strength of reinforcing bars”, *ACI Structural Journal*, Vol. 100, No. 3, pp. 314-320.
- Naha, A., Islam, G.S. and Chowdhury, M.A.I. (2021). “Bond strength of epoxy-coated reinforcement in concrete”, *Proc., International Conference on Planning, Architecture & Civil Engineering*, pp. 120-125.
- Selmy, A., Elsesi, A., Azab, N. and Abd El-baky, M. (2012). “Interlaminar shear behavior of unidirectional glass fiber (U)/random glass fiber (R)/epoxy hybrid and non-hybrid composite laminates”, *Composites Part B: Engineering*, Vol. 43, No. 4, pp. 1714-1719.
- Sena-Cruz, J., Cunha, V.M., Camões, A., Barros, J.A. and Cruz, P.J. (2009). “Modelling of bond between galvanized steel rebars and concrete”, *Proc., Congreso de Métodos Numéricos en Ingeniería*,

Shang, H., Shao, S. and Wang, W. (2021). “Bond behavior between graphene modified epoxy coated steel bars and concrete”, *Journal of Building Engineering*, Vol. 42, No. 102481.

Wang, X.-H., Chen, B. and Tang, P. (2018). “Experimental and analytical study on bond strength of normal uncoated and epoxy-coated reinforcing bars”, *Construction and Building Materials*, Vol. 189, pp. 612-628.



(a) Crescent-ribbed steel rebars



(b) Screw-thread steel rebars

Figure 6.1 Steel rebars with different rib patterns



Figure 6.2 Compression test equipment.

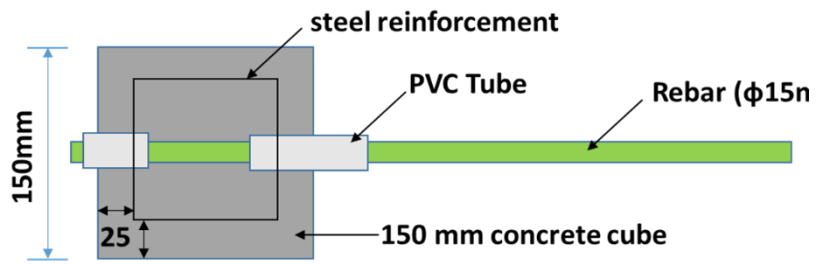


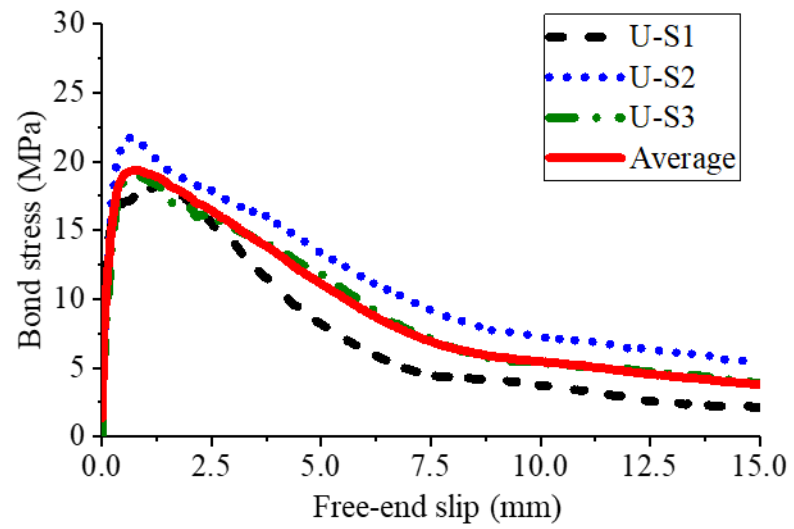
Figure 6.3 Dimensions and details of the pull-out specimen



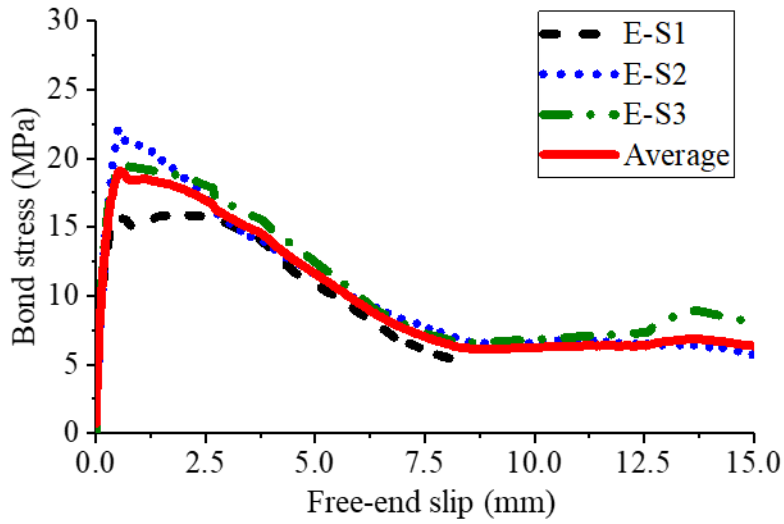
Figure 6.4 Setup for pull-out tests



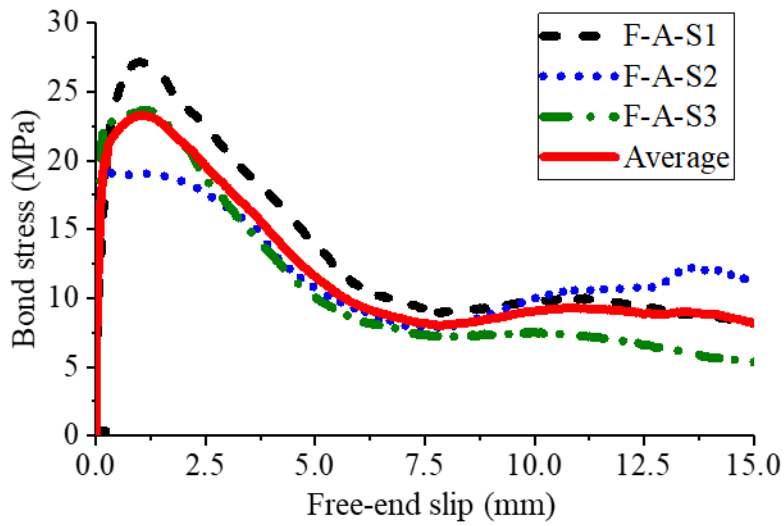
Figure 6.5 Typical failure mode of specimens



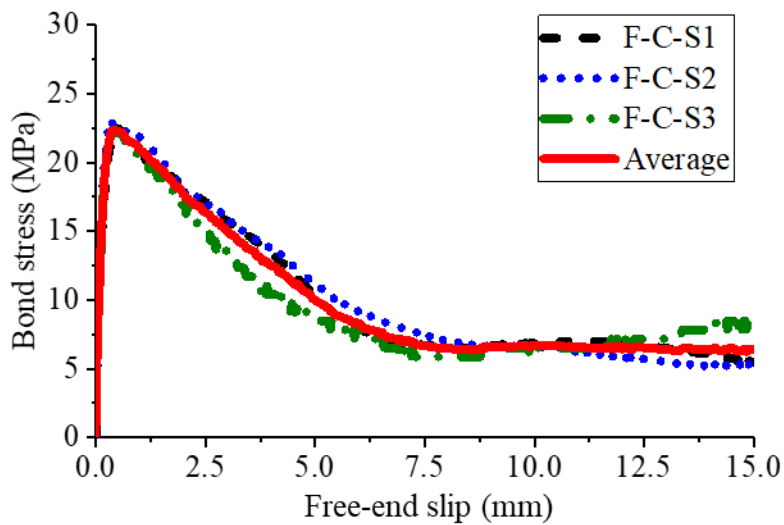
(a) Uncoated STS rebars



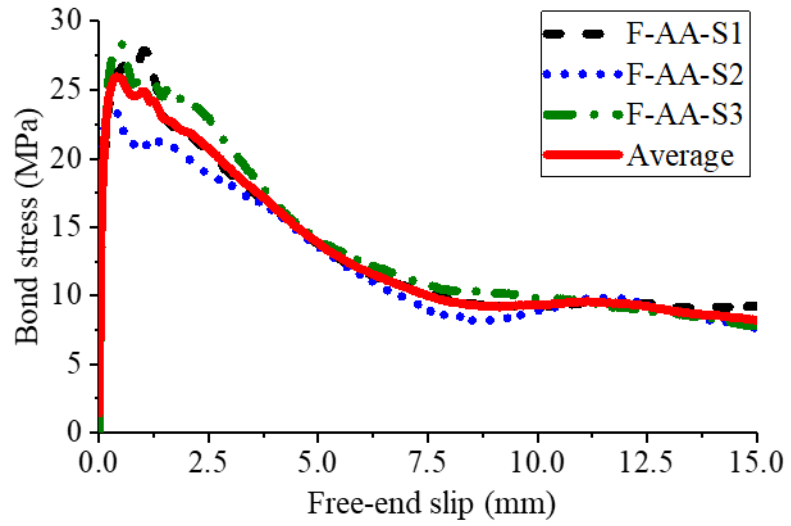
(b) Epoxy-coated STS rebars



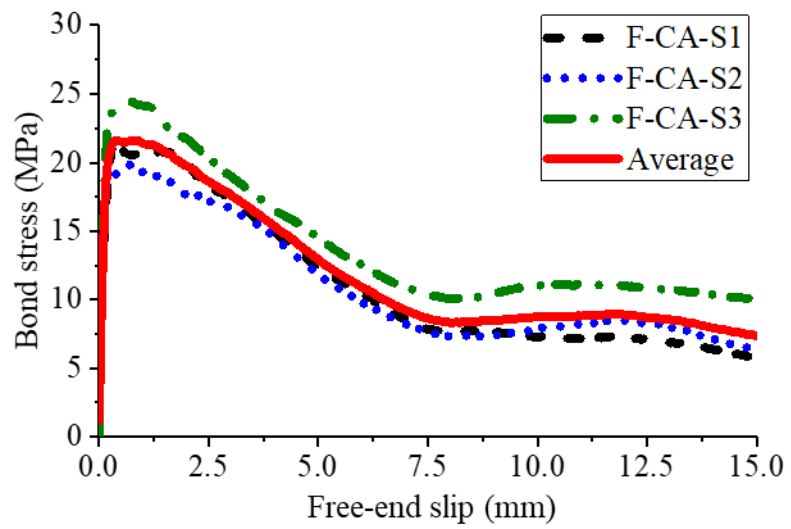
(c) One-ply (+86.5°) FRP-coated STS rebars



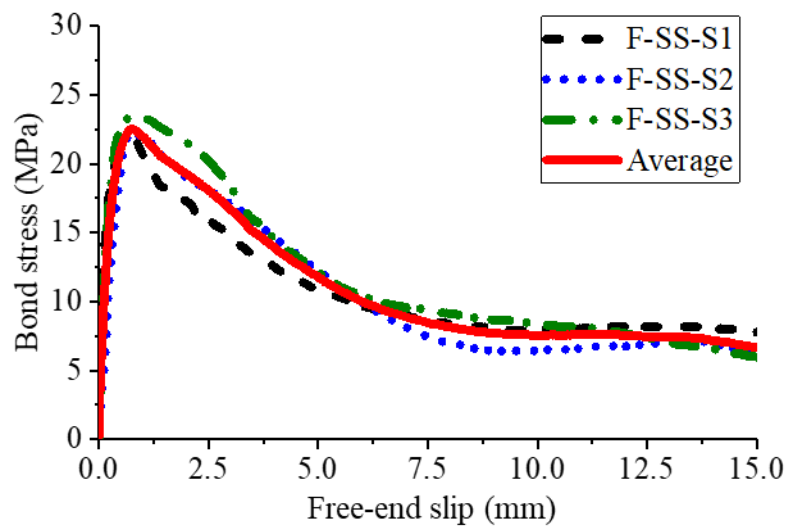
(d) One-ply (-86.5°) FRP-coated STS rebars



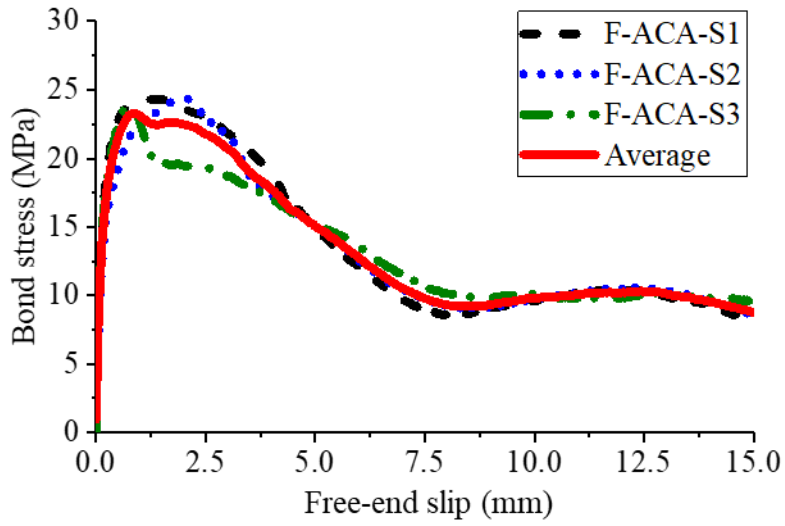
(e) Two-ply (+86.5°/+86.5°) FRP-coated STS rebars



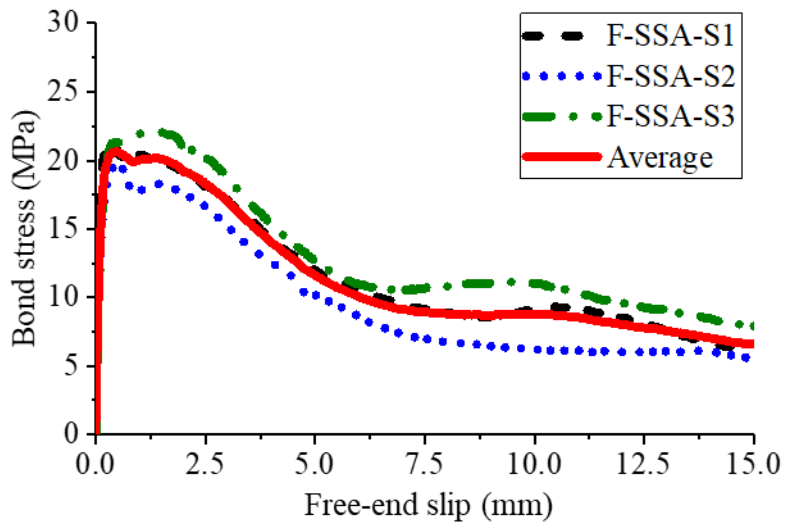
(f) Two-ply (-86.5°/+86.5°) FRP-coated STS rebars



(g) Two-ply (+60°/-60°) FRP-coated STS rebars

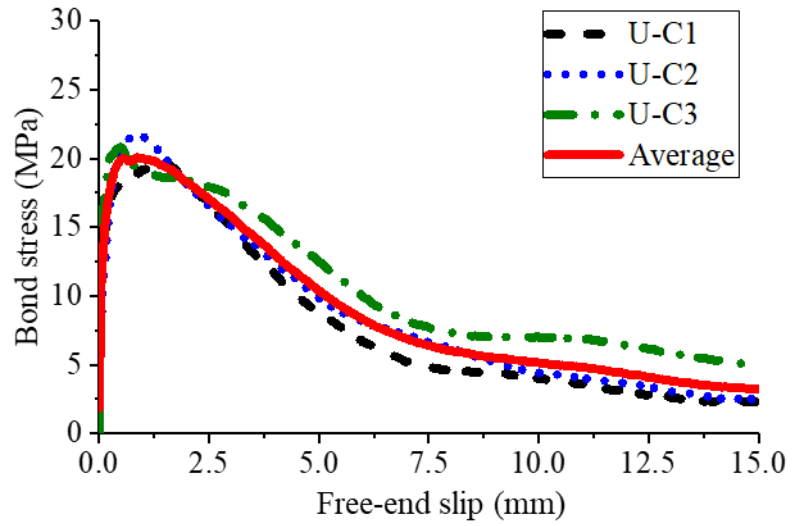


(h) Three-ply (+86.5°/-86.5°/+86.5°) FRP-coated STS rebars

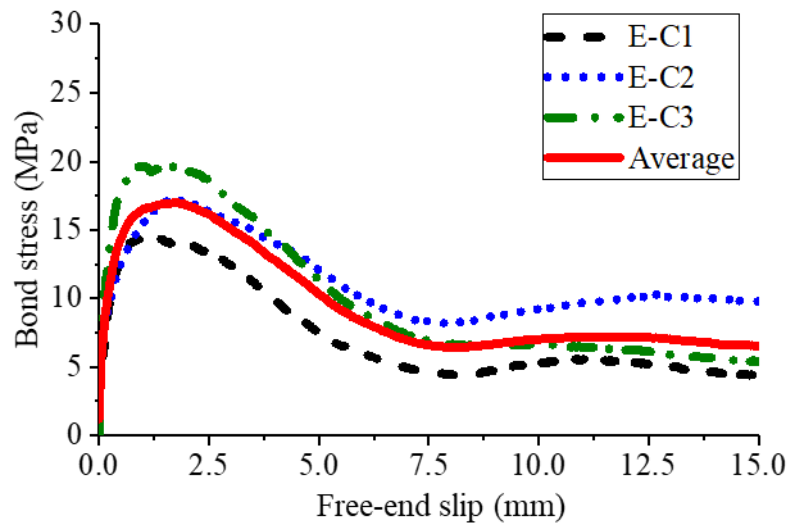


(i) Three-ply (+60°/-60°/+60°) FRP-coated STS rebars

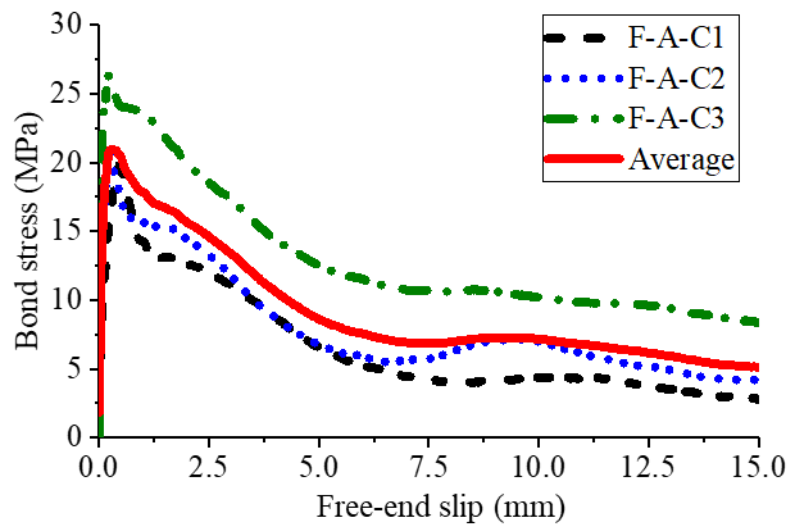
Figure 6.6 Local bond stress-slip curves of screw-thread steel (STS) rebars in concrete



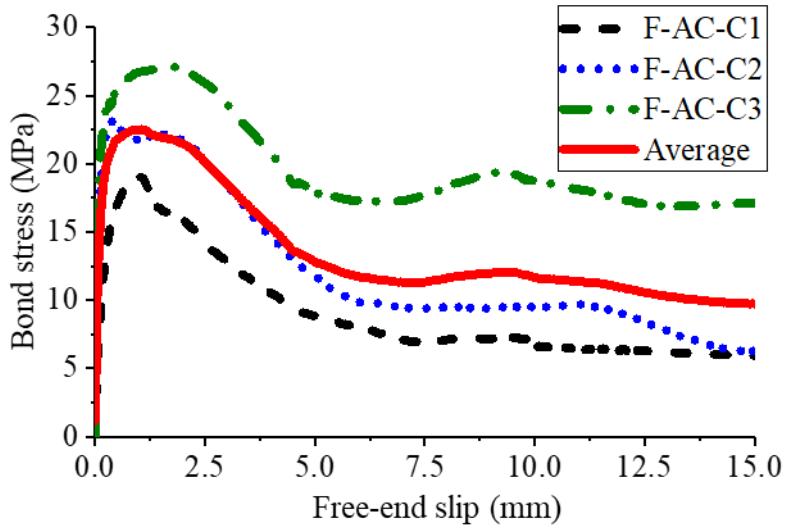
(a) Uncoated CRS rebars



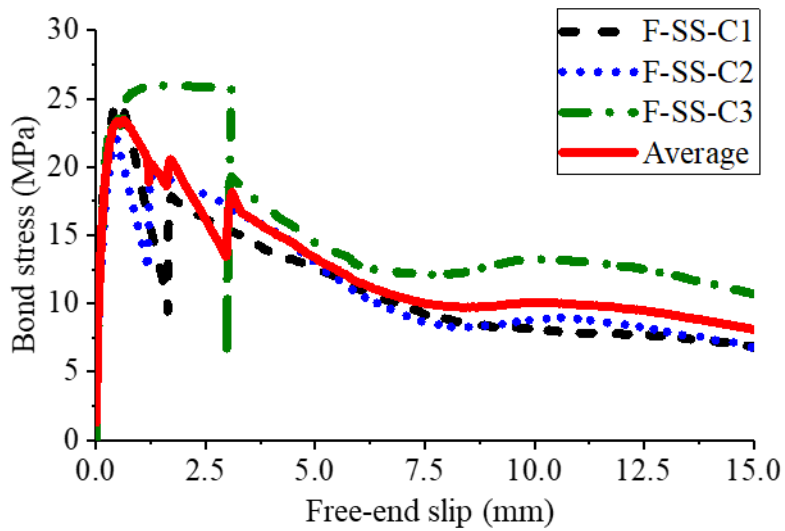
(b) Epoxy-coated CRS rebars



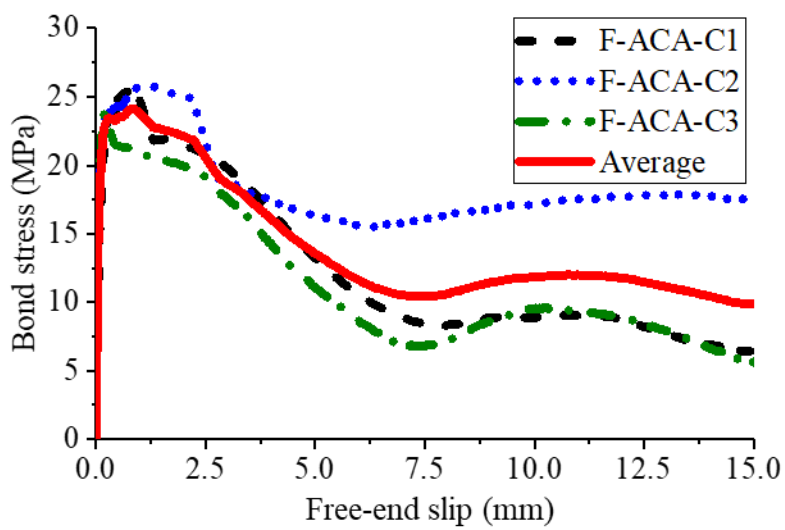
(c) One-ply (+86.5°) FRP-coated CRS rebars



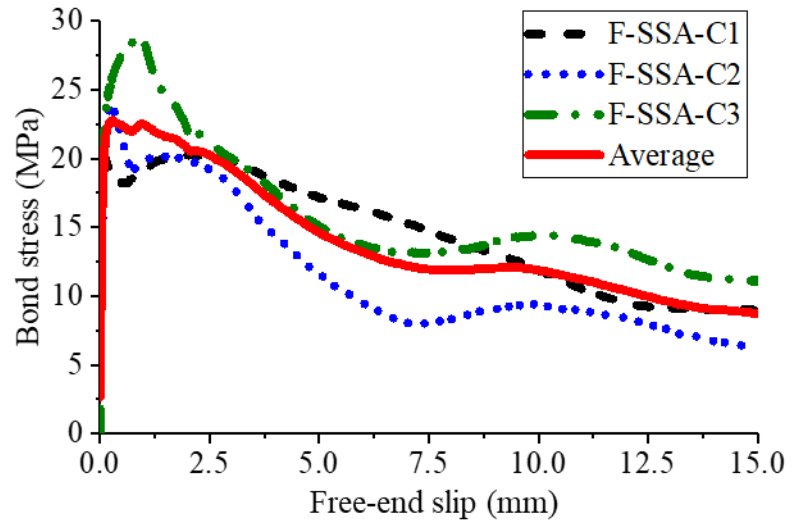
(d) Two-ply (+86.5°/-86.5°) FRP-coated CRS rebars



(e) Two-ply (+60°/-60°) FRP-coated CRS rebars



(f) Three-ply (+86.5°/-86.5°/+86.5°) FRP-coated CRS rebars



(g) Three-ply (+60°/-60°/+60°) FRP-coated CRS rebars

Figure 6.7 Local bond stress-slip curves of crescent-ribbed steel (CRS) rebars in concrete

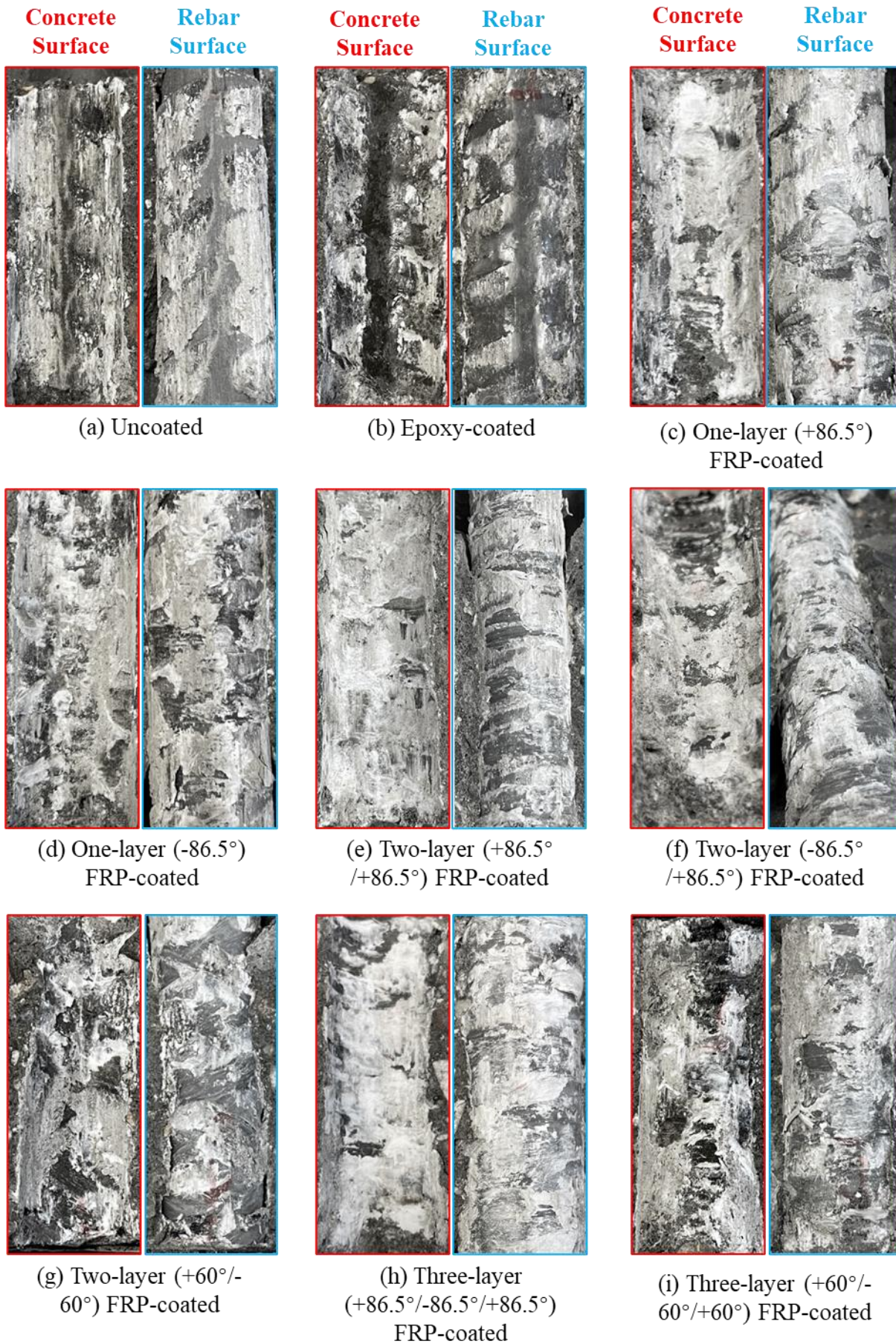


Figure 6.8 Rebar/concrete interface of failed pull-out specimens embedded with screw-thread steel rebars

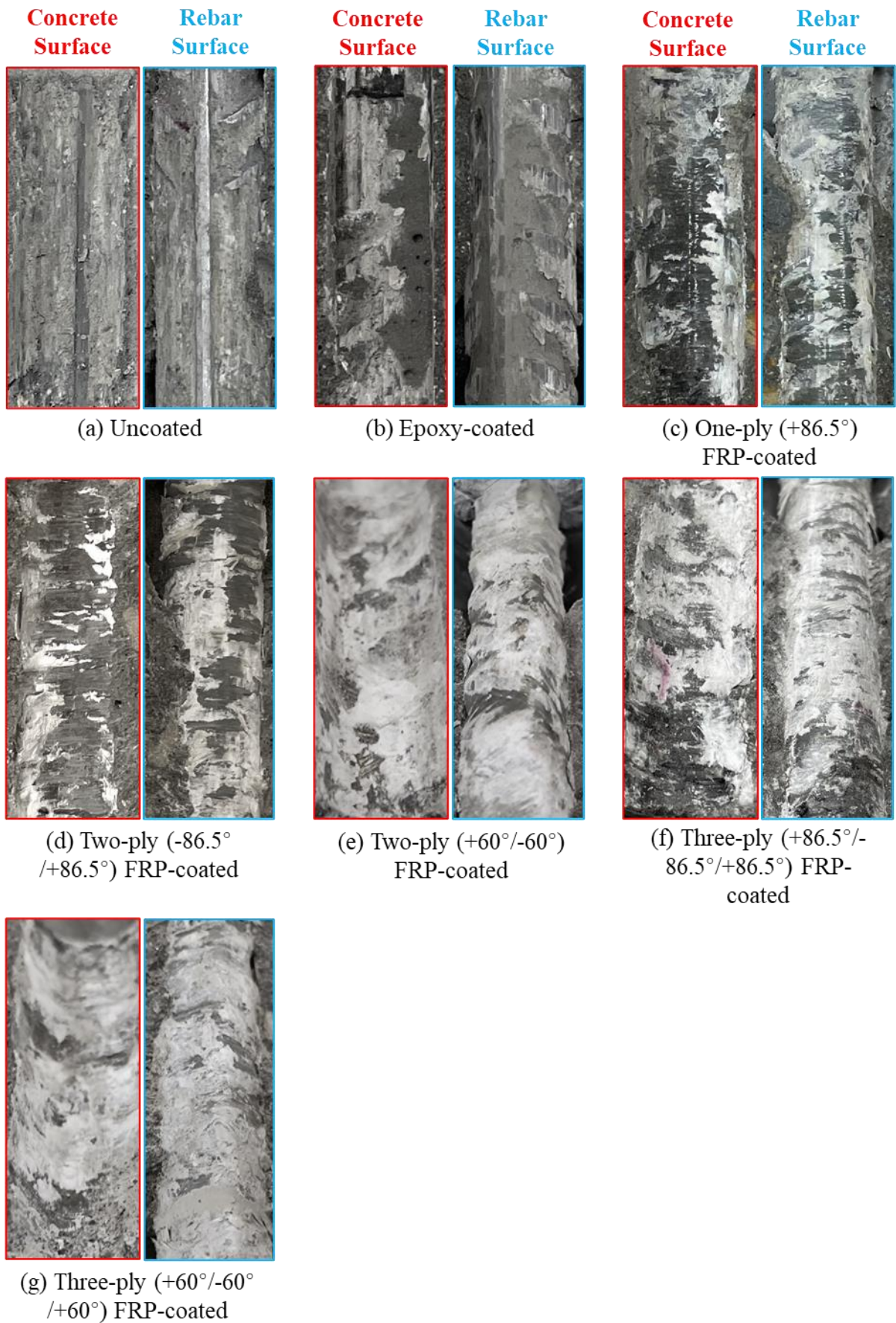
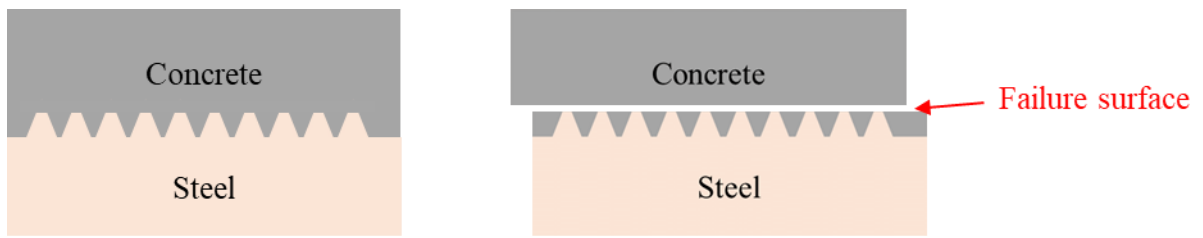
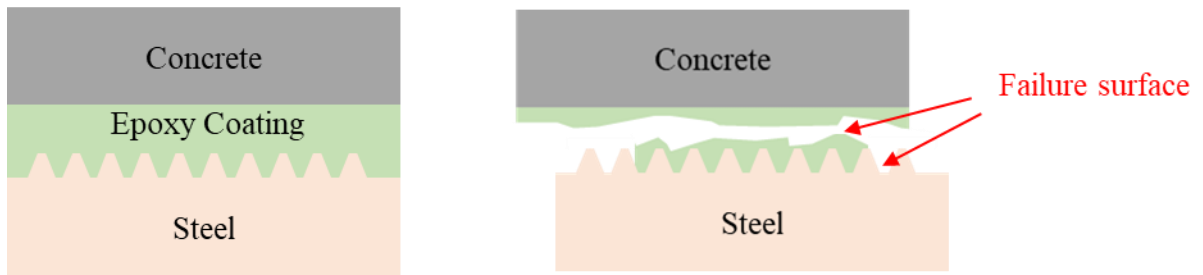


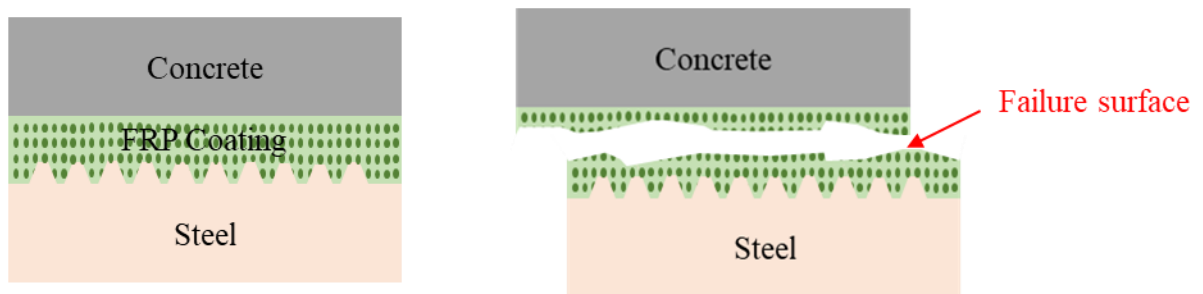
Figure 6.9 Rebar/concrete interface of failed pull-out specimens embedded crescent-ribbed steel rebars



(a) UCSRs: inside the concrete



(b) ECSRs: inside epoxy and at epoxy/steel interface



(c) FCSRs: inside the FRP coating layer

Figure 6.10 Sketch maps of failure surfaces of pull-out specimens with different steel rebars

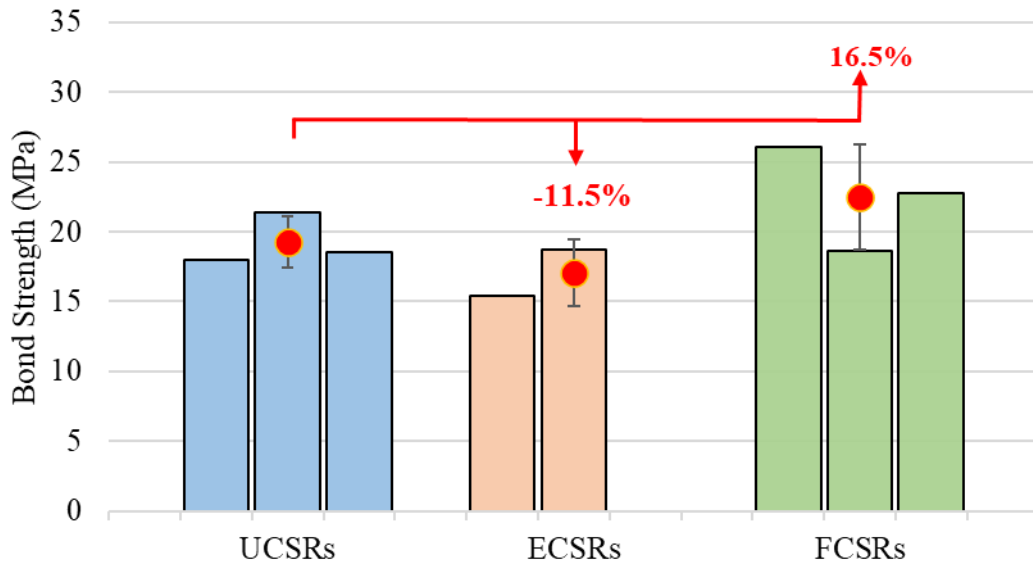


Figure 6.11 Bond strength of screw-thread steel rebars with different types of coating materials

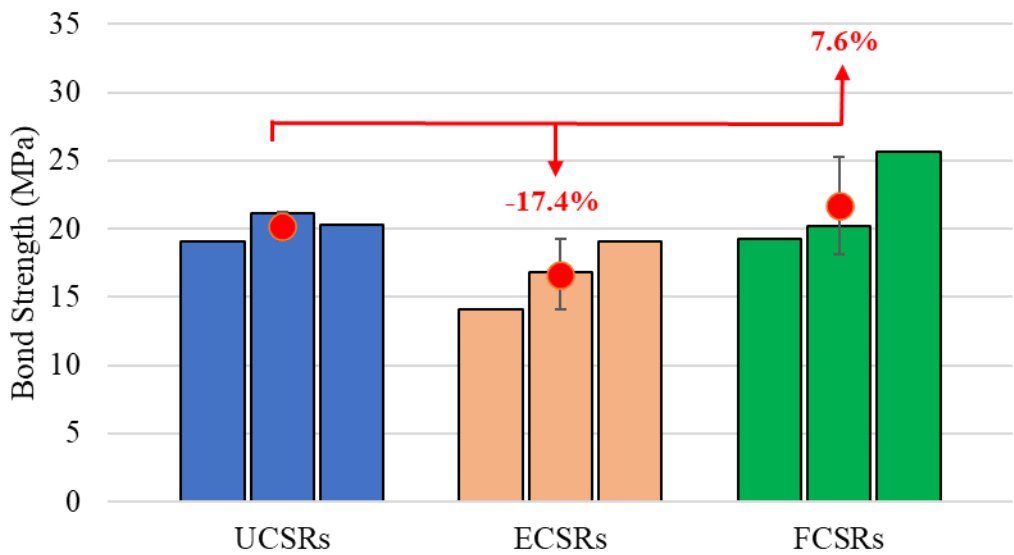


Figure 6.12 Bond strength of crescent-ribbed steel rebars with different types of coating materials

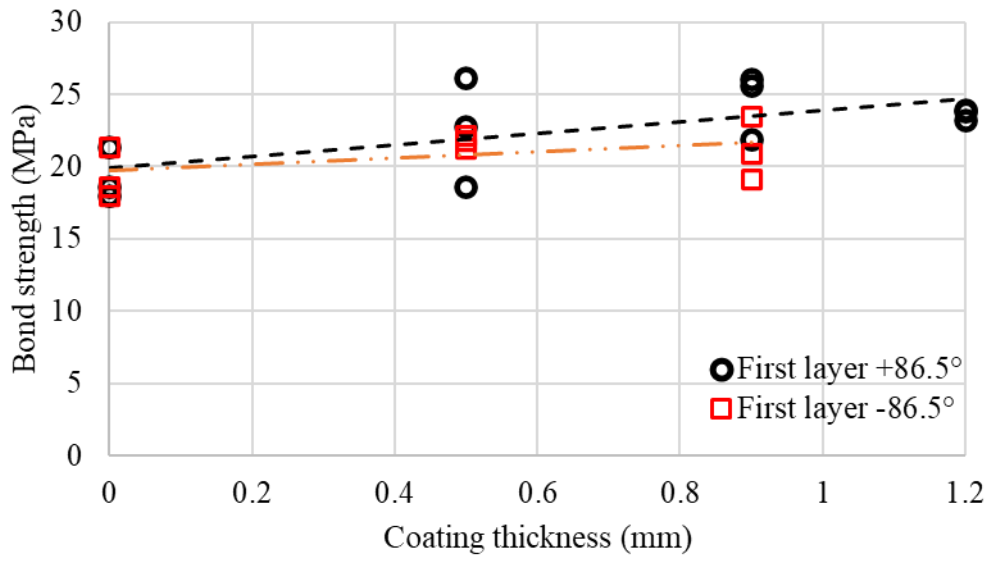


Figure 6.13 Bond strength of FRP-coated STS rebars with different coating thicknesses

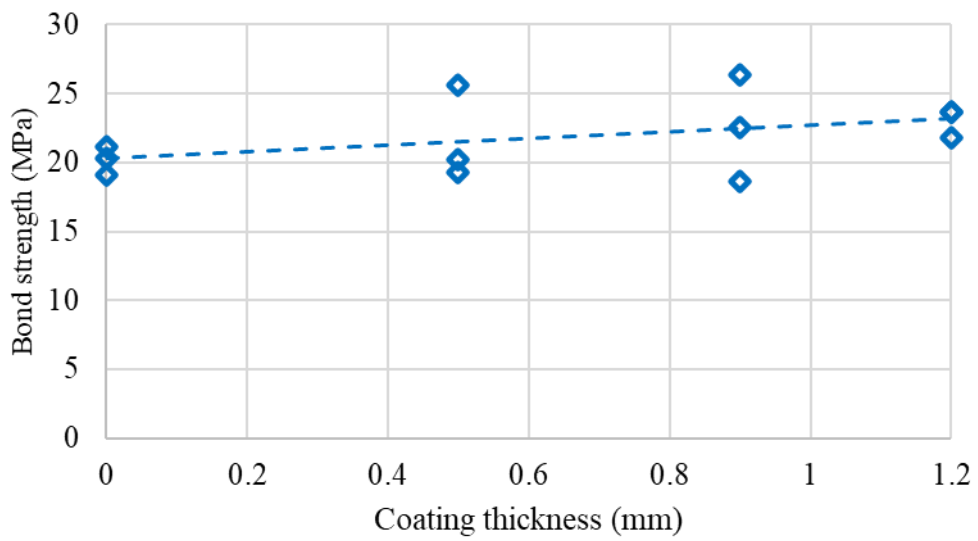


Figure 6.14 Bond strength of FRP-coated CRS rebars with different coating thicknesses

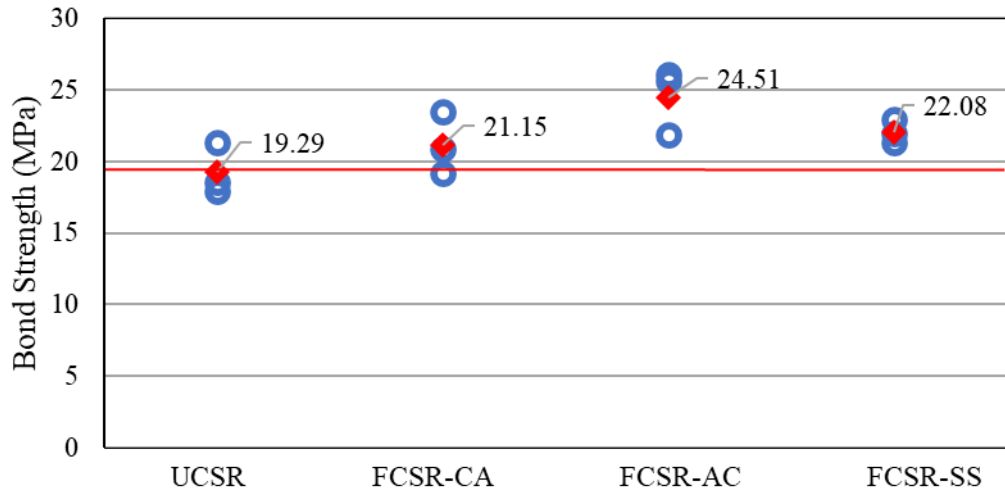


Figure 6.15 Bond strength of two-ply FRP-coated STS rebars with different winding angles

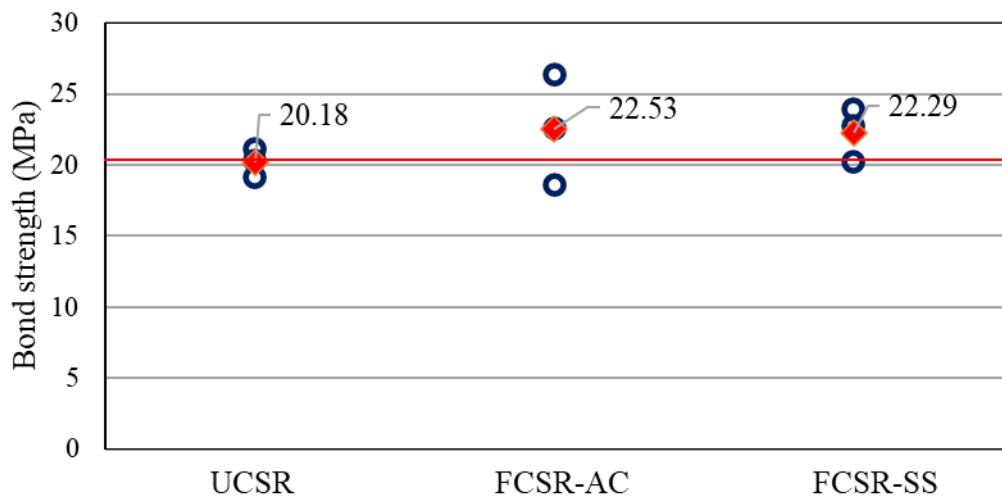


Figure 6.16 Bond strength of two-ply FRP-coated CRS rebars with different winding angles

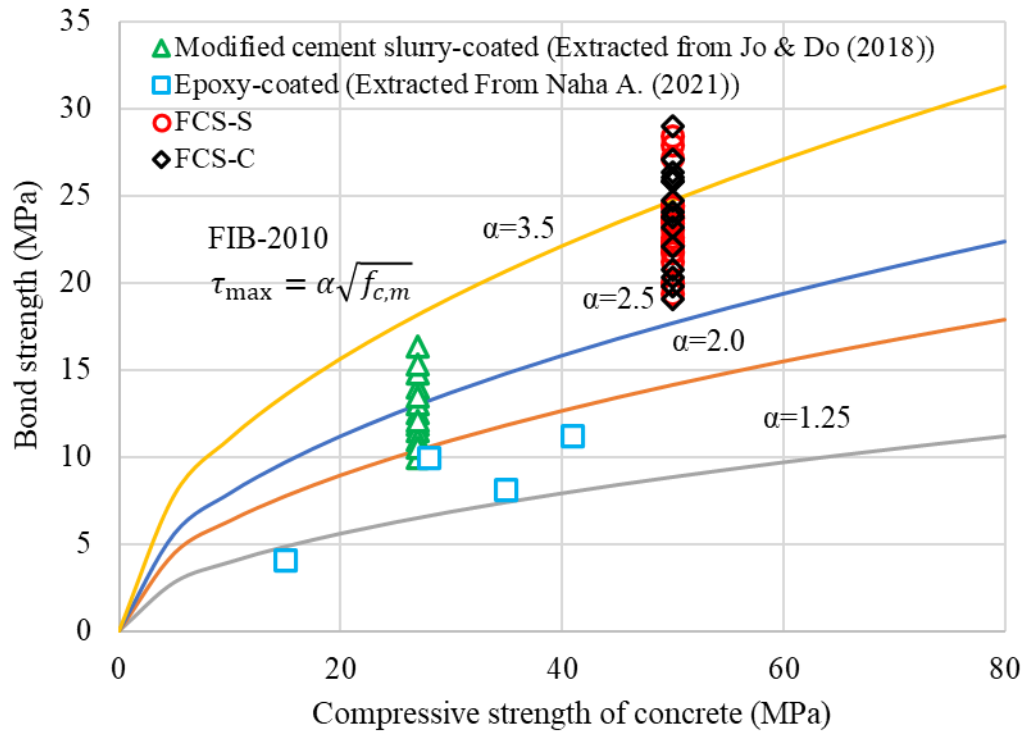
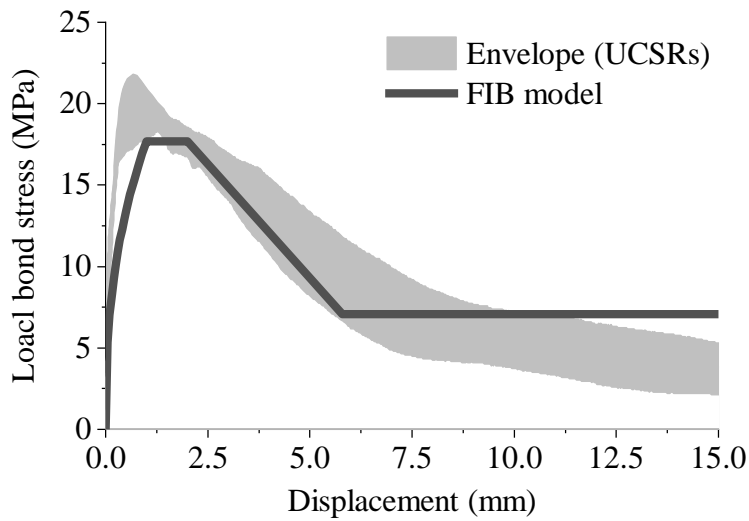
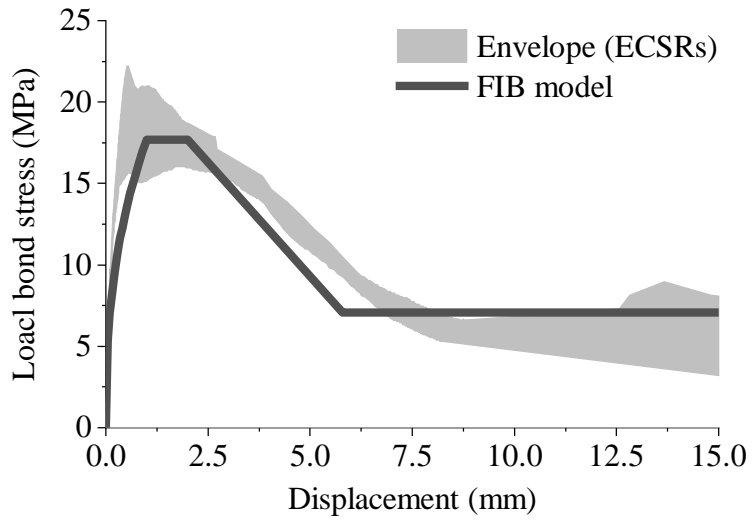


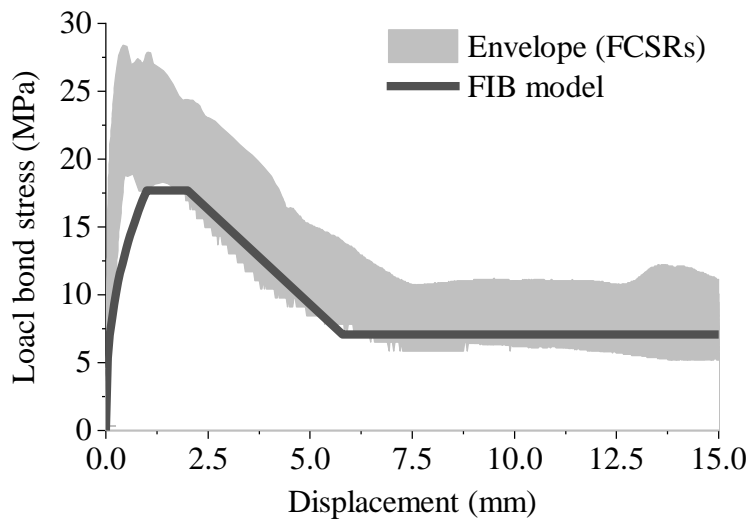
Figure 6.17 Comparison of the bond strengths of different types of coated steel rebars



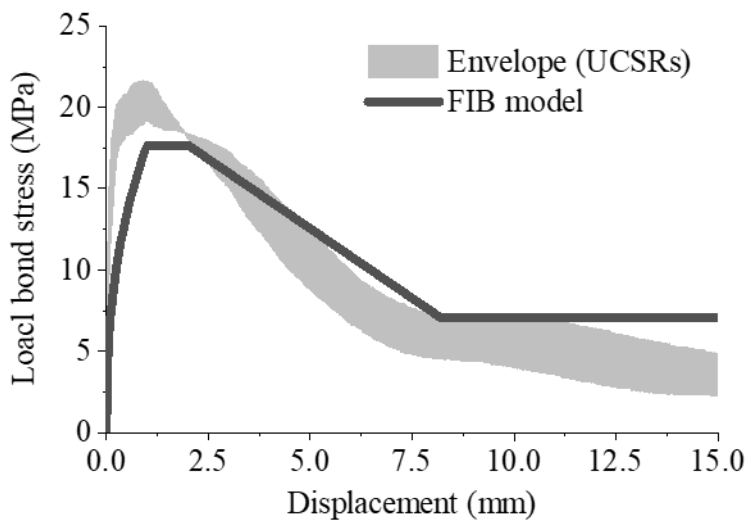
(a) Uncoated screw-thread steel rebars



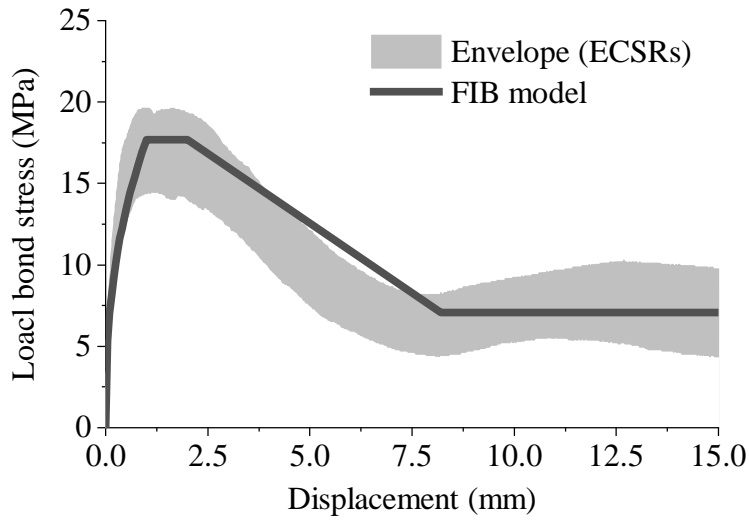
(b) Epoxy-coated screw-thread steel rebars



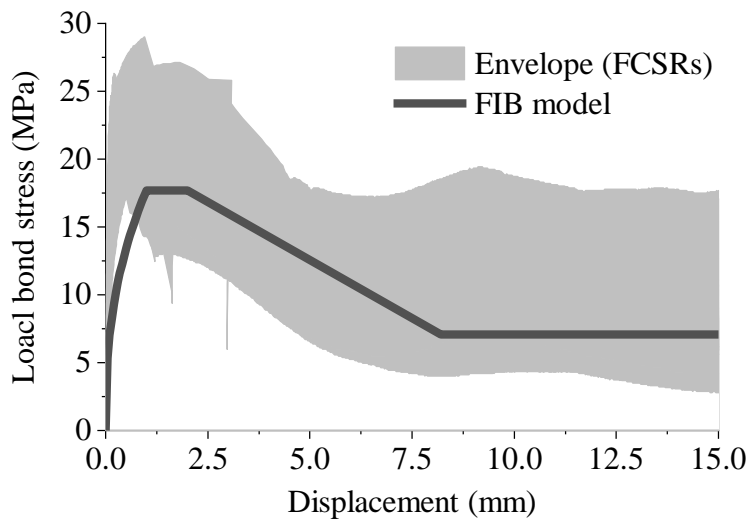
(c) FRP-coated screw-thread steel rebars



(d) Uncoated-coated crescent-ribbed steel rebars

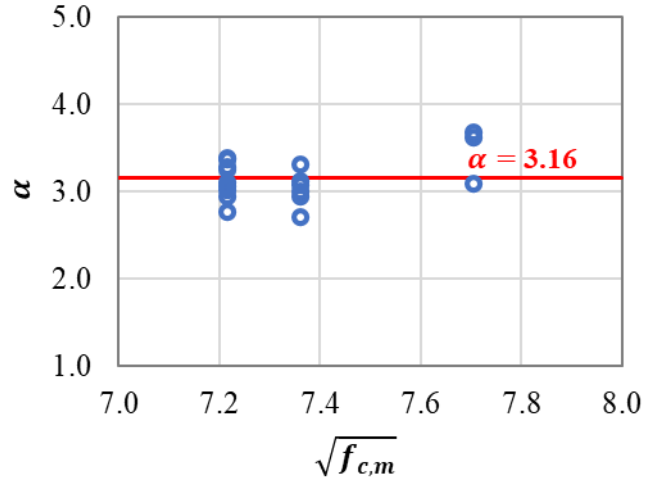


(e) Epoxy-coated crescent-ribbed steel rebars

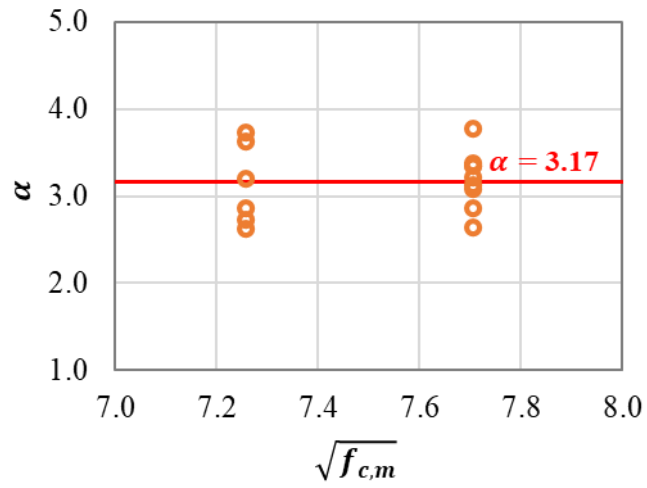


(f) FRP-coated crescent-ribbed steel rebars

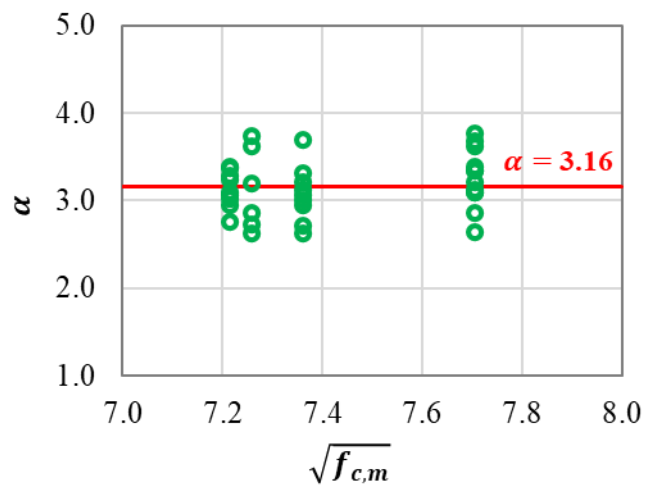
Figure 6.18 Comparison between experimental and theoretical local bond stress-slip curves



(a) Screw-thread steel rebars

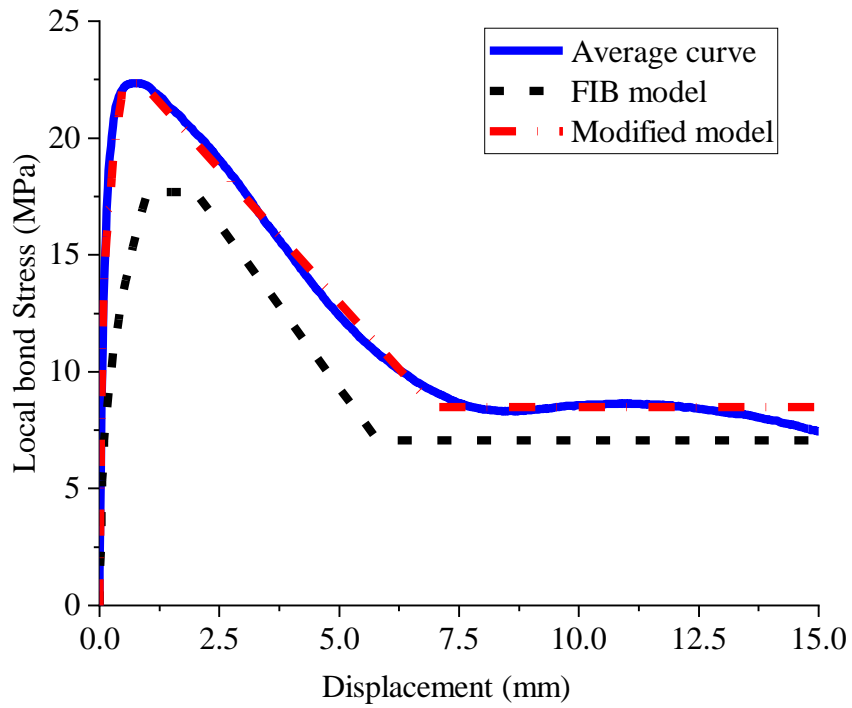


(b) Crescent-ribbed steel rebars

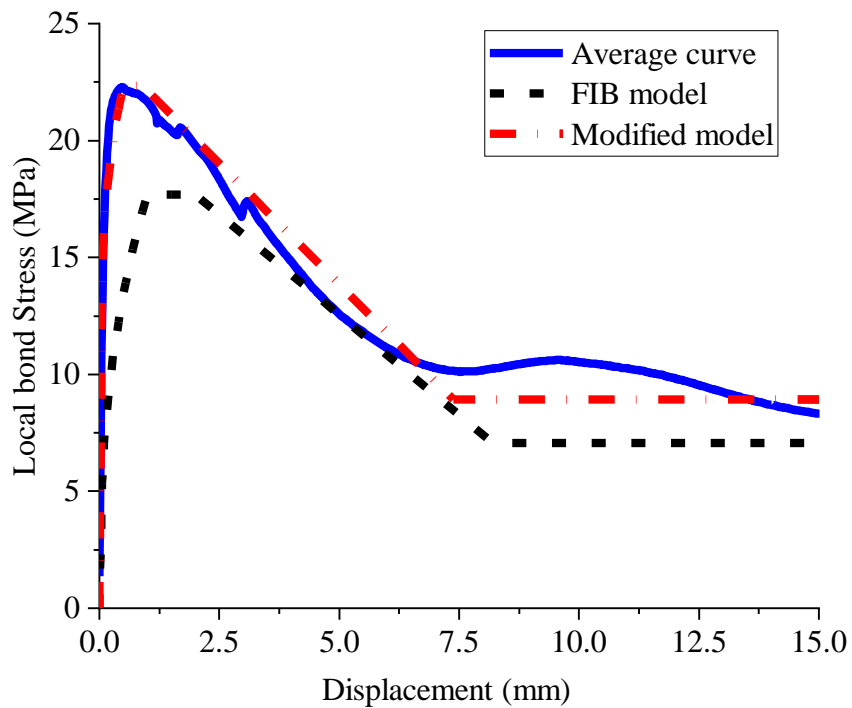


(c) Screw-thread and crescent-ribbed steel rebars

Figure 6.19 Fitting results of α for FRP-coated steel rebars



(a) FRP-coated screw-thread steel rebars



(b) FRP-coated crescent-ribbed steel rebars

Figure 6.20 Modified local bond stress-slip model for FCSRs with different rib patterns

Table 6.1 Test matrix for pull-out tests

Group	Series	Rib pattern	Coating material	Number of plies	Winding angle(s)							
1	UCSR-S1	Screw-thread	--	--	--							
	UCSR-S2											
	UCSR-S3											
2	ECSR-S1		Screw-thread	Epoxy	1	--						
	ECSR-S2											
	ECSR-S3											
3	FCSR-A-S1			Screw-thread	FRP	1	+86.5°					
	FCSR-A-S2											
	FCSR-A-S3											
4	FCSR-C-S1				Screw-thread	FRP	1	-86.5°				
	FCSR-C-S2											
	FCSR-C-S3											
5	FCSR-CA-S1					Screw-thread	FRP	2	+86.5° / -86.5°			
	FCSR-CA-S2											
	FCSR-CA-S3											
6	FCSR-AA-S1						Screw-thread	FRP	2	+86.5° / +86.5°		
	FCSR-AA-S2											
	FCSR-AA-S3											
7	FCSR-SS-S1							Screw-thread	FRP	2	+60° / -60°	
	FCSR-SS-S2											
	FCSR-SS-S3											
8	FCSR-SSA-S1								Screw-thread	FRP	3	+60° / -60° / +86.5°
	FCSR-SSA-S2											
	FCSR-SSA-S3											
9	FCSR-ACA-S1	Screw-thread								FRP	3	+86.5° / -86.5° / +86.5°
	FCSR-ACA-S2											
	FCSR-ACA-S3											
10	UCSR-C1		Crescent							--	--	--
	UCSR-C2											
	UCSR-C3											

11	ECSR-C1	Epoxy	1	--
	ECSR-C2			
	ECSR-C3			
12	FCSR-A-C1	FRP	1	+86.5°
	FCSR-A-C2			
	FCSR-A-C3			
13	FCSR-CA-C1	FRP	2	+86.5° / -86.5°
	FCSR-CA-C2			
	FCSR-CA-C3			
14	FCSR-SS-C1	FRP	2	+60° / -60°
	FCSR-SS-C2			
	FCSR-SS-C3			
15	FCSR-SSA-C1	FRP	3	+60° / -60° / +86.5°
	FCSR-SSA-C2			
	FCSR-SSA-C3			
16	FCSR-ACA-C1	FRP	3	+86.5° / -86.5° / +86.5°
	FCSR-ACA-C2			
	FCSR-ACA-C3			

Note:

- a) UCSR is uncoated steel rebar;
- b) ECSR is epoxy-coated steel rebar;
- c) FCSR is FRP-coated steel rebars;
- d) S1-S3 represent specimens 1 to 3 in the same group for screw-thread steel rebars;
- e) C1-C3 represent specimens 1 to 3 in the same group for crescent-ribbed steel rebars;
- f) A and C represent one fibre ply with a winding angle of +86.5° and -86.5°, respectively;
- g) SS represents two fibre plies with a winding angle combination of +60°/-60°;
- h) CA represents two fibre plies with a winding angle combination of +86.5°/-86.5°.

Table 6.2 Parameters of steel rebars

Rebar type	Diameter (mm)	Yield stress (Mpa)	Tensile strength (Mpa)
Crescent-ribbed steel rebar	14	455	625
Screw-thread steel rebars	15	996	1120

Table 6.3 Mechanical properties of glass fibres filaments

Glass type	Sizing agent	Fibre diameter	Linear density	Tensile strength
ECR-Glass	Silane	17 to 22 μm	1200 Tex	≥ 0.3 N/Tex

Table 6.4 Concrete mix for pull-out specimens (unit: kg per m^3)

Water	Cement	Fly ash	10 mm aggregate	Sand	Superplasticizer
175	300	200	845	812	5

Table 6.5 Key results of pull-out tests

Group	Specimens	Failure mode	f_c (Mpa)	s_1 (mm)	τ_{max} (Mpa)	τ'_{max} (Mpa)
1	UCSR-S1	PO	52.1	0.53	18.3	17.9
	UCSR-S2			0.67	21.8	21.4
	UCSR-S3			0.64	19.0	18.6
2	ECSR-S1	PO	54.1	0.57	15.7	15.1
	ECSR-S2			0.52	22.2	21.3
	ECSR-S3			0.54	19.5	18.8
3	FCSR-A-S1	PO	54.1	0.97	27.2	26.1
	FCSR-A-S2			0.2	19.4	18.6
	FCSR-A-S3			0.56	23.7	22.7
4	FCSR-C-S1	PO	54.1	0.45	22.6	21.7
	FCSR-C-S2			0.33	23.0	22.1
	FCSR-C-S3			0.33	22.1	21.3
5	FCSR-CA-S1	PO	54.1	0.36	27.9	26.8
	FCSR-CA-S2			0.28	23.8	22.9
	FCSR-CA-S3			0.42	28.4	27.3
6	FCSR-AA-S1	PO	59.4	0.4	21.7	19.9
	FCSR-AA-S2			0.22	19.9	18.3
	FCSR-AA-S3			0.37	24.4	22.4
7	FCSR-SS-S1	PO	52.1	0.83	21.8	21.4
	FCSR-SS-S2			0.7	22.4	21.9
	FCSR-SS-S3			0.69	23.4	23.0
8	FCSR-SSA-S1	PO	52.1	0.23	21.2	20.8
	FCSR-SSA-S2			0.47	19.9	19.5
	FCSR-SSA-S3			0.44	22.1	21.7
9	FCSR-ACA-S1	PO	52.1	0.97	24.3	23.8
	FCSR-ACA-S2			1.21	24.4	23.9
	FCSR-ACA-S3			0.75	24.1	23.6
10	UCSR-C1	PO	52.7	0.53	19.6	19.1
	UCSR-C2			0.42	21.7	21.1
	UCSR-C3			0.26	20.8	20.3
11	ECSR-C1	PO	52.7	0.73	14.5	14.1

	ECSR-C2			1.45	17.3	16.8
	ECSR-C3			0.81	19.6	19.1
12	FCSR-A-C1	PO	52.7	0.45	19.8	19.3
	FCSR-A-C2			0.21	20.74	20.21
	FCSR-A-C3	Y		0.21	26.32	25.64
13	FCSR-CA-C1	PO	52.7	0.86	19.09	18.59
	FCSR-CA-C2			0.42	23.18	22.58
	FCSR-CA-C3	Y		0.22	27.11	26.40
14	FCSR-SS-C1	PO	59.4	0.44	24.75	22.72
	FCSR-SS-C2			0.44	22.05	20.24
	FCSR-SS-C3	Y		0.31	26.06	23.92
15	FCSR-SSA-C1	PO	59.4	0.1	20.31	18.64
	FCSR-SSA-C2			0.28	24.06	22.08
	FCSR-SSA-C3	Y		0.3	29.02	26.63
16	FCSR-ACA-C1	Y	59.4	0.29	25.80	23.68
	FCSR-ACA-C2	Y		0.23	25.80	23.68
	FCSR-ACA-C3	PO		0.21	23.79	21.84

Note:

- a) “PO” represents the pulling out of steel rebars from concrete;
- b) “Y” represents the yielding of core steel rebars;
- c) f_c is the concrete strength of the corresponding batch of specimens;
- e) s_1 is the slip corresponding to the maximum load;
- f) τ_{max} is bond strength;
- g) τ'_{max} is the normalised bond strength.

Table 6.6 Parameters define the modified local bond stress-slip model

Type	α	s_1	s_2	β	τ_f	s_3
STS	3.16	0.5 mm	1.0 mm	0.29	$0.38 \tau_{max}$	$1.2 l_r$
CRS				0.20	$0.40 \tau_{max}$	$0.9 l_r$

Note: l_r is the clear distance between two steel ribs

CHAPTER 7

FLEXURAL PERFORMANCE OF CONCRETE BEAMS REINFORCED WITH FRP-COATED STEEL REBARS

7.1 INTRODUCTION

This chapter presents an experimental study on the flexural behaviour of concrete beams reinforced with FCSRs (i.e., FCSR beams). As revealed in the previous chapter, the bond performance of FRP-coated steel rebars (FCSRs) in concrete is comparable with or even better than that of uncoated steel rebars (UCSRs) and is superior to that of epoxy-coated steel rebars (ECSRs). However, the existing research has shown that the flexural performance of concrete beams reinforced with ECSRs (ECSR beams) is generally worse than that of concrete beams reinforced with UCSRs (UCSR beams). Subbaram and Komarasamy (2021) studied the flexural behaviour of concrete beams reinforced with hybrid FRP-wrapped steel bars and found that the load capacity of the beams reinforced with this type of innovative bars decreased to 50% of UCSR beams. The failure mode of the beam changed to shear failure for hybrid FRP-wrapped steel bar-reinforced concrete beams with a stirrup spacing of 300 mm. The flexural toughness was smaller than one-third of the UCSR beams. These test observations confirmed the poor bond performance of this type of

innovative bar to concrete. The types of fibre used in hybrid FRP-wrapped steel bars showed almost no influence on the flexural performance of the beams (Sijavandi *et al.* 2021). Shang et al. (2022) found that the flexural performance of the graphene/epoxy-coated steel rebar-reinforced concrete beams is comparable to that of UCSR beams, while the maximum crack width and the average crack spacing increased.

In view of the detrimental effects of the coating layer on the flexural performance of steel-reinforced concrete (RC) beams, this chapter aims to study and analyse the flexural performance of FCSR beams. A total of 16 beams were tested with the research parameters, including the number and the winding angle(s) of fibre plies in the FRP coating layer. The test results were compared with those of UCSR beams and ECSR beams.

7.2 EXPERIMENTAL PROGRAMME

7.2.1 Materials

(1) Steel Rebars

Grade HRB400 steel rebars with crescent ribs and nominal diameters of 14 mm and 10 mm, respectively, conforming to GB/T 1499.2-2018 (GB/T-1499.2 2018) were used to produce the longitudinal FCSRs and placed at the bottom side of beams. Construction rebars of the same grade and diameter were placed at the top side of the beams. Grade HRB400 steel rebars with crescent ribs and a nominal diameter of 6 mm conforming to GB/T 1499.2-2018 (GB/T-1499.2 2018) were used to manufacture stirrups. The mechanical properties of these rebars are shown in Table

7.1. As two batches of the $\Phi 14$ Grade HRB400 steel rebars were purchased at different times from the same supplier, they are referred to as batches I and II in Table 7.1 for clarity.

(2) FCSRs

FCSRs were prepared with the manufacturing procedure that has been introduced in Chapter 3. AM-8910 epoxy resin (Wells Advanced Materials Co., Ltd.) and ECT469L-1200 glass fibre filaments (CPIC) with a linear density of 1200 tex were used to produce the FRP coating layer. The critical properties of the steel rebars, epoxy resin, and glass fibre that are used to produce FCSRs are given in Tables 3.1-3.3, respectively. The framework for FCSR beams is shown in Figure 7.2.

(3) Concrete

The concrete used for casting the FCSR beams was provided by Multi-way Industries company, Hong Kong. The concrete used coarse aggregate with a maximum size of 10 mm and had a slump of about 150 mm in its fresh state. Nine standard concrete cylinders were also cast to measure the concrete strengths at different time periods. Compressive tests were carried out with a MATEST compression machine at the ages of 28, 52, and 93 days; three cylinders were tested at each age. The mean axial compressive strengths were 39.7 MPa, 42.12 MPa, and 41.16 MPa at 28, 52, and 93 days, respectively. It should be noted that the ages of 52 days and 93 days correspond to the start and end of the flexural tests on FCSR beams, respectively.

7.2.2 Specimen Design and Fabrication

A total of 16 beams were designed and prepared. These beams were divided into eight groups with variables of winding angle(s) and the number of fibre plies, as detailed in Table 7.2. B-I and B-II represent beams in reference groups that were reinforced with the first batch and the second batch of the UCSRs, respectively. E and F represent the beams reinforced with ECSRs and FCSRs, respectively. The letters followed by 'F' represent the winding angle of each ply of the FRP coating, e.g., A represents a ply of FRP coating with a winding angle of $+86.5^\circ$; AC represents two plies of FRP coating with a winding angle combination of $+86.5^\circ/-86.5^\circ$; SSA represents three plies of FRP coating with a winding angle combination of $+60^\circ/-60^\circ/+86.5^\circ$. In each group, there were two identical beams. Each beam has a total length of 1.6 m and a cross-section of 140 mm \times 190 mm. Two 10 mm construction steel rebars were set at the compression zone of each beam; 6 mm diameter steel stirrups were arranged in the shear section of each beam with a spacing of 100 mm, as shown in Figure 7.3.

7.2.3 Methodology

Flexural tests were carried out on a reaction frame where the load was manually loaded with a jack, as shown in Figure 7.7. The distance between the supporting points was 1400 mm, and the pure bending zone was designed as 400 mm, which is smaller than one-third of the clear span, in order to ensure the flexural failure mode for the beams.

7.2.4 Instrumentation

A total of eight strain gauges, each with a gauge length of 10 mm, were affixed on the longitudinal rebars (including FCSRs and construction steel rebars) to measure the strain development of the tensile rebars and compressive rebars in concrete, as shown in Figure 7.3. For construction steel rebars in the compression zone, their middle span surface was first polished and cleaned with alcohol, and then three strain gauges were attached to the cleaned surface. After that, the SB tape (Tokyo Measuring Instruments Lab. Co., Ltd., TML) was used to protect strain gauges against collision and water during concrete casting. For FCSRs in the tension zone, their middle span surface was first applied with a thin layer of PS adhesive (TML) for levelling. Then, a strain gauge was attached to the levelled surface and protected by covering it with SB tape. Figure 7.5 shows the details of the installation.

Five 80 mm long strain gauges were affixed onto one side of each beam at its middle span and distributed along the height of the beam to measure the concrete strain distribution, as shown in Figure 7.4. Another two strain gauges were affixed on the rear side surface at the same height as the first and fifth strain gauges mounted at the front side. Besides, two strain gauges with the same gauge length were affixed on the top surface of each beam at its middle span along the length direction to measure the concrete compression strain.

Digital Image Correlation (DIC) method was used for further monitoring of concrete strain distribution and development and crack propagation during the loading process. The side surface of each beam with only two strain gauges was selected to paint speckle patterns. The concrete surface was first evenly sprayed with a layer of white

paint, and then the black paint was stochastically applied to the surface in tiny dots, as shown in Figure 7.6.

Seven linear variable differential transformers (LVDTs) were installed for the displacement measurements of each beam at the supporting points, the loading points, the middle-span point, and the ends of the tensile rebars in the beam, respectively. The two LVDTs installed at FCSRs' ends were used to monitor the possible slippage between FCSRs and concrete. The load and displacement signals were recorded during the whole loading process utilising a data acquisition system.

7.3 TEST RESULTS

7.3.1 Crack Patterns and Load-deflection Responses

Figure 7.8 shows the failure modes and the crack pattern at the failure of each beam. It is seen that all beams exhibited a typical flexural failure pattern, i.e., concrete at the compression side crushed after the yielding of tensile rebars. Such an observation indicates that using FCSRs to replace conventional steel rebars will not change the failure mode of concrete beams.

Figure 7.9 shows the load-deflection curves of all groups. Here, the deflection refers to the deflection at the middle span of a beam. As expected, the load-deflection curves for steel-reinforced concrete beams, as shown in Figures 7.9(a) and (b), could be divided into four stages: first, the elastic stage before concrete cracking; second, the service stage with concrete cracking before the yielding of tensile rebars; third, the post-yielding stage before concrete crushing; fourth, the post-peak stage after concrete crushing.

Table 7.3 gives the key results of beam tests, including the loads at the formation of the first crack (P_{cr}), the load at the yielding of the tensile reinforcements (P_y) and the ultimate load at the crushing of concrete (P_{ul}). Figure 7.10 further compares these three loads. As compared in Figure 7.10, the values of P_{cr} are close to each other among different groups, which could be understood that concrete cracking is governed by the tensile strength of concrete (Zhou *et al.* 2021). Both P_y and P_{ul} of ECSR-reinforced concrete beams, one-layer and two-layer FCSR beams were slightly smaller than or comparable to (-6.6% ~ 0.3%) the control group, while the P_y and P_{ul} of three-layer FCSR beams were slightly higher (4.0% ~ 10.9%) than the control group.

7.3.2 Failure Process

The typical failure process of the beams was also analysed by DIC strain fields, as shown in Figure 7.9, at four different loading stages, e.g., the stage before cracking load, the stage between cracking load and yielding load, the yielding load stage, and the ultimate load stage. It is clear that cracks appeared after the cracking loading, and the number and length of the cracks increased with the loading increasing. The crack numbers almost kept constant after rebar yielding. The concrete at the top of the beam was crushed after the beam reached its ultimate load. It should be noted that most beams reinforced with FCSRs showed comparable crack numbers and distributions to UCSR beams. The only exception is the beams reinforced with two-ply FCSRs that were manufactured with a winding angle combination of $+60^\circ/-60^\circ$ as fewer cracks with larger crack widths were developed, which are similar to those observed on ECSR beams.

7.3.3 Strain of FCSRs

Figure 7.11 shows the strain development of compressive rebars with increasing load. Each load-strain curve in Figure 7.11 is the average of the curves of two identical beams. Note that the strain gauges were destroyed near the yielding of tensile rebars, so the valid strain shown in the following figures is the data collated before the yielding of the steel rebars. It can be noted that all the steel rebars yield when strain approaches 0.2%.

Figure 7.12 shows the strain development of tensile rebars with increasing loading. Each load-strain curve in Figure 7.12 is the average of the curves of two identical beams. All curves show a bilinear trend before the yielding of steel rebars. The turning point in each curve is related to the cracking strength of the specimens. The data was valid before the failure of strain gauges, which generally occurred after the yielding of steel rebars.

7.3.4 Strain Profile and Maximum Crack Width of Concrete

The concrete strains over the beam height at three different loading stages are displayed in Figure 7.13. The strain in this figure is from the data of DIC measurements. The strains plotted along the height of the beam were calculated according to the horizontal line segments with a 300 mm length located at the midspan of the beam. The line segments can be regarded as strain gauges to monitor the horizontal strain variation of the beams during the loading process. Those “strain gauges” were distributed along the section height at a distance of 10 mm from each other. Therefore, the strain profile at each load level can be drawn according to the twenty strains over the beam height. The strain profiles of FCSR beams were quite

close to that of the UCSR beams. Moreover, the strain profiles of all beams varied linearly among the section heights at different load levels, which indicates the plane section assumption is also valid for FCSR beams.

The maximum crack width (MCW) development of beams reinforced with different types of rebars with increasing loading is shown in Figure 7.14. The curves of each group were obtained by averaging the curves of two specimens in the same group. The crack width was calculated according to the methods of Huang *et al.* (2021), three line segments were drawn perpendicular to the crack, and then the elongation of each segment was defined as the crack width. To ensure the accuracy of the calculation, the two points used to define the segment should be close to two edges of the cracks. As shown in Figure 7.14 (a), one-ply FCSR beams developed a larger MCW than the reference group but a smaller MCW than ECSR beams at a specific load. Moreover, Figure 7.14 (b) exhibits the MCM development of the beams reinforced with different plies of FRP coating. It should be noted first that specimens in two reference groups that were reinforced with the different batches of UCSRs showed a similar trend. Therefore, the developments of MCW of one-ply, two-ply, and three-ply FCSR beams were directly compared in Figure 7.14 (b). It is noted that with the increase of fibre plies, the crack control ability of the beams was also improved, and the crack resistance of three-ply FCSR beams was nearly the same as that reinforced with UCSRs. Figure 7.14 (c) compares the MCW of the beams reinforced with FCSRs that are manufactured with different winding angle combinations. For two-ply FCSR beams, FCSRs with a winding angle combination of $+86.5^\circ/-86.5^\circ$ exhibited a better crack control ability than the winding angle combination of $+60^\circ/-60^\circ$. For three-ply FCSR beams, a winding angle combination of $+60^\circ/-60^\circ/+86.5^\circ$ had a better performance than that of $+86.5^\circ/-86.5^\circ/+86.5^\circ$. The

more significant improvement between the winding angle combination of $+60^\circ/-60^\circ$ and $+60^\circ/-60^\circ/+86.5^\circ$ than that between the winding angle combination of $+86.5^\circ/-86.5^\circ$ and $+86.5^\circ/-86.5^\circ/+86.5^\circ$ illustrates that not only the number of the FRP plies can influence the crack control ability of the reinforcements, the winding angle of the outmost ply would also play a role on the crack resistance of FCSRs.

7.4 ANALYSIS AND DISCUSSIONS

7.4.1 Flexural Tests

Figure 7.11 shows the relationship between load and the strain of the construction steel rebars at the compressive zone of all beams (referred to as compressive rebars). It is seen that the strain of the compressive rebars was comparable to that of UCSRs concrete beams. Figure 7.12 shows the relationship between load and the strain of the steel rebars at the tensile zone of all beams (referred to as tensile rebars). Figure 7.12(a) compares the load-strain curves of beams reinforced with different types of rebars and suggests that the coating material has little effect on the tensile rebar strain. However, for beams reinforced with steel-FRP composite rebars, a noticeable decrease in the stiffness with the increasing loading was observed when compared with that reinforced with UCSRs (Zhou *et al.* 2021). Figure 7.12(b) compares the load-tensile reinforcement strain curves of concrete beams reinforced with FCSRs of different numbers of fibre plies. The results show that the rebars with two fibre plies and a winding angle combination of $+86.5^\circ/-86.5^\circ$ have a relatively lower stiffness after the cracking, while other coated steel rebars almost have identical properties. The deviation of this group might be attributed to the experimental error induced by the setups. Figure 7.12(c) shows the load-tensile reinforcement strain curves of the

beam reinforced with FCSRs with the different winding angle(s), which clearly show that changing the winding angle(s) (from 60° to 86.5°) of the inner winding layer would seldom affect the flexural performance of coated steel rebars in concrete.

The concrete beams reinforced with FCSRs exhibited comparable flexural performance to those reinforced with UCSRs, except the beams reinforced with two-ply FCSRs with a winding combination of +60°/-60°, which showed a closer behaviour to that reinforced with ECSRs, which was also approved by the failure process and the maximum crack width analyzed by DIC technology, but this trend was changed when comparing the results between FACA and FSSA group. The reason can be attributed to the outermost ply of the FRP coating, as the more perpendicular winding angle can create more small grooves on the FRP coating surface, which enhances the bond performance of FCSRs to concrete and, therefore, limits the development of crack widths.

7.4.2 Performance Evaluation Indexes

The flexural performance of the beams was analysed and compared in this section. The stiffness of an RC beam is defined as the secant slopes of specific segments on its load-deflection curve (Sun *et al.* 2012). The initial stiffness K_1 , the post-cracking stiffness K_2 , and the post-yielding stiffness K_3 are defined as:

$$K_1 = \frac{P_{cr}}{\Delta_{cr}} \quad (7-1)$$

$$K_2 = \frac{P_y - P_{cr}}{\Delta_y - \Delta_{cr}} \quad (7-2)$$

$$K_3 = \frac{P_{ut} - P_y}{\Delta_{ut} - \Delta_y} \quad (7-3)$$

where P_{cr} and Δ_{cr} are load and deflection correspond to concrete cracking; P_y and Δ_y are load and deflection correspond to the yielding of tensile rebars; P_{ul} and Δ_{ul} are load and deflection correspond to concrete crushing. Figure 7.15 illustrates the determination of these loads and deflections on a typical load-deflection curve.

The flexural stiffness of all the specimens decreased after the cracking developed, which indicates that effective section stiffness dominated the flexural behaviour of the cracked beams. After the yielding, the beams went into the “hardening” stage with a significant stiffness decreasing until the concrete crushing, then the specimen failed.

Except for the flexural stiffness, the ductility can also be used as an index to evaluate the flexural performance of the reinforced concrete beams.

The ductility of RC beams can be defined as the ratio of the ultimate deflection (Δ_{ul}) to the yield deflection (Δ_y) or the ratio of the ultimate energy (E_{ul}) to the yield energy (E_y) (Wang and Belarbi 2011; Li *et al.* 2021). Here E_{ul} and E_y are the areas under the load-deflection curve representing the energy dissipation capacity of the beam, as shown in Figure 7.15.

$$\mu_{\Delta} = \frac{\Delta_{ul}}{\Delta_y} \quad (7-4)$$

$$\mu_E = \frac{E_{ul}}{E_y} \quad (7-5)$$

$$E_y = \int_0^{\Delta_y} P \quad (7-6)$$

$$E_{ul} = \int_{\Delta_y}^{\Delta_{ul}} P \quad (7-7)$$

Table 7.4 summarises the loads, deflections, and estimated performance evaluation indexes. The results suggest that the thickness of the FRP coating layer influences the

ductility of the beam. It is seen that the use of one-ply FCSRs enhanced ductility by 9.98% over that of UCSRs. By contrast, the beams reinforced with two- and three-ply FCSRs exhibited a reduction in ductility ranging from 0.41% to 12.98% when compared with those reinforced with UCSRs.

7.4.3 Theoretical Analysis

According to Section 6.2.10 of GB50010-2015 (GB50010 2015), the moment capacity per equation 7-6 is based on the conventional sectional analysis of rectangular RC beams that considers equilibrium and strain compatibility.

$$M = \alpha_1 f_c b x \left(h_0 - \frac{x}{2} \right) + f_y' A_s' (h_0 - a_s') \quad (7-6)$$

where x , the depth of the compressive stress block, can be estimated by:

$$\alpha_1 f_c b x = f_y A_s - f_y' A_s' \quad (7-7)$$

where α_1 is a coefficient that is taken as 1.0 in accordance with GB50010-2015 (GB50010 2015); f_c , the cylinder compressive strength of concrete, averaged from the two concrete cylinder compressive strengths obtained at the beginning and the end of the testing period respectively in this study, is 41.6 MPa; b is the section width of the beam, which is 140 mm in this study; A_s' and f_y' are the cross-section area and yield stress of compressive rebars; h_0 is the effective depth of the beam section; a_s' is the distance between the centre of compressive rebars and the edge of the compressive zone; f_y and A_s are the cross-sectional area and yield stress of tensile rebars, respectively.

In this study, as the estimated x is smaller than $2a'_s$, the ultimate load of the beam can be estimated according to Equation 7-8:

$$M_u = f_y A_s (h_0 - a_s - a'_s) \quad (7-8)$$

The estimated ultimate loads of all groups are summarised in Table 7.5. Figure 7.16 compares the theoretical load capacity of the beams with the tested experimental results. It is seen that the experimental results exceed 10%~20% of the theoretical values calculated based on Code GB50010-2015, suggesting that the code tends to give a conservative prediction of the ultimate load of a beam reinforced with FCSRs.

The cracking moment, the external moment exerted by the load at which the first crack appears on the beam, can be estimated in accordance with Code GB50010-2015 (GB50010 2015) according to the following equation:

$$M_{cr} = \gamma f_{tk} W_0 \quad (7-9)$$

where γ is the plastic influence coefficient of the section resistance moment of concrete members. For section height smaller than 400 mm, γ is taken as 1.55. f_{tk} is the standard tensile strength of the concrete, which is taken according to Table 4.1.3-2 in Code GB50010 (2015). W_0 is the section modulus of the beam. The theoretical cracking moment and the experimental results are summarised and compared in Table 7.5. The experimental results are closely aligned with the theoretical predictions, which means that both the cracking moment and loading capacity of the FCSR beam can be designed and calculated according to Code GB50010-2015.

The deflection of the beam can be calculated by can be calculated by integrating curvatures along the beam length. The short-term stiffness of an RC beam cross-

section can be calculated according to equation 7-10 in accordance with GB50010-2015:

$$\beta_s = \frac{E_s A_s h_0^2}{1.15\varphi + 0.2 + 6\alpha_E \rho} \quad (7-10)$$

$$\varphi = 1.1 - 0.65 \frac{f_{tk}}{\rho_{te} \sigma_s} \quad (7-11)$$

$$\rho_{te} = \frac{A_s}{A_{te}} \quad (7-12)$$

where φ is the strain non-uniformity coefficient of longitudinal tensile ordinary reinforcement between cracks, can be taken according to section 7.1.2 in the code; α_E is the ratio of the elastic modulus of steel to concrete; ρ is the reinforcement ratio of longitudinal tensile rebars, which is taken as A_s/bh_0 . A_{te} is the effective section area of concrete under tension, which is taken as $0.5bh$.

The maximum deflection of the beam can be calculated according to equations 7-13:

$$f = S \frac{M l_0^2}{B} \quad (7-13)$$

where S is the deflection coefficient depending on the loading form and support condition; M is the moment, l_0 is the span length of the beam, and B is the stiffness of the beam. Therefore, the theoretical yield deflection of each beam specimen can be calculated based on their yield stress. The results show again that the experimental results are quite close to the theoretical value calculated based on Code GB50010-2015.

7.5 CONCLUSIONS

In this Chapter, a total of eight groups of reinforced concrete beams were prepared and tested. The research parameters included the coating material (e.g., epoxy and FRP), the number of fibre plies (e.g., one, two and three), and the winding angle(s) of fibre plies (e.g., $+60^\circ$, -60° , $+86.5^\circ$ and -86.5°). The test results and discussions provided in this chapter lead to the following conclusions:

- (1) The flexural performance of FCSR beams is comparable to UCSR beams and is superior to ECSR beams. As evidenced by the test results, at the yielding of tensile steel rebars, the average crack spacing of FCSR beams was close to that of UCSR beams but smaller than that of ECSR beams; the mean crack width of FCSR beams was slightly higher than that of UCSR beams but was significantly lower than that of ECSR beams.
- (2) The flexural ductility of FCSR beams is influenced by the winding configuration of the FRP coating layer, including the number and the winding angle(s) of fibre plies.
- (3) The design equations for UCSR beams in Chinese Code GB50010-2015 tend to underestimate the load capacity and the deflection at the failure of FCSR beams. It is suggested to use Chinese Code GB50010-2015 for the design of FCSR beams as it offers conservative predictions of flexural performance. No extra design equations are essentially needed to be established from the perspective of the promotion of a new type of building material.

7.6 REFERENCES

- GB50010 (2015). *GB50010*. Code for Design of Concrete Structures, Ministry of Housing and Urban-Rural Construction of the People's Republic of China, China.
- GB/T-1499.2 (2018). *GB/T 1499.2*. Steel for the Reinforcement of Concrete—Part 2: Hot Rolled Ribbed Bars, China Building Industry Press, Beijing, China.
- Huang, B.-T., Dai, J.-G., Weng, K.-F., Zhu, J.-X. and Shah, S.P. (2021). “Flexural performance of UHPC–concrete–ECC composite member reinforced with perforated steel plates”, *Journal of Structural Engineering*, Vol. 147, No. 6, pp. 04021065.
- Li, Z., Zhu, H., Zhen, X., Wen, C. and Chen, G. (2021). “Effects of steel fiber on the flexural behavior and ductility of concrete beams reinforced with BFRP rebars under repeated loading”, *Composite Structures*, Vol. 270.
- Shang, H.S., Wang, W.Z., Liu, X.H., Guo, S.Y. and Zhao, W.Y. (2022). “Study on flexural behavior of graphene/epoxy-coated-rebar reinforced concrete beams”, *Journal of Building Structures*, Vol. 43, No. 1, pp. 146-152 [in Chinese].
- Sijavandi, K., Sharbatdar, M.K. and Kheyroddin, A. (2021). “Experimental evaluation of flexural behavior of high-performance fiber reinforced concrete beams using GFRP and high strength steel bars”, *Structures*, Vol. 33, pp. 4256-4268.
- Subbaram, S. and Komarasamy, C. (2021). “Experimental and numerical studies on the flexural behavior of fibre reinforced concrete beams with innovative

hybrid FRP-wrapped steel bars”, *Journal of Asian Architecture and Building Engineering*, Vol. 20, No. 5, pp. 520-532.

Sun, Z.Y., Yang, Y., Qin, W.H., Ren, S.T. and Wu, G. (2012). “Experimental study on flexural behavior of concrete beams reinforced by steel-fiber reinforced polymer composite bars”, *Journal of Reinforced Plastics and Composites*, Vol. 31, No. 24, pp. 1737-1745.

Wang, H. and Belarbi, A. (2011). “Ductility characteristics of fiber-reinforced-concrete beams reinforced with FRP rebars”, *Construction and Building Materials*, Vol. 25, No. 5, pp. 2391-2401.

Zhou, Y., Gao, H., Hu, Z., Qiu, Y., Guo, M., Huang, X. and Hu, B. (2021). “Ductile, durable, and reliable alternative to FRP bars for reinforcing seawater sea-sand recycled concrete beams: steel/FRP composite bars”, *Construction and Building Materials*, Vol. 269, No. 121264.



(a) The first batch



(b) The second batch

Figure 7.1 Steel rebars for manufacturing FCSRs



Figure 7.2 Framework of FCSR beam

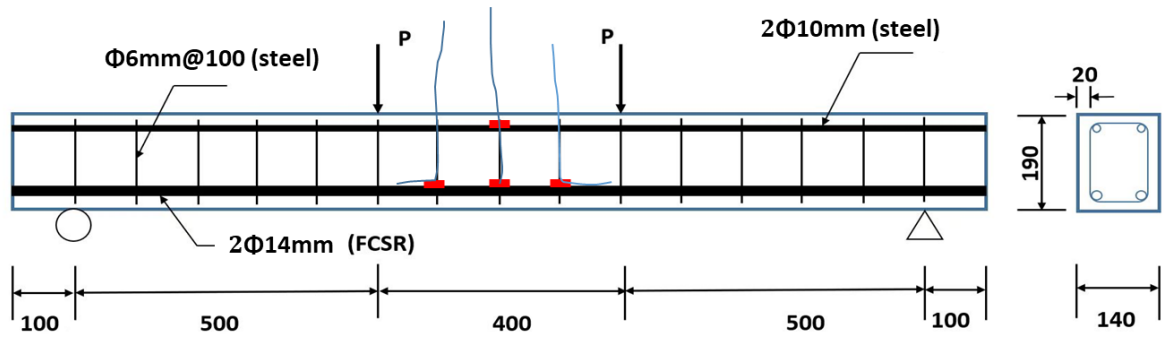


Figure 7.3 Dimensions and reinforcement details of the beam specimen

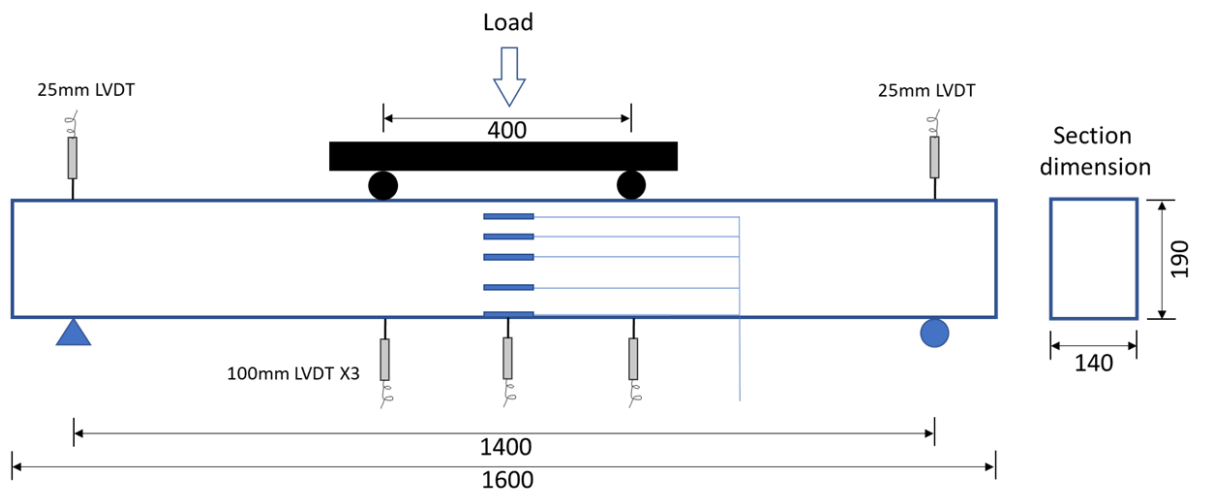
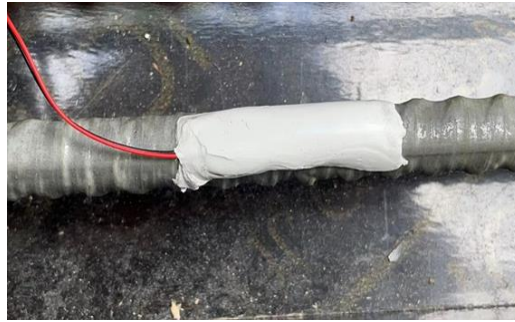


Figure 7.4 Arrangement of strain gauges

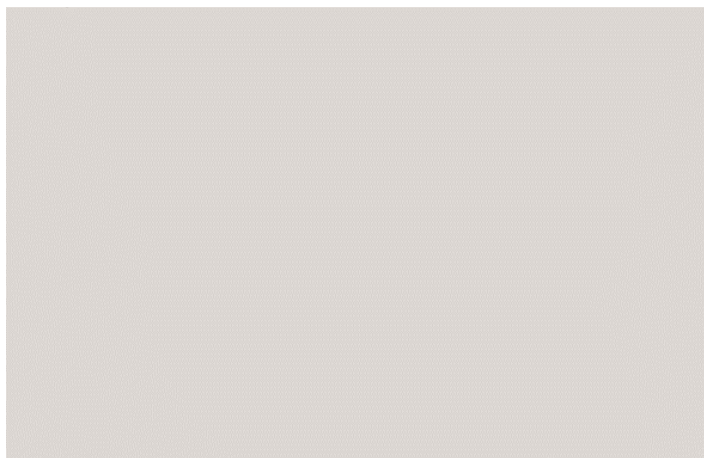


(a) polish steel rebars



(b) cover the SB tape on SGs

Figure 7.5 Processes to attach strain gauges (SGs)



(a) Spray white paint evenly onto the concrete surface



(b) Spray black dot paint to form irregular patterns

Figure 7.6 Surface preparation for DIC measurements

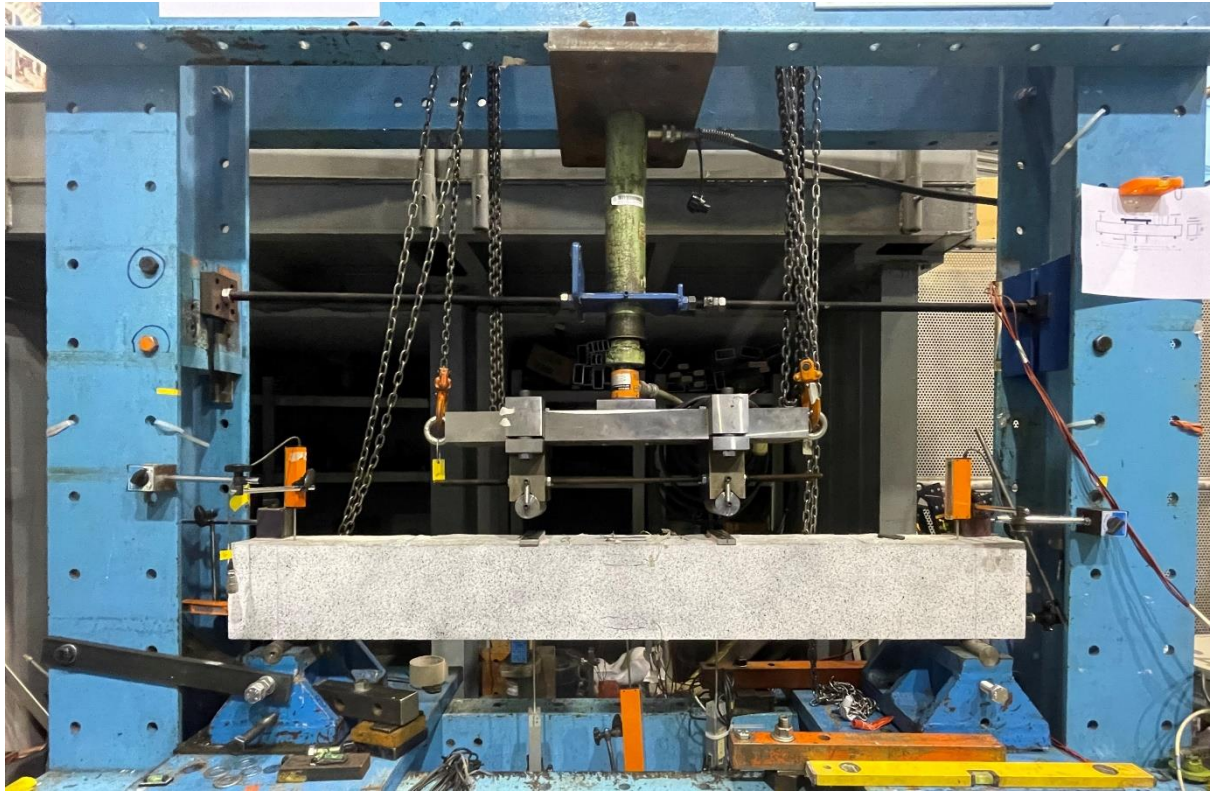
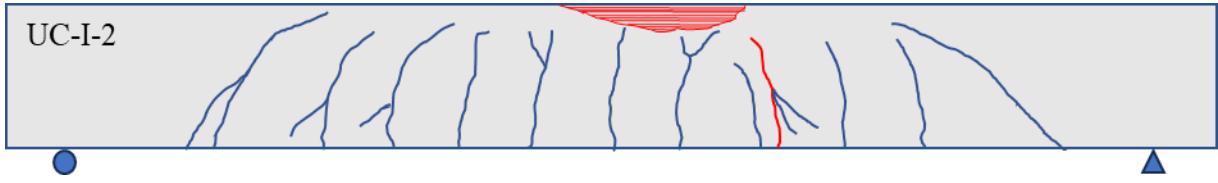
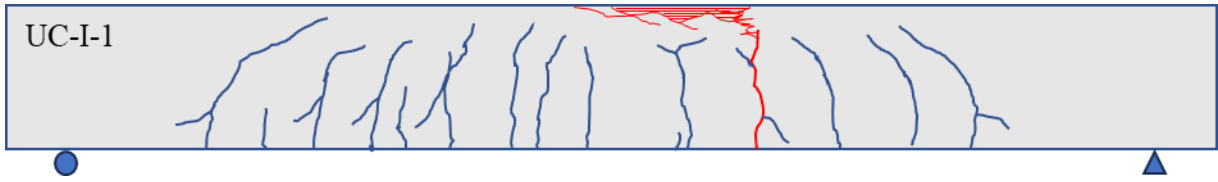
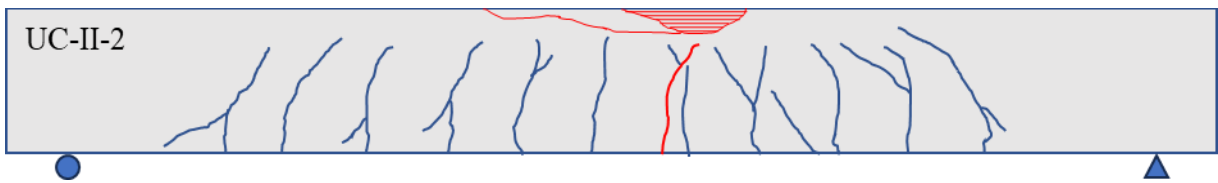
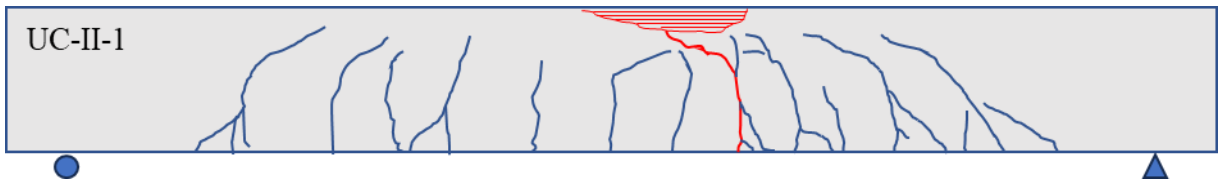


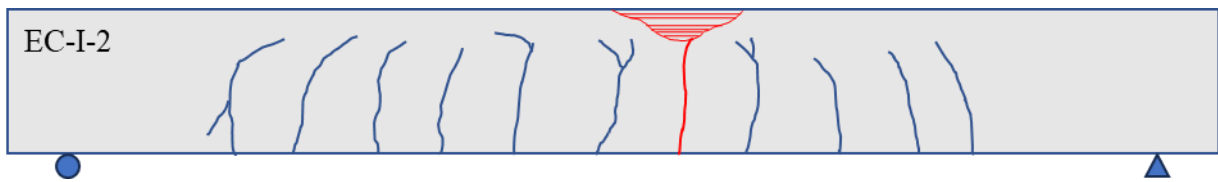
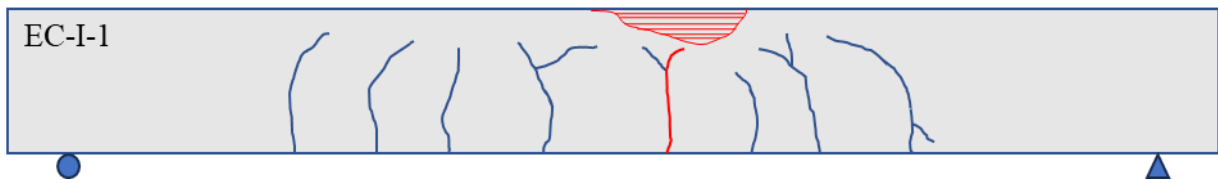
Figure 7.7 Setup for four-point bending beam tests



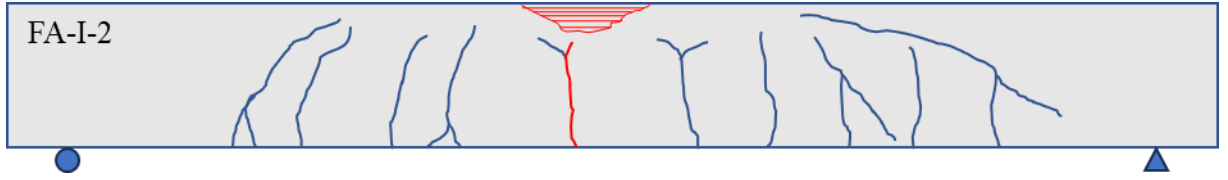
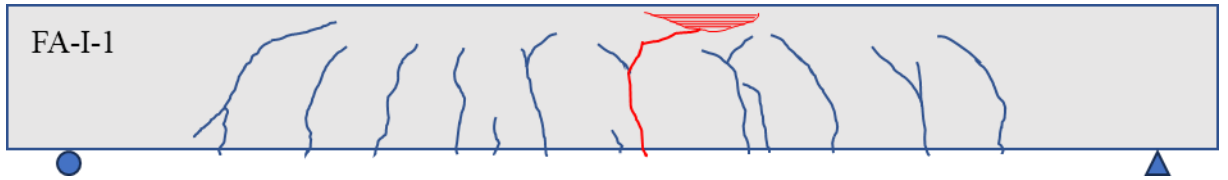
(a) UCSR beams (1st batch of steel rebars)



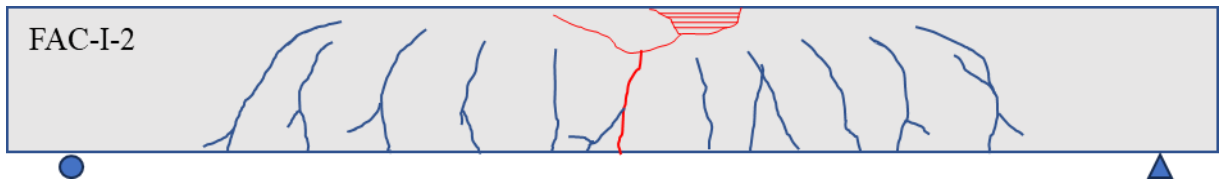
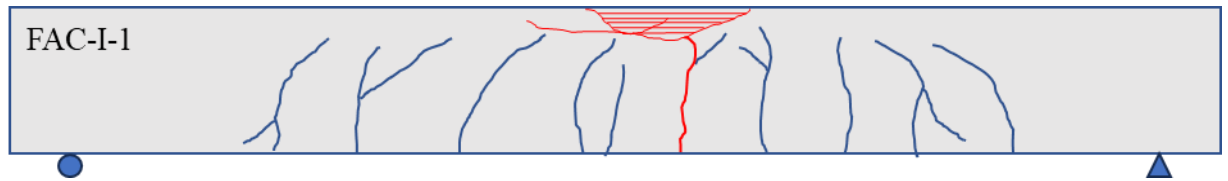
(b) UCSR beams (2nd batch of steel rebars)



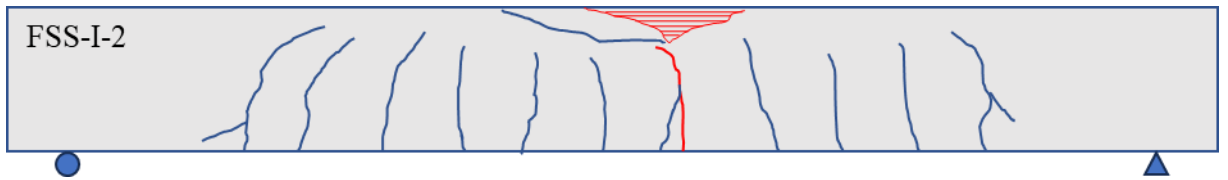
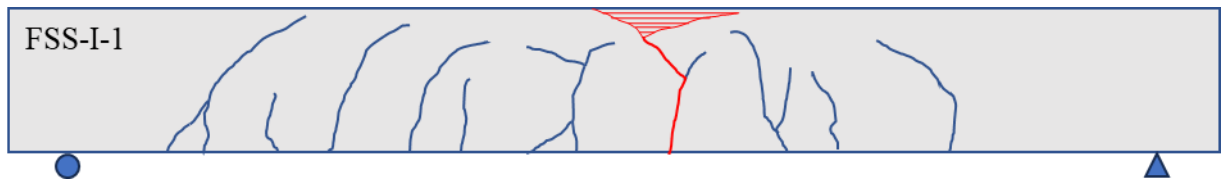
(c) ECSR beams



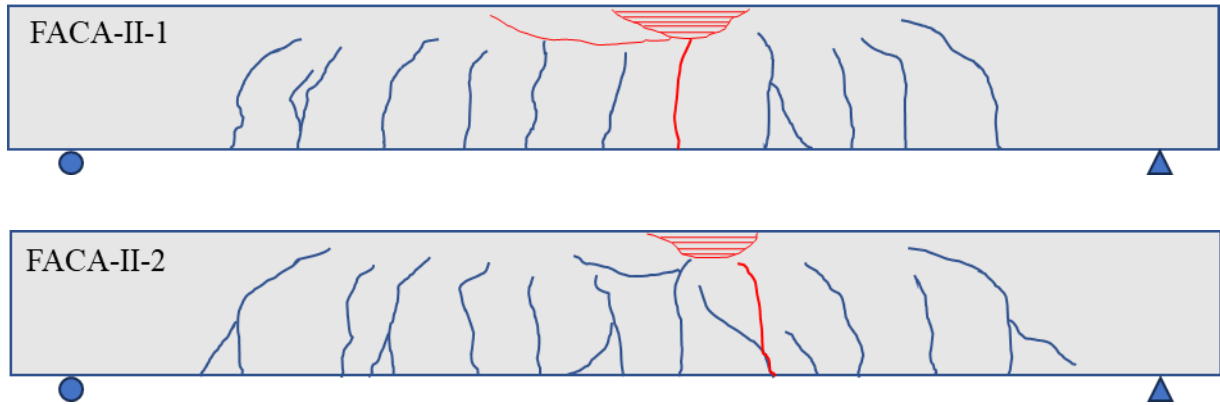
(d) One-ply (+86.5°) FCSR beams



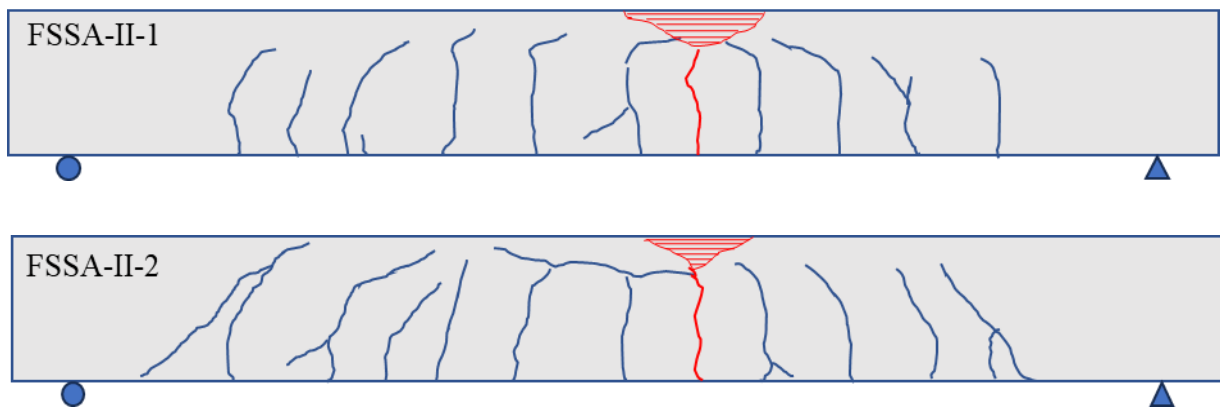
(e) Two-ply (+86.5°/-86.5°) FCSR beams



(f) Two-ply (+60°/-60°) FCSR beams

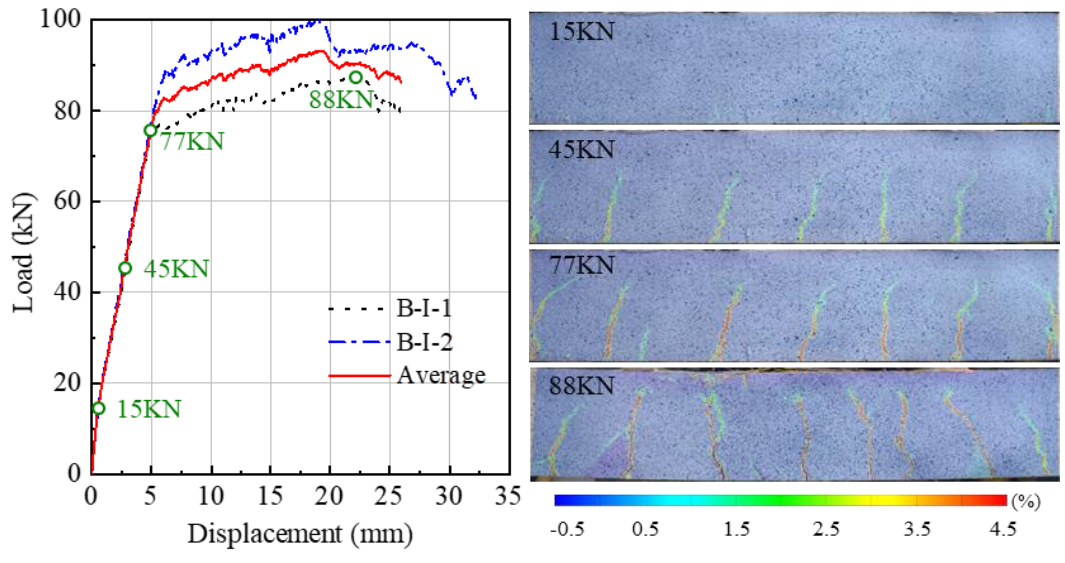


(g) Three-ply (+86.5°/-86.5°/+86.5) FCSR beams

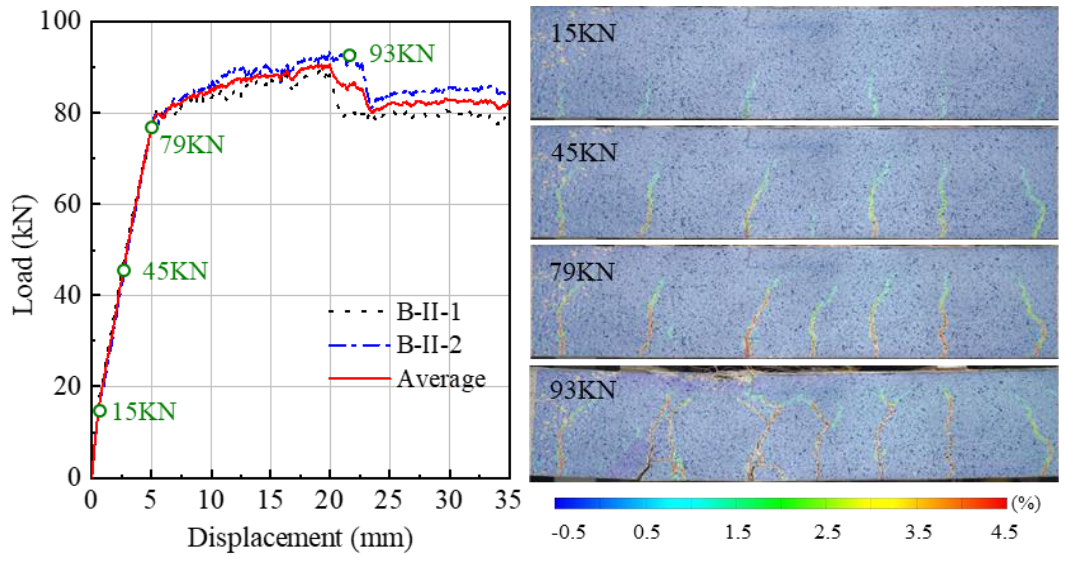


(h) Three-ply (+60°/-60°/+86.5) FCSR beams

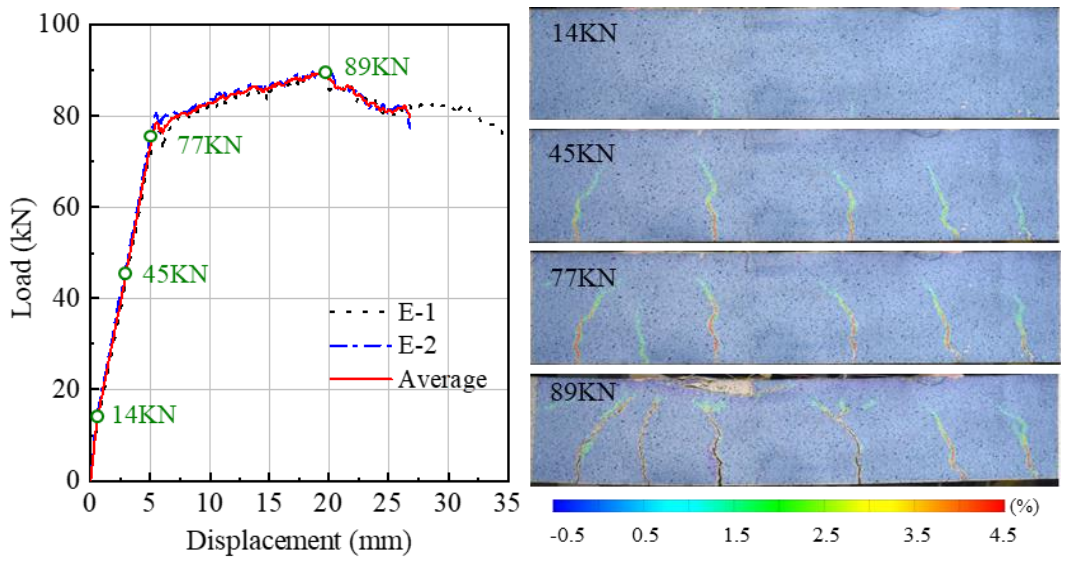
Figure 7.8 Crack patterns of beam specimens at failure



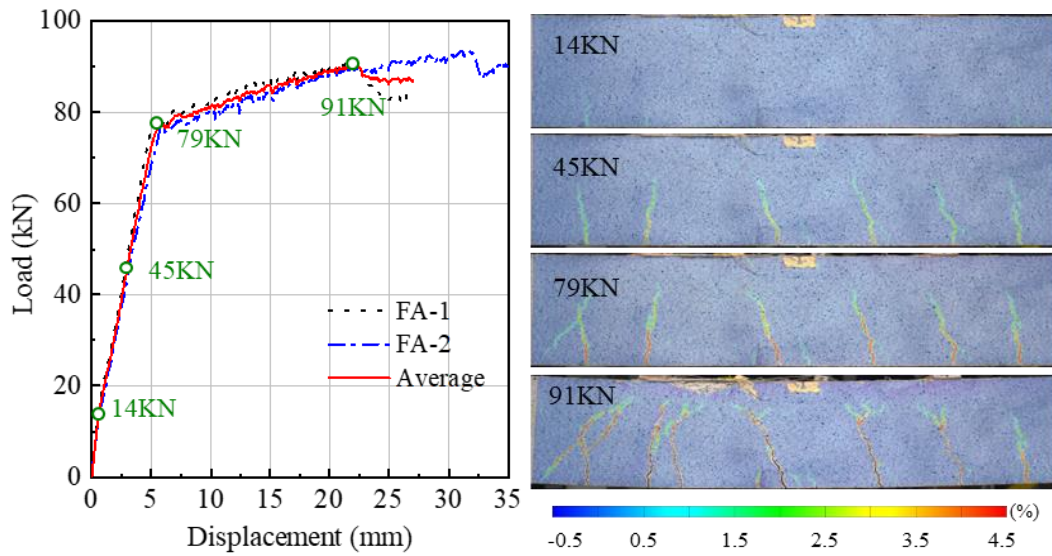
(a) UCSR-I



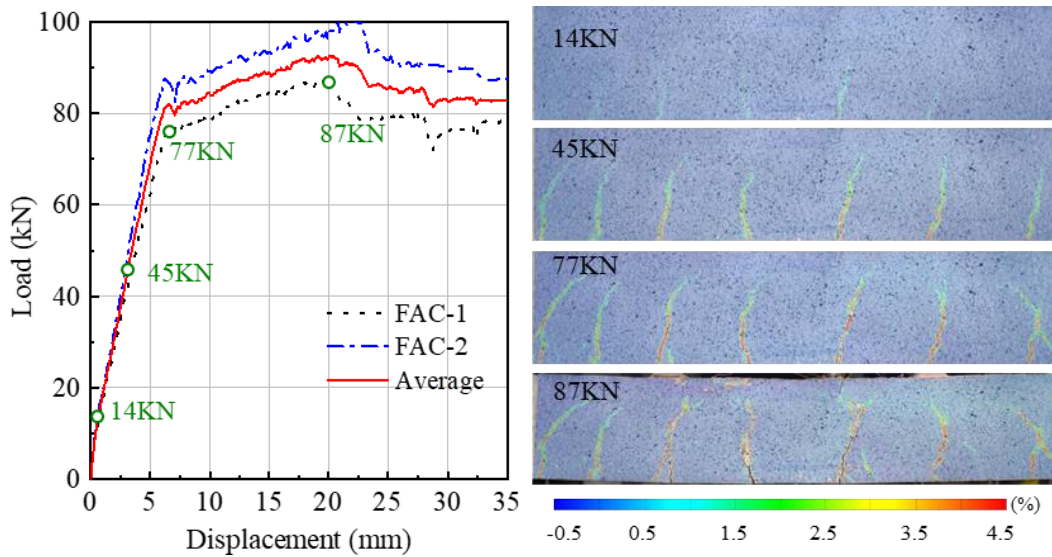
(b) UCSR-II



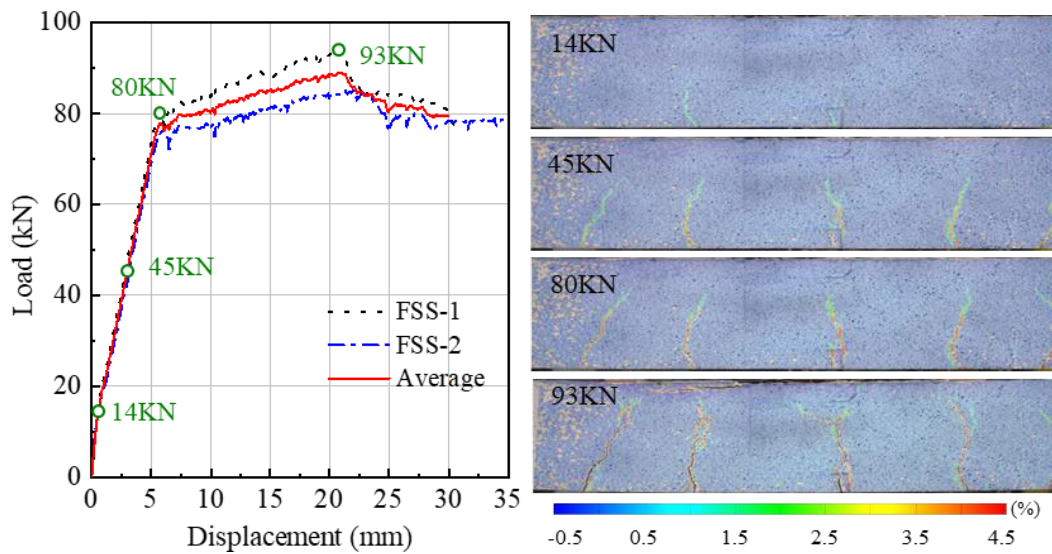
(c) ECSR



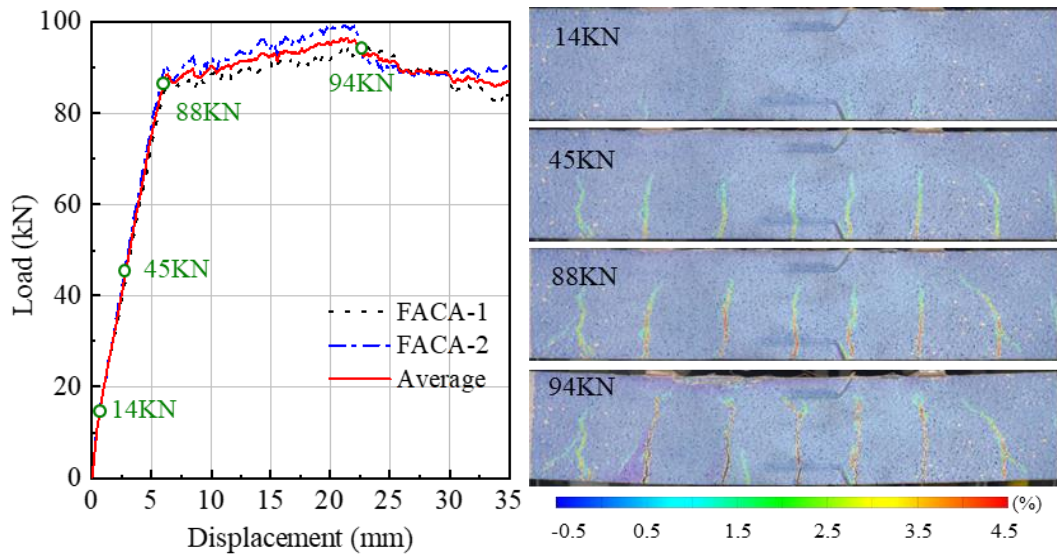
(d) FCSR-A (+86.5°)



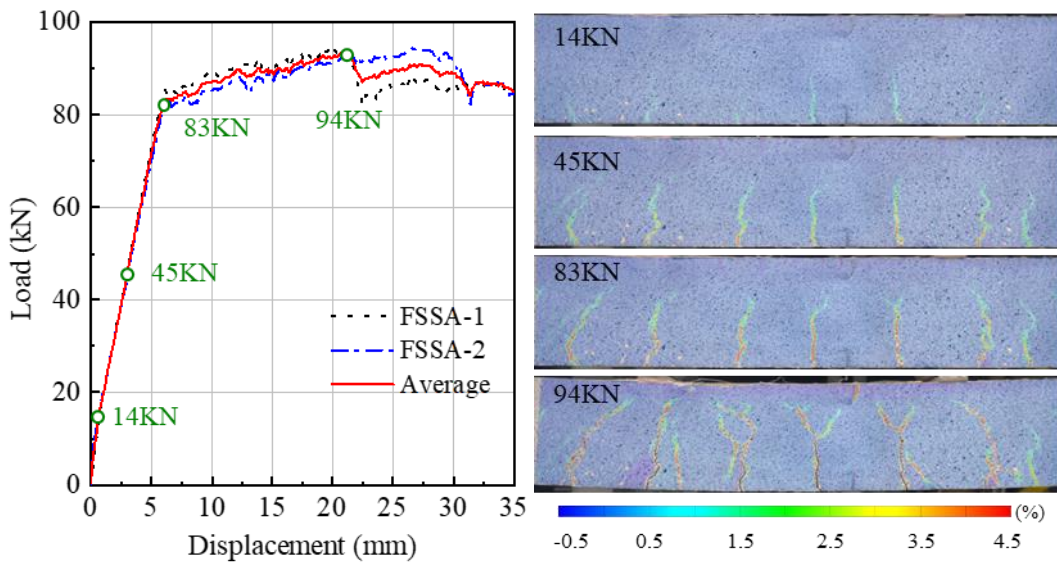
(e) FCSR-AC (+86.5°/-86.5°)



(f) FCSR-SS (+60°/-60°)



(g) FCSR-ACA (+86.5°/-86.5°/+86.5°)



(h) FCSR-SSA (+60°/-60°/+86.5°)

Figure 7.9 Load-displacement curves of concrete beams reinforced with different types of steel rebars

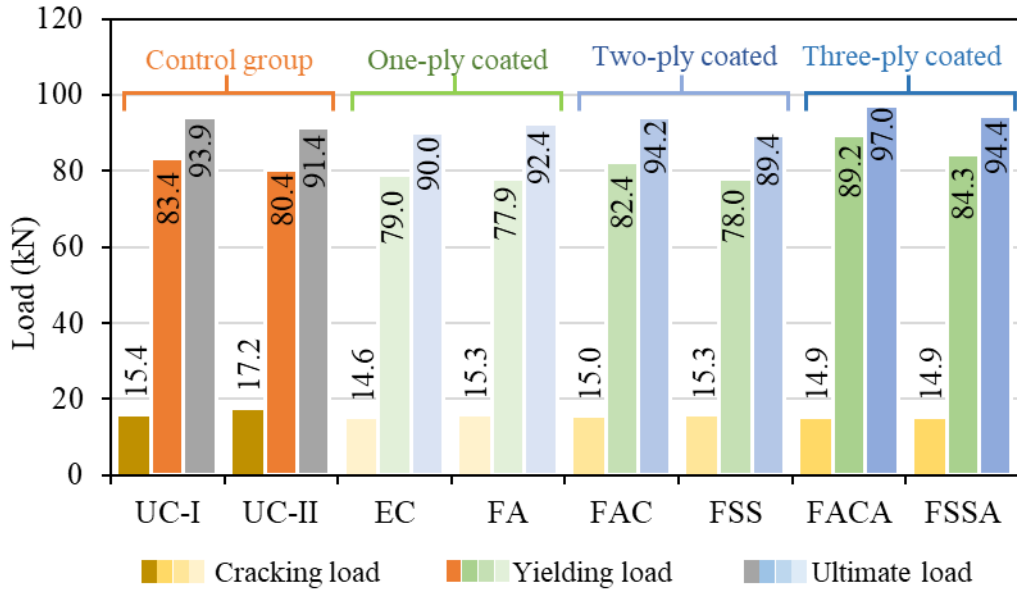


Figure 7.10 Cracking load, yielding load and ultimate load of concrete beams reinforced with different types of steel rebars

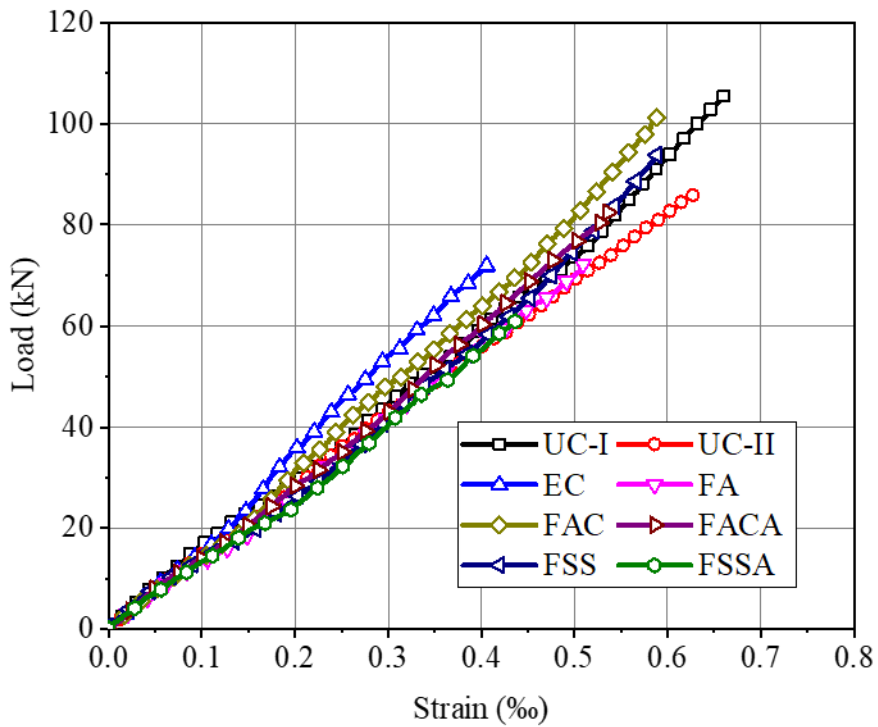
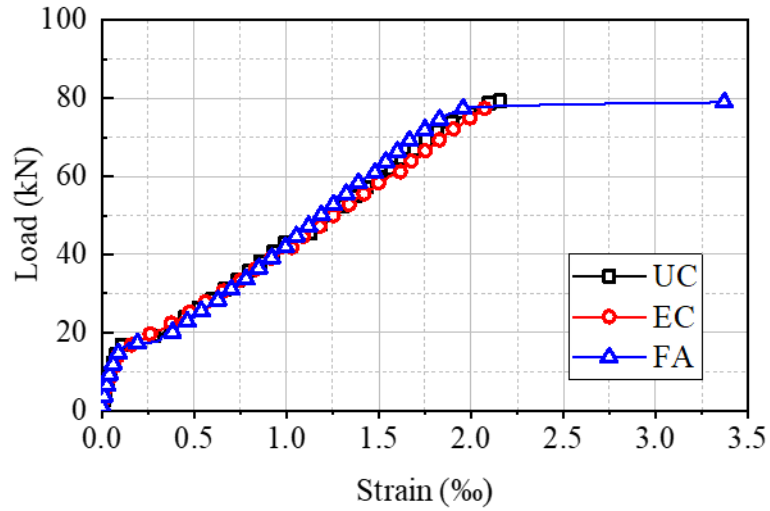
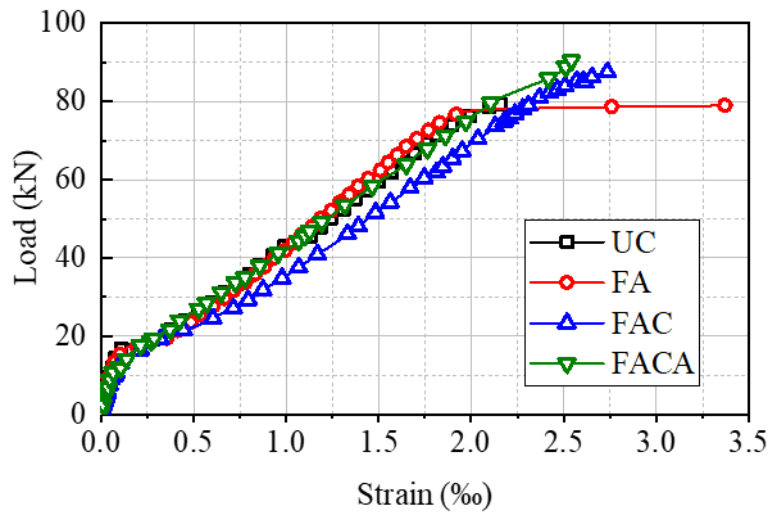


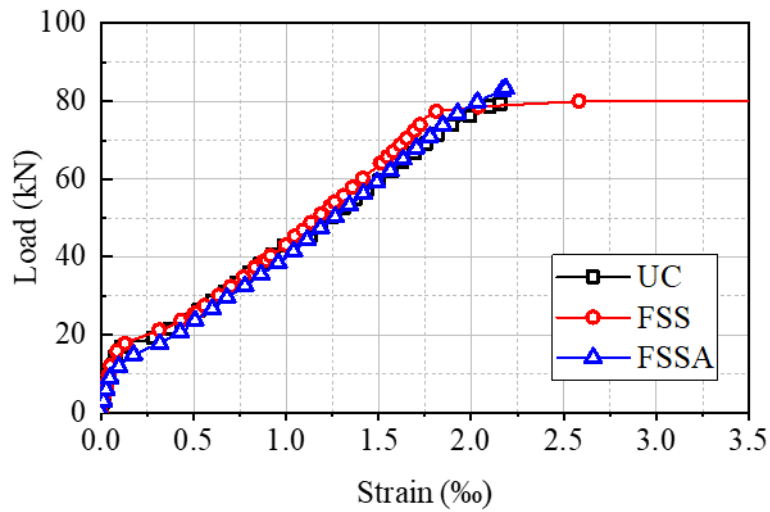
Figure 7.11 Load-strain curves of compressive rebars



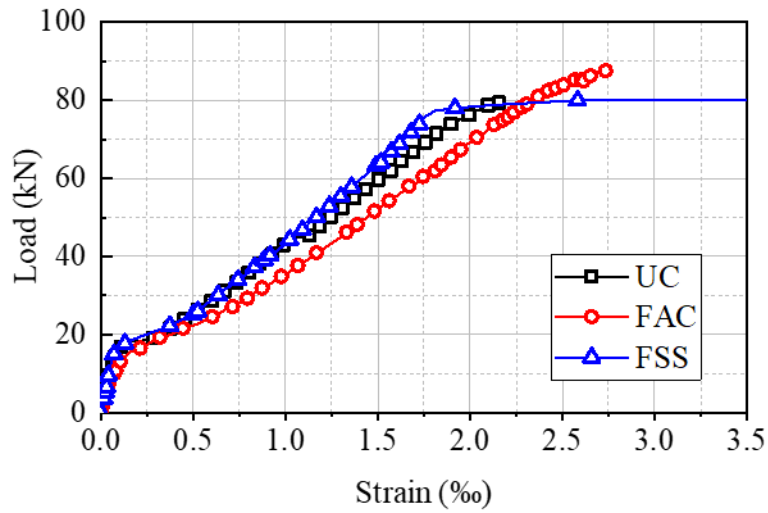
(a) Steel rebars with different types of coating materials



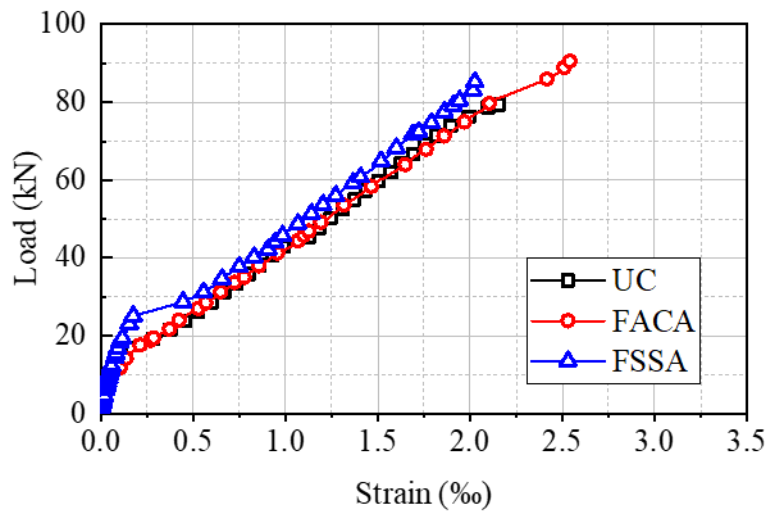
(b) FCSRs with different numbers of 86.5° fibre plies



(c) FCSRs with different numbers of 60° fibre plies

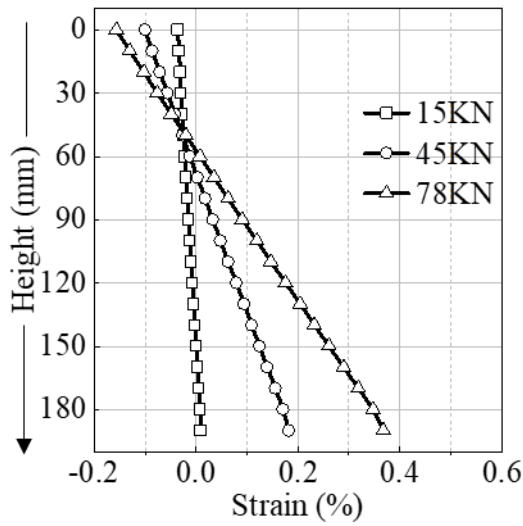


(d) Two-ply FCSRs with different winding angles (AC: $\pm 86.5^\circ$; SS: $\pm 60^\circ$)

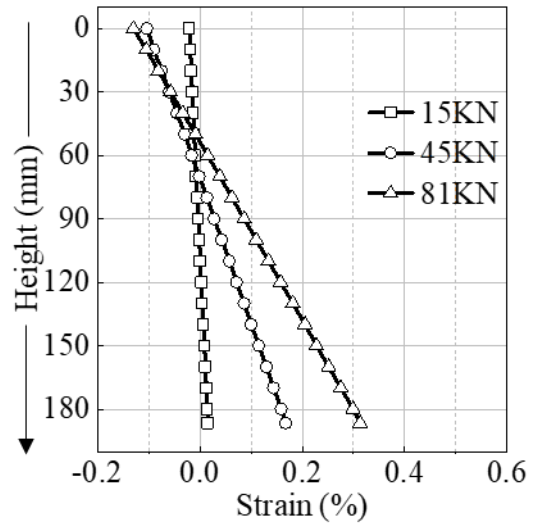


(e) Three-ply FCSRs with different winding angles (ACA: $+86.5^\circ/-86.5^\circ/+86.5^\circ$; SSA: $+60^\circ/-60^\circ/+86.5^\circ$)

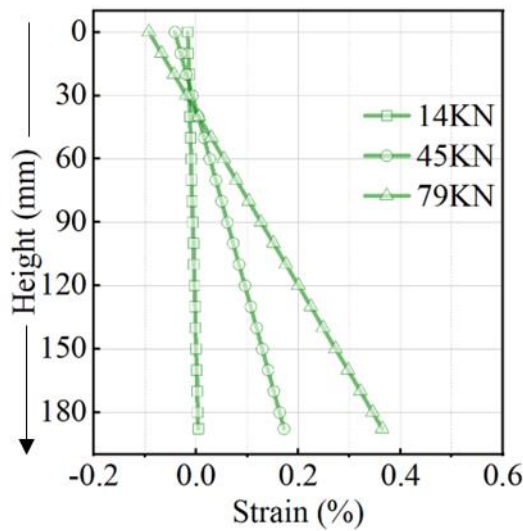
Figure 7.12 Comparisons of the load-strain curves of different types of tensile steel rebars



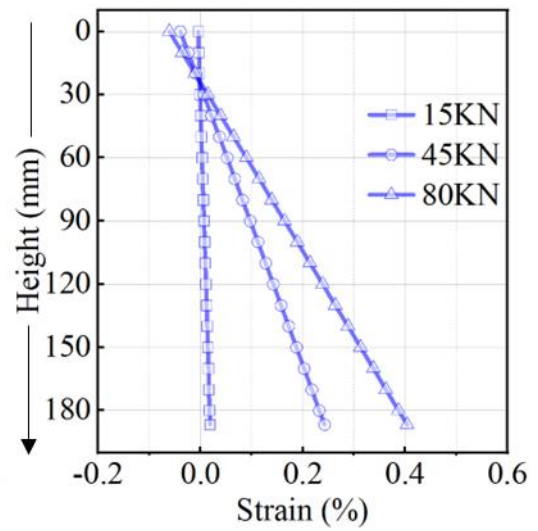
(a) UCSR-I



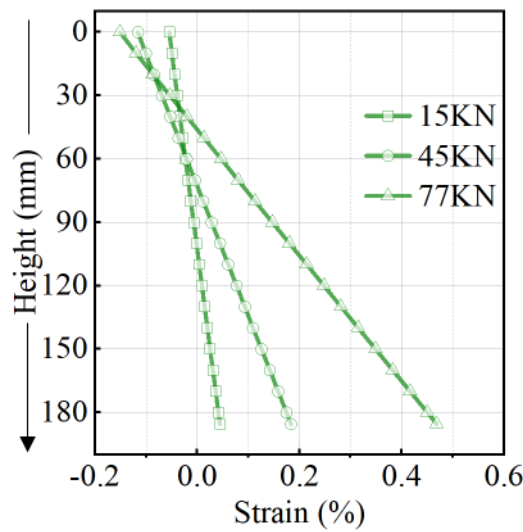
(b) UCSR-II



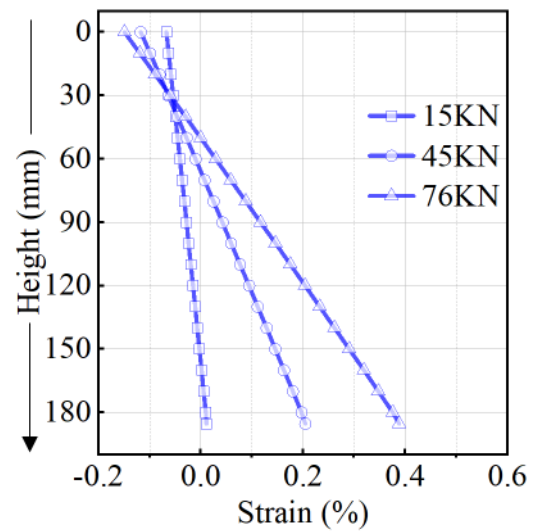
(c) FCSR-A (+86.5°)



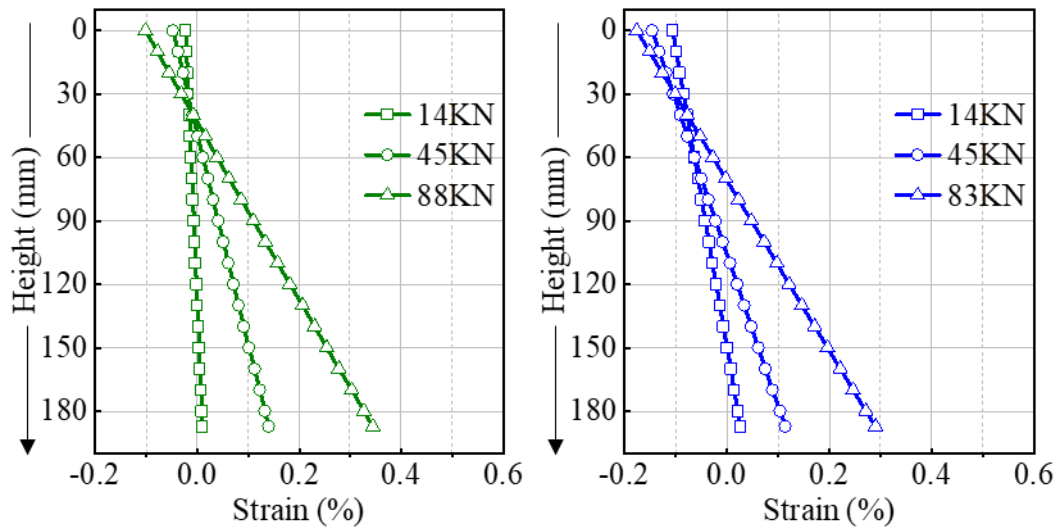
(d) ECSR



(e) FCSR-AC (+86.5°/-86.5°)



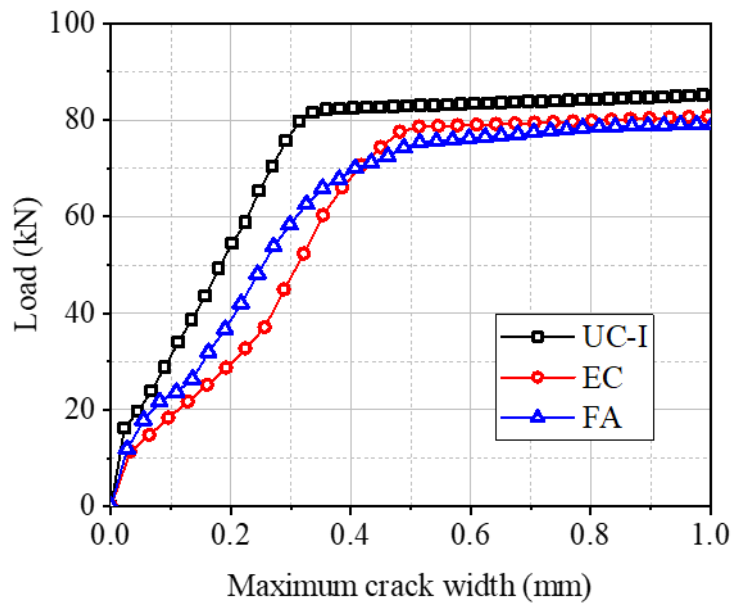
(f) FCSR-SS (+60°/-60°)



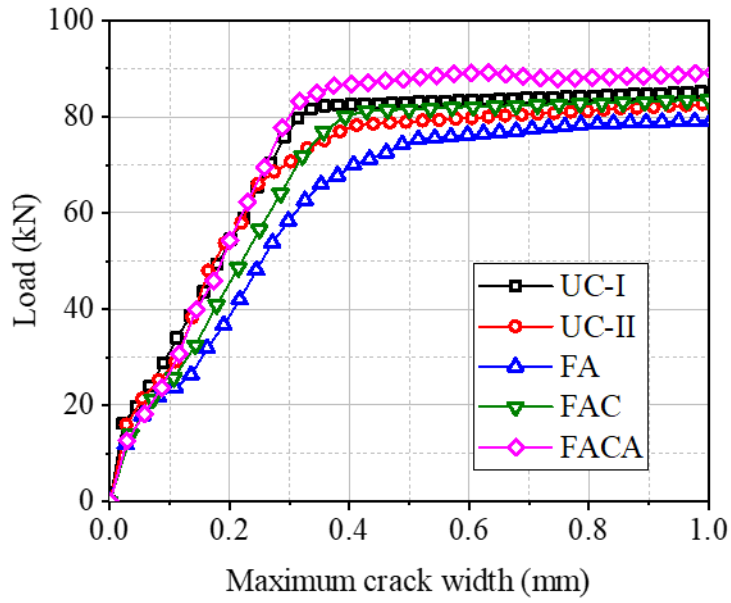
(g) FCSR-ACA (+86.5°/-86.5°/+86.5°)

(h) FCSR-SSA (+60°/-60°/+86.5°)

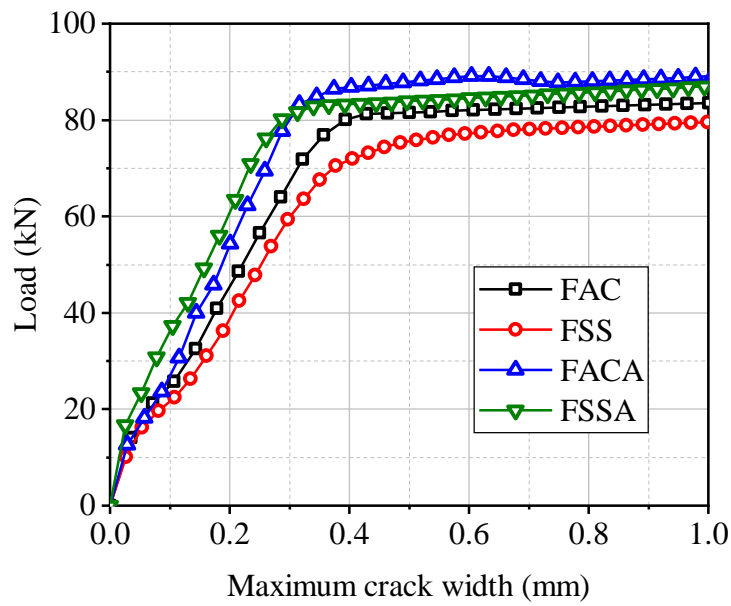
Figure 7.13 The strain profiles of concrete beams reinforced with different types of steel rebars



(a) Steel rebars with different types of coating materials



(b) FCSRs with different numbers of fibre plies



(c) FCSRs with different winding angles of fibre plies

Figure 7.14 Comparisons of the maximum crack width developments of concrete beams reinforced with different types of steel rebars

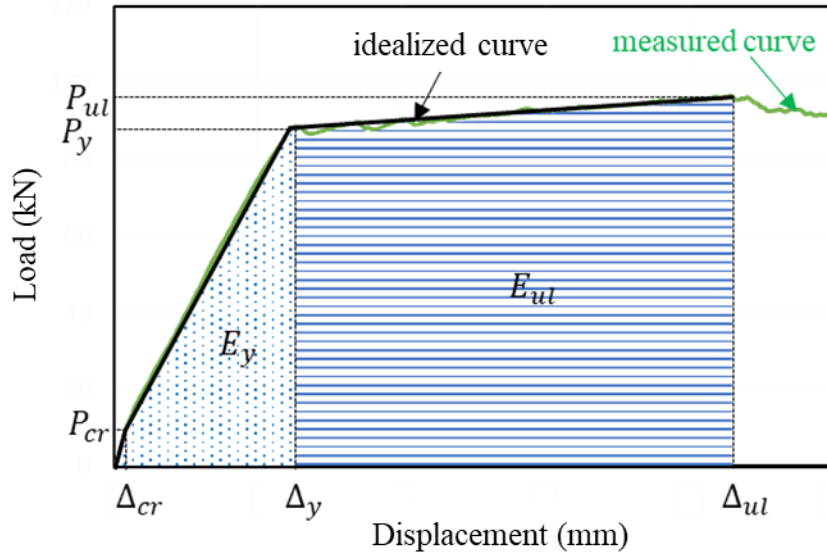
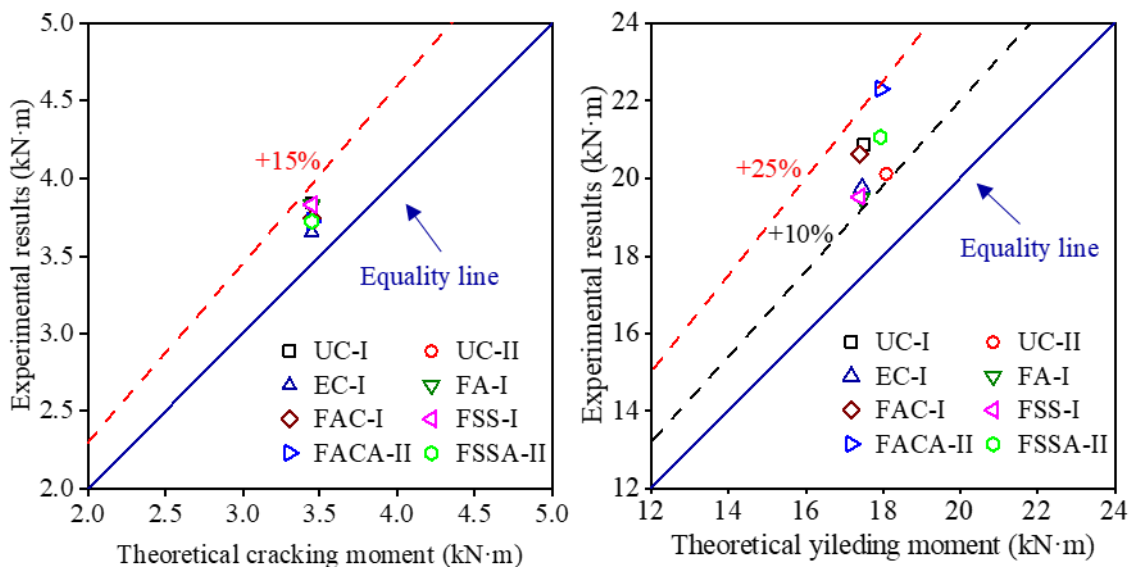


Figure 7.15 Parameters relevant to the ductility index calculation



(a) Cracking moment

(b) Yielding moment

Figure 7.16 Comparisons between theoretical and experimental moments

Table 7.1 Mechanical properties of steel rebars

Rebar batch	Diameter (mm)	Yield stress (MPa)	Tensile strength (MPa)
I	14	455	625
II	14	470	570

Table 7.2 Test matrix for flexural behavior of reinforced concrete beams

Group	Series	Rebar batch	Coating material	Number of coating layers	Winding angle(s)
1	UC-I-1	I	--	--	--
	UC-I-2				
2	UC-II-1	II	--	--	--
	UC-II-2				
3	EC-1	I	Epoxy	1	--
	EC-2				
4	FA-1	I	FRP	1	+86.5°
	FA-2				
5	FAC-1	I	FRP	2	+86.5° / -86.5°
	FAC-2				
6	FSS-1	I	FRP	2	+60° / -60°
	FSS-2				
7	FACA-1	II	FRP	3	+86.5°/- 86.5°/+86.5°
	FACA-2				
8	FSSA-1	II	FRP	3	+60°/-60°/+86.5°
	FSSA-2				

Note:

- a) UC-I and UC-II represent the reference beams reinforced with the 1st batch and the 2nd batch of UCSRs, respectively;
- b) EC represents the beams reinforced with ECSRs;
- c) FA represents the beams reinforced with one-ply FCSRs and a winding angle of +86.5°;
- d) FAC and FSS represent the beams reinforced with two-ply FCSRs, which were manufactured with winding angles of +86.5°/-86.5° and +60°/-60°, respectively;
- e) FACA and FSSA represent the beams reinforced with three-ply FCSRs, which were manufactured with winding angles of +86.5°/-86.5°/+86.5° and +60°/-60°/+86.5°, respectively.

Table 7.3 Key results of four-point bending beam tests

	P_{cr} (kN)	P_y (kN)	P_{ul} (kN)
UC-I-1	15.3	77.6	87.7
UC-I-2	15.6	89.3	100.0
UC-II-1	16.1	81.5	89.2
UC-II-2	18.3	79.3	93.6
EC-1	14.1	77.4	89.3
EC-2	15.1	80.6	90.7
FA-1	15.4	79.0	91.3
FA-2	15.2	76.8	93.4
FAC-1	14.4	77.4	87.2
FAC-2	15.5	87.5	101.2
FSS-1	15.7	80.2	93.8
FSS-2	14.9	75.9	85.0
FACA-1	14.2	88.0	94.8
FACA-2	15.5	90.4	99.1
FSSA-1	15.4	85.3	94.5
FSSA-2	14.3	83.2	94.3

Table 7.4 Stiffness and ductility coefficients of all groups

Group	K_1	K_2	E_{ul}	E_y	E_{ul}/E_y	Δ_y	Δ_{ul}	Δ_{ul}/Δ_y
UC-I	14.6	0.94	246	1476	6.01	5.46	19.5	3.56
UC-II	14.8	0.74	242	1500	6.20	5.37	20.0	3.72
EC	14.1	0.77	238	1430	6.01	5.56	19.7	3.54
FA	13.5	0.80	249	1647	6.61	5.73	22.3	3.90
FAC	13.0	0.69	283	1554	5.49	6.28	20.8	3.32
FSS	13.4	0.72	256	1530	5.98	5.82	21.1	3.62
FACA	13.9	0.53	314	1696	5.39	6.37	21.4	3.36
FSSA	13.5	0.65	285	1623	5.70	6.15	21.1	3.44

Table 7.5 Comparisons of the theoretical and experimental results on the cracking and yielding moments

Group	M_y^t	M_y^e	M_y^e/M_y^t	M_{cr}^t	M_{cr}^e	M_{cr}^e/M_{cr}^t
UC-I	17.5	20.9	1.19	3.45	3.84	1.11
UC-II	18.1	20.1	1.11	3.45	3.71	1.08
EC	17.8	19.8	1.13	3.45	3.65	1.06
FA	17.4	19.5	1.12	3.45	3.83	1.11
FAC	17.4	20.6	1.18	3.45	3.74	1.09
FSS	17.4	19.5	1.12	3.45	3.83	1.11
FACA	18.0	22.3	1.24	3.45	3.72	1.08
FSSA	18.0	21.1	1.17	3.45	3.72	1.08

Note:

- a) M_{cr}^t is theoretical cracking moment;
- b) M_y^t is theoretical yielding moment;
- c) M_{cr}^e is experimental measured cracking moment;
- d) M_y^e is experimental measured yielding moment.

CHAPTER 8

PRACTICAL IMPLEMENTATION OF FRP-COATED STEEL REBARS IN CONCRETE STRUCTURES

8.1 INTRODUCTION

Previous chapters have verified the excellent corrosion resistance (Chapter 4), impact resistance (Chapter 5) and structurally-related performance (Chapters 6 and 7) of FRP-coated steel rebars (FCSRs). In this chapter, two field engineering projects that employed FCSRs as part of reinforcement materials have been introduced to demonstrate the practical implementation of FCSRs further. One project adopts FCSRs as the dowel bars of road pavements at Shatin Sewage Treatment Works, Hong Kong SAR, China. The other project adopts FCSRs as the reinforcement of four beams of a concrete frame on Guishan Island, Zhuhai, China. In both applications, FCSRs are used together with seawater sea-sand concrete (SSC), which contains a huge amount of chloride ions and needs to be reinforced with corrosion-resistant rebars. This chapter gives detailed information on the two applications and discusses the difficulties encountered during the construction process.

8.2 USE OF FCSRS AS DOWEL BARS IN SSC PAVEMENT

8.2.1 Pavement Design

A specially designed prefabricated porous pavement system with water-draining road bases, which aimed to improve the overall drainage capacity of the drainage infrastructure, was designed and constructed at Ma Liu Shui, Hong Kong. This project was guested by Professor Yuhong WANG and Professor Tao YU, which utilised a series of new technologies. The total length of this special pavement was 10.3 meters, and the width was 3 meters, which was divided into three parts, as illustrated in Figure 8.1. A total of 16 dowel bars with 8 FCSRs were used in this project to connect three parts of the pavement which was cast on 23 August 2022.

Dowel bars are short bars used to connect two structural members, e.g., slabs, columns and pavements, for the shear load transfer from one slab to the adjacent one (Abo-Qudais and Al-Qadi 2000). However, steel dowel bars are easy to be corroded due to the joint openings when liquids easily invade. Corrosion of the dowel bars would lead to the level difference between two adjacent members, a decrease in the load transfer efficiency, etc. Although joint sealants, cathodic protection, galvanization, epoxy-coating, enamel coating, stainless steel rebars, and FRP bars have been adopted to retard the corrosion that occurs in the dowel bars, the corrosion can still not be completely obviated. The joint sealant would fail due to the heavy truck traffic as well as the slab expansion and contraction that are controlled by the temperature variation. (Park *et al.* 2008), epoxy-coated and enamel-coated steel dowel bars can still corrode due to the initial defects or the damages caused during the shipping and construction (Bajaj *et al.* 2014; Lee 2018). The epoxy coating was

easily debonding from the steel substrate of the dowel bars, which would lead to the pitting and rusting of the dowel (Larson and Smith 2011), the load transfer efficiency of the FRP dowel bars was low, and the shear strength deterioration of the FRP bars in the alkaline environments would reduce the load transfer efficiency (Park *et al.* 2008; Larson and Smith 2011).

The drainage system and the existence of the joint openings between pavements make the dowel bars more easily exposed to a harsh environment that has more frequently wind-driven rain and stormwater that contains aggressive agents such as chloride ions. Moreover, the FRP-reinforced seawater sea-sand concrete (FRP-SSC) was used to construct these paving slabs. The abundance of chloride ions existing in SSC would jeopardize the dowel bars since the chloride ions might be brought to the dowel bar by rainwater. FCSRs have exhibited excellent structural performance and corrosion resistance as the FRP coating layer will not change the mechanical properties of the core steel rebars and can maintain the structural performance of the rebars in the concrete, which makes FCSRs superior to FRP rebars, epoxy-coated steel rebars (ECSRs), galvanized steel rebars (GSRs), etc. Under this circumstance, FCSRs were considered as an alternative to 304 stainless steel dowel bars to connect the pavements at the $\frac{1}{2}$ height of the road base.

8.2.2 *Demonstration Plan*

The prepared specimens and the location of each dowel bar were arranged as illustrated in Figure 8.2 and Figure 8.3, respectively. Each group contains four specimens, with two kept intact while another two were impacted with an energy of 10.7 J to simulate the impacting damages that might occur during the transportation,

storage, and installation process. A group of uncoated 304 stainless steel dowel bars and a group of epoxy-coated 304 stainless steel dowel bars were prepared as reference groups. For FCSRs, two groups of specimens with different winding angles, 86.5° and 60° , were manufactured, respectively. The influence of the winding configurations on the corrosion protection behaviour of FCSRs with and without impact damages can therefore be studied.

The test matrix of the specimens is shown in Table 8.1. specimen numbers “1-2” represent the specimens without impact damages, and specimen numbers “3-4” represent the specimens that sustained the impact loadings.

8.2.3 On-Site Installation and Monitoring

In order to monitor the corrosion status of each specimen after construction, two ends of each specimen were sealed with waterproof material, with one end connected to the copper wires, as shown in Figure 8.2. Figure 8.4 exhibits the installation process of the FCSRs dowel bar adopted in this pavement project.

The wires connected to each specimen were attached to the reinforcement cages and led out to the data acquisition station near the pavement before casting the concrete. The open circuit potential (OCP) can be measured and monitored between the dowel bar, which works as the working electrode, and a piece of stainless steel rebar that is attached close to each dowel bar as the counter electrode. The relevant measurements will be performed at least once every two years.

8.3 USE OF FCSRS AS REINFORCEMENT OF SSC BEAMS

A project led by Professor Tao YU, which aims to verify the performance of various construction materials, including glass fibre-reinforced polymer rebars, newly developed wavy-shaped hybrid rebars, and FCSRs, was carried out in Guishan Island, Zhuhai. This project constructed a frame structure with various construction materials mentioned above. The detail of the frame structure and the construction layout of the FCSRs is shown in Figure 8.5-6.

Although the current research work has approved the various advantages of the FCSRs compared with the UCSRs or other types of corrosion-resistant rebars, some limitations do exist in the current products. The unbendable property of the current products limits the reprocessing of the rebars at the construction sites. Therefore, to enhance the connection between the beam and the column, a special anchorage has been designed and welded to the ends of the FCSRs, as schematically shown in Figure 8.7. The outer diameter of the steel ring is 50 mm with a width of 20 mm. It was welded onto the steel rebars with a diameter of 16mm.

The length of the steel rebars was 1600 mm, and the distance between the two steel rings was 1500 mm. Due to the restriction of the anchorage system at the steel rebars, only the section between two anchorages was wound with the FRP layer by the winding machine, and the anchorage system was then wetted layup with the impregnated GFRP cloth at the two sides of the rings and wound with prepreg thermoplastic GFRP strips at the circumferential areas. The end sections outside the anchorages were then brushed with the epoxy for ease of operation. The details of the manufactured rebars are displayed in Figure 8.8.

16 FCSRs are installed in four short beams (beam-1 and beam-2 on each side, as highlighted in yellow in Figure 8.5) of the mock-up frame structure, with two rebars installed with the distributed optical fibre sensors to monitor the performance of FCSRs periodically. The frame structure was cast on 26 May 2023 and started to be exposed to the marine environment on 31 May 2023. The inspection and monitoring of the FCSRs in the concrete structure in a marine environment will be carried out at least once every two years.

8.4 CONCLUSIONS

Two practical projects that implement FRP-coated steel rebars (FCSRs) as part of reinforcing materials have been introduced in this chapter. The first project adopts FCSRs as the dowel bars of road pavements at Shatin Sewage Treatment Works, Hong Kong SAR, China. The second project adopts FCSRs as the reinforcement of four beams of a concrete frame on Guishan Island, Zhuhai, China. In both applications, FCSRs were used together with SSC, which contains a huge amount of chloride ions and needs to be reinforced with corrosion-resistant rebars. The field demonstrations and observations allow the following conclusions to be drawn:

- (1) The successful implementation of FCSRs in the two demonstration projects demonstrates the great potential of FCSRs to be used as a substitute for corrosion-resistant steel rebars in RC structures in aggressive environments, e.g., coastal, and marine concrete structures.
- (2) The successful construction of the two demonstration projects has provided a reference for the promotion and application of FCSRs.
- (3) FCSRs are superior to epoxy-coated steel rebars and galvanized steel

rebars in storing, transporting, and handling at construction sites.

8.5 REFERENCES

- Abo-Qudais, S.A. and Al-Qadi, I.L. (2000). “Dowel bars corrosion in concrete pavement”, *Canadian Journal of Civil Engineering*, Vol. 27, No. 6, pp. 1240-1247.
- Bajaj, S., Patnaik, A., Payer, J., Liang, R.L., Manigandan, K. and Srivatsan, T.S. (2014). “Extrinsic influence of environment on the corrosion behaviour of enamel-coated steel dowel bars”, *Emerging Materials Research*, Vol. 3, No. 4, pp. 158-168.
- Larson, R.M. and Smith, K.D. (2011). *Evaluation of Alternative Dowel Bar Materials and Coatings*, Office of Research and Development, Ohio. Department. of Transportation, United States.
- Lee, S.K. (2018). *Laboratory Evaluation of Corrosion Resistance of Various Metallic Dowel Bars*, Office of Infrastructure Research and Development, Federal Highway Administration, United States.
- Park, C.G., Jang, C.I., Lee, S.W. and Won, J.P. (2008). “Microstructural investigation of long - term degradation mechanisms in GFRP dowel bars for jointed concrete pavement”, *Journal of Applied Polymer Science*, Vol. 108, No. 5, pp. 3128-3137.

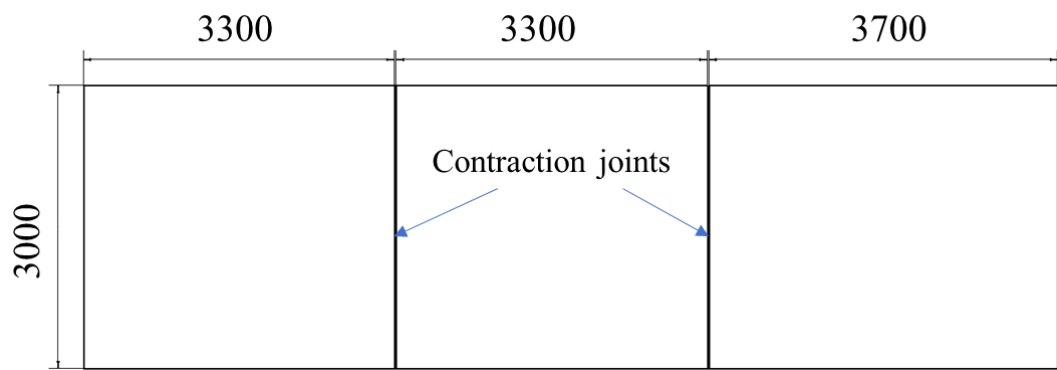


Figure 8.1 Layout of the pavement (unit: mm)



(a) Impacted specimens (b) Intact specimens (c) Uncoated specimens

Figure 8.2 Different groups of dowel bars

Impacted		Intact	
UCSR-1	=====	UCSR-3	=====
ECSR-1	=====	ECSR-3	=====
FEE-1	=====	FEE-3	=====
FSS-1	=====	FSS-3	=====
UCSR-2	=====	UCSR-4	=====
ECSR-2	=====	ECSR-4	=====
FEE-2	=====	FEE-4	=====
FSS-2	=====	FSS-4	=====
Pavement - I		Pavement - III	
		Pavement - II	

Figure 8.3 Arrangement of dowel bars on pavements

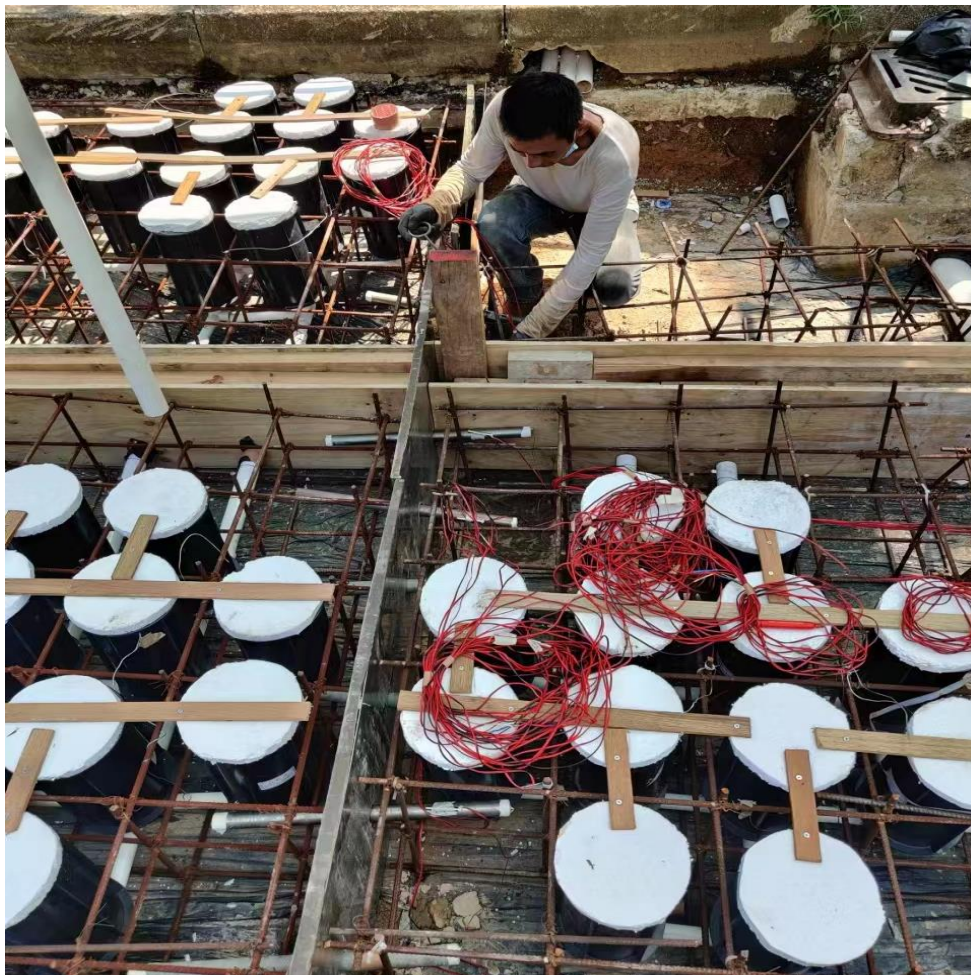


Figure 8.4 Installation of dowel bars

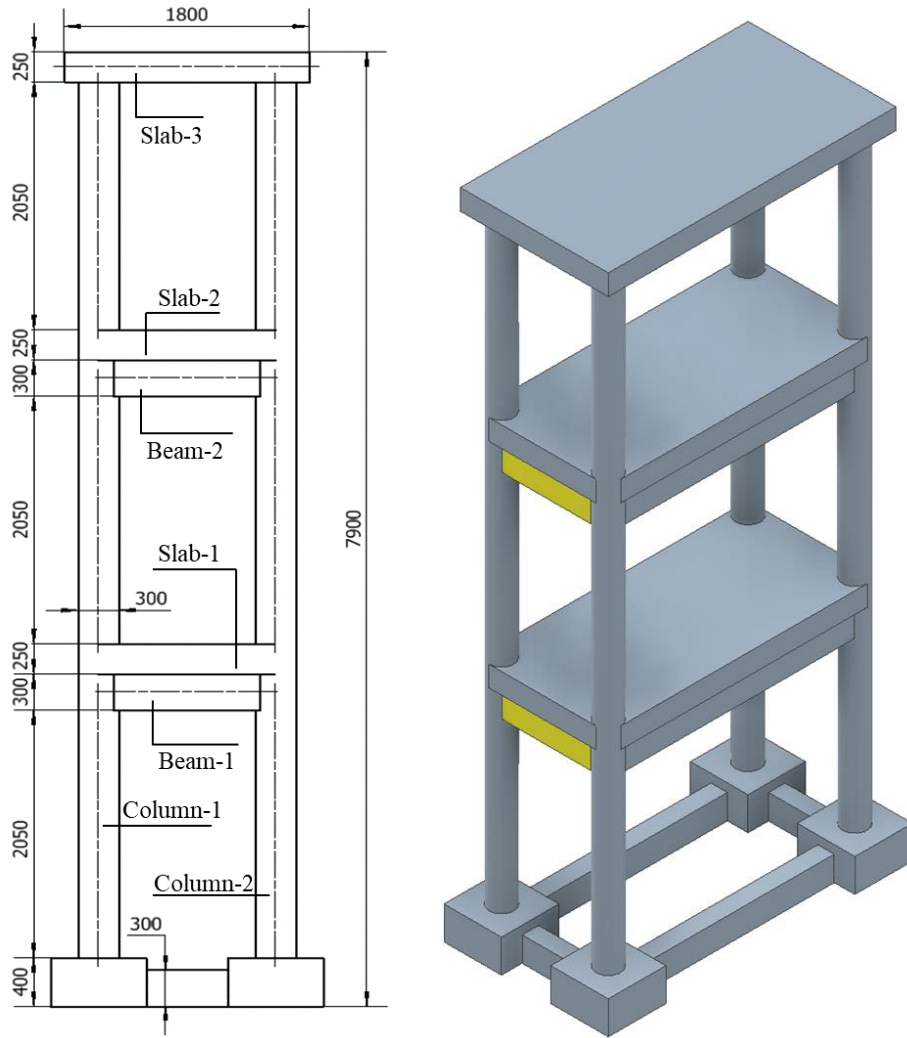


Figure 8.5 View of the three-story concrete frame

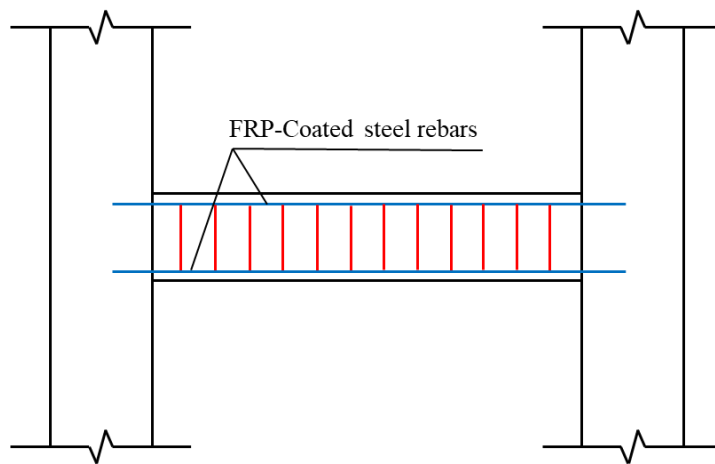


Figure 8.6 Layout of the FCSR beams

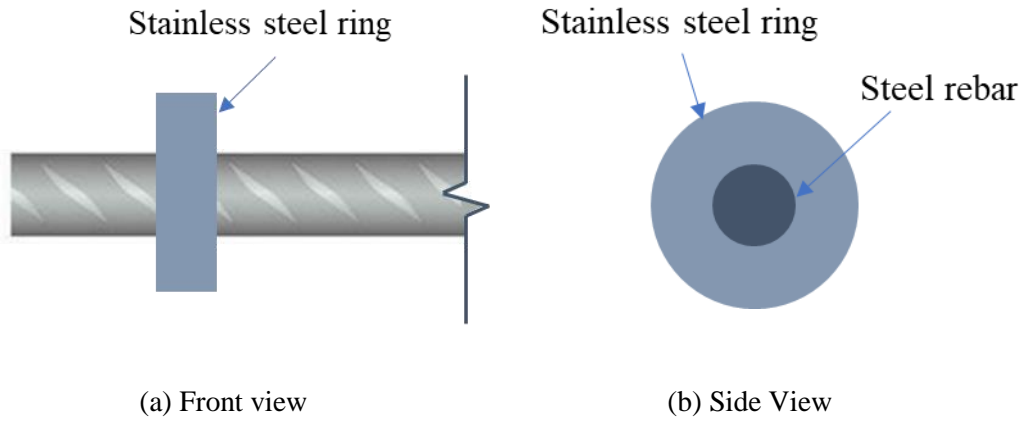


Figure 8.7 Welded anchorage to the FCSR

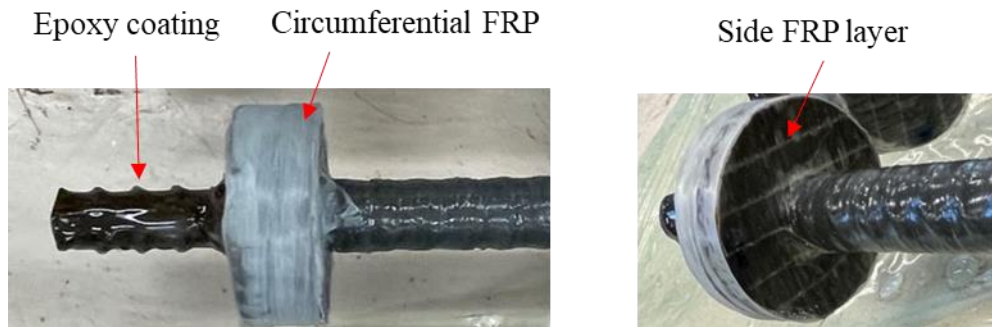


Figure 8.8 Details of the steel ring anchor of an FCSR



Figure 8.9 Field installation of the frame

Table 8.1 Details of the dowel bars in pavements

Group	Winding Angle	Impacted	Intact
UCSR	--	1-2	3-4
ECSR	--	1-2	3-4
FCSR-EE	+89°/-89°	1-2	3-4
FCSR-SS	+60°/-60°	1-2	3-4

Note:

- a) "UCSR" represents uncoated steel rebar;
- b) "ECSR" represents the epoxy-coated steel rebars;
- c) "EE" represents two fibre plies with a winding angle combination of +89°/-89°;
- d) "SS" represents two fibre plies with a winding angle combination of +60°/-60°.

CHAPTER 9

CONCLUSIONS

9.1 INTRODUCTION

Corrosion of steel has become a major challenge for the durability of infrastructure, and this is especially true for concrete structures reinforced with conventional steel rebars in marine and other corrosive environments. Up to the present, many possibilities have been explored to enhance the durability of steel-RC structures, such as using corrosion-resistant rebars, including epoxy-coated steel rebars (ECSRs), galvanized steel rebars (GSRs), stainless steel rebars, fibre-reinforced polymer (FRP) rebars, etc. However, both ECSRs and GSRs are susceptible to impact-induced local damage, which dramatically compromises their corrosion resistance. Stainless steel rebars are mainly limited by their high cost. FRP rebars have linear-elastic-brittle properties, which may cause ductility issues in structural applications.

Against the above background, this thesis has presented a research programme into the development and performance of a new type of corrosion-resistant steel rebars, which are highly durable and cost-effective. These novel rebars, referred to as FRP-coated steel rebars (FCSRs), consist of a steel rebar as the core component and a thin FRP layer (i.e., the FRP coating layer) formed using the filament winding technique.

Chapter 1 introduced the background of this research. Chapter 2 reviewed the previous studies on corrosion-resistant rebars. Chapters 3 to 5 presented the results of a series of experimental studies on the concept, manufacturing process, physical and mechanical properties, and corrosion resistance of FCSRs. Chapters 6 and 7 presented the structurally-related performance of FCSRs, including the bond performance to concrete and the flexural performance of reinforced concrete (RC) beams reinforced with FCSRs. Furthermore, two practical implementations of FCSRs were discussed in Chapter 8 to show the feasibility of utilising FCSRs as reinforcement for seawater sea-sand concrete (SSC) structures.

9.2 MANUFACTURING PROCESS AND PROPERTIES

Chapter 3 introduced two types of manufacturing methods, namely filament winding with in-line impregnation (FWII) and filament winding with vacuum-assisted resin infusion (FWVARI). The major difference between the two methods is that FWII impregnates fibre filaments first without vacuum assistance, followed by filament winding of wet filaments, whereas FWVARI winds dry fibres first, followed by vacuum-assisted impregnation. After evaluating both product quality and economy, FWII was selected as the method for manufacturing FCSRs in the subsequent studies presented in this thesis. Chapter 3 presented a systematic experimental investigation on the mechanical properties (tensile and compressive behaviour), thermal properties (the coefficient of thermal expansion and glass transition temperature) and physical properties (coating thickness and surface roughness) of FCSRs. The following conclusions were drawn on the basis of the test results and discussions presented in this chapter:

- (1) Both FWVARI and FWII are feasible for producing FCSRs of high quality. The quality of FCSRs made with FWVARI is slightly better than that made with FWII as evidenced by a lower porosity in the FRP coating layer of the former. However, due to the use of vacuum assistance in the former, the manufacturing cost of FWVARI is higher than FWII.
- (2) In addition, as the quality of FCSRs made with FWII could be refined by many costless measures, e.g., lowering the winding speed, FWII has higher cost-effectiveness than FWVARI.
- (3) The mechanical behaviour of an FCSR is very similar to that of the core steel rebar, so an FCSR retains almost all the ductility of the core steel rebar.
- (4) The coating thicknesses of FCSRs with one- and two-ply FRP coating layers were about 576 μm and 1087 μm , respectively, which are thicker than the values of ECSRs. The test observations suggest that the permeability of the coating layer of FCSRs is lower than that of ECSRs.
- (5) The larger surface roughness of FCSRs than ECSRs suggests better bond performance to concrete when they are utilised as reinforcement for concrete structures.

9.3 CORROSION AND IMPACT RESISTANCE

Chapters 4 and 5 presented experimental studies into the corrosion and impact resistance of FCSRs. Electrochemical tests were performed to understand the

corrosion evolution of FCSRs with different numbers of fibre plies, and the results were compared with those of epoxy-coated steel rebars (ECSRs). A novel method that enables a quantitative assessment of the impact-induced damage of the coating layer of coated steel rebars was developed and utilised in this chapter. Chapter 4 focused on the exposure tests of FCSRs, including immersion in 3.5 wt% NaCl solution in the laboratory, exposure to the outdoor atmospheric environment of Hong Kong, and field exposure at an artificial island of the Hong Kong-Zhuhai-Macao bridge. Chapter 5 presented a systematic experimental study on the impact resistance of FCSRs with the research parameters, including the number and the winding angle(s) of fibre plies in the FRP coating layer. The following conclusions were drawn based on the studies presented in Chapters 4 and 5:

- (1) The FRP coating layer protects well the core steel rebar against electrochemical corrosion. As evidenced by the test results, after half a year of exposure to the outdoor atmospheric environment of Hong Kong, or one year of immersion in 3.5 wt% NaCl solution or two years of exposure in the splash zone at an artificial island of the Hong Kong-Zhuhai-Macao Bridge, FCSRs remained uncorroded.
- (2) The corrosion rates of FCSRs are many orders of magnitude lower than those of UCSRs and ECSRs when immersed in 3.5 wt% NaCl solution under ambient conditions.
- (3) An FRP coating layer is far superior to an epoxy coating layer in terms of impact resistance and peel resistance during the construction process. The superior performance of the FRP coating layer is due to the fact that the use of continuous fibres as reinforcement minimises/constraints cracks and avoids through-cracks in the coating layer, and the use of the

filament winding technique ensures tight contact between the FRP coating layer and the core steel rebar.

- (4) The impact resistance of the FRP coating layer of FCSRs improves with an increasing number of fibre plies and is greatly influenced by the winding angle(s) of the fibre plies in the FRP coating layer.
- (5) The novel impact damage assessment method indirectly quantifies impact-induced coating damage by testing the post-impact electrochemical behaviour of coated steel rebars. It is an alternative to the existing visually-based impact damage assessment methods for coated steel rebars.

9.4 STRUCTURALLY-RELATED PERFORMANCE

Chapters 6 and 7 focused on the structurally-related performance of FCSRs to demonstrate their performance as reinforcement for concrete structures. Chapter 6 presented an experimental investigation on the bond performance of FCSRs to concrete with the test parameters being the number (i.e., one, two and three) and the winding angles (i.e., $+86.5^\circ/-86.5^\circ$ and $+60^\circ/-60^\circ$) of fibre plies in the FRP coating layer and the rib patterns of the core steel rebar (i.e., crescent and screw-thread). Chapter 7 presented an experimental study into the flexural performance of concrete beams reinforced with FCSRs with the test parameters being the number and the winding angles of fibre plies in the FRP coating layer. The following conclusions were drawn:

- (1) The bond performance of FCSRs to concrete is comparable to or even

better than that of UCSRs and is superior to that of ECSRs. As evidenced by the test results, the bond strengths of FCSRs made with crescent-ribbed and screw-thread steel rebars were 7.6% and 16.5% higher than those of UCSRs, respectively. By contrast, the bond strengths of ECSRs made with crescent-ribbed and screw-thread steel rebars were 17.4% and 11.5% lower than that of UCSRs, respectively.

- (2) The bond performance enhancement resulting from the FRP coating layer could be understood from two aspects: (i) the larger roughness of the FRP coating layers results in better mechanical interlocking between the reinforcement and concrete; (ii) the enlargement of diameter by the FRP coating layer while as local bond stresses were deduced using the nominal diameter of the core steel rebar.
- (3) The winding configuration of the FRP coating layer, including the number and the winding angle(s) of fibre plies, greatly influences the bond performance of FCSRs to concrete.
- (4) Comparisons were made between the test local bond stress-slip curves and the predictions based on Model Code 2010 (CEB-FIP 2010). The model in Model Code 2010 for UCSRs gives conservative predictions of the bond performance of FCSRs to concrete.
- (5) A local bond stress-slip model was proposed for FCSRs based on modifications of the model in Model Code 2010 for UCSRs. The modified local bond stress-slip model provides more accurate predictions of the bond strength and stiffness for FCSRs.
- (6) The flexural performance of concrete beams reinforced with FCSRs (referred to as FCSR beams) is comparable to that of concrete beams

reinforced with UCSRs (referred to as UCSR beams) and is superior to that of concrete beams reinforced with ECSRs (referred to as ECSR beams). As evidenced by the test results, at the yielding of tensile steel rebars, the average crack spacing of FCSR beams was close to that of UCSR beams but smaller than that of ECSR beams; the mean crack width of FCSR beams was slightly higher than that of UCSR beams but greatly lower than that of ECSR beams.

- (7) The flexural ductility of FCSR beams is influenced by the winding configuration of the FRP coating layer, including the winding angle(s) and the number of fibre plies.
- (8) The design equations for UCSR beams in the Chinese Code GB50010-2015 tend to slightly underestimate the load capacity and the deflection at the failure of FCSR beams. From use in practical engineering, the Chinese Code GB50010-2015 is sufficient for the designing of concrete beams reinforced with FCSRs, and no extra design equations are needed.

9.5 PRACTICAL IMPLEMENTATION

Chapter 8 presented the details of two practical implementations of FCSRs in RC structures. In the first project, FCSRs were adopted as the dowel bars of road pavements at Shatin Sewage Treatment Works, Hong Kong SAR, China. In the second project, FCSRs were used as the reinforcement of two beams of a concrete frame on the Guishan Island, Zhuhai, China. In both applications, FCSRs were used together with SSC, which contains a huge amount of chloride ions and needs to be reinforced with corrosion-resistant rebars. The successful implementation of these

two demonstration projects provided a practical reference for the application of FCSRs. The field practice suggests that FCSRs are superior to epoxy-coated steel rebars and galvanized steel rebars in storing, transporting and handling at construction sites.

9.6 FUTURE RESEARCH

This thesis has primarily been concerned with the development and fundamental performance of FCSRs. The presented test results and discussions have led to a thorough understanding of the manufacturing methods, physical and mechanical properties, corrosion resistance and structurally-related performance of FCSRs. Although FCSRs have been shown to possess great potential to replace traditional corrosion-resistance reinforcements and to be used in corrosive environments for concrete structures, further research is required in many aspects, some of which are outlined below:

- (1) Optimization of the winding angles and the number of fibre plies of FCSRs for application in different environments.
- (2) The development of a new generation of FCSRs that could be bent at construction sites would be necessary and imperative to facilitate the application of FCSRs.
- (3) Further investigations of the quantitative relationship between the impact resistance and the winding configurations of FCSRs.
- (4) Further investigations of the impact resistance of FCSRs in aggressive environments, as some researchers have found that the impact resistance of GFRP composites decreases with moisture uptake (Strait *et al.* 1992).

- (5) The development of structural health monitoring techniques for concrete structures reinforced with FCSRs.
- (6) Further investigations of other structurally-related behaviours, such as shear behaviour, fatigue behaviour, and fire resistance of FCSRs in concrete members.

9.7 REFERENCES

CEB-FIP. (2010). *Model Code for Concrete Structures*. Thomas Telford Services Ltd., London.

Strait, L.H., Karasek, M.L. and Amateau, M.F. (1992). "Effects of seawater immersion on the impact resistance of glass fiber reinforced epoxy composites", *Journal of Composite Materials*, Vol. 26, No. 14, pp. 2118-2133.